CFD Modelling of Ogee Spillway Hydraulics and Comparison with Physical Model Tests

by

Placide Nshuti Kanyabujinja

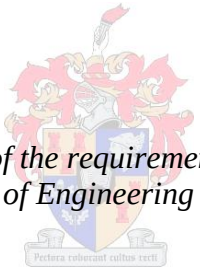

Thesis presented in fulfilment of the requirements for the degree of Master of Engineering in the Faculty of Engineering at Stellenbosch University

Supervisor: Prof. G.R. Basson

March 2015

DECLARATION

By submitting this thesis electronically, I declare that the entirety of the work contained therein is my own, original work, that I am the sole author thereof (save to the extent explicitly otherwise stated), that reproduction and publication thereof by Stellenbosch University will not infringe any third party rights and that I have not previously in its entirety or in part submitted it for obtaining any qualification.

Signed ……. Date …….

ABSTRACT

Modern Computational Fluid Dynamics modelling (CFD) are becoming common design and analysis tools in the engineering field. Nowadays, project designs involve the use of CFD techniques along with physical scale modelling to analyse the complex rapidly varied and turbulent flows which would not be easily analysed by physical modelling. In particular, the consideration and/or use of CFD modelling in the Hydraulic Engineering field remains on the increase. Apart from being used for comparison with other design techniques, CFD may in future become a standalone modelling technique in hydraulic structures design.

This research aims to use CFD models to validate the simulation of the flow over two ogee dam spillways which are installed in the Hydraulic Laboratory of Stellenbosch University. To achieve this simulation of the flow which involves an interaction between water and air, the flow behaviour has been mapped by the Volume of Fluid (VOF) and the realisable "$k-\varepsilon$" turbulence numerical models. The Volume of Fluid (VOF) and the realisable "$k-\varepsilon$" models simulate the free surface of two-phase flow and the flow turbulence, respectively.

Firstly, the study embarks with details on the actual design approaches of a typical ogee dam spillway. It subsequently presents the geometry and dimensions of the physical models, the testing procedure and the experimental test results achieved from this modelling exercise. For CFD modelling, a commercially available Computational Fluid Dynamics (CFD) package, Ansys-Fluent, was used. To model the physical model, the use of Reynolds-averaged Navier-Stokes equations in combination with the realisable k-ε eddy-viscosity closure model was adopted. The process of CFD model development and the underlying theory of it are discussed in this thesis. Different test scenarios including steady and fully hydrodynamic states simulation for two and three-dimensional geometries were considered in this simulation to achieve the most accurate results. In order to determine the required mesh size, the mesh sensitivity tests were conducted on the 2 dimensional and 3 dimensional models.

Finally, the pressure readings and water levels produced by numerical models are discussed through a validation process by comparing the CFD model results with the results obtained from physical models. The outcome proved that CFD models are able to map the behaviour of both flow phases since they exhibited a close correlation to those achieved in the physical models. Even though some slight differences in values were revealed, the graphical trend remains reasonably similar for all test results.

OPSOMMING

Moderne gerekenariseerde vloeidinamika numeriese modelle (CFD) word deesdae dikwels deur ingenieurs gebruik. Projekontwerpe sluit tans die gebruik van CFD tegnieke asook fisiese skaalmodellering in om komplekse, vinnig-veranderede en turbulente vloei te ontleed. Hierdie tipe vloeie is moeilik om met fisiese modellering te ontleed. Die gebruik van CFD numeriese modelle in hidrouliese ingenieurswese is besig om toe te neem, Die bevindinge van CFD modelering word tans vergelyk met die bevindinge van ander ontwerptegnieke, maar in die toekoms mag dit moontlik gebruik word as die enigste modelleringstegniek in hidrouliese struktuurontwerp.

Die doel met hierdie navorsing is om CFD modelering te gebruik om die vloei oor twee ogee-vormige afvoergeute wat in die hidrouliese labrotorium van die Universiteit van Stellenbosch ge-installeer is, te ondersoek. Ten einde hierdie vloei, wat die interaksie tussen water en lug insluit, te simuleer, is die vloeigedrag deur ”volume van vloeistof” (VOF) en die "$k-\varepsilon$" turbulensie numeriese modules, gemodeleer. Die VOF en "$k-\varepsilon$" numeriese modules simuleer onderskeidelik die vry oppervlakte vloei van die twee-fase vloei en turbulente vloei.

Die ontwerp van ’n tipiese ”ogee”-tipe dam oorloop word bespreek, gevolg deur die beskrywing van die geometrie van die fisiese modelle, die toetsprosedure en die eksperimentele toetsresultate. Vir die CFD modellering is die CFD pakket, Ansys-Fluent, gebruik. Vir die simulering van die fisiese model is die Reynolds-gemiddeld Navier-Stokes vergelykings tesame met die k-ε eddy-viskositeit geslote module gebruik.

Die proses van CFD ontwikkeling en die onderliggende teorie daarvan word bespreek. Verskillende toets-scenario’s wat 2D en 3D simulasies insluit, uitgevoer. Ten einde die toepaslike berekeningsrooster grootte vir die numeriese model te verkry, is sensitiewiteitstoetse uitgevoer op die twee- en drie-dimensionele numeriese modelle.

Laastens is die CFD numeries gesimuleerde drukke en die watervlakke met die van die fisiese modelle vergelyk om die akkuraatheid van die CFD resultate te verkry. Die uitkomstes het getoon dat CFD modelle gebruik kan word om die gedrag van albei vloei fases te simuleer aangesien dit goed vergelyk het met die uitkomstes van die fisiese modellering. Daar was wel klein verskille in die druk waardes, maar die tendense in drukverspreiding was ooreenstemmend.

DEDICATION

To my beautiful wife:

Agnes Nshuti Mukaruziga

and our lovely Daughter:

Bénie Oranne Nshuti.

ACKNOWLEDGEMENTS

First and foremost, I would like to express my heartfelt appreciation to my study leader and proponent, Professor Gerrit R. Basson for his immense support and encouragement. Without his valuable guidance, advice and instructions, this work would not have been successful and timeous. Apart from inestimable academic support gained from him, he is also a professional person, hardworking and humble to everyone. He is a model to me and I owe him much respect.

I would like to thank Mr Christian Visser, Mr Msadala Vincent, Mr Deside Chibwe, Mr Ousmane Sawadogo and Mr Frederic Isingizwe for their advice and generosity to discuss different challenges of my research project. I appreciate also the Stellenbosch Water Laboratory technicians for their assistance with the physical modelling exercise.

Cordial and special thanks to my beloved wife Agnes Nshuti Mukaruziga and our dearly loved daughter Beny Oranne Nshuti, who despite the distance have always been the source of strength towards the accomplishment of this thesis. Their love is too immense to express adequately in words but I owe them a very special gratitude. This is the case also with my parents, siblings and friends who gave me enormous encouragement and support in one way or another along this journey.

I extend my deep-felt thanks to my postgraduate colleagues for their companionship during these two years. I acknowledge also each and every one who has contributed to the success of this thesis. May God the Almighty bless them abundantly.

The treasury of this thesis and my fulltime attendance at Stellenbosch University would not have been possible if it were not for the generosity of my country. I thank the Government of Rwanda, which through Rwanda Education Board (REB) funded my studies and made my endeavour a success.

Lastly but not the least, I have a million reasons to thank The Almighty God for the abundant blessings that He has poured onto me as well as on my family; from my birth till now. If it had not been by his grace, I would not have managed to move an inch on my own.

Glory and praise be to Thee Lord.

Table of Contents

List of Figures

List of Tables

List of Symbols and Acronyms

C	Coefficient of discharge
CFD	Computational Fluid Dynamics
DPM	Dispersed Phase Model
Fr	Froude number
FSL	Full Supply Level
G	Gravitational force
G_b	Turbulent kinetic energy generation due to buoyancy
G_k	Turbulent kinetic energy generation due to mean velocity gradients
H	Water level measured above the crest
H_e	Head on the crest
H_o	Design head for ogee weir
h_v	Velocity Head
ICOLD	International Commission on Large Dams
K_a	Abutment contraction coefficient
L	Lateral crest width
L’	Net length of the crest
N	Pier contraction coefficient
P	Weir height
PDEs	Partial Differential Equations
PISO	Pressure-Implicit Split-Operator
Q	Discharge
R	Radius of abutment
RANS	Reynolds-average Navier-Stokes

Re	Reynolds number
USACE-WES	United States Army Corps of Engineers-Waterways Experiment Station
USBR	United States Bureau of Reclamation
V	Velocity
VOF	Volume of Fluid

CHAPTER 1: GENERAL INTRODUCTION

This chapter contains the general introduction, which consists of background and motivation, objectives, research methodology and the layout of the thesis.

1.1 Background and motivation

An increasing need of water supply, flood control, navigation, hydroelectric power generation, fishing and recreation has made dam construction a high priority throughout the world. As water is of critical importance to protect, technological improvements in the design and analysis of dams are needed for a better management of water resources.

All dams are equipped with spillways as a safety measure against overtopping. They are provided to safely carry water away from the reservoir, when water levels exceed the full supply level (FSL). In the recent years, there has been an increase in the frequency of large floods leading to high inflows into reservoirs. From the catalogue of Dam Failure in South Africa, it is clear that inadequate spillway design is the main cause of dam failure with a rate of 58% (Hattingh, 2012). Therefore, the appropriate design of spillways remains relevant so as to avoid overtopping of the non-overspill part of dams (Mays, 1999).

Ogee spillways, which have a control weir with an S-shape in profile, have been substantially applied. They are deemed to be the most commonly used spillways due to their proper function, ability to control floodwater and high safety factor (Daneshkhah & Vosoughifar, 2012). Although much is understood about general ogee shape and its flow characteristics, a slight distortion in the standard design automatically affects its flow properties (Kim & Park, 2005). However, these modifications in the standard shape require engineers to evaluate the crest performance.

For over 100 years, physical modelling was the only analysis tool available used as the baseline to validate other methods (Johnson & Savage, 2006). To date, with recent advances in computational and numerical techniques, new design tools are evolving to assess rapidly varied flow situations (Savage *et al*, 2004). This development has led to the widespread use of numerical modelling as a standard design tool in various disciplines of engineering. This study seeks to examine the ability and the application of commercial Computational Fluid Dynamics (CFD) software namely “ANSYS-FLUENT” to model ogee spillways.

Computational Fluid Dynamics (CFD) is a branch of numerical modelling that has been developed for solving problems involving fluid flow. Currently a number of CFD packages are available that could be used to model a range of compressible and incompressible, laminar and turbulent fluid flow problems. Some of these include PHOENICS, FLOW-3D, STAR-CD and ANSYS Fluent which was applied in this study.

This technique has been gradually accepted by the Hydraulic/ Dam engineering community not only as an investigative tool in the research institutions (Kjellesvig, 1996; Savage & Johnson, 2001) but also as a useful design tool (Gessler, 2005). With this complementary use of CFD techniques and physical scale modelling in Hydraulic Engineering, it has become not only important but also necessary to use physical models to validate CFD modelling (Guo *et al*, 1998). In addition, it has been of paramount benefit to use CFD modelling to identify the early problematic flow features for prototype cases.

In the spillway flow field, CFD modelling is commonly used to analyse the complex hydraulic conditions such as air entrainment, flow separation, turbulence and shock waves. Savage and Johnson (2001) employed Reynolds Average Navier-Stockes (RANS) equations to study the flow over an ogee spillway. Their results for predicting the pressure heads over the spillway surface and flow rates were in good agreement with the experimental results.

Although a number of previous studies, such as Savage & Johnson (2001), Guo *et al*. (1998), Chatila & Tabbara (2004), shows a good agreement between CFD and physical modelling, a need for validation of CFD modelling with particular physical models of particular cases is still arising as there is no single universal spillway design that could work for every flow scenario. In addition to this, there is still a significant lack of calibration and validation studies between CFD and physical modelling (ICOLD, 2012).

1.2 Objectives

The main purpose of this work is to compare the numerical simulation of the hydraulics of the ogee spillway by employing physical modelling. This is done for a few cases of different discharges simulated with the CFD package called Ansys-Fluent and compared to the laboratory test data.

The specific objectives of this research include:

1. To review the analytical methods used to design ogee spillway based on USBR, USACE and other methods.
2. To carry out experimental tests on two physical models installed in the laboratory flume and to yield the basic parameters such as flow surcharge, pressure distribution on the crest and negative pressure for discharges greater than the design head.
3. To perform 2D and 3D CFD simulations of a selected spillway for steady and fully hydrodynamic scenarios with the same spillway geometry and flow conditions applied in the laboratory.
4. To determine the accuracy of the CFD results by comparing it with experimental results.
5. To determine the advantages and limitations of CFD modelling tools in the analysis of flow over an ogee spillway.

1.3 Research methodology

The research embarks with an extensive literature study to provide a state of knowledge concerning spillway design and flow characteristics for ogee spillways. In this context, various books, scientific journals and reports were reviewed.

In the literature study, firstly, the analytical methods used to analyse flow over ogee spillway were detailed. Secondly, the basic theory used in CFD modelling was reviewed.

For the experimental work, two physical models were set up in the laboratory flume. In this regard, two phases have been considered to obtain the most efficient results:

- An adjustment phase which included geometric study and preliminary trials to reveal model defects and inadequacies, and
- Testing which included a systematic examination of each feature of the proposed ogee design.

Computer modelling was applied to the experimental data tests in order to conduct a numerical analysis and provide detailed information of the complete flow regime. The computational modelling results were validated by a comparison to the results obtained from physical models. Figure 1-1 provides the layout of the validation process.

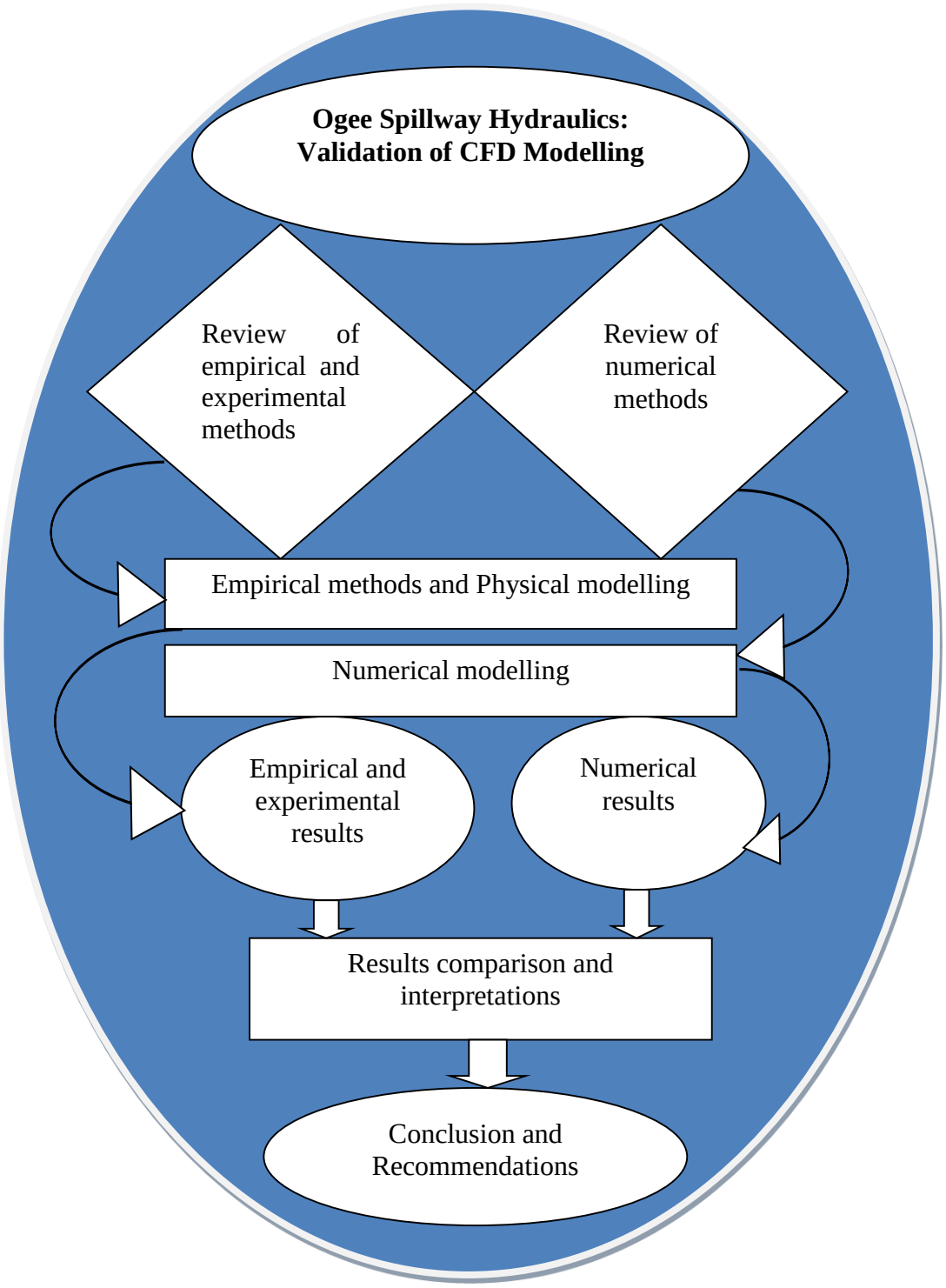

Figure 1-1: Evaluation of CFD modelling of ogee spillways

1.4 Research Outline

This research project is subdivided into six chapters and structured as stated below:

Chapter one, namely general introduction, presents the background and motivation of carrying out this research, objectives, the research methodology and research outline. Briefly, it depicts the framework of the research project.

Chapter two consists of a literature with basic details on analytical and numerical methods carried out in the past about flow over ogee spillways. This chapter includes the hydraulics of spillways in general and ogee spillways in particular. The recent advances in the numerical modelling of spillways are also described.

Chapter three provides an insight into the physical modelling concepts. It also provides the laboratory investigations executed on two physical models installed in a laboratory flume.

Chapter four describes the CFD modelling including modelling set-up, two and three-dimensional simulations for steady and fully hydrodynamic states.

Chapter five consists of the comparison of the results of the numerical and physical modelling and their interpretation.

In Chapter six the results are discussed and conclusions drawn. Recommendations for future research are also presented here.

CHAPTER 2: LITERATURE REVIEW

2.1 Introduction and overview of the chapter

This chapter presents the literature review of the study on spillways in general and ogee spillways in particular. It details different aspects that are considered while designing an ogee spillway, the discharge computation, pressure distribution, as well as the factors defining the hydraulic crest performance of ogee spillways.

It also includes a conceptual description of CFD where the design and methodology used for designing and testing an ogee spillway is examined. This section also presents the underlying theory of CFD modelling and the advantages of using CFD in flow modelling. Figure 2-1 gives a concise overview of this chapter.

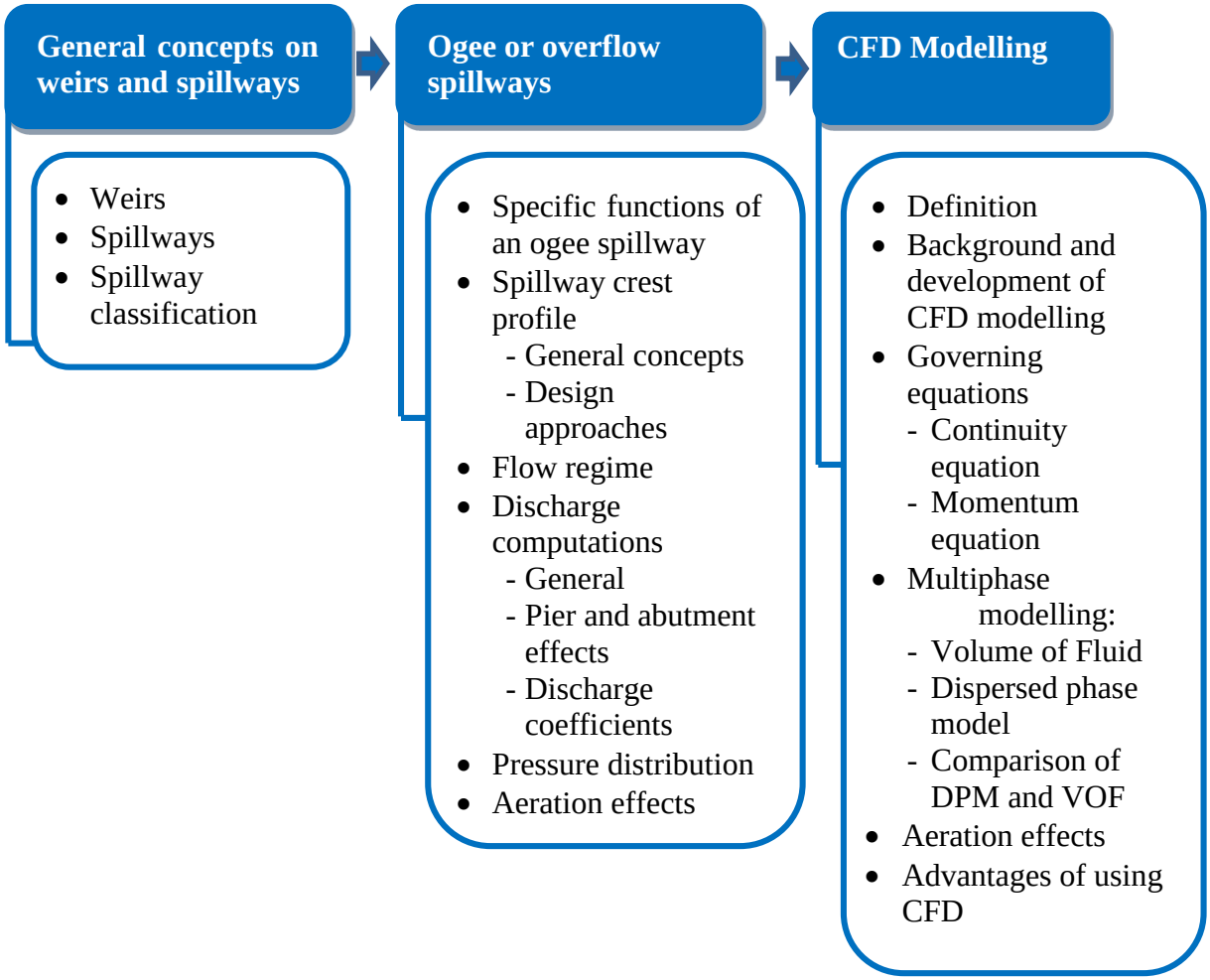

Figure 2-1: Overview of the chapter

2.2 General concepts on weirs and spillways

2.2.1 Weirs

A weir is referred to as an artificial barrier in a watercourse exhibiting an edge used to regulate or to measure flow rate and water depths (Ghare *et al*., 2008). They are common in different hydraulic structures such as storm water systems and stream engineering (Brown *et al*., 2012). The edge or surface over which water flows is called the crest as defined in Figure 2-2. Based on the notch shape, Brater et al. (1996) classified weirs into four types: rectangular weirs, triangular or V-notch weirs, trapezoidal weirs and parabolic weirs.

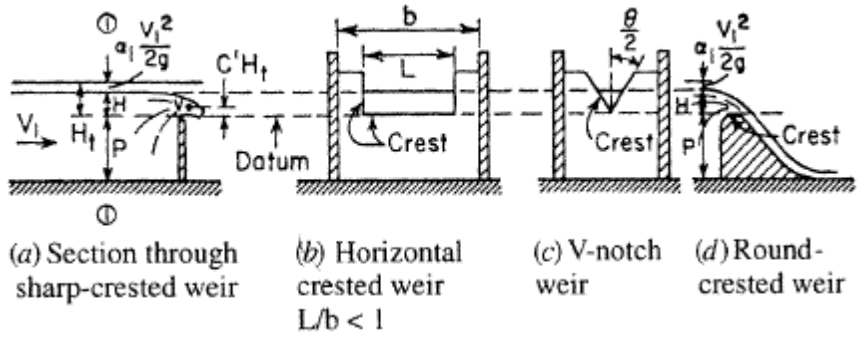

Figure 2-2: Weir definition sketch (Brater et al., 1996)

For particular situations, weir selection is made with respect to the range of discharges to be measured, the accuracy desired and the calibration needed (Brater *et al*., 1996).

2.2.2 Spillways

Spillways are control appurtenances which are constructed at the dams and/ or impounding reservoirs to provide the controlled release of flows exceeding the dam's full supply level (FSL) to the downstream side. Excess water is conveyed downstream while an appropriate structure dissipates the high kinetic energy of the flow that may lead to serious scour of the channel bed. If the scour is not properly controlled at the spillway toe, it may extend backward and endanger the entire spillway as well as the dam. In some cases, the energy dissipaters are included along its slope for reducing the amount of space required to efficiently discharge the flow without jeopardising the dam (USBR, 1973).

Of all dam safety measures, the spillway capacity is of paramount importance for different kinds of dams, especially earthfill and rockfill dams, which may probably fail once, overtopped.

Concrete spillways must be built with adequate structural protection from frost damage and erosion/abrasion from water and water-borne debris.

Ruskin Dam spillway in Canada, as a prototype case, was resurfaced to repair concrete damages (Lihe, *et al.*, 2011). Such remedies must be avoided as they are very expensive.

Each dam, thus, should be equipped with an adequate device to prevent the overtopping. In South Africa many serious incidents have occurred in the past resulting in loss of lives and property damage. It appears that the leading causes of incidents for active dams are slope instability, overtopping and earthquakes (ICOLD, 2001). Blight *et al.*, (1981) reported on the Bafokeng dam failure where 12 deaths occurred and 3 million m^3 of slurry flowed for 45 km. Another tragic disaster occurred on 22, February, 1994 at Merriespruit Dam where 500,000 m^3 of mud flows moved for 2 km and killed seventeen people (Strydom & Willams, 1999). Therefore, all dams should be constructed with high safety device to prevent such risks.

A part from the functions discussed here above, Takasu & Yamaguchi (1988) provided seven more functions of a safe spillway:

1. Maintaining normal river water functions
2. Discharging water for utilisation
3. Maintaining initial water level in the flood-control operation
4. Controlling floods
5. Controlling additional floods
6. Releasing surplus water
7. Lowering water levels (depleting water levels in an emergency)

2.2.3 Spillway Classification

Spillways can be classified based on various factors: Function (service spillway and auxiliary spillways); regulatory or control structure (Gated spillway, ungated spillways and orifice of sluice spillway) with the latter being the most pertinent feature (Khatsuria, 2005).

According to Şentrürk (1994), while selecting a spillway type, the following factors should be considered:

- Type of the dam to be constructed,
- Dam storage and outlet capacity,
- Topography and geological conditions of the spillway site,

- Hydrological and hydraulic factors, and
- Cost and risks involved.

Factors involved in the selection of each spillway type are briefly discussed in the Table 2-1.

Table 2-1: Factors governing the spillway type selection

Spillway type	Selection factors
Ogee Spillway	This type is suitable for a variety of situations because of its high efficiency to control flows (Savage *et al.*, 2001), such as in most control crests of other spillways and in high dams.
Chute Spillway	Provided to dams where the site permits a limited channel with sufficient depth of excavation for the foundation.
Side channel Spillway	Chosen as it is suitable for dams where the sides are steep and have a considerable height above the dam such as in canyons.
Shaft/Tunnel Spillway	Used for dams that are located in narrow canyons and in dam sites where the space downstream of the dam is not enough for other spillway types.
Siphon Spillway	Selected when the dam must operate automatically without mechanical tools, with a small discharge to be conveyed.
Free over-fall Spillway	This type is specifically appropriate for arch dams.
Labyrinth Spillway	Adopted as an economical measure for passing large floods as they provide an increased unit discharge when compared to conventional weirs for a given head (Darvas, 1971). They are used, therefore, in dams where an extra crest length is needed.
Stepped Spillway	Suitable for dissipating the energy of the overflow and to reduce the size of the energy dissipater needed at downstream of the spillway.

2.3 Ogee or Overflow Spillways

Several types of spillways currently exist, as discussed in the preceding section, but only the uncontrolled ogee-shaped spillways will be reviewed in this thesis, as others are outside of the scope of this thesis.

An ogee spillway, as shown in Figure 2-3, exhibits a control weir that is in form of ogee or S-shaped profile (USBR, 1987). According to USACE (1990), the crest of an ogee spillway is basically a sharp-crested weir with an empty space below the lower nappe replaced with concrete.

In fact, the shapes are based on a simple parabola designed conditionally to fit the trajectory of the lower nappe. The profile below the upper curve is prolonged tangentially, along the slope, to support the sheet on the face of the overflow and flow up to the apron of a stilling basin or into the spillway discharge channel.

Flow over the crest should adhere to the face of the profile, for preventing access of air underneath of the sheet. For discharges with a designed head, the flow glides over the crest with no interference from the boundary surface and attains near-maximum discharge efficiency.

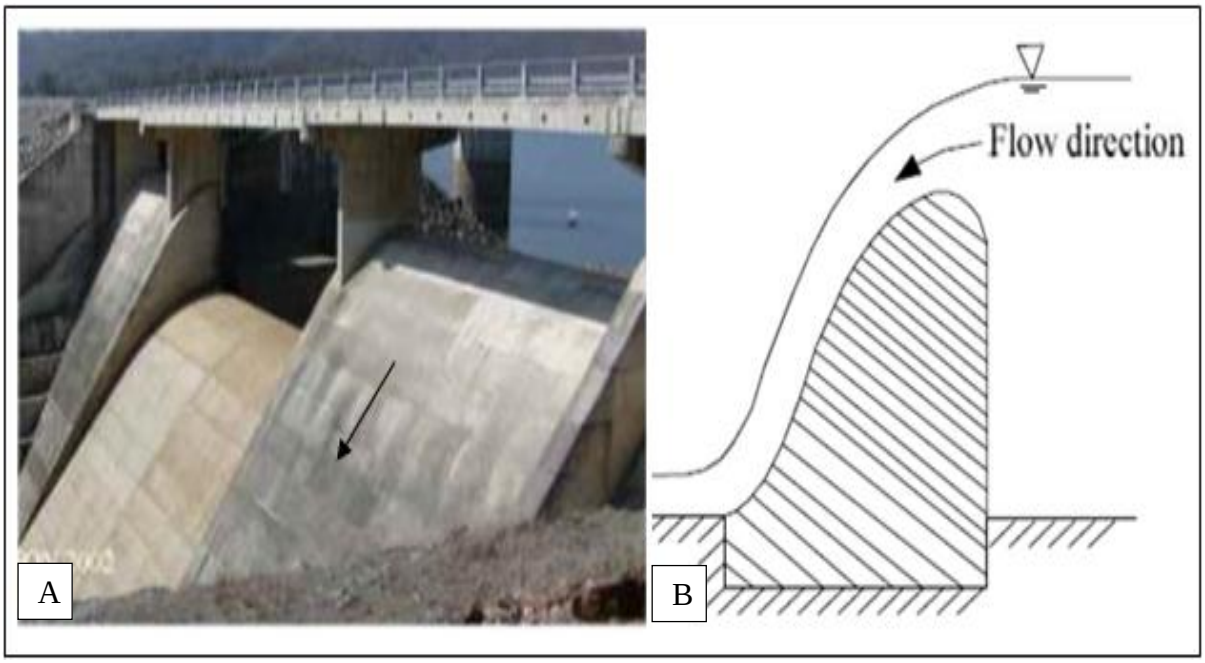

Figure 2-3: Ogee spillway type. A: Ogee spillway front view and B: Sectional view. Source: (Chanson, 2002)

2.3.1 Specific functions of an ogee spillway

An Ogee spillway is the most commonly used type especially in high dams. Its ability to pass flows efficiently and safely, when properly designed and with relatively good flow measuring capabilities, has enabled engineers to use it in a wide variety of situations (Savage *et al.* 2001; USBR, 1987).

Based on the regulatory or control structure, three different designs for spillway control are distinguished and can be classified as: uncontrolled devices which do not use a hydraulic gate in its operation, movable crest devices and regulating devices (USBR, 1973).

Uncontrolled crests are generally applied on small spillways and weirs when the release of water is only required in case the reservoir head exceeds the design level. One of the advantages of this design is that the constant supervision of an operator, maintenance and repair costs are not needed (USBR, 1973).

Movable crest and regulating devices are often employed when there is a sufficiently long uncontrolled crest or when the spillway crest is located under the normal operating level of the reservoir (USBR, 1973).

2.3.2 Spillway crest profile

2.3.2.1 General concepts

Considerable work has been conducted to get the shape of the crest of an overflow spillway and different design approaches have been provided that are based upon the relative height and the slope of spillway upstream face (Maynord, 1985). As cited by Horton (1907), Bazin (1888) completed an extensive laboratory investigation which was the first study to determine the ogee shape. These experiments have served as the basis of many early designs, including various USACE and USBR publications that are considered as the most used all over the world (Maynord, 1985).

As discussed previously, the ogee-crested shape is derived from the lower surface of an aerated nappe flowing over the sharp-crested weir as illustrated by Loftin (1999) in Figure 2-4.

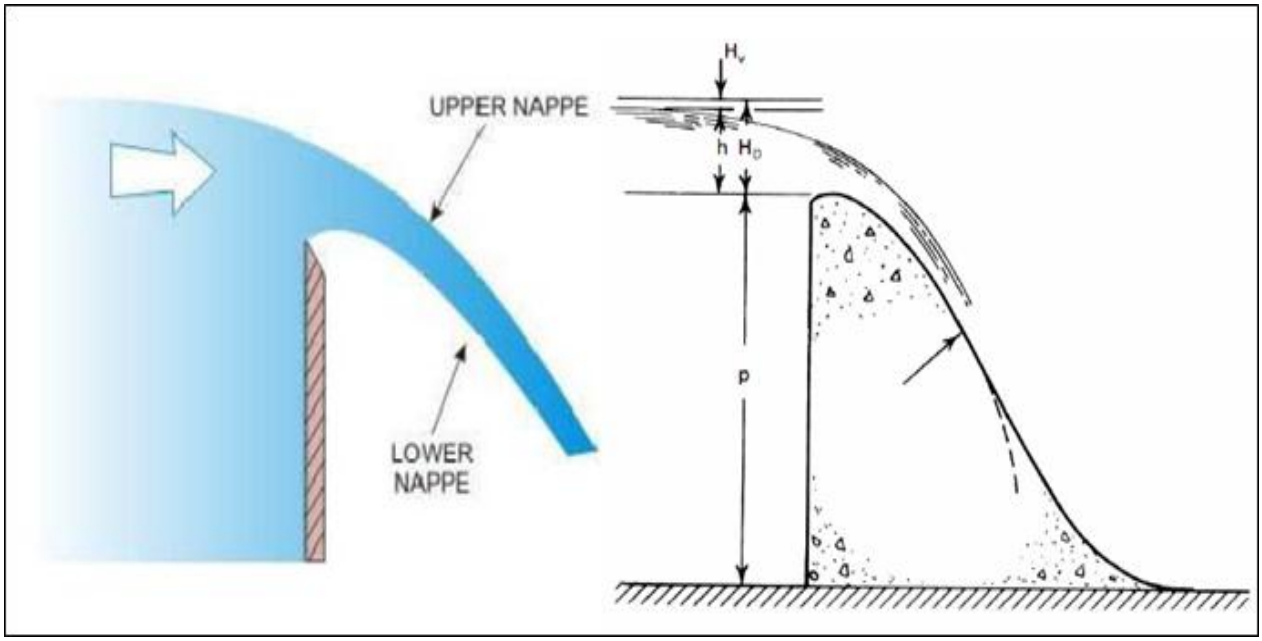

Figure 2-4: Sketch of a sharp-crested and ogee weir (Loftin, 1999)

Şentrürk (1994) confirms that the stability of this nappe is not altered even if the empty space underneath the nappe is filled with concrete or other material. According to Chow (1959), the shape of this flow nappe can be interpreted by the principle of projectile, as depicted in Figure 2-5. It is assumed that the horizontal velocity component is constant and the only acting force on the nappe is gravity. During an interval of time "t", a particle of water in the lower surface of the nappe will cover horizontally a distance– x, from the face of the weir as defined in Equation (2-1):

$$x = v_o t \cos\theta \qquad (2\text{-}1)$$

where

x = Horizontal distance (m)

v_o = Velocity at the point where $x = 0$ (m/s)

θ = Angle of inclination of "v_o"with the horizontal (degrees)

t = Time (s)

Simultaneously, the particle will travel a vertical distance as defined in the equation (2-2):

$$y = -v_o t \sin\theta + \frac{1}{2} g t^2 + C' \qquad (2\text{-}2)$$

where

$C' =$ The value of y at x= 0

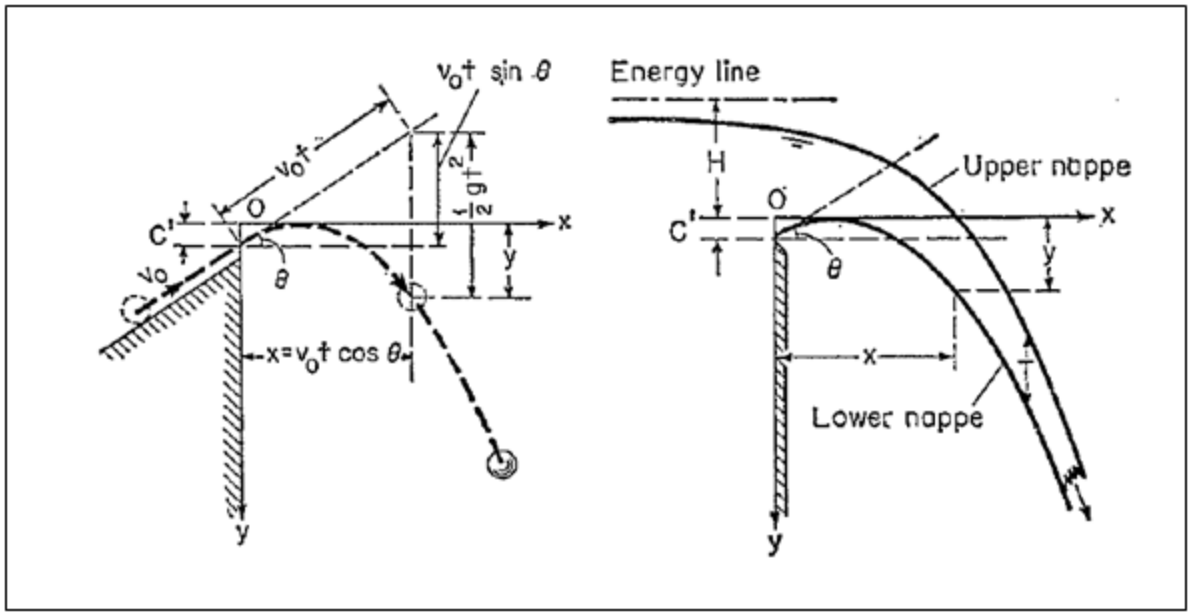

Figure 2-5: Derivation of nappe profile over a sharp-crested weir by the principle of projectile (Chow, 1959)

An ogee crest is designed for a single total head (energy head), called the design head H_o. When an ogee weir is discharging at the design head, the flow glides over the crest with no interference from the boundary surface and attains near-maximum discharge efficiency (Loftin, 1999). The following sub-section discusses some design approaches that are commonly applied.

2.3.2.2 Design approaches

The design and/or evaluation of an ogee spillway performance often require a profound study to confirm its capacity before construction. Many spillway designs have been tested and a compendium of standard operational curves has been published primarily by the USACE and the USBR since the mid 1900's (Savage &Johnson, 2001). The publications from both agencies are considered as the basis for the existing information. A wealth information on ogee-crested spillways is found in USACE (1990), Maynord (1985), USBR (1977, 1987), Chow (1959), and Brater *et al.*, (1996).

United States Bureau of Reclamation

United States Bureau of Reclamation (1948), based on Bazin's laboratory findings of nappe shapes, developed coordinates defining the nappe profile for vertical and various sloped face spillways.

The shape was designed as such that it fits the shape of a well-aerated nappe profile at a design head. According to United States Bureau of Reclamation (1987) this shape depends mainly upon three important parameters:

- The head
- The inclination of the upstream face of the ogee spillway section
- The height of overflow sections above the floor including the influences of the approach velocity to the crest.

The profile shape, made up of two quadrants, is defined as it relates to axes at the apex of crest. The upstream quadrant is defined as either a single curve and a tangent or as a compound of circular arcs whereas the downstream quadrant conforms to Equation (2-3):

$$\frac{y}{H_d} = -K\left(\frac{x}{H_d}\right)^n \qquad (2\text{-}3)$$

where

H_d = Design head (m)

$x\ and\ y$ = Horizontal and vertical coordinates of the crest, respectively, with the origin at the highest point of the crest (m)

$K\ and\ n$ = Constants whose values depend on the upstream inclination and approach velocity as detailed in Figure 2-6.

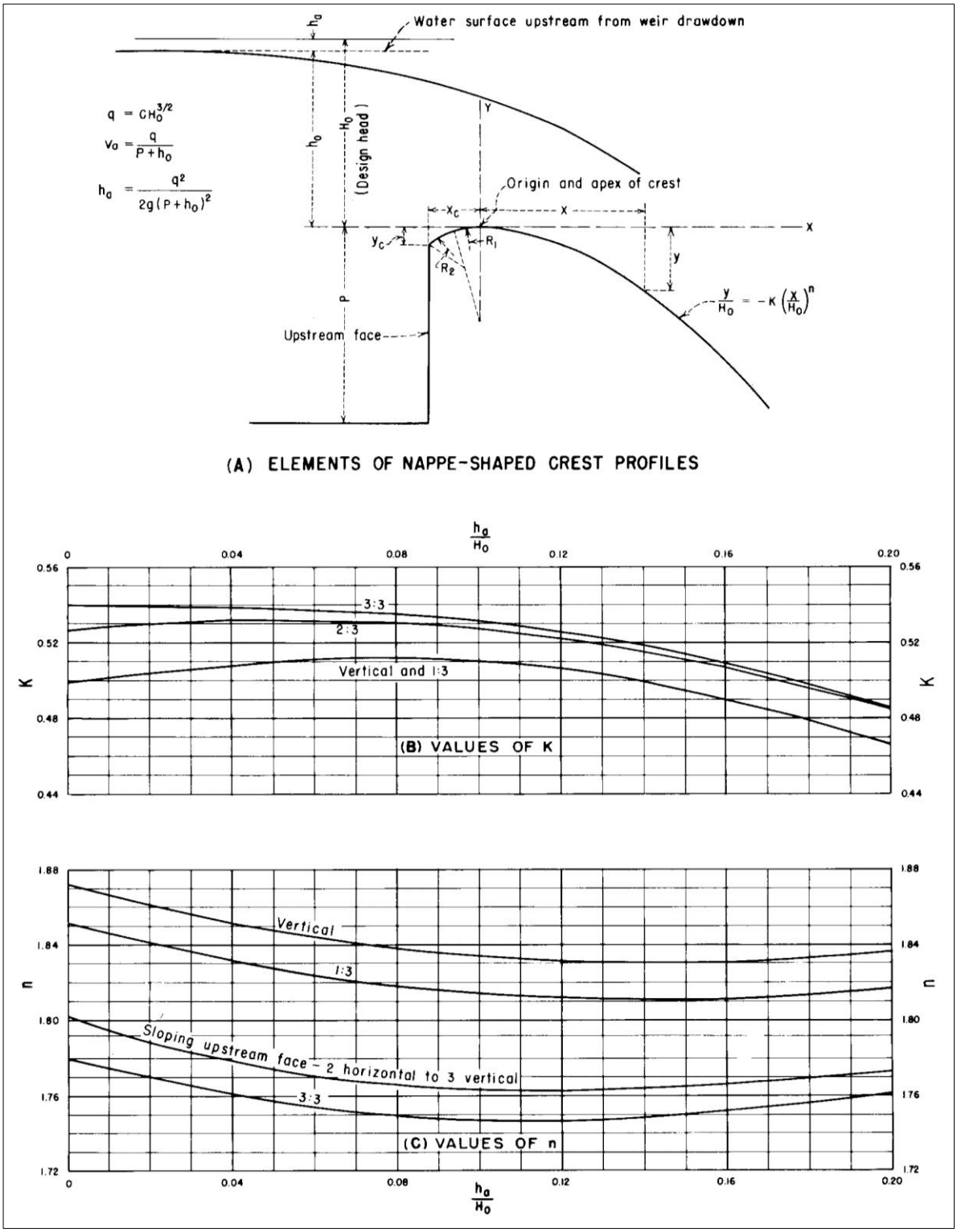

Figure 2-6: Factors for definition of nappe-shaped crest profiles (USBR, 1987)

United States Army Corps of Engineers

USACE (1952), at its research station "Waterways Experiment Station" carried out a series of experiments on the basis of Bureau of Reclamation data and developed several standard shapes. Such shapes, known as WES spillways shapes (Chow, 1959), can be represented by Equation (2-4)

$$x^n = k\, H_d^{n-1} y \qquad (2\text{-}4)$$

Where values of k and n are always influenced by the upstream face of the control structure. Table 2-2 gives the values of k and n with respect to the upstream inclination.

Table 2-2: Variation of the parameter k and n in WES profile

Slope of the upstream face	k	n
Vertical	2.000	1.850
3 on 1	1.936	1.836
3 on 2	1.936	1.810
3 on 3	1.873	1.776

The upstream quadrant, originally defined as a compound of circular arcs, resulted in surface discontinuity at the intersection of the spillway crest and the upstream face (Maynord, 1985). Murphy (1973), a WES Engineer, proposed another method of eliminating that discontinuity which is applicable to any upstream face slope and approach velocity. In response to this, using the same design data of USBR, the upstream quadrant was shaped as an ellipse as in Equation (2-5).

An amelioration of 3% increase in the discharge coefficient has been achieved after this small discontinuity was removed (Murphy, 1973).

$$\frac{X^2}{A^2} + \frac{Y^2}{B^2} = 1 \qquad (2\text{-}5)$$

Where

A = Semi-major axis (functions of the ratio of approach depth to design head)

B = Semi-minor axis

$X\ and\ Y =$ Horizontal and vertical coordinates of the crest, respectively, with the origin at the highest point of the crest (m).

The shape continues with downstream until it reaches the energy dissipating structure. Between the end of the sloping surface of the spillway and the energy dissipater, a bucket is provided to create a smooth transition of flow from the spillway surface to the downstream part of the spillway. This transition is a circular arc, tangential to both rear slope and apron with a minimum radius of 3 times the depth of the entering flow (Khasturia, 2005).

Brater et al. (1996)

In the hydraulic handbook by Brater *et al.* (1982), which is considered as one of the more widely referenced sources used by practicing engineers, an equation of the crest shape has been provided. This crest was developed, with the same principle as other researches, to fit the shape of the underside of the nappe of a sharp-crested weir as detailed in Equation (2-6). A circular curve with a radius of $0.4H_o$ for the upstream quadrant is also used to define the upstream quadrant.

$$y = 1.22\ x^{1.80} \qquad (2\text{-}6)$$

Where

$H_o =$ The design head (m)

$X\ and\ Y =$ Horizontal and vertical coordinates of the crest (m)

Chanson (2004) recapitulated, in Table 2-3, different profiles for vertical-faced ogee crests developed by some other researches.

Table 2-3: Spillway profiles for vertical-faced ogee crests (Chanson, 2004)

Profile (1)	Equation (2)	Comments (3)
Creager (1917) profile	$Y = 0.47\frac{X^{1.80}}{(H_{des} - \Delta z)^{0.80}}$	For $X \geq 0$; derived from Bazin's (1888-1898) experiments
Scimemi (1930) profile	$Y = 0.50\frac{X^{1.85}}{(H_{des} - \Delta z)^{0.85}}$	For $X \geq 0$; also called WES profile
Knapp (1960)	$\frac{Y}{H_{des} - \Delta z} = \frac{X}{H_{des} - \Delta z} - \ln\left(1 + \frac{X}{0.689(H_{des} - \Delta z)}\right)$	Continuous spillway profile for crest region only (as given by Montes, 1992a)
Hager (1991)	$\frac{Y}{H_{des} - \Delta z} = 0.1360 + 0.482625\left(\frac{X}{H_{des} - \Delta z} + 0.2818\right) \times \ln\left(1.3055\left(\frac{X}{H_{des}\Delta z} + 0.2818\right)\right)$	Continuous spillway profile with continuous curvature radius: $-0.498 < \frac{X}{H_{des} - \Delta z} < 0.484$
Montes (1992a)	$\frac{R_1}{H_{des} - \Delta z} = 0.05 + 1.47\frac{s}{H_{des} - \Delta z}$	Continuous spillway profile with continuous curvature radius R Lower asymptote: i.e for small values of $s/(H_{des} - \Delta z)$
	$\frac{R}{H_{des} - \Delta z} = \frac{R_1}{H_{des} - \Delta z}\left(1 + \left(\frac{R_u}{R_1}\right)^{2.625}\right)^{1/2.625}$	Smooth variation between the asymptotes
	$\frac{R_u}{H_{des} - \Delta z} = 1.68\left(\frac{s}{H_{des} - \Delta z}\right)^{1.625}$	Upper asymptote: i.e. for large values of $s/(H_{des} - \Delta z)$

The flow over an ogee spillway is characterised by the changes in its state from a subcritical to a supercritical regime caused by a sudden change in its geometry after the crest.

As documented by USBR (1987), in Design of Small Dams publication, and Bradley (1945), five different flow regimes can occur and they are clearly distinguished below an overflow crest depending on the relative positions of the apron and the downstream water surface:

- A supercritical flow staying attached on the length of the spillway;
- An incomplete hydraulic jump may form directly downstream from the crest;
- A fully or true hydraulic jump can occur;
- A drowned jump can occur in which the flow with a high-velocity jet will follow the face of the ogee spillway for a considerable distance under the tail water and then continue in an unpredictable and fluctuating path; and
- In other cases, no jump may occur. The jet breaks up from the face of the spillway, flows on the spillway surface for a short trajectory, then rides along the surface for a short distance before erratically intermixing with the slow flowing water below.

2.3.3 Discharge computations

2.3.3.1 General

The most commonly used equation for computing the discharge of ogee spillways was developed from early experiments by James B. Francis (Horton, 1907). This discharge relationship, which is of the same form as other weirs, is often referred to as the "Weir Equation", as shown in Equation (2-7):

$$Q = CLH_e^{1.5} \tag{2-7}$$

Where

$Q =$ Discharge (m^3/s)

$L =$ Lateral crest length or width (m)

$C =$ Discharge coefficient $(m^{0.5}/s)$

$H_e =$ The total energy head upstream from the crest which is defined as follows:

$$H = h + H_v$$
$$\therefore H_v = \frac{v^2}{2g} \tag{2-8}$$

The following terms from equation (2-8) mean:

h = Measured water level above the weir crest (m)

H_v = Velocity head (m/s)

It is also important to note that, the total head on the crest, H_e, does not count for approach channel friction losses or other losses.

2.3.3.2 Pier and abutment effects

Crest piers are needed when gates are to be installed to control the flow passing down the spillway or for an uncontrolled spillway when a road bridge is to be provided.

According to USBR (1987), piers and abutments are installed on the crest to induce side contraction of the overflow. The effective crest length, however, will become slightly less than the net length of the crest as shown in equation (2-9).

$$L = L' - 2(N\,K_p + K_a)H_e \qquad (2\text{-}9)$$

Where:

L = Effective length of the crest

L' = Net length of crest

N = Number of piers

K_p = Pier contraction coefficient

K_a = Abutment contraction coefficient and

H_e = Actual head on crest

The pier contraction coefficient depends upon a number of factors such as location of the pier nose, the thickness of the pier nose, the design head and the approach velocity. For the flow at the design head, the average values of K_p are detailed below:

- For square-nosed piers, with corners rounded on a radius equal to about 0.1 of pier thickness: K_p =0.02
- For rounded-nosed piers: $K_p = 0.01$
- For Pointed-nosed piers: $K_p = 0.00$

The value of the abutment contraction coefficient depends upon the shape of the abutment, the angle between the upstream approach wall and the axis of the flow, the head in relation to the design head and the approach velocity. For flow conditions at the design head, H_o, abutments coefficients may be approximated as follows:

- For square abutments with head at 90° to direction of flow: $K_a = 0.02$
- For rounded abutments with headwall at 90° to direction of flow, when $0.5H_o \geq r \geq 0.15H_o$; $K_a = 0.10$
- For rounded abutments where $r > 0.5H_o$ and headwall is placed not more than 45° to direction of flow $K_a = 0.0$

Where $r =$ radius of abutment rounding

2.3.3.3 Determination of Discharge Coefficients

An ogee spillway is characterised by a relatively high value of discharge coefficient because of its shape. However, this coefficient is not constant. It is influenced by a number of factors including the depth of the approach, relation of the actual crest shape to the ideal nappe shape, the upstream face slope downstream apron interface and downstream submergence.

As documented by USBR (1987), the design discharge coefficients for ogee weirs with a vertical upstream face are depicted in Figure 2-7. Thence, these coefficients are valid only when the ogee confirms to the ideal nappe shape; that is, when $H_e/H_o = 1$. When crest shapes are different from the ideal shape or when it has been made for heads greater or smaller than the design head, the coefficient changes as depicted in Figure 2-8.

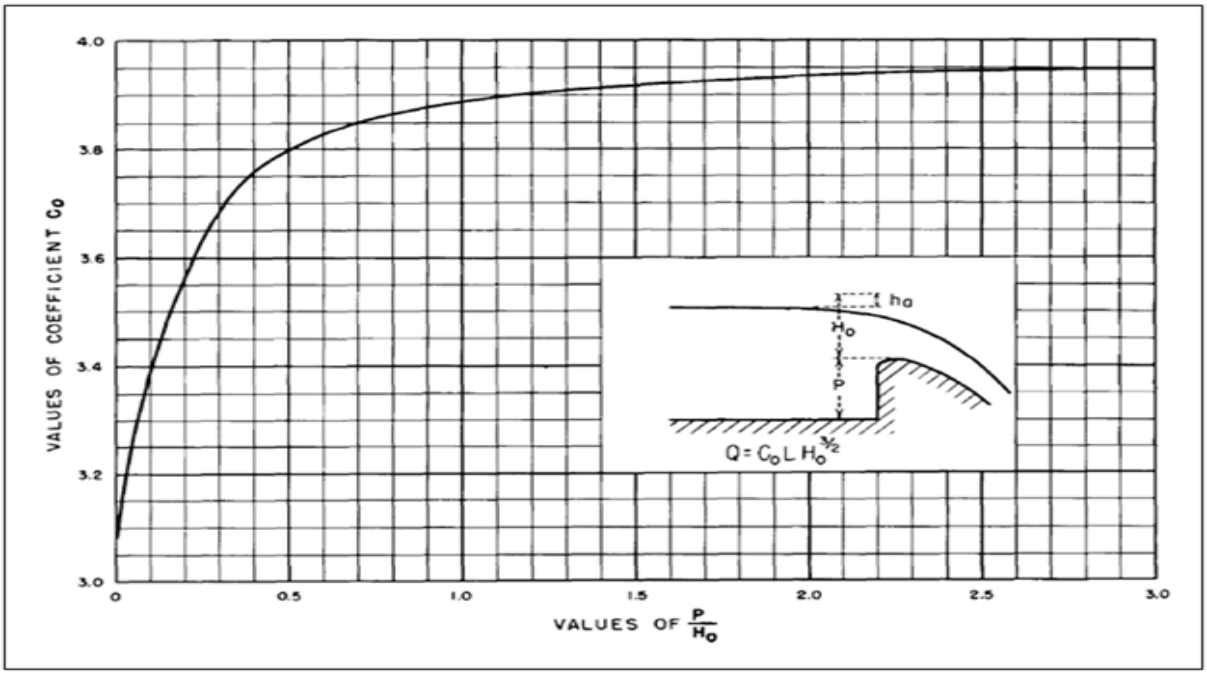

Figure 2-7: Discharge coefficient for vertical faced ogee crest (USBR, 1987)

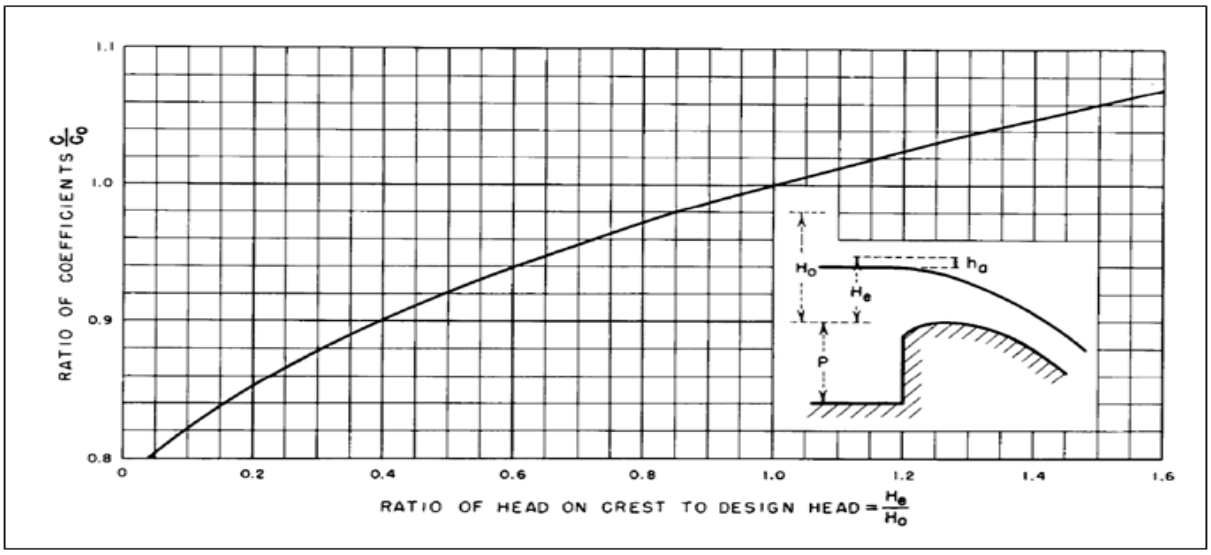

Figure 2-8: Discharge coefficients for other than the design head (USBR, 1987)

The upstream sloped face of spillway causes a change in the coefficient of discharge. According to USBR, (1987), for small ratios of the approach depth to the head on the crest, the inclined upstream face causes an increase in the discharge coefficient especially for the heights other than the design head.

For large ratios, the effect causes a decrease in coefficient of discharge. Discharge coefficients for an ogee-shaped crest with a sloping upstream face are depicted in Figure 2-9.

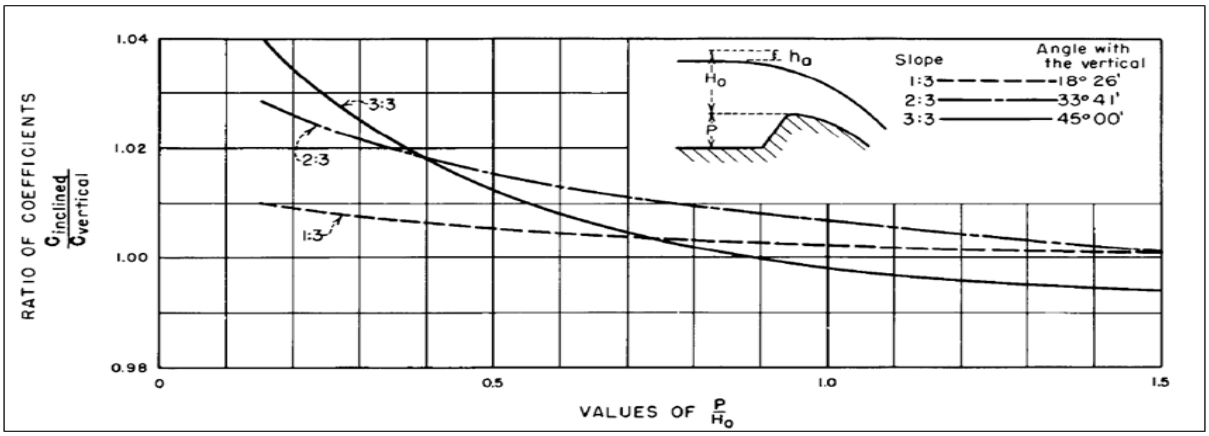

Figure 2-9: Discharge coefficients for ogee-shaped crest with sloping upstream face

Coefficients of discharge are also affected by the downstream apron and spillway submergence as shown in Figure 2-10 and Figure 2-11, respectively.

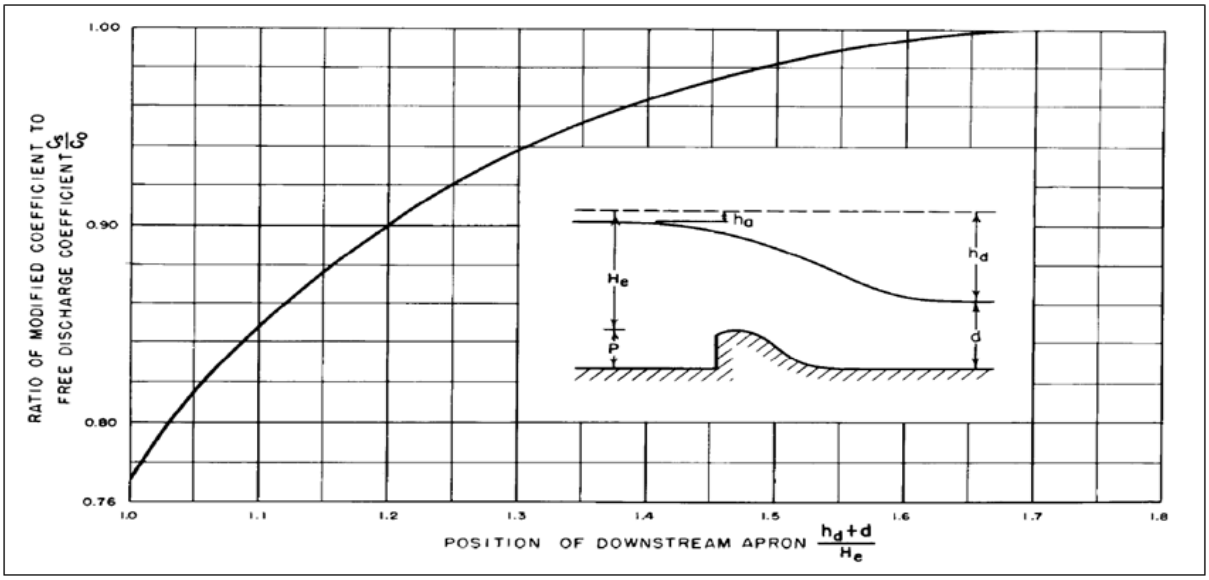

Figure 2-10: Ratio of discharge coefficients resulting from apron effects (USBR, 1987)

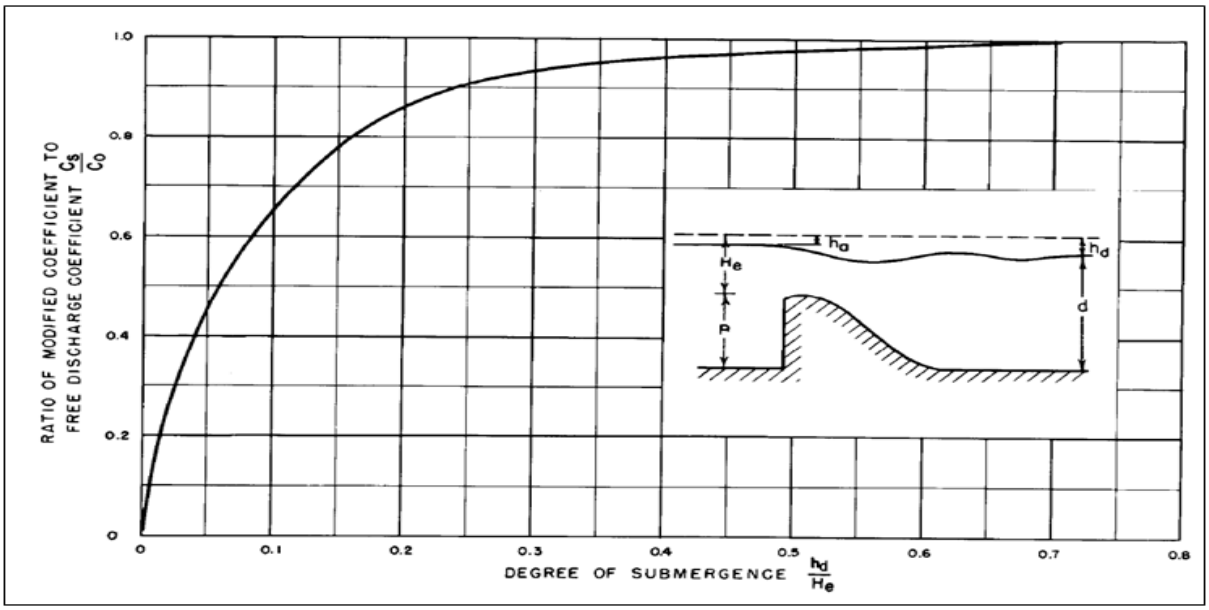

Figure 2-11: Ratio of discharge coefficients caused by tailwater effects (USBR, 1987)

2.3.4 Pressure distribution

The design head is generally chosen to give the maximum hydraulic efficiency, in keeping with the operational requirements, structural stability and economy. At the design head "H_o", ogee crests operate with the design discharge coefficient "C_o" , exhibiting the atmospheric pressures.

For heads "H_e" less than the design head, the coefficients of discharge "C" are less than the design coefficient of discharge "C_o" and positive pressures develop on the crest. For heads greater than the design head, the coefficient of discharge "C" become greater than the design coefficient of discharge with negative pressure on the crest, thereby, increasing the discharge capacity.

The findings from USBR (1987), in the *Design of Small Dams* publication, showed that the Safety Evaluation Flood (SEF) should be passed at a head H_e equal to 1.33 times the design head (H_o). This head level, however, creates sub-atmospheric pressures at the crest equal to approximately half of H_o.

Design engineers should not allow crest pressures to become too negative, as accentuated crest negative pressures cause cavitation damage, spillway destabilisation and possible failure of the entire structure.

Chanson (2004) shows, in Table 2-4, that crest pressures decrease linearly with the increase of the upstream head on the crest thereby increasing the discharge coefficients.

Table 2-4: Pressures on an ogee crest for design and non-design flow conditions (Chanson, 2004)

Upstream head (1)	Pressure on crest (2)	Discharge coefficient (3)
$H_1 = H_{des}$	Quasi-atmospheric	$C = C_{des}$
$H_1 > H_{des}$	Less than atmospheric	$C > C_{des}$
$H_1 < H_{des}$	Larger than atmospheric	$C < C_{des}$
$H_1 \ll H_{des}$	Larger than atmospheric	$C \approx 1.70\ m^{0.5}/s$

2.3.5 Aeration effects

Naturally, air flows are commonly encountered at the water flow surface (Chanson, 2004). The falling nappe is considered aerated and it is subjected to atmospheric pressures. The aeration observed has led to the suggestion that the point at which aeration commences coincides with the point at which the boundary layer depth meets the free surface (Henderson, 1996; Keller, 1972; Cain & Wood, 1981). Figure 2-12 depicts boundary layer development in the flow over the ogee spillway.

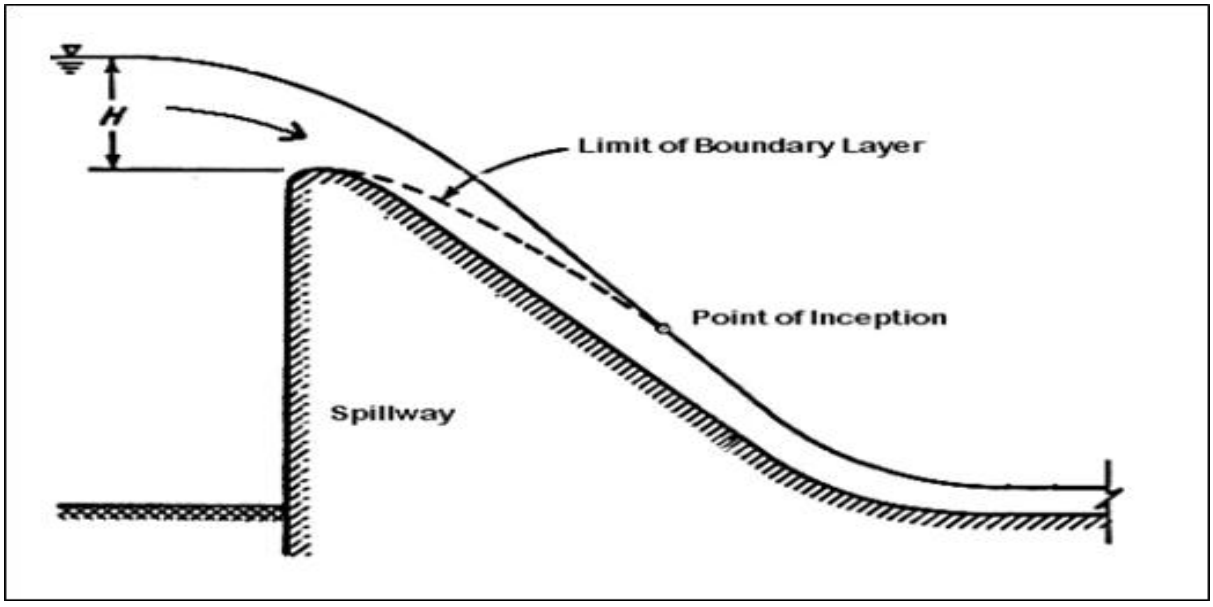

Figure 2-12: Boundary layer developed on ogee spillway flow (Bhajantri et al., 2006)

The insufficient aeration of the nappe will cause the reduction in pressure thereby leading to the abrupt change of the nappe shape for which the spillway crest is designed.

These pressures can theoretically be as low as the vapour pressure of water, which causes structural damage due to destructive cavitation and vibration, and are therefore to be avoided from an operational and structural point of view.

Şentrürk (1994) discusses three problems solved for an aerated spillway flow:

- Increase in flow depth due to air entrainment,
- Aeration of the lower nappe avoids pulsating flow,
- The downstream channel is free of cavitation if the lower nappe is aerated.

2.4 Computational Fluid Dynamics Modelling

2.4.1 Definition

Computational Fluid Dynamics (CFD) is a computer-based tool that is used to represent and analyse systems that involve fluid flow, heat transfer and chemical reactions, by using numerical methods that are based on partial differential equations describing these systems (Versteeg & Malalasekera, 2007).

2.4.2 Background and development of CFD modelling

Over 100 years, hydraulic engineering practice has been relying on physical modelling for the design of most hydraulic structures. Because of the rigid and expensive nature of scale models, more alternative methods have been developed for the sake of accuracy and time optimisation. Modern Computational Fluid Dynamics (CFD) was born in the 1950's when digital computers were introduced (Chung, 2002). There has been a rush in development and application to all aspects of fluid dynamics from the late 1960s where the aerospace industry profited from its use, especially for the design and manufacturing processes (Parviz & John, 1997).

In hydraulic engineering, computational modelling of spillway flows is increasingly being used in the industry. However, a validation from a physical model is still required to ensure that the physical processes are accurate. Several approaches have been developed, including modelling in one, two or three dimensions which use various equations and discretisation techniques. One-dimensional models are generally applied to verify the river stage and the water surface profile upstream and along the length of the spillway (Song & Zhou 1999). Berger & Winant (1991) simulated the flow over a spillway by solving a modified form of the shallow water equation in one dimension and a reasonable agreement was achieved. On the other hand, a one-dimensional model has presented some limitations as it is not adapted to variable-geometric structures such as junctions, steep slope, curved surfaces or to any other change of size or shape of the channel (Franz & Melching, 1997). However, more details have been found in two- and three-dimensional models which allow perturbations of flow caused by obstructions, curved obstacles, wall boundaries or other complex geometries (Causon *et al*., 1999). The following subsections detail the basic theory which is behind Computational Fluid Dynamics (CFD).

2.4.3 Governing equations

The fundamental principles for all numerical models remain similar where the problems are stated, physically, by a set of partial differential equations. In the same way, CFD techniques are governed by a number of equations which must be solved in each control volume. Depending on the properties of fluid flow to simulate, the physical phenomena are represented by mathematical statements that are referred to as governing equations of fluid flow and heat transfer (Versteeg & Malalasekera, 2007). These equations include mass conservation or continuity, momentum and energy equations also known as the Navier-Stokes equations. Based on the theory documented by Wendet (2009), mass conservation and momentum equations can be described as follows:

2.4.3.1 Mass conservation (continuity) equation

The mass conservation equation or continuity equation states that the mass of a closed system of substances will remain constant, regardless of the processes acting inside the system. Fluid flow has a fixed mass even if its shape and volume may change as it moves. The illustration is made in Equation (2-10) and Figure 2-13:

$$dm = \rho dV \tag{2-10}$$

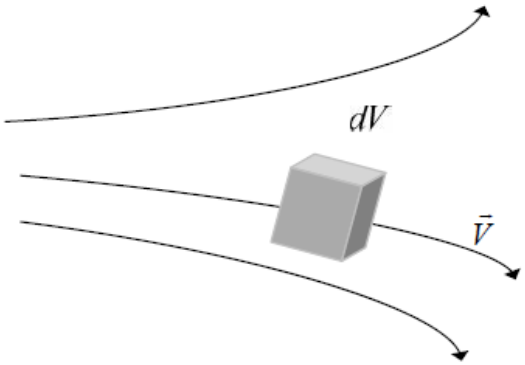

Figure 2-13: Definition sketch for moving fluid (Kositgittiwong, 2012)

During the time interval Dt, the principle of conservation of mass states that the rate of change of mass of a fluid element is zero as the mass flow entering is equivalent to the mass flow leaving as shown in equation (2-11).

$$\frac{D(dm)}{Dt} = 0 \tag{2-11}$$

Substituting Equation (2-10) into Equation (2-11), we get Equation (2-12)

$$\frac{D(\rho dV)}{Dt} = dV\ \frac{D\rho}{Dt} + \rho\frac{D(dV)}{Dt} = 0 \qquad (2\text{-}12)$$

When all terms are arranged on the left hand side of the equal sign, Equation (2-12) becomes Equation (2-13) as follows:

$$\frac{D\rho}{Dt} + \rho\left[\frac{1}{dV}\frac{D(dV)}{Dt}\right] = 0 \qquad (2\text{-}13)$$

If the product rule is applied for each of the spatial differentiations and the definition of substantial derivative is used, Equation (2-13) is written in a more compact notation and becomes Equation (2-14).

$$\frac{\partial\rho}{\partial t} + \nabla\cdot\left(\rho\,\vec{V}\right) = 0 \qquad (2\text{-}14)$$

where

$dm =$ Change of mass in the system (kg)

ρ = Density (kg/m^3)

V = Velocity (m/s)

Dt = Time interval (s)

∇= Partial derivative of a quantity with respect to all directions

2.4.3.2 Momentum conservation equation

The momentum equation is a statement of Newton's Second Law and relates the sum of all the forces acting on a particle of fluid (Chadwick, *et. al*., 2004; Versteeg & Malalasekera, 2007). The moving fluid element model is sketched with more details in Figure 2-14.

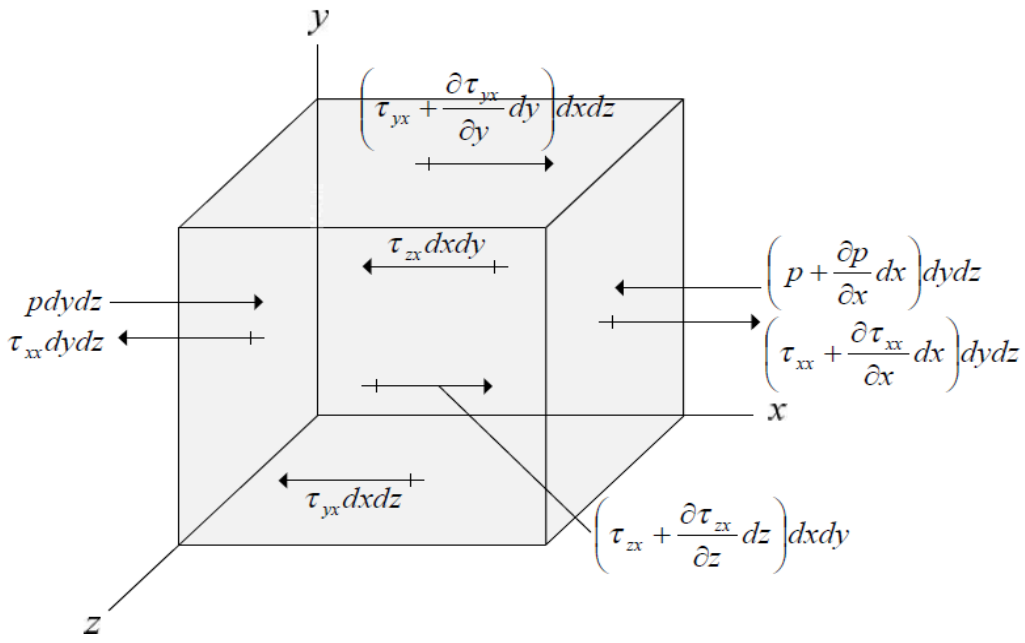

Figure 2-14: Moving particle element model for the x component (Kositgittiwong, 2012)

The general equation for conservation of momentum can be written as follows:

$$\frac{\partial}{\partial t}(\rho\vec{v})+\nabla\cdot(\rho\vec{v}\vec{v})=-\left(\frac{\partial P}{\partial x}\right)+\nabla\cdot(\mu\nabla\mu)+S_m \qquad (2\text{-}15)$$

where

P = Static pressure (Pa)

μ = Kinetic viscosity (m^2/s)

ρ = Density (kg/m^3)

S_m= Source term (Constant)

v = Overall velocity vector (m/s)

The left hand side of Equation (2-15) contains terms as defined for the mass conservation equation and its right hand side contains the pressure source term and the diffusion source term respectively. As documented by Ansys Inc. in Fluent, (2009), for the theory guide, this equation is implemented in FLUENT as follows:

$$\frac{\partial}{\partial t}(\rho\vec{v})+\nabla\cdot(\rho\vec{v}\vec{v})=\nabla P+\nabla\cdot(\bar{\bar{\tau}})+\rho\vec{g}+\vec{F} \qquad (2\text{-}16)$$

where,

$P =$ Static pressure (Pa)

$\rho g =$ Gravitational body force (kg/m^2S^2)

$\vec{F} =$ External body forces (N)

$\bar{\bar{\tau}} =$ Stress tensor (Pa), defined by Equation (2-17):

$$\bar{\bar{\tau}} = \mu\left[(\nabla\vec{v} + \nabla\vec{v}^T) - \frac{2}{3}\nabla\vec{v}I\right] \tag{2-17}$$

where

$I =$ The momentum of inertia.

When the VOF-method is used to treat multiphase-phase models, the mass conservation equation becomes slightly modified and the momentum conservation equation will remain the same because of the dependence on of the variables ρ and μ on the volume fraction.

2.4.4 Multiphase modelling

Multiphase modelling is a technique which simulates flow in the simultaneous presence of different phases. All the three phases (gas, liquid and solid) are identifiable with a distinct particular inertial response to an interaction with the flow and the potential field. There are four main categories of multiphase flows; gas-liquid, gas-solid, liquid-solid and three-phase flows (Murrone & Villedieu, 2011). Such complex systems have been made possible with the availability of two broad approaches for the numerical calculation, namely Euler-Euler (Volume of Fluid model or VOF model) and Euler-Lagrange (Discrete Phase Model) approaches.

2.4.4.1 Volume of Fluid (VOF) model

The volume of fluid model, as documented by Hirt & Nichols (1981), is designed for two or more immiscible fluids where the position of the interface between the fluids is of interest. It is an interface capturing scheme for the free surface flow where the interface of each fluid is the point of focus (Nikseresht *et al*., 2008). In the VOF model, the phases are treated separately and one set of conservation equations are solved for each phase.

Due to the volume fraction of each phase throughout the same control volume, the fields for velocity, pressure and temperature are made to be the same.

Thus, conservation equations for each phase are derived to obtain a set of equations, which have a similar structure for all phases. The equations, continuity Equation (2-18) and momentum equation (2-19), solved in the VOF method are shown below:

$$\frac{\partial \rho}{\partial t} + \frac{\partial \rho u_i}{\partial x_i} = 0 \tag{2-18}$$

$$\frac{\partial \rho u_i}{\partial t} + \frac{\partial \rho u_i u_j}{\partial x_j} = -\frac{\partial P}{\partial x_i} + \frac{\partial}{\partial x_j}(\mu + \mu_t)\left(\frac{\partial u_i}{\partial x_j} + \frac{\partial u_j}{\partial x_i}\right) \tag{2-19}$$

Where

u_j = Velocity in x_j–direction (m/s)

μ_t = Turbulence viscosity, which can be calculated by the turbulent kinetic energy, *k*, and turbulent dissipation rate, ε, in the turbulence model.

Tracking the interface(s) between the phases is performed by the solution of a continuity equation for the volume fraction of one (or more) of the phases. For the q^{th} phase, this equation has the form (2-20).

$$\frac{1}{\rho_q}\left(\frac{\partial}{\partial t}(\alpha_q \rho_q) + \nabla \cdot \alpha_q \rho_q \overrightarrow{v_q} = S_{\alpha q} + \sum_{p=1}^{n}(\dot{m}_{pq} - \dot{m}_{qp})\right) \tag{2-20}$$

The equation of volume fraction is not solved for the primary phase; the primary phase volume fraction is computed with Equation (2-21):

$$\sum_{q=1}^{n} \alpha_q = 1 \tag{2-21}$$

In the statements mentioned above, $\rho q\ (kgm^3)$ is the density of the q^{th} phase,α_q, is the q^{th} phase, $\dot{m}_{qp}$ is the mass transfer from phase q to phase p whereas $\dot{m}_{pq}$ is the mass transfer from phase p to phase q and $S_{\alpha q}$, which is the source term, is zero but for each phase the mass source can be specified.

2.4.4.2 Dispersed Phase Model (DPM)

The dispersed phase model is used to describe discrete particles as they traverse through and interact with fluid flow in space and time, through tracking the motion and computing the rates of change of conserved properties by integrating the force balance on the particle (Versteeg & Malalasekera, 2007; Fluent, 2008; Panton, 1984).

It can model *n* phases by the continuity and momentum equations for the mixture, and the volume fraction equation for the secondary phases. The continuity equation for the mixture is stated as below:

$$\frac{\partial \rho_m}{\partial t} + \frac{\partial \rho_m u_{mi}}{\partial x_i} = 0 \qquad (2\text{-}22)$$

Where u_{mi} and ρ_m are the mixture velocity in x_i −direction and mixture density respectively.

The momentum equation for the mixture can be obtained by adding the individual momentum equations for all phases, as shown in Equation (2-23).

$$\frac{\partial}{\partial t}\left(\rho_m u_{mi}\right) + \frac{\partial\left(\rho_m u_{mi} u_{mj}\right)}{\partial x_j} = -\frac{\partial p_{mi}}{\partial x} + \frac{\partial\left[\sum_{k=1}^{n} \alpha_k \tau_k - \sum_{k=1}^{n} \alpha_k \overline{\rho_{Ik} u_{Fki} u_{Fkj}}\right]}{\partial x_j} - \frac{\partial\left(\sum_{k=1}^{n} \alpha_k \rho_k u_{Mki} u_{Mkj}\right)}{\partial x_j} + \rho_m g + M_m \qquad (2\text{-}23)$$

Where

The first term on the right hand side is the mixture pressure which can be assumed that it is equal to the pressure of the q^{th} −phase pressure.

The second term shows the average viscous stress in which τ_k means the k^{th} − Phase.

In the third term which is the turbulent stress, ρ_{IK} is the local velocity of the k^{th} − Phase and u_{Fki} and u_{Fkj} are the fluctuating velocity components of k^{th} − Phase in x_i and x_j respectively. In the fourth term, that is, the diffusion stress u_{Mki} and u_{Mkj} are the diffusion velocities which mean the difference between k^{th} – Phase and the velocity at the centre of mixture mass in x_i and x_j −direction respectively.

The last term, M_m , stands for the momentum of the mixture, that is, the effect of surface tension force. For each phase it can be computed by the sum of momentum.

2.4.4.3 Comparison of DPM and VOF

Comparing DPM to VOF modelling, DPM modelling application proves to be more challenging than VOF. VOF is more useful and computationally affordable. This inconvenience of DPM is due to the formulation of position vectors as the solids respond to shear stresses. In VOF formulations, physical laws do not possess the position vectors and the velocity appears as the major variable thereby revealing all fluid flow patterns necessary.

This is due to the fact that the turbulent fluids which are subjected to shear stress deform continuously when the stress is applied (Panton, 1984). The importance and usefulness of VOF, however, can be achieved at high computational grid resolution (Cloete *et al.,* 2009). As a common drawback, both models cannot be used with density-based solvers; only the pressure based solver is allowed.

2.4.5 Aeration effects in multiphase modelling

Chatila & Tabbara (2004) conducted a study with a CFD software package called ADINA-F to compare water surface profiles over an ogee spillway geometrically similar to the physical model. The spillway profile was free of piers and water free surface was measured at the centreline to avoid an influence from the wall boundaries. The results achieved show that, even if qualitative solutions are reasonably consistent with general flow patterns, an inconsistency was found. In all three simulated discharges, ADINA-F, predicted water surface levels much lower than the experimental water levels along the spillway length. These inconsistencies were found to be caused by air entrainment effects which were not accounted for the CFD model used. The same happened in the research of Song & Zhou (1999) due to the use of the marker and cell method to track the free surface. They used different CFD software in their research, called Flow-3D for modelling the Keeyask spillway. The results produced by Flow-3D included the effects of air entrainment because of the use of the volume of fluid method (VOF).

Although some differences appeared at the entrance and exit of the numerical domain, the computed results were in good agreement with those measured in the physical modelling.

2.4.6 Advantages of using CFD

CFD has grown from a mathematical field to become a crosscutting tool in nearly every branch of fluid dynamics. It assists in analysis of fluid mechanics and its impact on the structure through/on which water is flowing. In the engineering field, CFD is used to analyse new designs before they are implemented. A number of clear advantages can be summarised as follows:

- CFD can give an insight into flow patterns, weight losses, mass and heat transfer, flow separation, etc. Thence, all of these parameters may help implementers with a much better and thorough understanding of what is happening on the field (Wanot, 1996).
- CFD reveals complex features that could not be achieved by physical modelling such as high temperature.
- CFD can be used to test dangerous experiments with cheaper means and without risks such as accident scenarios or safety studies

2.5 Summary

The literature review shows that the design process of an ogee spillway is reasonably well understood. A number of approaches have been developed by various researchers and most of them are based on USBR and USACE publications.

These theories provide the design parameters such as the design head (H_o) and the discharge coefficients (C_o) for which the ogee profile can be designed and the discharges computed. However, this is not enough to ensure a better performance and stability of a spillway; it is necessary to determine and analyse all hydrodynamic pressures generated from water flows (Johnson & Savage, 2006).

These hydrodynamic pressures are complex and they are determined at both accelerating and decelerating regions to predict the pressure distribution on a spillway. In addition, aeration of the nappe is the key factor which must be considered in spillway design since it has a great impact on the spillway performance Şentrürk (1994).

The advances in numerical methods as well as the development of computing power are attempting to improve the quantification of hydrodynamic pressures and aeration in the spillway flow nappe.

These factors are very important for improving the spillway performance and to limit negative pressures which could damage the concrete surface of a spillway.

Amongst numerical methods, Computational Fluid Dynamics (CFD) is found to be increasingly used in the spillway flow field. A clear advantage of these methods lies in their ability to simulate the effects of turbulence and multiphase flow since most of the flows in nature are turbulent and multiphase.

However, the CFD method is not used as a standalone method in the spillway design, the physical modelling is always required for a validation. This comparative study is used so as to allow engineers to verify the degree of accuracy of CFD results.

CHAPTER 3: PHYSICAL MODEL INVESTIGATION

3.1 Introduction

In this chapter the detailed presentation of the experimental test process carried out in the laboratory is outlined. The focus is on different considerations and assumptions made with regard to obtaining the experimental results for a comparison with the results from CFD modelling. The hydraulic aspects that are investigated are mainly the hydrodynamic characteristics of flows and water surcharge upstream and along the spillway downstream face.

3.2 Background and importance of physical models

Physical models play a key role in the hydraulic design process in order to optimise a structure and to ensure its safe operation. Although the capabilities to model hydraulic performance computationally are constantly developing, physical modelling has not become obsolete. It keeps pace with mathematical modelling and in most cases they make progress together. Physical models continue to be developed, especially, for the use of validation of other methods (including computational methods) and they still remain the main tool to rely on. They are considered to be the basis with which all other methods are compared (Savage & Johnson 2001).

Ogee spillways, specifically those which exhibit a complex geometry have been widely modelled in order to determine the flow regime and to reveal early problematic features before their construction. In this context, the physical model employed in this study was adopted to monitor various parameters such as pressure head and water surcharge.

3.3 Physical model set-up and laboratory facilities

The physical modelling tests for this study were carried out in the Hydraulic Laboratory of Stellenbosch University, located in the Western Cape Province, Republic of South Africa. The physical modelling consisted of two ogee spillways installed, one after another, in a glass flume of 1.25 m high, 0.60 m wide and 22 m in length. The maximum flow rate that could be obtained in the laboratory from a constant head tank was 130 l/s. The laboratory set-up was a closed loop system whereby the outflow system was set up in a way that allowed the flow to be re-used. The conceptual laboratory set-up is shown in Figure 3-1

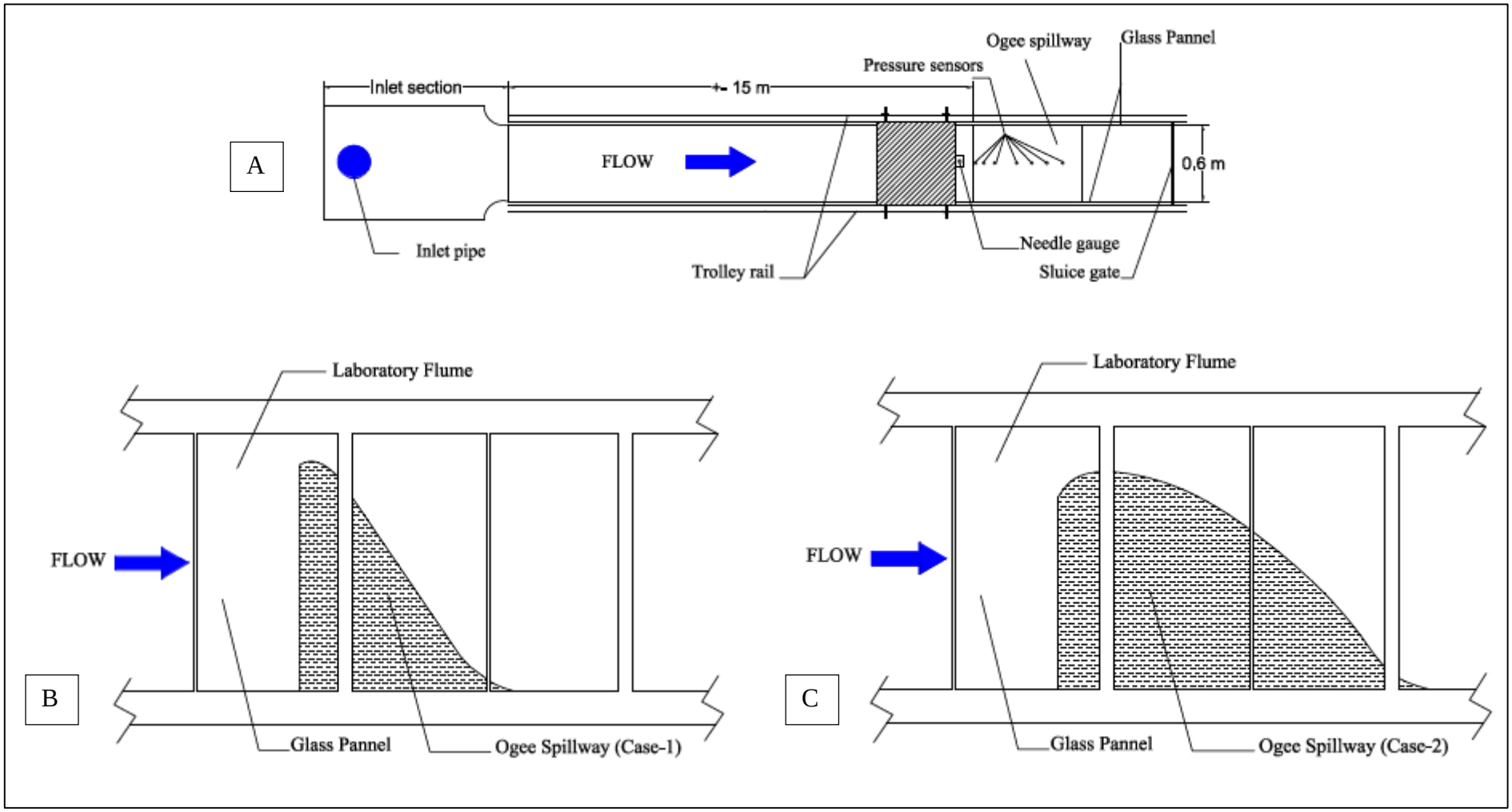

Figure 3-1: Conceptual laboratory setup: A: Plan view, B: Side view of Case-1, C: Side View of Case-2

To complete the laboratory work, a number of instruments were used. A manually operated trolley system equipped with a needle gauge (point), allowed with the vertical movement along the flume, was selected as a better way to measure water surcharge along the ogee spillway. This needle gauge had one degree of freedom, that is, to operate vertically and perpendicularly to the channel bed of the flume. The crest pressure readings were collected with the use of a laptop computer which was connected to seven pressure transducers.

The flow meter and adjustable valve installed in the supply system were used to regulate different flows. To obtain enough flow, however, a system composed of two high capacity pumps pumping water from an under-ground tank to the constant head tank, and a reticulation pipe with a flow control valve were used to provide the release of different flows. In addition, video and photograph recordings were made to record the flow patterns at all sides of the physical model. Figure 3-2 depicts the set- up of the physical model.

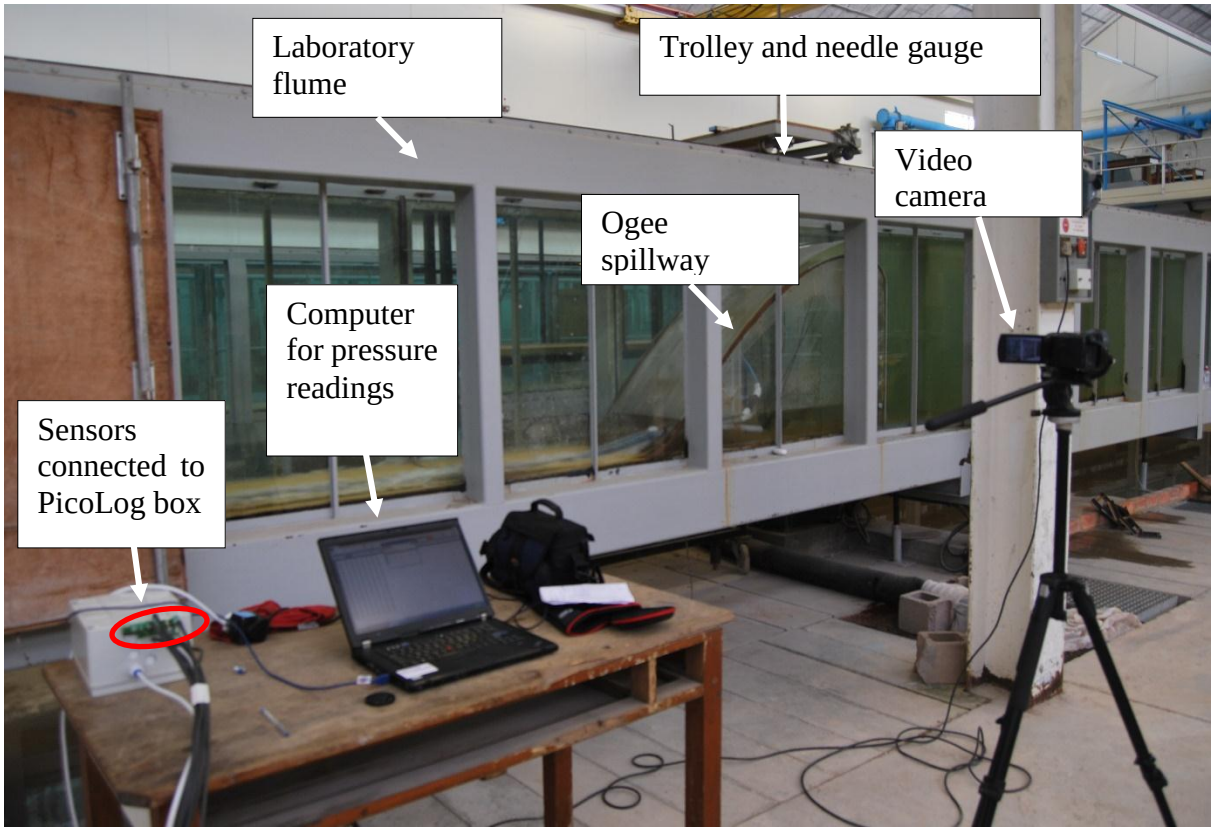

Figure 3-2: Laboratory set-up

3.4 Physical Model Design

In this section, the hydraulic and geometric designs of the two ogee spillways that were used for physical modelling are detailed. The design approach was based on the procedure documented in Small Dam Design by USBR (1987).

In this research, two physical models were tested. The primary spillway model is 1:30 scale of a large sized-dam[1] . The secondary spillway model is ten times the size of the upper part of the primary model as depicted in Figure 3-3. This second scenario was performed with the overall objective of getting more details at the crest of an ogee spillway. However, the experimental results were not scaled up to the prototype as the objective of this study was to compare the results produced by CFD models with physical model results.

In this investigation, the primary and secondary models are referred to as Case-1 and Case-2, respectively.

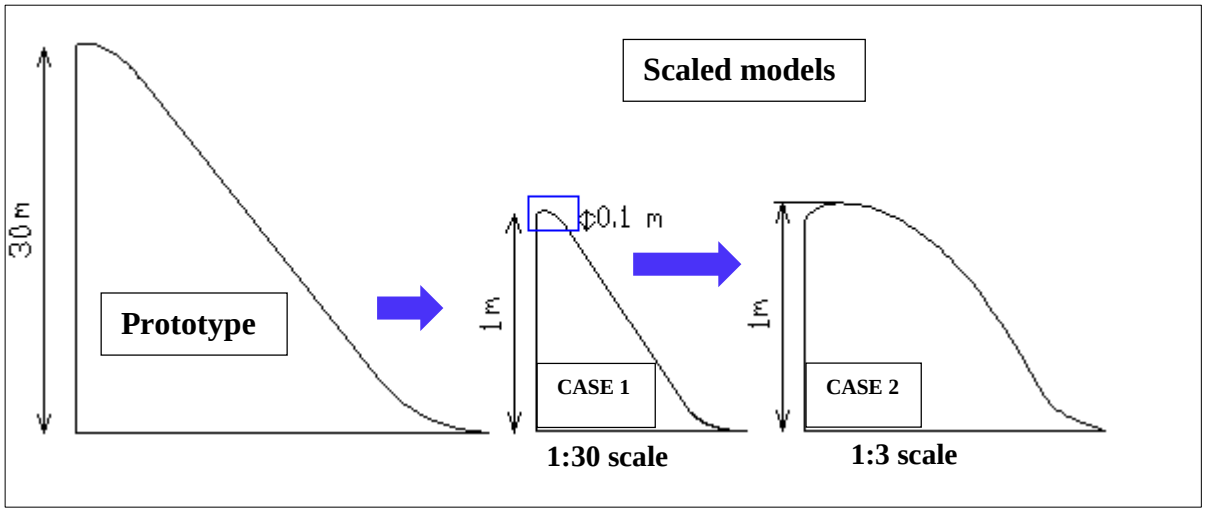

Figure 3-3: Schematic representation of the spillway prototype and scaled models

3.4.1 Physical model dimensions

Upon the completion of the model construction, it was necessary to carry out a geometric survey in order to check that the design dimensions were not altered. To achieve this, a topographic survey with an accurate total station was used as the most trusted technique to obtain all the dimensions with a minimum of errors.

[1] The term large-sized dams refers to all dams which have an approach depth (P) ranging from 12 to 30m (SANCOLD, 2011).

Figure 3-4 and Figure 3-5 give all geometric dimensions, in millimetres, of the first and second case respectively.

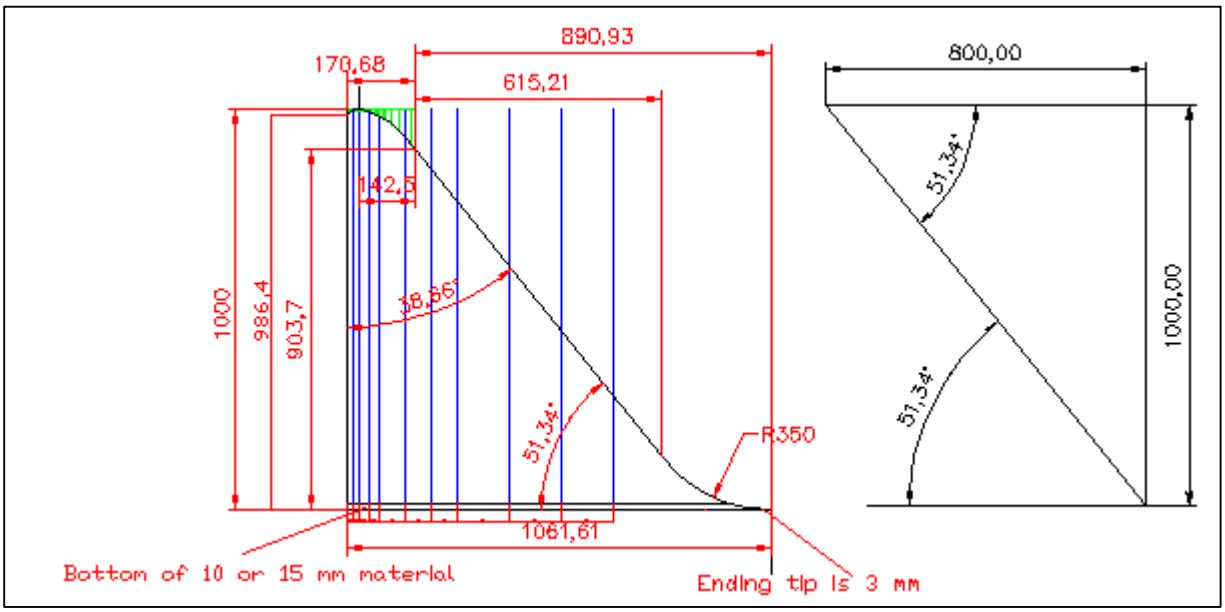

Figure 3-4: Physical model geometry of 1:30 scale model, i.e. Case -1 (dimensions in mm)

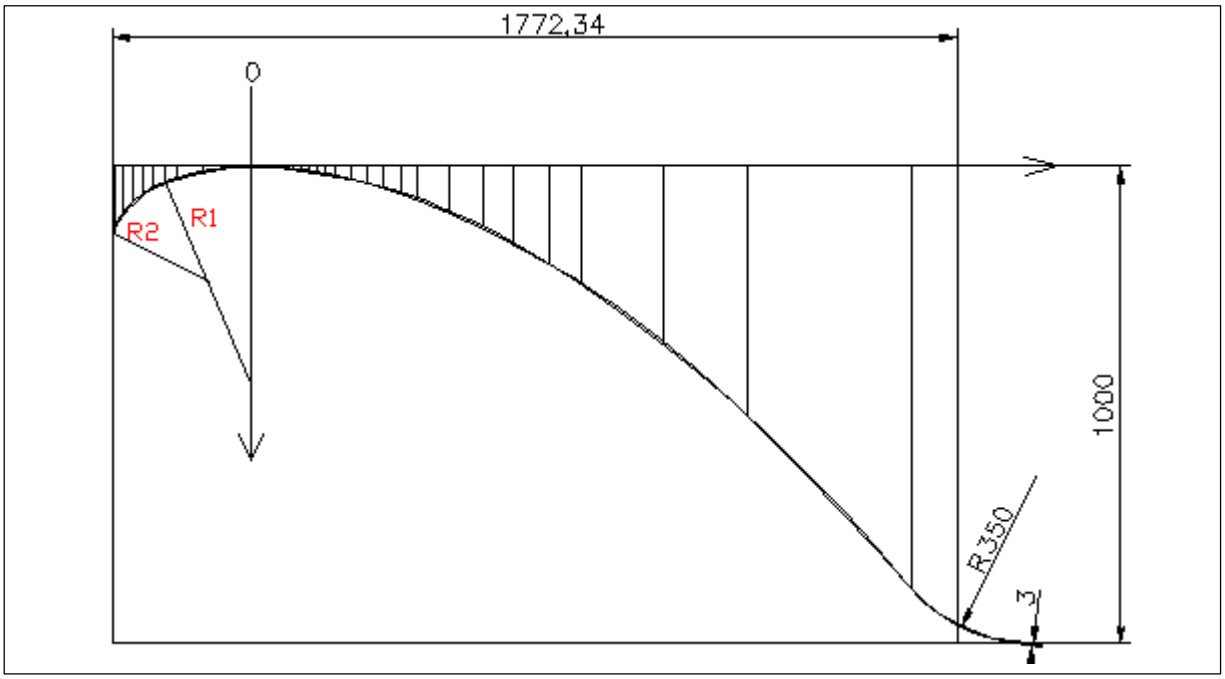

Figure 3-5: Physical model geometry of 1:3 scale model, i.e. Case -2 (dimensions in mm)

The geometric dimensions for both cases are summarised in Table 3-1. It is noted that since the same flume of 0.6 m wide was used in the laboratory, the prototype width modelled by the 1:3 model is 3*0.6=1.8 m and that for the 1:30 model is 30*0.6=18 m.

Table 3-1: Model dimensions

Model Type	Spillway approach depth (m)	Crest width (m)	Radii (m)	
			R_1	R_2
Case-1	1.00	0.60	0.05	0.02
Case-2	1.00	0.60	0.50	0.20

3.4.2 Flow parameters

During the planning phase, the flow conditions for various tests had to be determined. The discharge over each spillway section was determined using Equation 2-7, found in Section 2.3.4, and each discharge was determined with respect to the following major variables:

- Head over the crest (He)
- Discharge coefficients (C)

Table 3-2 presents the design heads and discharge coefficients for both spillway models.

Table 3-2: Design Surcharge, coefficient of discharge and design discharge for each model

Model Type	Design surcharge (H_o) in m	Coefficient of discharge (C_o)	Design discharge (m^3/s)
Case-1	0.10	2.18	0.041
Case-2	1.00	2.18	1.308

Based on USBR (1987), the coefficients of discharge for different heads other than the design head and the rating curve showing the relationship between the discharge Q (m^3/s) and head (m), respectively, are presented in Figure 3-6 and Figure 3-7.

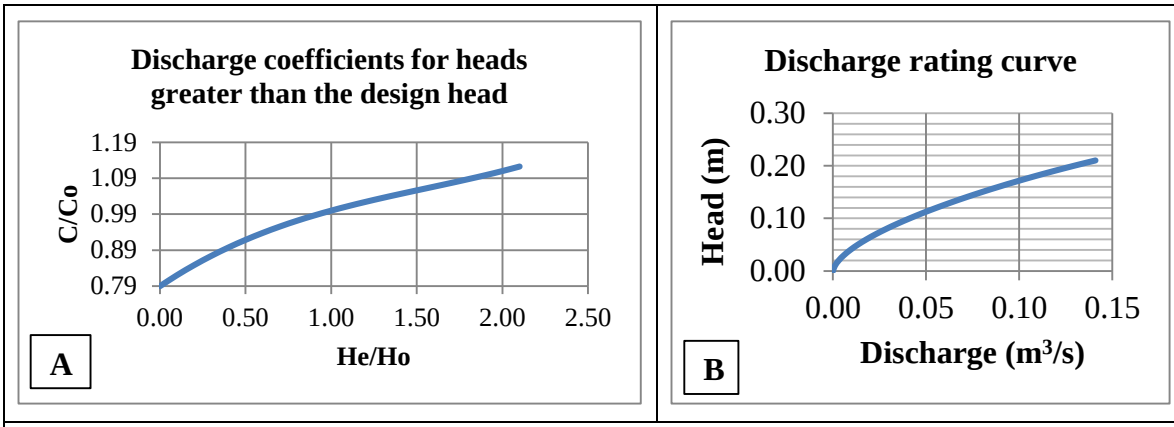

Figure 3-6: Discharge characteristics of the physical model (Case-1): A: Discharge coefficients, B: Discharge rating curve

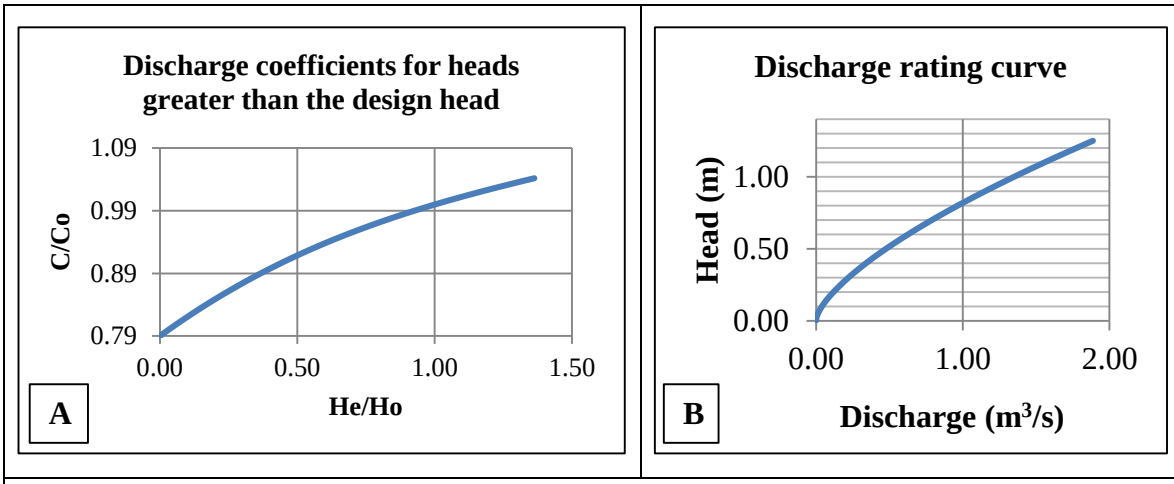

Figure 3-7: Discharge characteristics of the physical model (Case-2): A: Discharge coefficients, B: Discharge rating curve

3.5 Measuring Equipment and Techniques

During the physical modelling, much attention was paid to the necessary instrumentation. Their proper installation and use required a strong emphasis in order to yield accurate measurements which served as the basis for validation of the numerical model results.

3.5.1 Pressure sensors

Seven pressure transducers (WIKA S10) were mounted underneath the ogee spillway chute to measure hydrodynamic pressures. WIKA S10 transducers are fabricated with a high precision to fit most industrial pressure measurement applications (WIKA, 2013).

The transducers have a measuring pressure range of one meter of water (1 m H_2O) with an accuracy of 0.1% of the full range. All the data were collected with PicoLog data acquisition software connected to a laptop. They were anchored in seven holes drilled into the spillway face, arranged in a scattered pattern to avoid any chance of influence from one sensor to the next one.

To protect sensors from external influence, the transducers wiring was protected by a plastic tube underneath the ogee spillway. All of the wires were brought out of the spillway section through an outlet opening. Thereafter, the wires were connected to the power supply and data acquisition system. Proper operation of the pressure sensors was confirmed by three preliminary trials which produced the same pressure reading.

Figure 3-8 and Figure 3-9 depict the location of the seven sensors on both physical models.

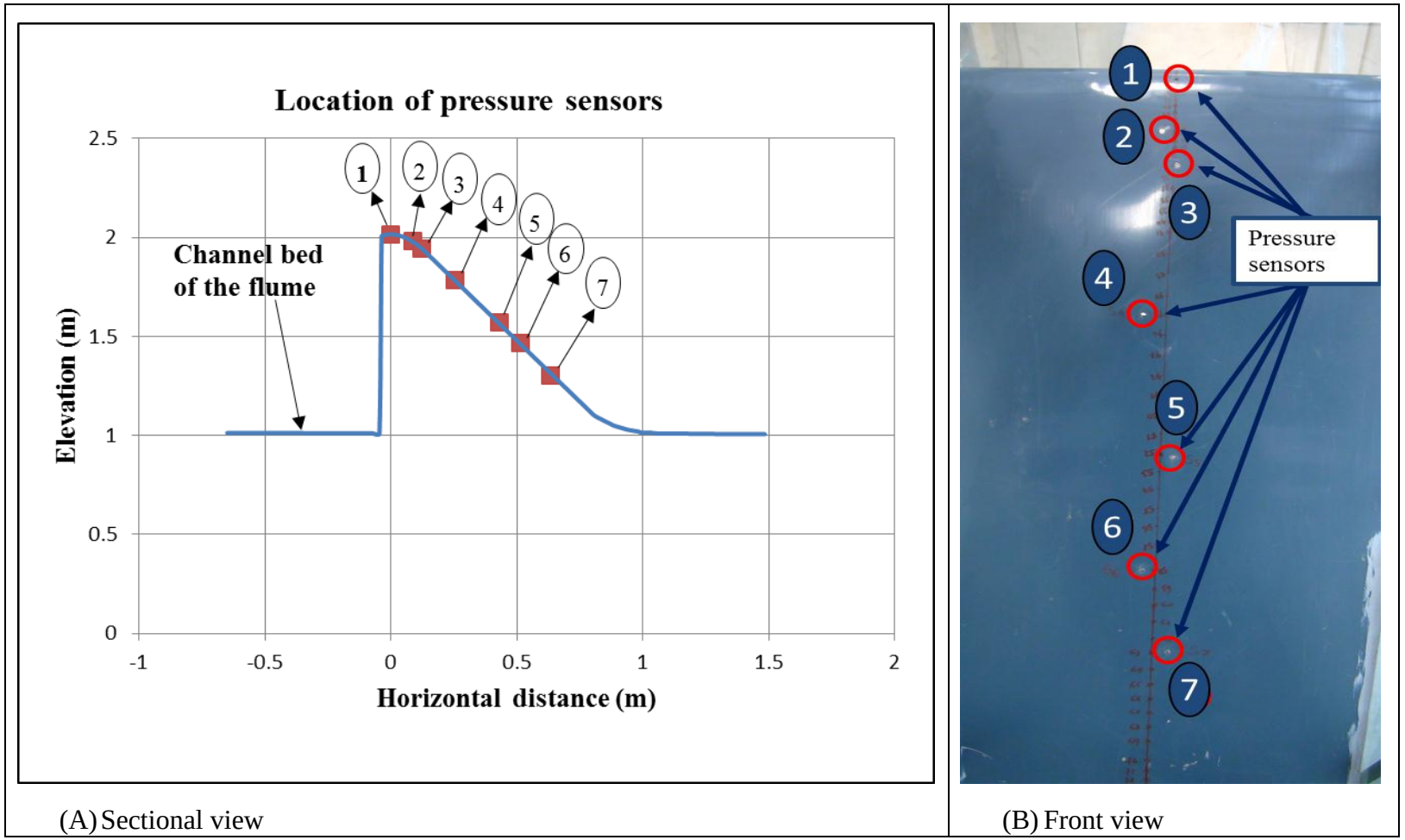

(A) Sectional view

(B) Front view

Figure 3-8: Positions of pressure transducers on Case-1

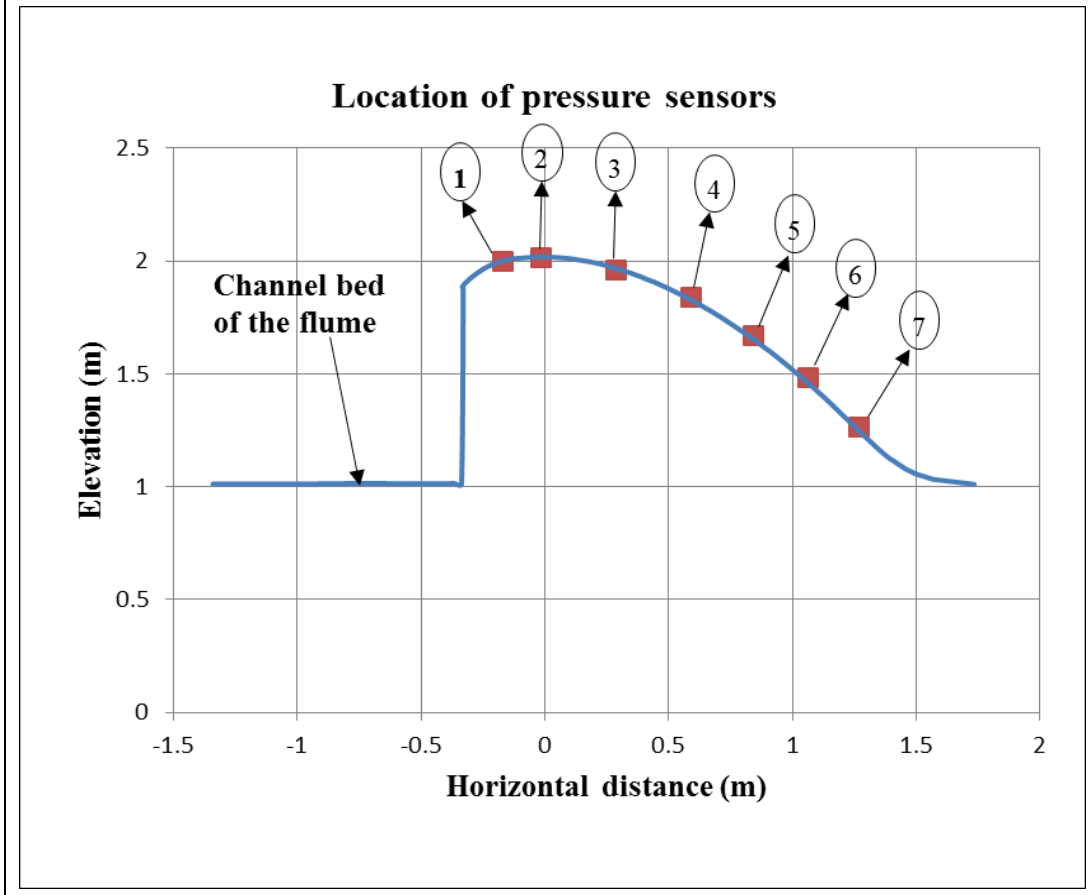

(A) Sectional view

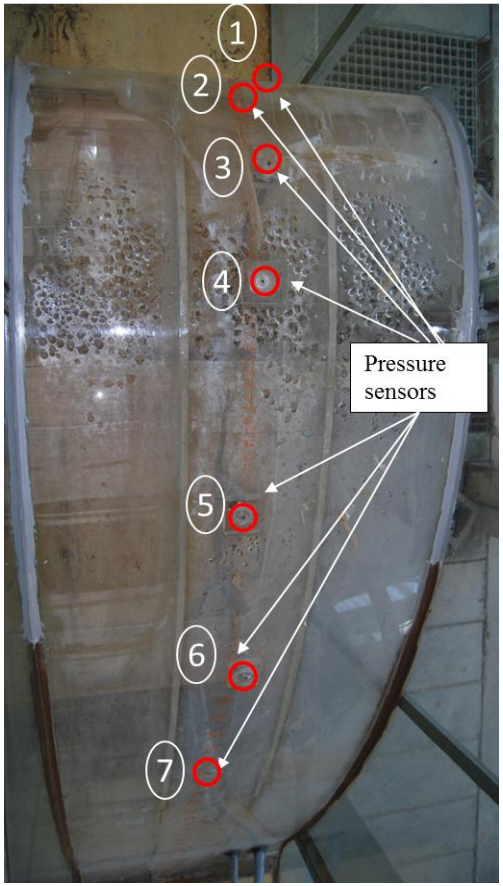

(B) Front view

Figure 3-9: Positions of pressure transducers on Case-2

3.6 Experimental procedure

Before conducting the tests, an adjustment phase which included the preliminary trials to check if the model was defective, were performed. In this regard, each model was checked cautiously to ensure a higher degree accuracy of the results. Some slight rehabilitation works were carried out on the flume, including the removal of protruding solid silicone sealant, and mending the cracked Plexiglas of the outer wall of flume. Before testing the targeted discharges, the flow was released to check if the model was ready enough to serve for testing. These preliminary trials proved that the physical models were in acceptable condition and ready to be used testing.

Initial pressure tests were conducted with no flow ($Q = 0\ l/s$) on the weir. The purpose of these measurements was to provide the reference point used to determine the change in pressure and flow surcharge at each flow increase. Using a controlling valve through a reticulation pipe, eight discharges for each model were tested. A flow meter in the supply pipe to the flume was located close the discharge end to the flume, while the spillway was installed close to the outlet. For each run, the pressure was recorded and the water surcharge were measured at a distance of 5H upstream of the weir as recommended by Chadwick *et al.* (2007). This was necessary in order to measure the water surcharge accurately without influence from the crest. As the channel had a constant head level, there was no problem with the measuring point located at 5H upstream.

A sampling frequency of 100 Hz and a recording period of five minutes (5 min) were selected for pressure recordings in the physical modelling as well as in the CFD modelling.

3.7 Physical modelling results

As discussed in the previous chapter, the results of model tests are very important in the design of ogee spillway structures to ensure an adequate and safe operation of the prototypes. The pressures and surcharge results obtained in the physical modelling are clearly presented and discussed in this section. However, Appendix A contains a number of graphs which contain the detailed information acquired, whilst Appendix B contains photographs taken during the testing. Furthermore, the results obtained from the physical modelling were compared to the CFD results in Chapter 5 which deals with the validation of CFD modelling.

3.7.1 Pressure results

3.7.1.1 Case- 1

Pressure readings for eight different discharges were recorded over a period of five minutes. For each discharge, it was necessary to wait for five to ten minutes (5-10 min) before recording, to allow the flow to become stable. A sample of pressure results at a discharge of 23 l/s is presented in Figure 3-10.

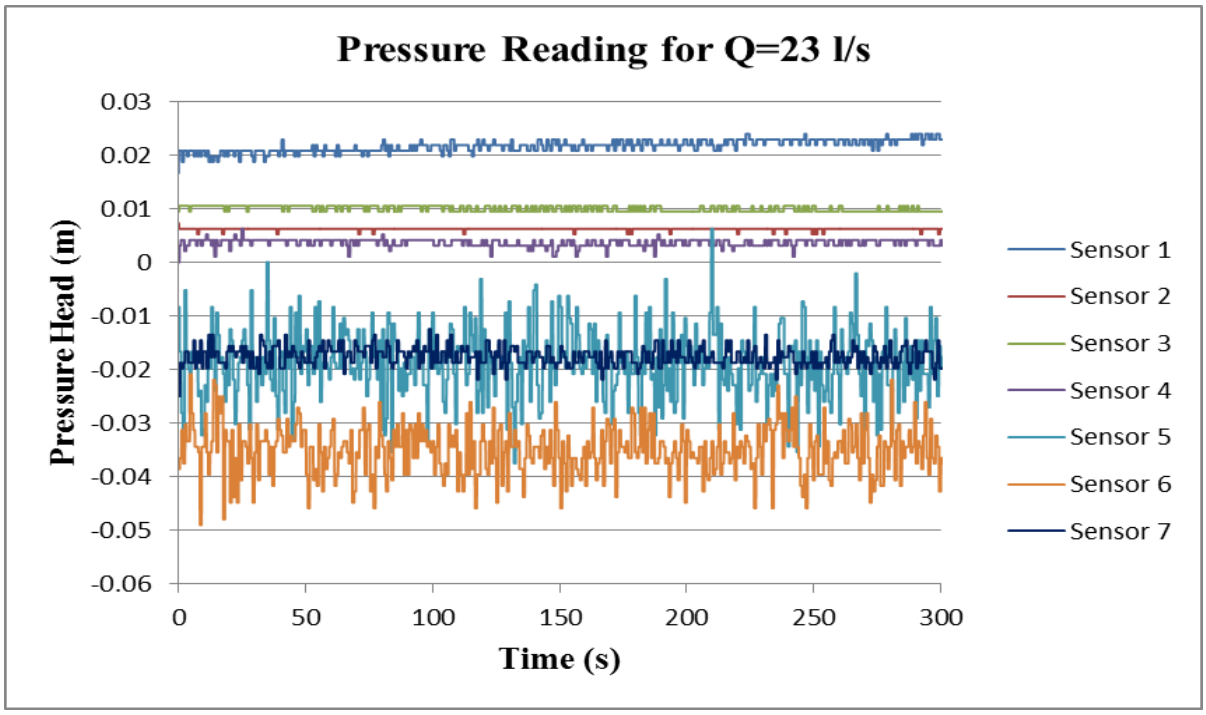

Figure 3-10: Physical modelling results for Case-1, for Q= 23 l/s

Figure 3-10 indicates slight positive pressures for the sensors located at the crest, that is, Sensors 1, 2 and 3. For the rest of the sensors a progressive reduction in pressure, with a negative pressure reading, is found at Sensors 5, 6 and 7. This shows that for a given discharge, the pressures differ along the spillway face.

In addition, the first four sensors (Sensors 1, 2, 3 and 4) do not indicate a high fluctuation in the graphical trends. This may be attributed to the location of the sensors. They are located above the inception point from which the self-aeration of spillway flow commences.

All of the average pressure results obtained from Case-1 are presented in Table 3-3 and Figure 3-11.

Table 3-3: Results summary for physical model testing (Case-1)

Targeted discharge (l/s)	Achieved Discharge (l/s)	Physical model: Average sensor pressure (m)						
		1	2	3	4	5	6	7
0	0	0	0	0	0	0	0	0
23	23.3	0.017	0.005	0.009	0.000	-0.037	-0.049	-0.025
35	35.5	0.032	0.004	0.011	-0.002	-0.035	-0.055	-0.022
41	41.2	0.028	0.003	0.006	0.001	-0.037	-0.054	-0.029
56	56.4	0.012	-0.003	0.009	0.005	-0.030	-0.055	-0.018
71	71.3	-0.005	-0.008	0.008	0.005	-0.029	-0.052	-0.015
89	89.3	-0.029	-0.026	0.006	0.014	-0.022	-0.049	-0.010
108	108.6	-0.056	-0.034	0.002	0.019	-0.019	-0.056	-0.012
130	130.7	-0.094	-0.050	-0.006	0.020	-0.017	-0.040	-0.004

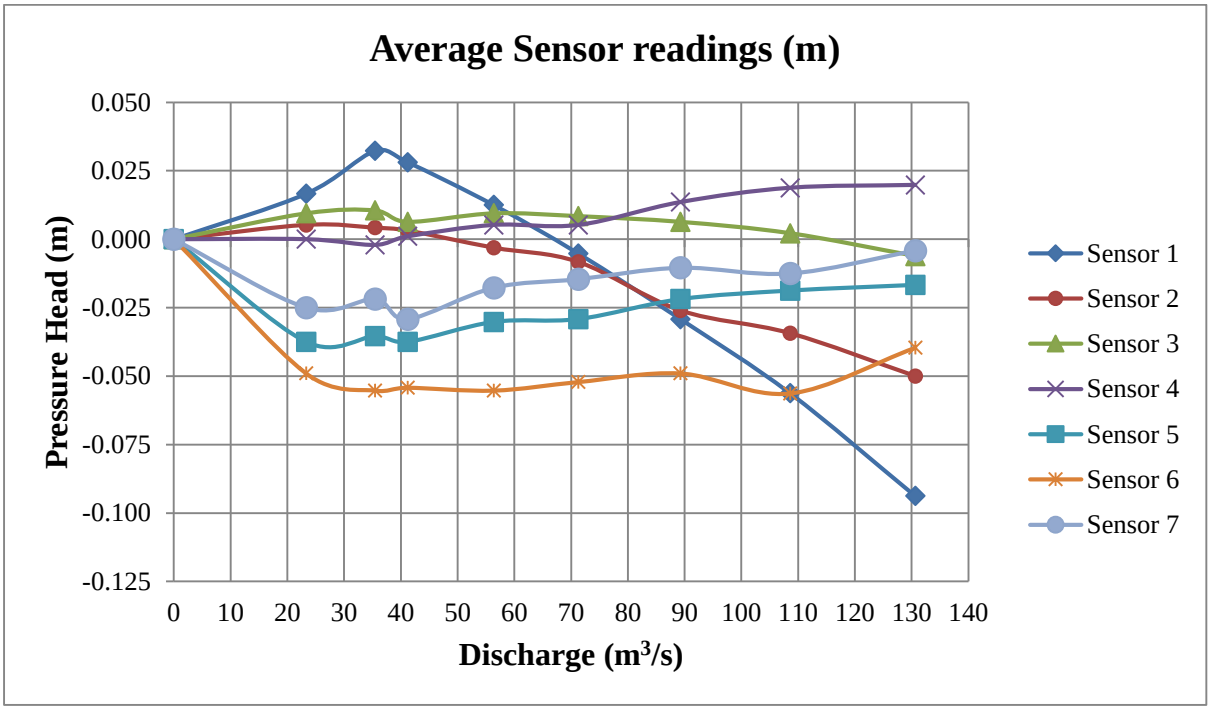

Figure 3-11: The average pressure readings obtained during testing of Case-1

As mentioned, Table 3-3 and Figure 3-11 present the average pressure results obtained from physical modelling of Case-1, for all seven pressure sensors and for all discharges tested. The sensors located at the crest (Sensors 1 and 2) indicate the reduction of average pressure from positive to negative value.

This pressure reduction is proportional to the increase of discharge. The most negative average pressure displayed in the results is -0.094 m recorded from sensor1 for a discharge of 130 l/s.

The most significant observation from the experiments that were carried out on the primary model (Case-1) was that for all discharges less and equal to the design discharge, the crest sensors indicated a positive pressure reading. For the discharges greater than the design discharge, a negative pressure reading was encountered at the same sensors.

3.7.1.2 Case-2

For Case-2, eight discharges were simulated while recording pressure readings at seven sensors as was done for Case-1. A sample of pressure readings for 25 l/s is presented in Figure 3-12.

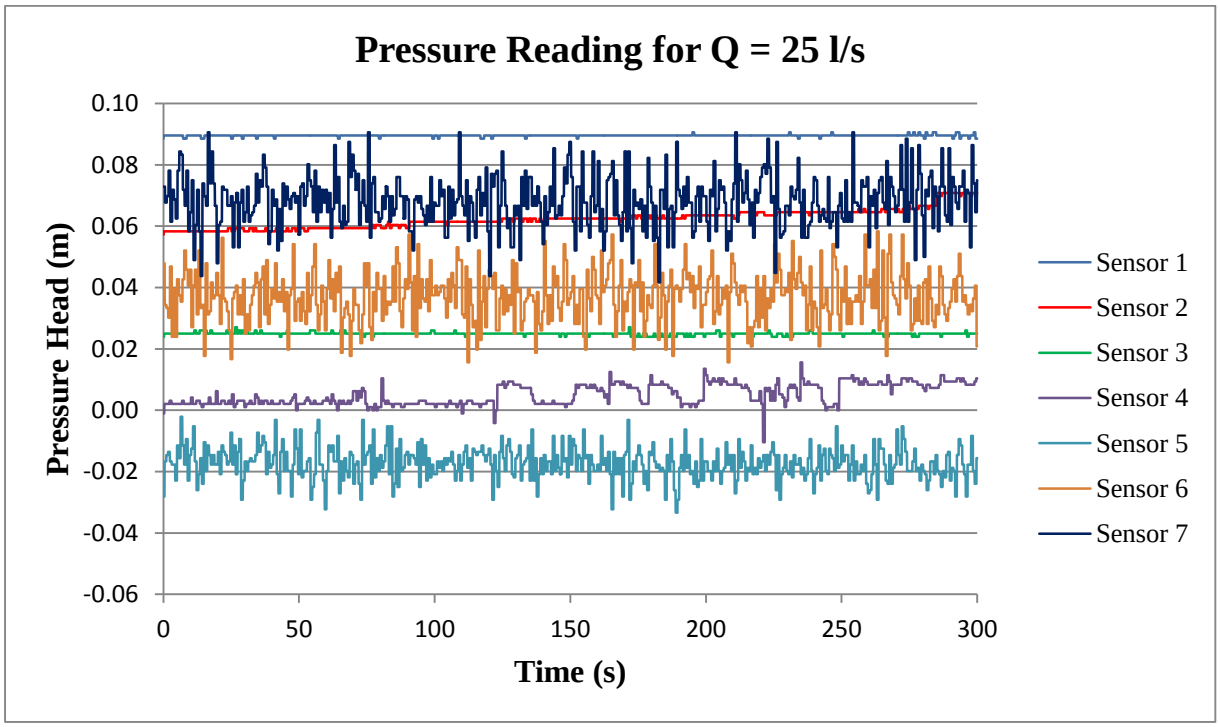

Figure 3-12: Physical modelling results for Case-2, for Q= 25 l/s

Figure 3-12 shows that the results obtained through physical modelling of Case-2 for a discharge of 25 l/s produced different pressure readings along the spillway. The first three sensors (Sensor 1, 2 and 3) do not exhibit a high fluctuation in graphical trend.

This means that these three sensors are located above the incipient point where self-aeration starts. This phenomenon was also observed in the results of case-1.

All of the results obtained from Case-2 have been summarized in a tabular and graphical form. Table 3-4 indicates the targeted discharges, achieved discharges and the average pressure heads measured at each sensor.

Table 3-4: Results summary for physical model testing (Case-2)

Targeted discharge (l/s)	**Achieved Discharge (l/s)**	**Physical modelling: Average sensor pressure (m)**						
		1	**2**	**3**	**4**	**5**	**6**	**7**
0	0.0	0	0	0	0	0	0	0
25	25.4	0.090	0.062	0.025	0.005	-0.017	0.037	0.068
37	37.7	0.106	0.083	0.030	0.003	-0.024	0.037	0.070
44	44.6	0.119	0.108	0.052	0.022	-0.016	0.096	0.095
51	51.4	0.125	0.114	0.055	0.023	-0.022	0.096	0.097
78	78.2	0.148	0.134	0.064	0.032	-0.032	0.099	0.099
85	85.5	0.155	0.141	0.073	0.035	0.003	0.100	0.101
95	95.4	0.163	0.147	0.077	0.038	0.004	0.103	0.102
117.2	117.2	0.176	0.160	0.084	0.043	0.006	0.105	0.106

The results presented in Table 3-4 were obtained from the physical modelling of Case-2 for all seven pressure sensors and for all discharges tested. The average negative pressures are indicated at sensor number 5 which is located at the downstream part of the spillway.

During the physical modelling of Case-2 all the discharges that were tested were less than the design discharge as the flume was limited at 0.25 m above the crest. This implies that the crest pressures (from sensors 1, 2 and 3) were positive. Figure 3-13 is the summarising graph presenting all average pressures attained from Case-2.

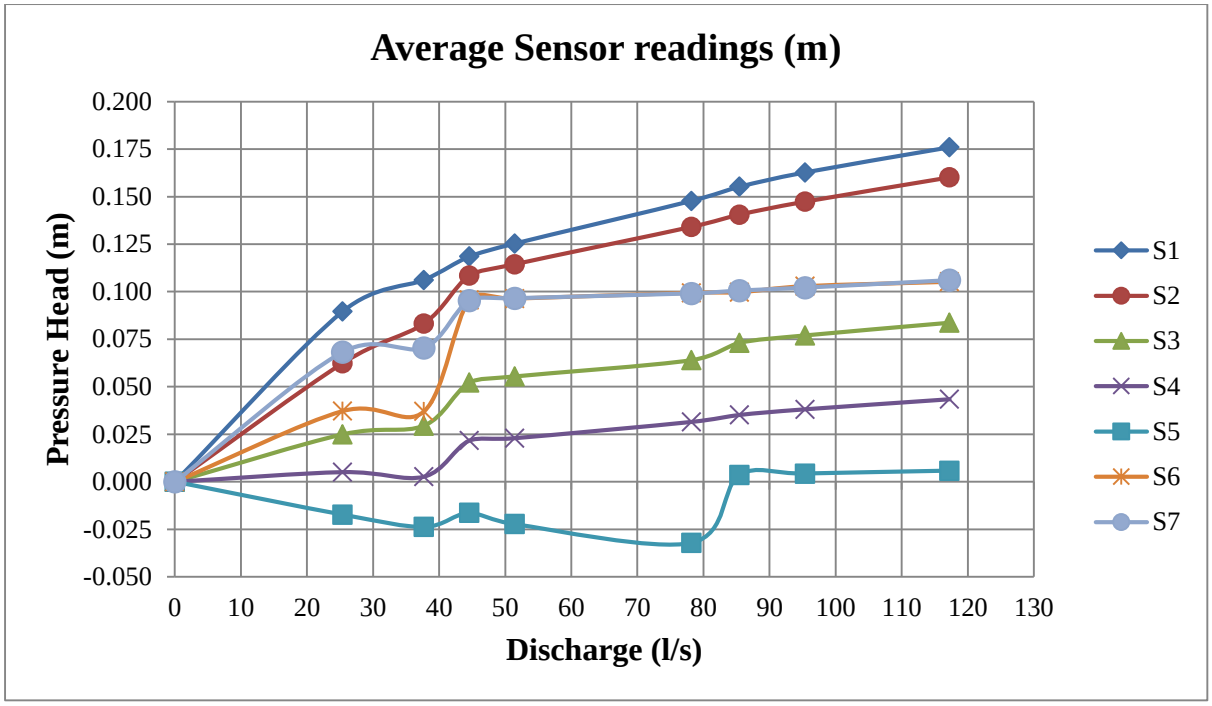

Figure 3-13: The average pressure readings obtained during testing of Case-2

Figure 3-13 is a good representation of the hydrodynamic pressure increase on the ogee spillway for the discharges less than the design discharge. The appraisal observation of this summary graph shows that pressures on the spillway increase with the increase of discharge.

On the other hand, for the discharges greater than the design discharge, the crest pressures drop to negative values as shown in Figure 3-11.

3.7.2 Water surcharge

3.7.2.1 Case-1

For proper performance of the ogee spillway, flow in the approach channel and on the spillway face should be relatively uniform without excessive turbulence. Rough water surfaces may be caused by the side walls effects and/or very sharp radii. As depicted in Figure 3-14 the flow surface at the design discharge is smooth.

Figure 3-14: Flow over ogee spillway Case-1 at the design head

As discussed previously, the water surcharge upstream of the physical model was measured at a distance equal to 5H, using the needle gauge. This water surcharge resulted from the difference of water surface level and the crest level of the spillway. The difference (%) between the empirical and measured water surcharge was calculated using Equation (3-1) and the highest percentage difference encountered was 5.2 %.

$$Difference\ \% = 100x(\frac{Empirical\ surcharge\ -experimental\ surcharge}{Empirical\ \ surcharge}) \quad (3\text{-}1)$$

Water surcharge results obtained from the theoretical calculations and experimental results are presented in Table 3-5 and Figure 3-15.

Table 3-5: Measured and empirical water surcharge for ogee spillway (Case-1)

SN°	Targeted Q (l/s)	Achieved Q (l/s)	Empirical Water surcharge (mm)	Measured Water surcharge (mm)	Difference (%)
1	0	0	0	0	0
2	23	23.3	70	70	0%
3	35	35.5	90	86	5%
4	41	41.2	100	98	2%
5	56	56.4	120	120	0%
6	71	71.3	140	137	2%
7	89	89.3	160	156	3%
8	108	108.6	180	175	3%
9	130	130.7	200	197	2%

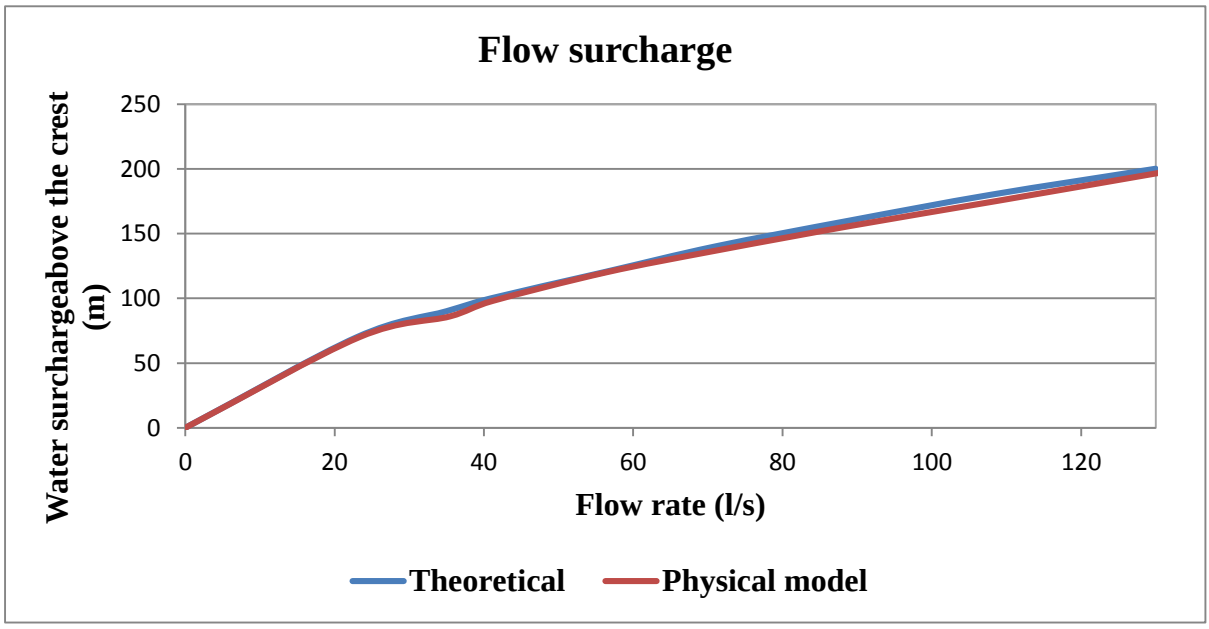

Figure 3-15: Theoretical and surcharge of flow over an ogee weir (Case-1) measured at 5H upstream

As shown in Table 3-5 and Figure 3-15, water surcharge from the theoretical calculations are compared to the experimental results.

3.7.2.2 Case-2

Water levels on the second ogee spillway model (Case-2) were measured in the same way as was done for the first case. The results are presented in Table 3-6 and Figure 3-16.

Table 3-6: Measured and empirical water surcharge for ogee spillway (Case-2)

SN°	Targeted Q (l/s)	Achieved Q (l/s)	Empirical Water surcharge (mm)	Measured Water surcharge (mm)	Difference (%)
1	0	0	0	0	0
2	25	25.4	83.3	79	5.2%
3	37	37.7	107.4	104	3.2%
4	45	44.6	119.6	118	1.3%
5	51	51.4	130.9	128	2.2%
7	77	78.2	171.0	166	3.0%
8	85	85.5	181.0	179	1.1%
9	95	95.4	193.9	192	1.0%
10	117	117.2	220.8	218	1.3%

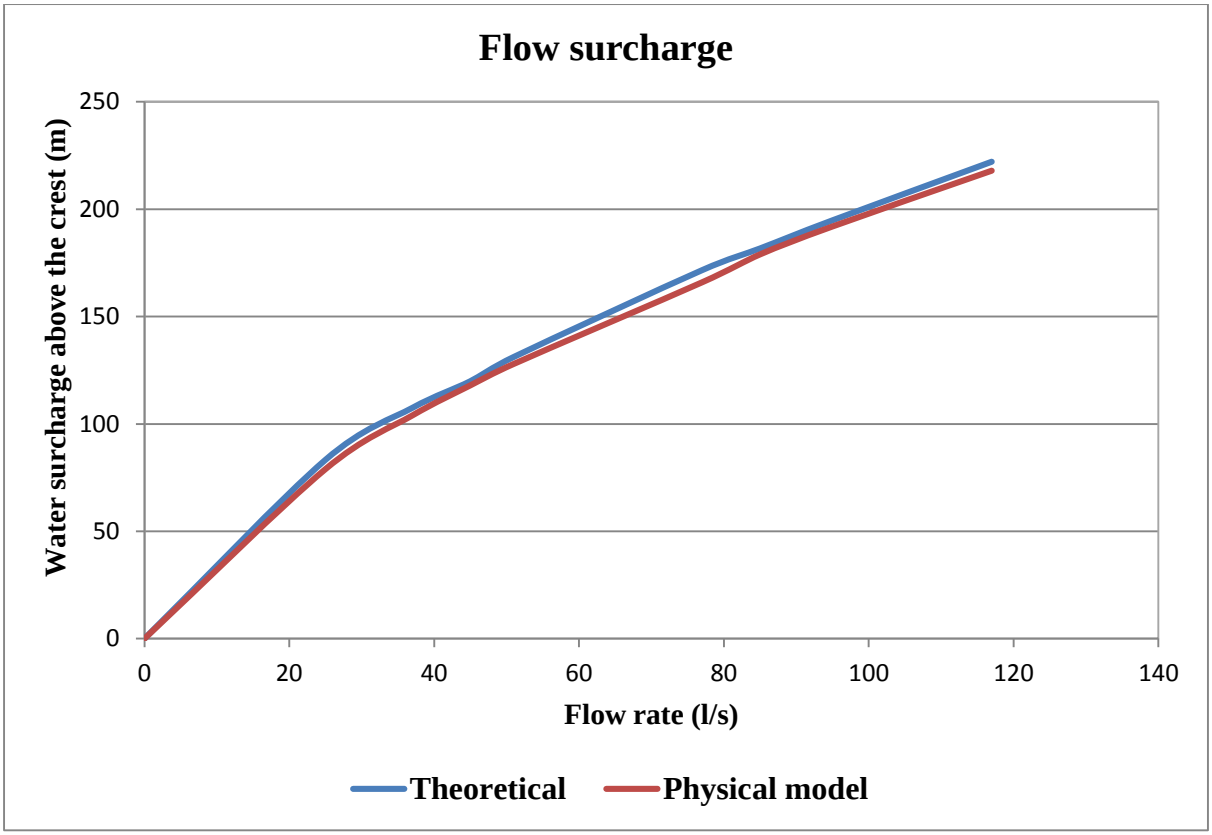

Figure 3-16: Theoretical and measured surcharge of flow over an ogee weir (Case-2) measured at 5H upstream

Apart from measuring the water surcharge at a distance of 5H upstream from the spillway, water free surfaces were investigated at the entire spillway surface. Profiles of the water surface over ogee spillways are measured to allow the determination of boundary wall height for uncontrolled ogee spillways. They also aid in positioning gates in controlled ogee spillways to ensure that the flow will be released or retained properly. These water surfaces were measured at the centreline of the spillway to avoid the boundary effects.

Figure 3-17and Figure 3-18 present a sample of water levels results measured for case-1 and Case-2 respectively.

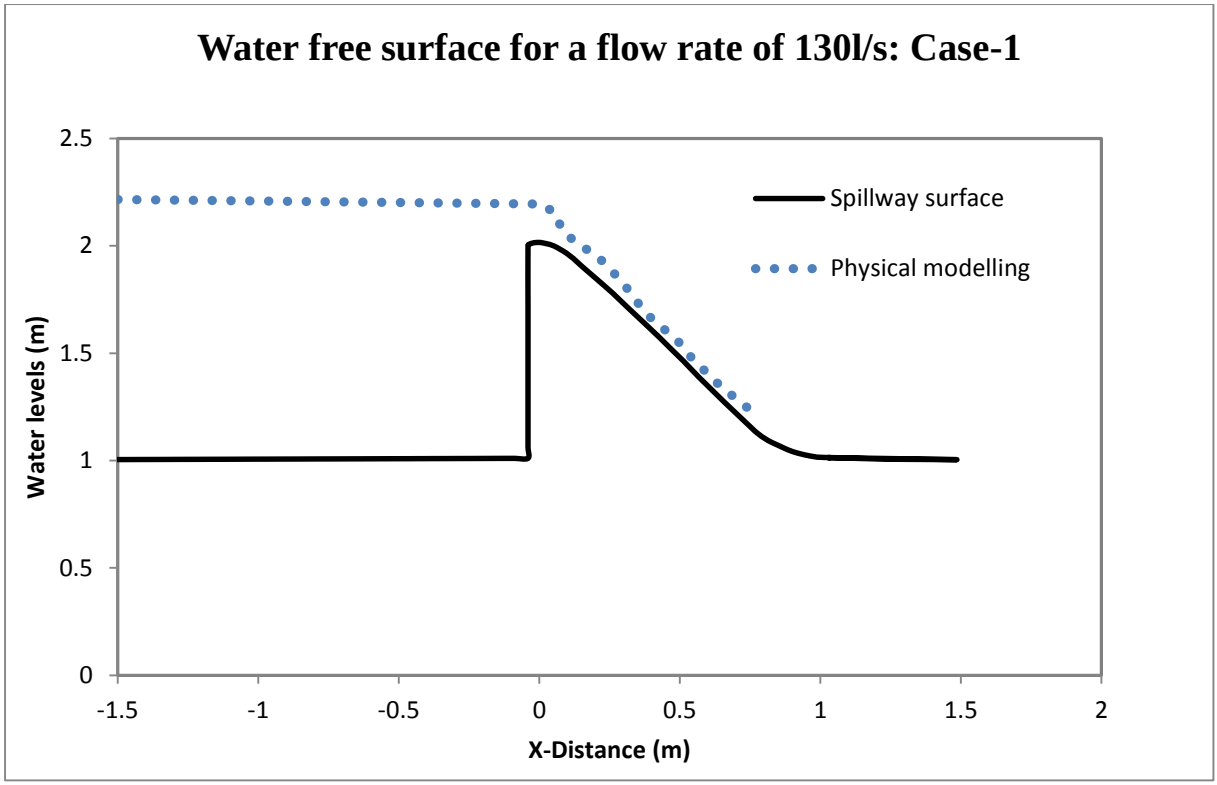

Figure 3-17: Water free surface over Case-1 spillway model for 130 l/s

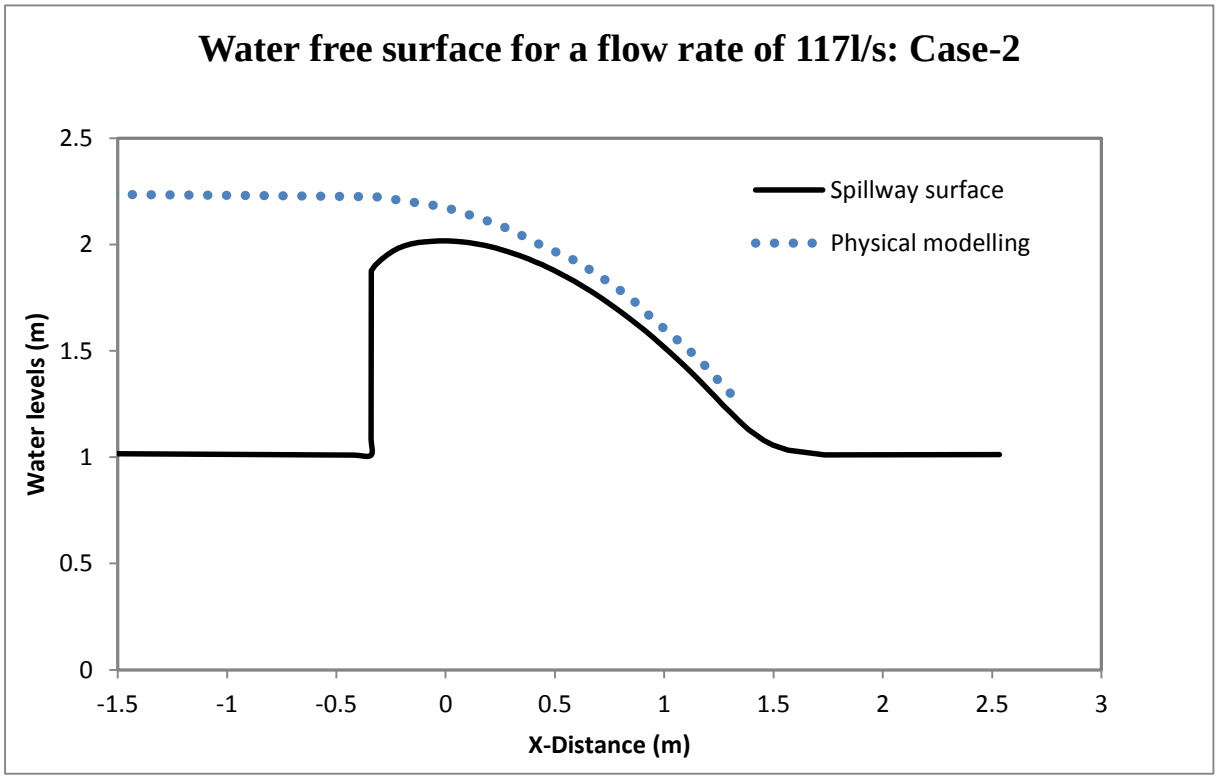

Figure 3-18: Water free surface over Case-2 spillway model for 117 l/s

Figure 3-17and Figure 3-18 present a sample of water levels results measured along the two ogee spillway models. The results achieved for this scenario will be discussed in depth in Chapter 5, where they serve as a basis for CFD validation.

3.7.3 Discussion of Results

Based on the results achieved in the physical modelling, it is clear that the pressures are different all along the spillway chute. Basically, pressure fluctuations may be attributed to:

- The wave on the free surface,
- The turbulence in the approach flow,
- The turbulence originating in the boundary walls.

In each scenario of the physical modelling, no wave was observed and those effects have been assumed insignificant.

As all sensors were located almost at the centreline, the side wall effects did not contribute to the pressure fluctuations. The only contributing factor was the turbulence in the approach flow. However, the correlation between analytical and experimental values was quite good as is clear in the tabular and graphical representation. The slight differences encountered may have been caused by errors in instrumentation of the flow gauge, slight leaks in the supply system and small vibrations generated by the pumping system.

3.8 Flow characteristics and aeration effects

Visual observations of the flow patterns were made so as to appreciate the aeration effects displayed by the physical model when the different discharges were tested. The streamlines following continuous paths and aeration on the water surface were visually observed. Figure 3-19 displays the photograph taken during physical modelling of Case-2 for 117l/s.

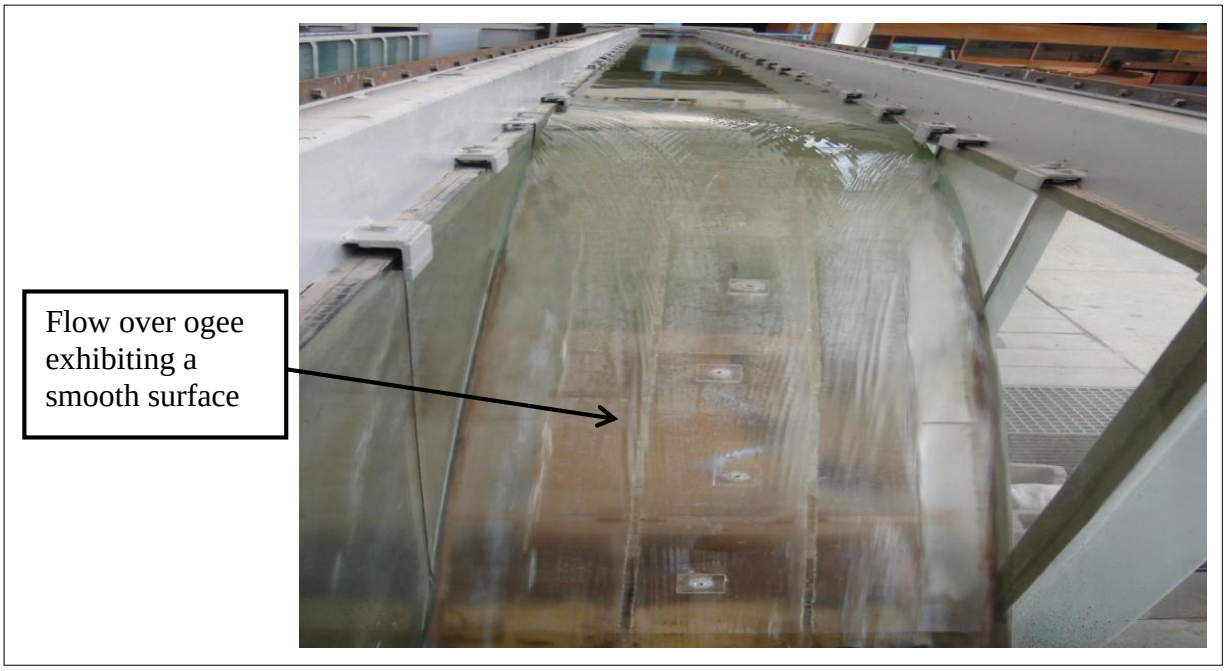

Figure 3-19: Ogee spillway model (Case-2) discharging Q= 117 l/s viewed from above

The flow separation was observed in Case-1 where it was possible to test different discharges greater than the design discharge.

The flow pulls away from the crest on the downstream side, creating fully aerated conditions. The flow was detached from the crest and reattached to the spillway chute a short distance away from the crest as viewed in Figure 3-20 and Figure 3-21. Under these flow conditions, the boundary layer and recirculating bubbles were clearly visible.

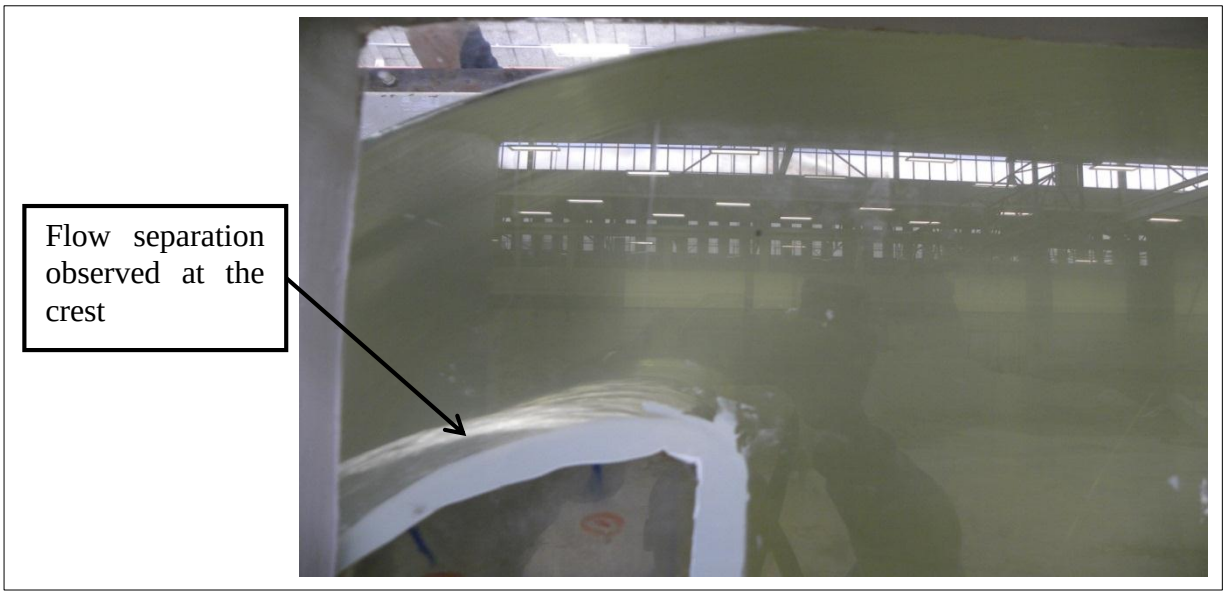

Figure 3-20: Flow separation for Q=130 l/s viewed from the left side of Case -1

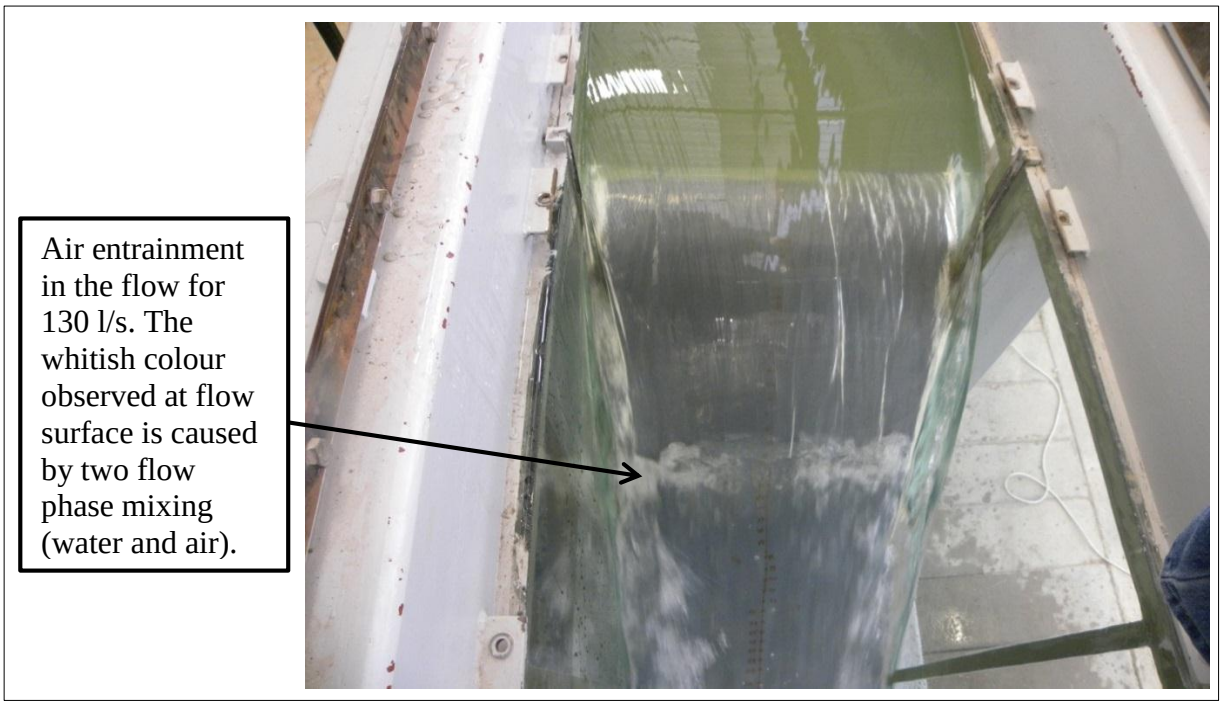

Figure 3-21: Flow detachment for 130l/s of the Physical model (Case-1) viewed from above

CHAPTER 4: NUMERICAL MODEL INVESTIGATION

4.1 Introduction

This chapter presents, firstly, the numerical procedure that was used to develop a CFD model and the logic behind each stage. Secondly, the formulations of physical phenomena are identified and discussed in this chapter. These formulations were based on turbulence modelling as the flow over an ogee spillway, like most of the other flows, is turbulent in nature. Finally, the results obtained from two and three-dimensional models for water surcharge and pressures are presented with a comparison between the results produced by steady and fully hydrodynamic state tests.

4.2 Numerical procedure

The numerical procedure is divided into three main dependent stages, namely: pre-processing, solving and post-processing. Each stage must be completed as listed, before starting the other. In the subsequent sections, these three stages are thoroughly explained.

4.2.1 Pre-processing

The first stage of numerical modelling was to transform a real hydraulic structure into a computable model. This involved the geometry building and boundary definition for the numerical domain. Over 50% of the time spent on CFD modelling was devoted to defining the solution domain and grid sizing. To achieve this, Ansys Fluent software was used. Ansys Fluent is a CFD package created by Ansys Inc., which is based on finite volume method. It uses both the Volume of Fluid (VOF) and Fractional Area-Volume Obstacle Representation (FAVOR) methods to simulate the free surface and the location of obstacles respectively (Fluent, 2009).

4.2.1.1 Geometry

Using the Ansys design modeller, CFD model geometry was built with the same dimensions as two cases of two available physical models. The prototype dimensions which these two physical models (of different scale) represent were not used to build their geometry for application in the numerical modelling. In the geometry builder, both surface and body were frozen to allow a fluid flow to pass through the modelling domain.

The following graphical representation shows the geometries that were developed for both two and three-dimensional cases.

Figure 4-1 and Figure 4-2 are two and three-dimensional geometries developed for case-1 physical model.

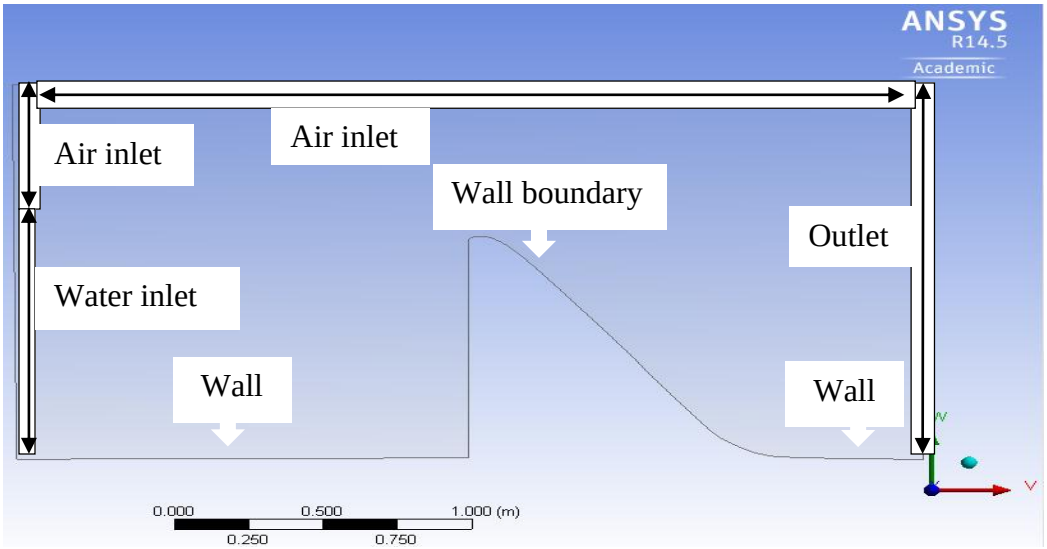

Figure 4-1: Model geometry constructed in 2-D with boundary labels (case-1)

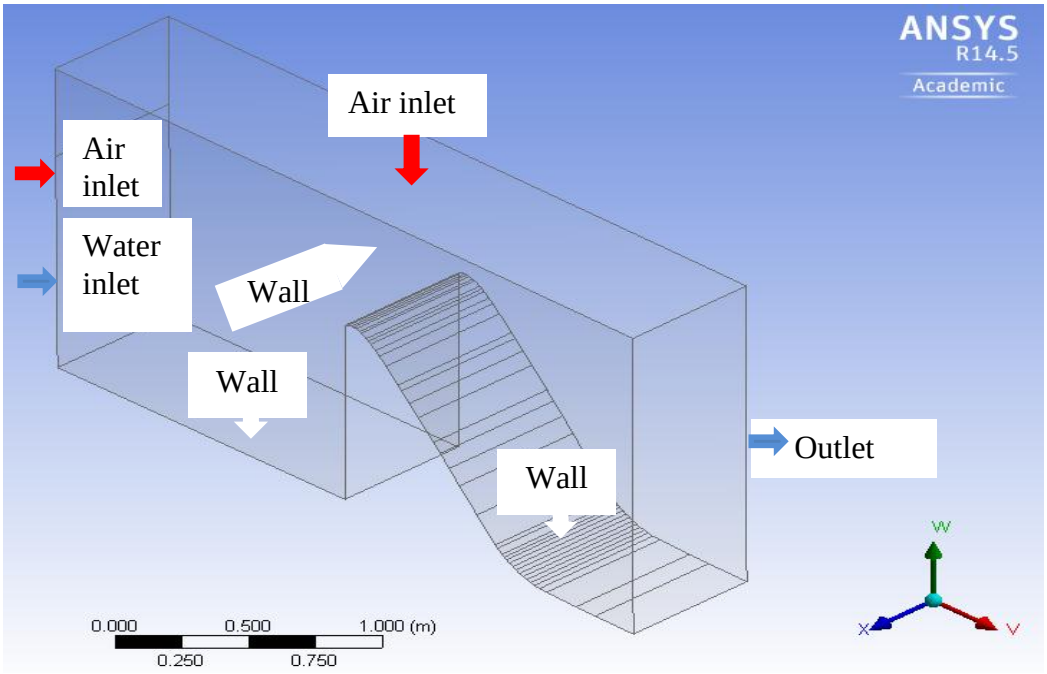

Figure 4-2: Model geometry constructed in 3-D with boundary labels (case-1)

The spillway model Case-2 was constructed in the same way as Case-1, and with the same boundary types. Both 2D and 3D geometries are depicted in Figure 4-3 and Figure 4-4.

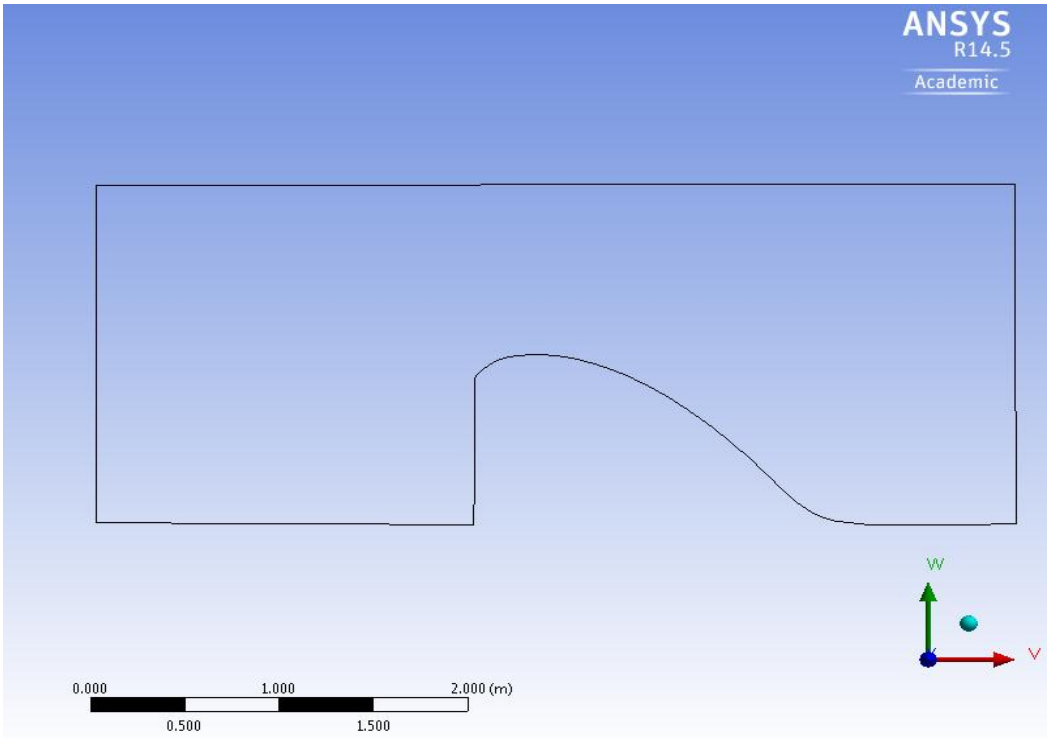

Figure 4-3: Geometry constructed in 2D for Case-2 model

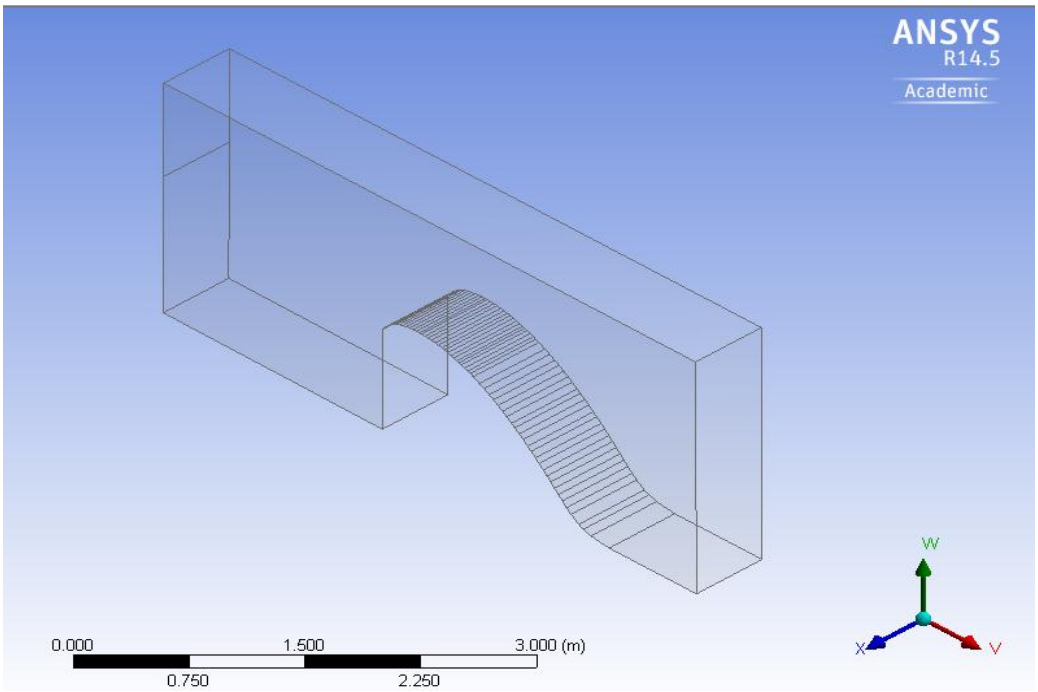

Figure 4-4: Geometry constructed in 3D for Case-2 model

4.2.1.2 Meshing

The meshing process is a very important stage in CFD modelling which requires much attention. In order to analyse the fluid flow, the domain had to be split into smaller cells within which the governing equations would be solved.

Basically, the accuracy of a CFD solution depends upon the number of cells in the mesh. The finer the meshing, the better the solution accuracy. A number of smaller and non-overlapping computational cells were performed in order to obtain the most suitable mesh for better solution accuracy. The areas of high solution interest have been meshed up with the finer mesh while the coarser mesh was implemented in areas with less solution interest. The main features of interest in the numerical domain are:

- the spillway crest,
- the downstream part where the turbulent phenomenon occurs, and
- the region of interface between the two phases (water and air).

Along the spillway crest, the surface needed to be adequately resolved with finer grid resolution in order to monitor the pressure accurately. The regions where the interaction between water and air was supposed to happen were meshed with a refined mesh to allow a clear interface.

In two-dimensional meshing, there are many options that can be applied such as triangular and quadrilateral meshing. In this study the meshing parameters were defined as follows:

- A structured grid, consisting of triangular mesh cells was used because of its superiority in producing more accurate results.
- At the spillway crest and in the turbulent area downstream, a refinement was applied.
- In order to allow a stable flow and accurate solution, a relevance centre and a medium smoothing were also included in the setup parameter.

Figure 4-5 depicts the schematic representation of two-dimensional model meshing for both cases.

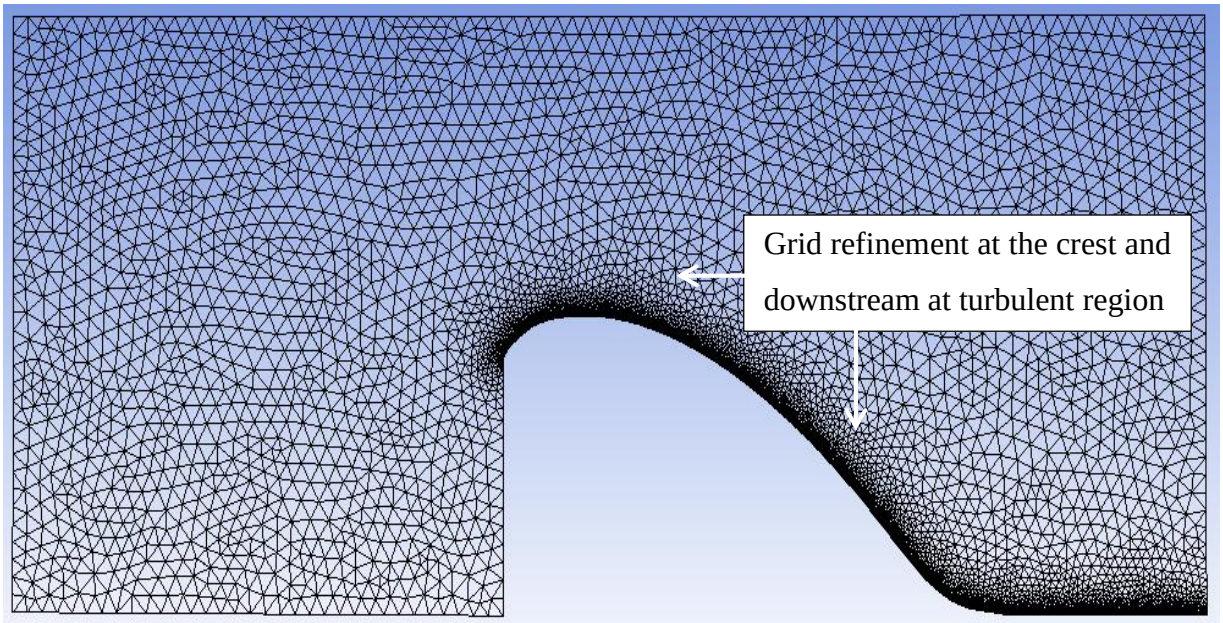

Figure 4-5: Representation of the geometry meshing of 2D model

For a 3D model, the mesh can be made up of either tetrahedrons, quadrilaterals or by a number of different combinations. For this scenario using a cutcell mesh which is made up of quadrilaterals, proved to be the best option. Another scenario, which used the tetrahedron meshing, was tried but the solution was unsuccessful, as it was repeatedly diverging.

However, the unstructured tetrahedral mesh elements were avoided as they were causing numerical diffusion and higher storage capacity. Another option that was tried was to slice the geometry into a number of smaller interconnected geometries and mesh every geometry with a different mesh type. The cutcell mesh was applied to the straight-lined approach flow and a tetrahedral mesh around the crest and in the turbulent area downstream. This did not work out as anticipated, as the solution kept on diverging. Figure 4-6 presents a cutcell meshing chosen for a 3D numerical domain for both cases.

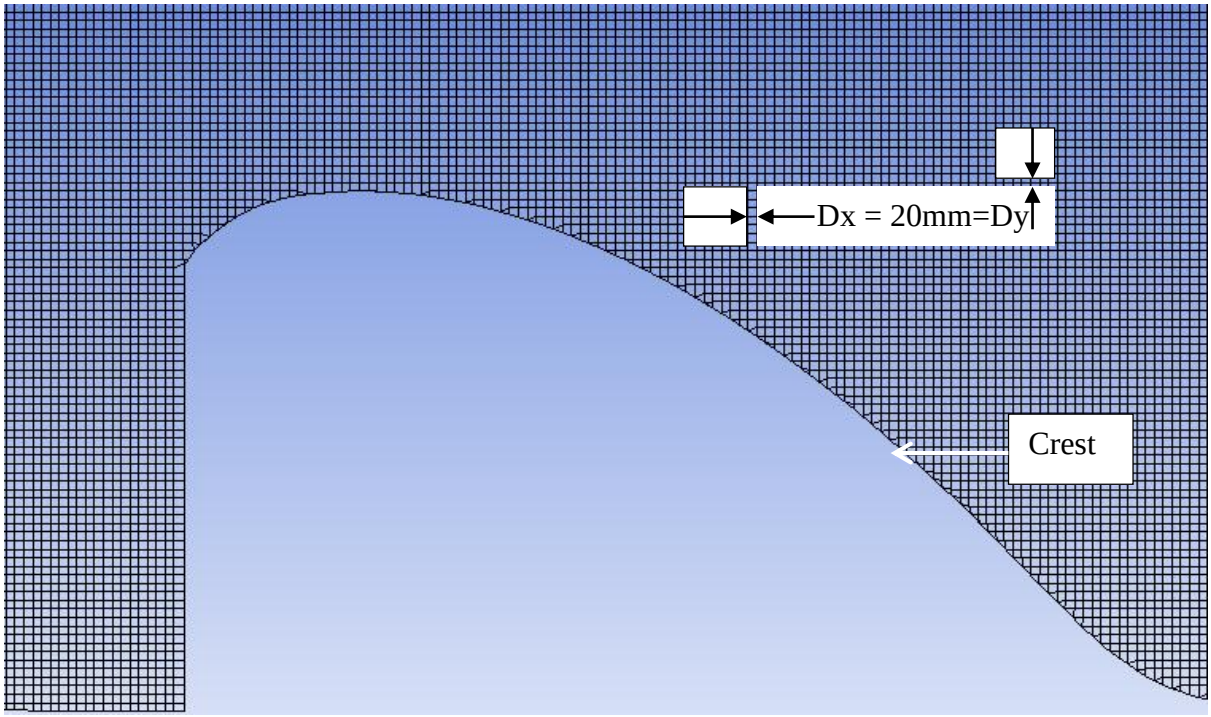

Figure 4-6: Representation of the geometry meshing of 3D model

After achieving the proper meshing type for each model, the mesh quality assessment and mesh sensitivity function were established.

- **Mesh quality analysis**

Mesh quality was assessed to avoid unwanted influence on the computational analysis in terms of solution accuracy and the time needed to achieve it. This aspect becomes especially relevant in case of inadequately conditioned problems and/or when fully hydrodynamic analyses are considered. In this context, the evaluation and assessment of the quality of meshing is very useful as it contributes to solving the problem and type of analysis under consideration.

As documented in Fluent. (2008), the list of quality criteria for mesh metric includes: element quality, aspect ratio, Jacobean ratio, warping factor, parallel deviation, maximum corner angle, skewness, and orthogonal quality. In this work, computational cell skewness and orthogonal quality have been adopted.

According to Ansys Inc. (2008), cell skewness is defined as the measured difference between the shape of the cell and the shape of an equilateral cell of equivalent area (for a 2D domain) or volume (for a 3D domain). Highly skewed computational cells can reduce the accuracy and stability of the solution. The following equation define equisize skewness calculation:

$$M_{eqs} = \frac{S_{eq} - S}{S_{eq}} \qquad (4\text{-}1)$$

In this equation, S and S_{eq} are the area (2D) or volume (3D) of the computational mesh element and the maximum area (2D) or volume (3D) of an equilateral element with the circumscribed radius which is identical to that of the computational mesh element.

The range of equisize skewness lies between 0 and 1 where cell skewness should not exceed 0.98. For all cases, computational cells (mesh) had equisize skewness less than 0.57 which indicates a good quality of mesh.

Another important indicator of mesh quality that ANSYS FLUENT uses is a quantity referred to as the orthogonal quality. The orthogonal quality (OQ) is derived directly from Fluent solver discretization. The range of orthogonal quality is 0-1, where the minimum orthogonal quality must be greater than 0.051. The orthogonal quality achieved for all numerical models was above 0.70 which corresponds to a very good quality of meshing.

4.2.2 Solver

4.2.2.1 Model Set-up

After creating the geometry of the model and meshing it up in the Ansys-Fluent package, the mesh was imported into fluent solver. Various parameters within the solver had to be set before the simulations could be started.

a. Turbulence Model Selection

Since most of the fluid flows are turbulent in reality, Computational Fluid Dynamics Modelling (CFD) use turbulent model to simulate fluid flows. Among the linear turbulence models, the widely used, two-equation model is based on the turbulent kinetic energy equation k and the turbulent eddy dissipation ε or the turbulent frequency ω. In this study, the realisable $k-\varepsilon$ model was selected as it contains a new formulation for the turbulent viscosity as well as new transport equation for the kinetic energy dissipation rate (Shih et al., 1995).

In $k-\varepsilon$ model, the turbulence kinetic energy and the kinetic energy dissipation rate ε are obtained from the following transport equations respectively:

$$\frac{\partial}{\partial t}(\rho k) + \frac{\partial}{\partial x_x}(\rho k v_x) = \frac{\partial}{\partial x_y}\left(\left(\mu + \frac{\mu_t}{\sigma_k}\right)\frac{\partial k}{\partial x_y}\right) + Gk + G_b - \rho\varepsilon - Y_M + S_k \qquad (4\text{-}2)$$

$$\frac{\partial}{\partial t}(\rho\varepsilon) + \frac{\partial}{\partial x_x}(\rho\varepsilon v_x) = \frac{\partial}{\partial x_y}\left(\left(\mu + \frac{\mu_t}{\sigma_\varepsilon}\right)\frac{\partial k}{\partial x_y}\right) + \rho C_1 \varepsilon - \rho C_2 \frac{\varepsilon^2}{k + \sqrt{v_y \varepsilon}} + C_{1\varepsilon}\frac{\varepsilon}{k} C_{3\varepsilon} G_b + S_\varepsilon \quad (4\text{-}3)$$

Where

$k =$ Turbulence kinetic energy,k $\left(\frac{m}{s^2}\right)$,

$\varepsilon =$ Kinetic energy dissipation rate ε $\left(\frac{m}{s^3}\right)$,

$\rho =$ Density $\left(\frac{kg}{m^3}\right)$,

$t =$ Time (s),

$\mu =$ Kinetic viscosity $\left(\frac{m^2}{s}\right)$,

$Gk =$ Represents the Generation of turbulence kinetic energy caused by the mean velocity gradients,

$G_b =$ Generation of turbulence kinetic energy due to buoyancy,

$Y_M =$ Dissipation rate, and

$S_k \; and \; S_\varepsilon =$ Kinetic energy and dissipation source terms respectively.

b. Multiphase model selection

The volume of fluid model (VOF) was chosen to simulate the multiphase flow. Two eulerian phases: air and water, were defined as primary and secondary phase respectively. Another alternative for setting eulerian phases was tried, that was, to define water as primary phase and air as secondary phase but this resulted into flow instability.

c. Boundary conditions

The precision of boundary conditions on the solution domain plays a capital role for the accuracy of the results. The boundary conditions to be specified consist of flow inlet and outlet boundaries, which have to be defined with the flow properties such as turbulence parameters, velocity and pressure.

Walls and internal faces which have a direct interaction with the flow have been defined as well. All of these boundary conditions are discussed below:

i. **Inlet boundary**: The inlet section is at the upstream of the spillway and consists of the inlet of water at the bottom and the inlet of air at the top. For water inlet, a "velocity-inlet" boundary condition was selected as it was the best option that produced a stable flow in the solution domain. For each discharge tested in physical modelling, the input velocity was calculated and set uniformly at the inlet. The air boundaries were defined as an inlet pressure with the atmospheric pressure conditions.

ii. **Outlet boundary:** The outlet of the domain at the downstream part was specified with an outlet pressure so that water and air can flow out freely. To ensure atmospheric conditions, the air phase was allowed to flow back into the model.

iii. **Walls:** Wall boundary conditions (walls and channel bed) were specified to simplify the operational conditions with no-slip conditions and to be in stationary conditions at all times.

d. Discretisation

The physical phenomena which govern this process are very complex and solutions are non-linear, thus an iterative method is required. In this study, Pressure-Implicit with Splitting of Operators (PISO) was chosen to simulate turbulence. PISO is the pressure-velocity coupling algorithm which is based on the higher degree of the approximate relation between the corrections for pressure and velocity. In the publication by (Ferzieger & Peric, 1996), PISO is recommended for fully hydrodynamic calculations on highly skewed meshes.

The under-relaxation factors were used in the pressure-based solver to stabilize the convergence behaviour. Four under-relaxation factors including pressure coefficient, momentum coefficient, k were set to default values.

Table 4.1below summarises other parameters that were defined for the running of the simulations.

Table 4-1: Default parameters adopted in the simulations

Model/ Solver parameter	Type	Value
$\boldsymbol{k-\varepsilon}$ Model (2eqn)	C2- Epsilon	1.9
	TKE Prandtl number	1
	TDR Prandtl number	1.2
Multiphase Model	Volume Fraction Cutoff	1e-06
Phase interaction	Continnum surface stress constant	0.0728
Cell Zone conditions	Operating pressure (Pa)	101325
	Gravity enabled (m/s^2)	9.81
Boundary conditions	Turbulence intensity (%)	5
	Roughness constant	0.5
Phase densities	Density of water (kg/m3)	998.2
	Density of Air (kg/m^3)	1.225
Reference values	Enthalpy (j/kg)	0
	Temperature (k)	288.16
	Ratio of specific heats	1.4
Scheme (Piso)	Skewness-Neighbor coupling	1
	Neighbor Correction	1
Under relaxation factors	Pressure	0.3
	Density	1
	Body Forces	1

e. Initialisation

For each test, it is necessary to initialise the model. This is done by setting initially all pressures to the atmospheric conditions. For these conditions, the solution domain was entirely filled with air. The flow computations were set to start from the inlet boundaries to allow stable conditions to be far from the spillway crest. For each model the tests were run under steady state conditions until it attained a convergence.

After a successful convergence, the model was changed from steady to fully hydrodynamic-state and the time length of five minutes was used to match the time of experimental tests for unsteady tests. The simulation results obtained are documented in post-processing section.

4.2.2.2 Tests Conducted

Numerical simulations were accomplished in several scenarios; each model had to be tested in 2D and 3D for a number of eight flow rates ranging from 23 l/s to 130 l/s. The 3D geometry was the full dimensions of the physical model while 2D modelled the centreline. These two scenarios were adopted to evaluate their accuracy in simulating the surcharge and hydrodynamic pressures over ogee spillway. After each numerical process, the steady and fully hydrodynamic test results were discussed and compared to each other. All results achieved in this work will be discussed in the subsequent sections.

i. Steady states

Upon a completion of a steady state simulation, the model convergence had to be monitored. In this study, convergence was judged by simultaneous examination of residual levels and nearness to zero of the mass balance between the flux entering and of that leaving the model. The difference in fluxes should not exceed 1% for a successful convergence. The results were recorded for 2500 iterations where a flux report was checked to confirm a converged solution.

ii. Fully hydrodynamic tests

To get a fully hydrodynamic test running, only small changes had to be made in the numerical model. These are to determine and set the time step for fully hydrodynamic testing and to define simulation length. Fully hydrodynamic tests were performed with the time step equal to 0.001.

To record pressures, seven pressure sensors were set up on the spillway face using surface monitors. They were set at the same locations as those used during the physical modelling. The water surcharge was measured, subsequently, by plotting the water phase from upstream to downstream of the spillway. It was very important to use a refined mesh in order to plot accurate water surcharge.

iii. Fully hydrodynamic test duration

Running the fully hydrodynamic tests in a CFD model, the target was to perform tests for the same five minutes as it was done for experimental tests. However, the preliminary simulation results proved that such time length was not necessary as the pressure results did not exhibit a fluctuating trend.

All pressure readings appeared to be in the same range; there were neither upward nor downward trends. This behaviour is clearly shown in Figure 4-7. The simulated fully hydrodynamic state results obtained for all pressure transducers, for a discharge of 117 l/s and for a test for duration of five minutes are presented.

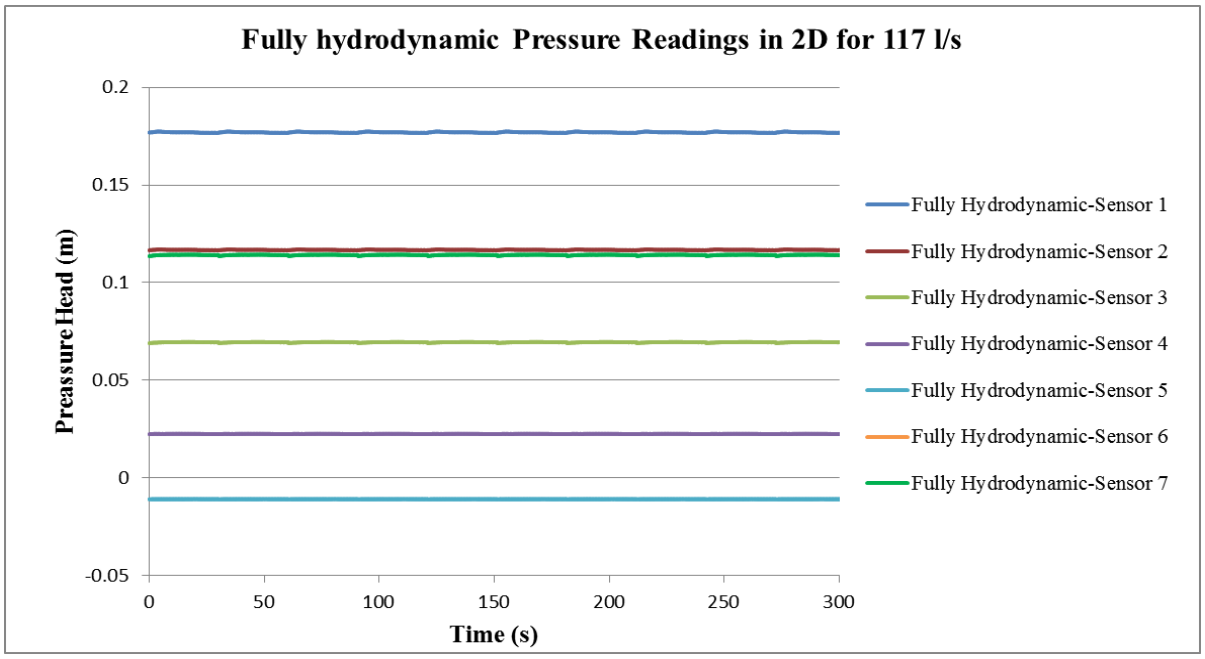

Figure 4-7: Fully hydrodynamic simulation results for a flow rate of 117 l/s (case-1)

The results shown in Figure 4-7 were performed to determine the duration of simulations required for testing the fully hydrodynamic state simulations. Before starting the fully hydrodynamic states tests, the model had to become stable.

Therefore, the pressure recorded during this test duration did not show any fluctuation in terms of trend. This resulted in a fixed duration of twenty seconds (20 s) for all other flow rates.

4.2.2.3 Mesh sensitivity analysis

As discussed previously, the grid refinement and coarsening has a great impact on the numerical solution. Sometimes a very fine mesh is not good as it can produce a poor convergence. On the other hand, computations performed with excessively coarse mesh may have considerable influence on the propagation of numerical errors which result in an imprecise solution.

Refinement was done until constant flow variables were achieved, thus grid independence achievement. Figure 4-8 shows the grid solution analysis for a 2D numerical model.

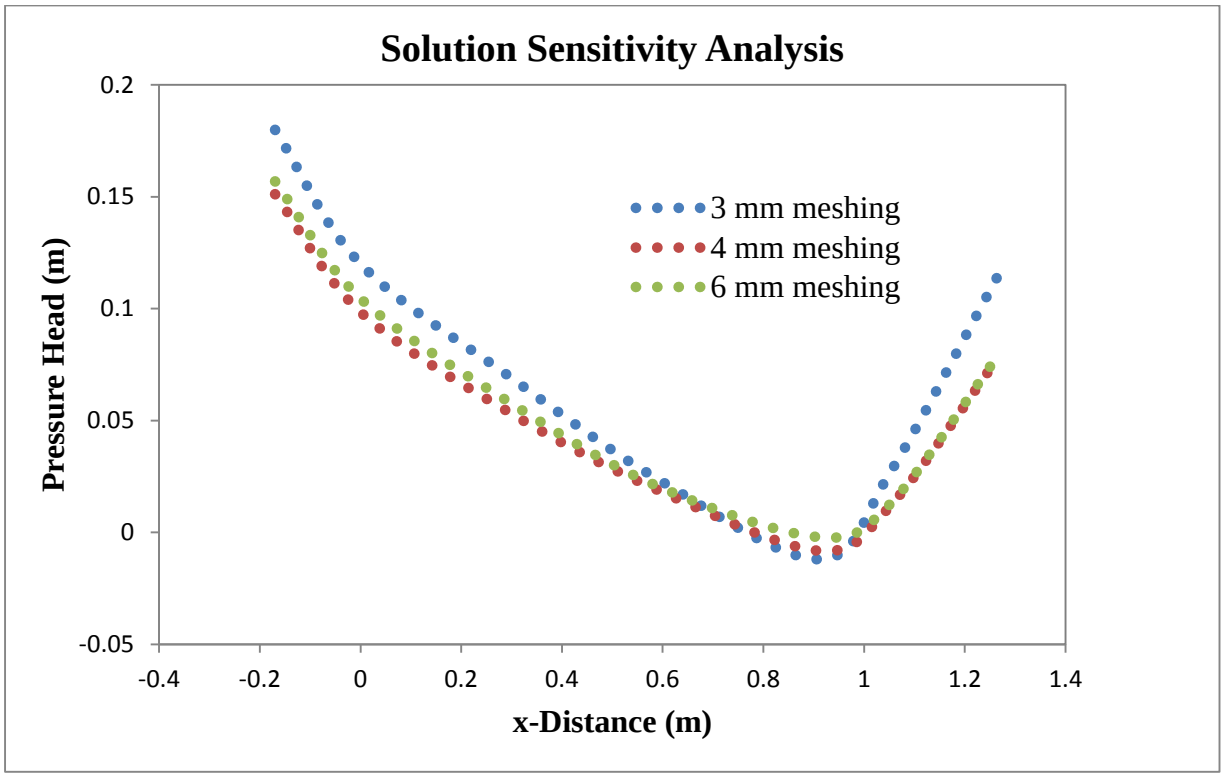

Figure 4-8: Grid solution sensitivity analysis for a 2D numerical model

Figure 4-8 demonstrates mesh sensitivity analysis results for the 2D numerical model. The data points for the three mesh sizes were considered. The target was to select a grid size which produces accurate results within the shortest time. Therefore, a grid size of 4 mm was finally adopted for 2D numerical modelling

In 3D modelling, the mesh sensitivity tests were performed in the same way. It was important that the results produced by the slightly coarse mesh correlate to those of the fine mesh. A maximum of 20 mm mesh was finally selected for 3D simulations as shown in Figure 4-9.

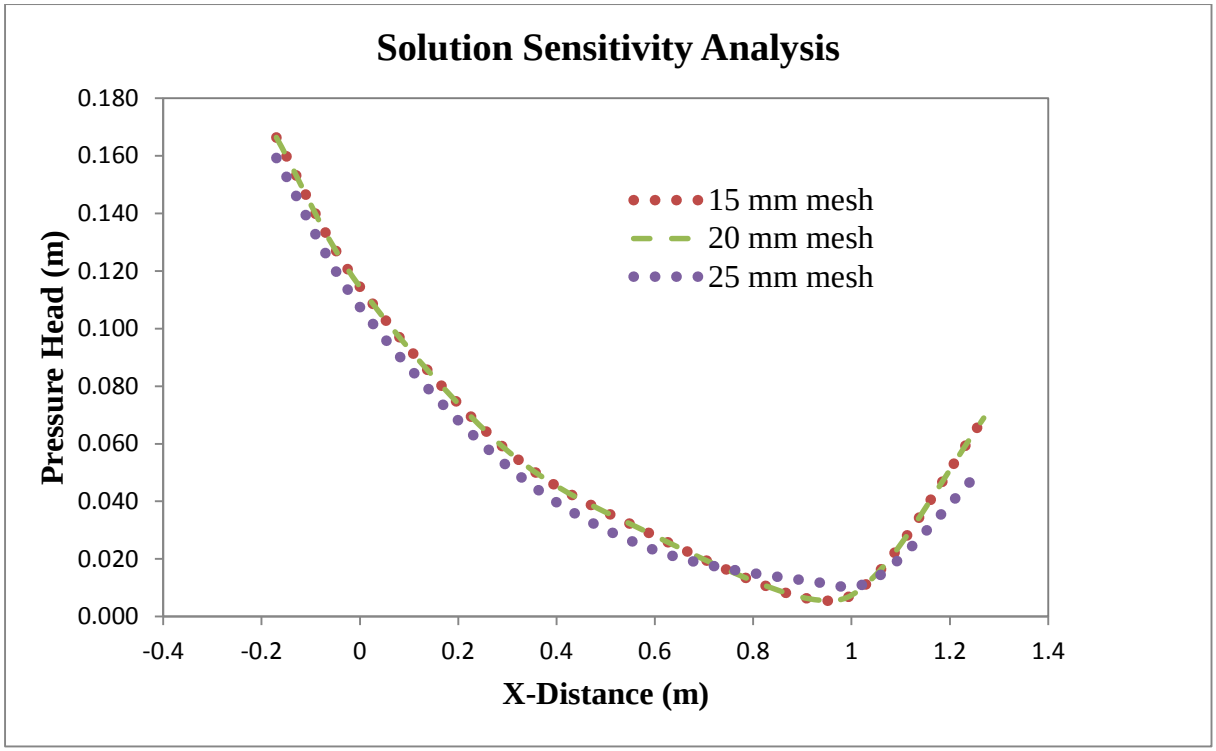

Figure 4-9: Grid solution sensitivity analysis for a 3D numerical model

Mesh sensitivity analysis was achieved after grid independence was obtained. Certain indicators including the pressure head readings, the water surface profiles were constant for increasingly finer meshes. This assured that there was no information missing due to the coarseness of the mesh size selected for either 2D or 3D model. The grid sizes that were chosen allowed accurate results within a moderate time.

4.2.3 Post-processing

When a solution was obtained from a numerical solver, the solutions were interpreted and presented in a convenient way. A number of commercial solvers have post-processing included in the software and the results may be presented instantaneously in the form of contours, graphs, tables and animations. In this study, some data were presented in the package solver and others have been processed manually using text data output programs.

4.2.3.1 Flow development

With the large extent of data recorded during simulations, different ways were used to visualise flow features. The density and pathline contours were employed in the visualisation of flow pattern in the domain. Figure 4-10 and Figure 4-11, included below; indicate the plotted densities of the multiphase flow in primary and secondary cases.

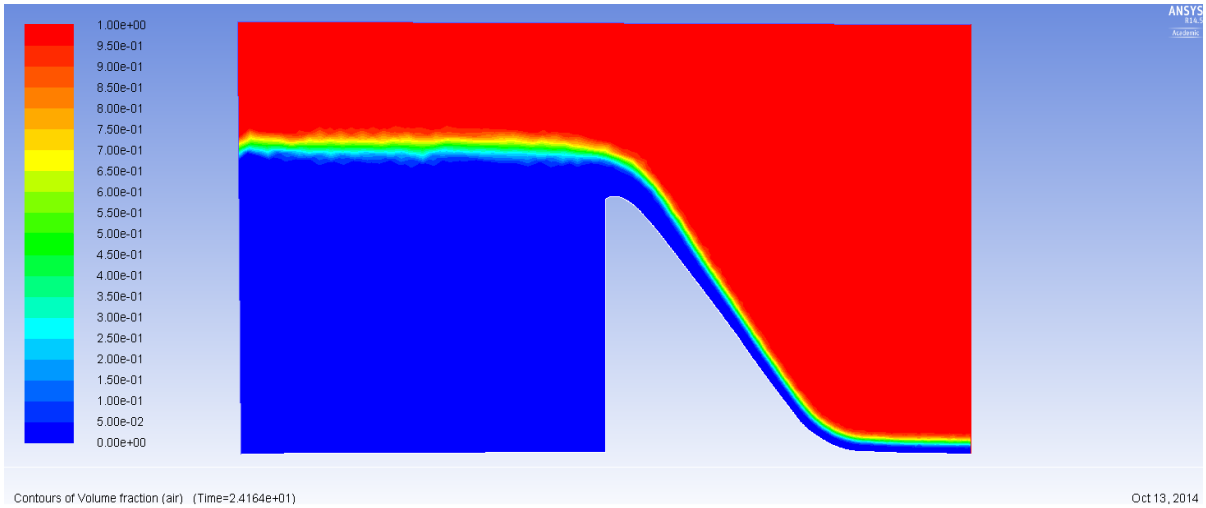

Figure 4-10: Density contours for a flow rate of 130 l/s simulated by CFD model Case-1

Water (dark blue colour) has a density of 998.2 kg/m^3, air (red colour) comprises a density of 1.225 kg/m^{3}and the yellowish colour in between represents the interface.

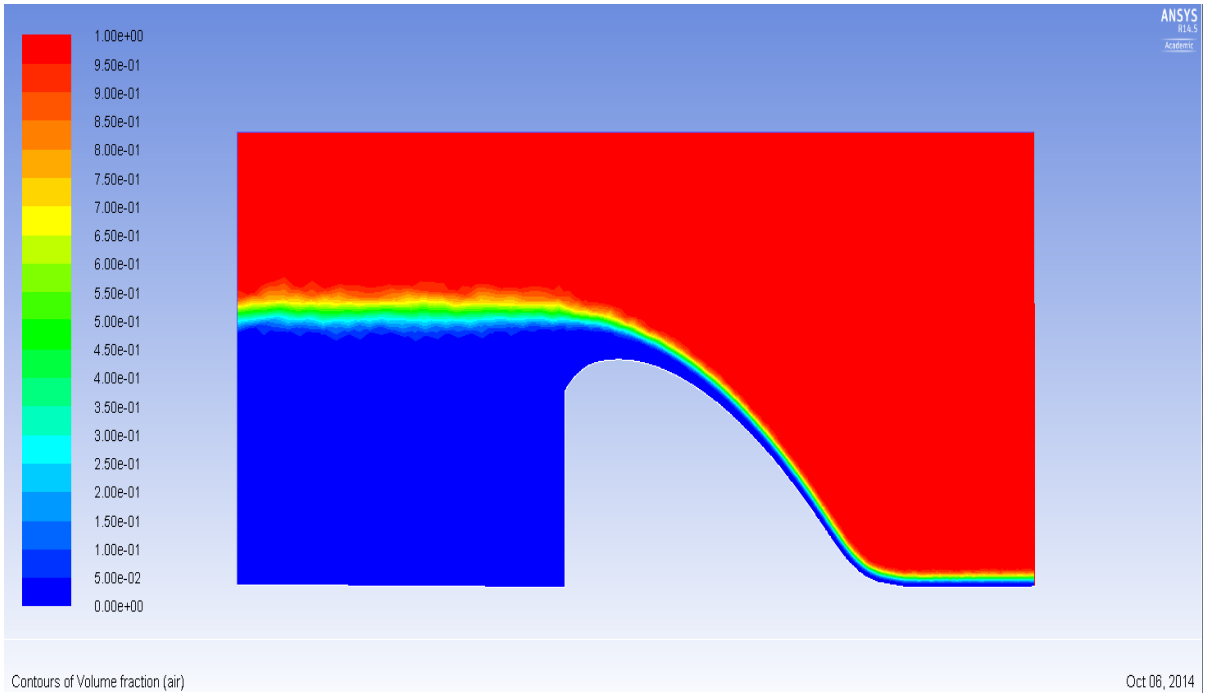

Figure 4-11: Density contours for a flow rate of 117 l/s simulated by CFD model Case-2

By plotting the pathline contours, the flow trajectories and the interaction between water and air phases have been visually tracked as depicted in Figure 4-12 and Figure 4-13.

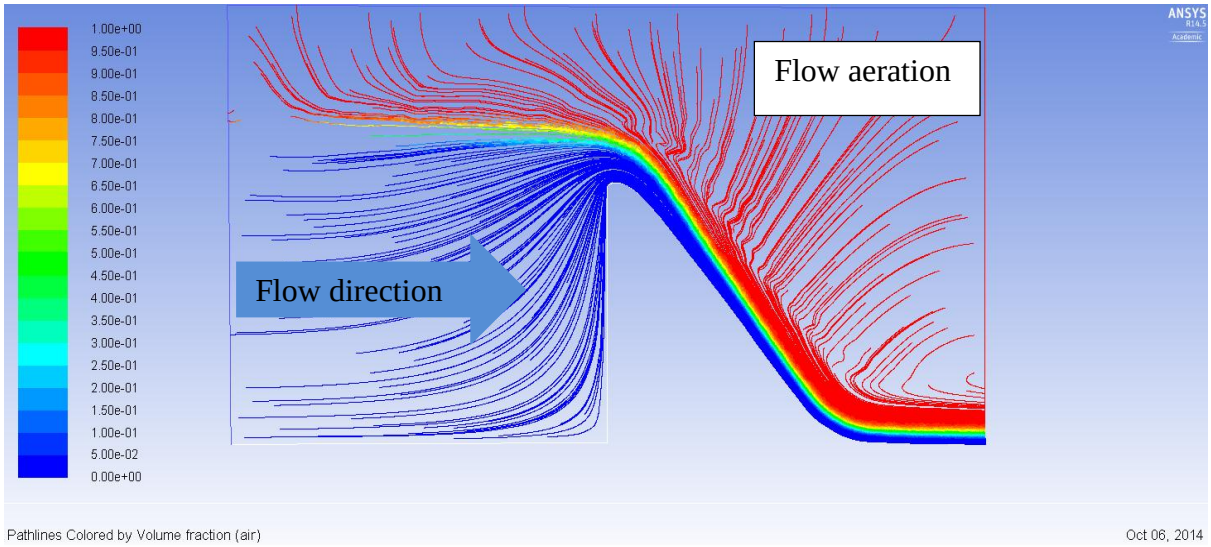

Figure 4-12: Simulated pathlines of particles for 130 l/s coloured by volume fraction of air for Case-1

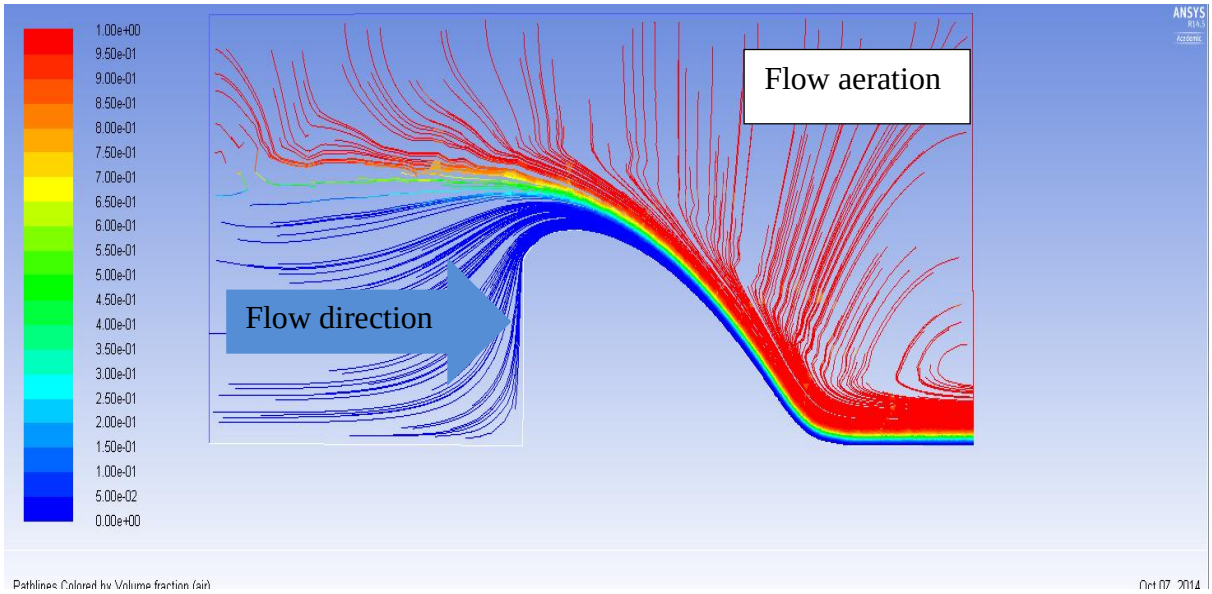

Figure 4-13: Simulated pathlines of particles for 117 l/s coloured by volume fraction of air for Case-2

In Figure 4-12 and Figure 4-13, the blue pathlines show that water moves from the inlet to the outlet following the same path direction, which confirms that the principle of mass conservation has been achieved. In addition, the aeration conditions over the weir are also significant. In all discharges simulated the aeration conditions were observed in the flow.

Figure 4-14 and Figure 4-15 depict of aeration in the flow for Case-1 and Case-2 for 23 l/s and 25 l/s respectively.

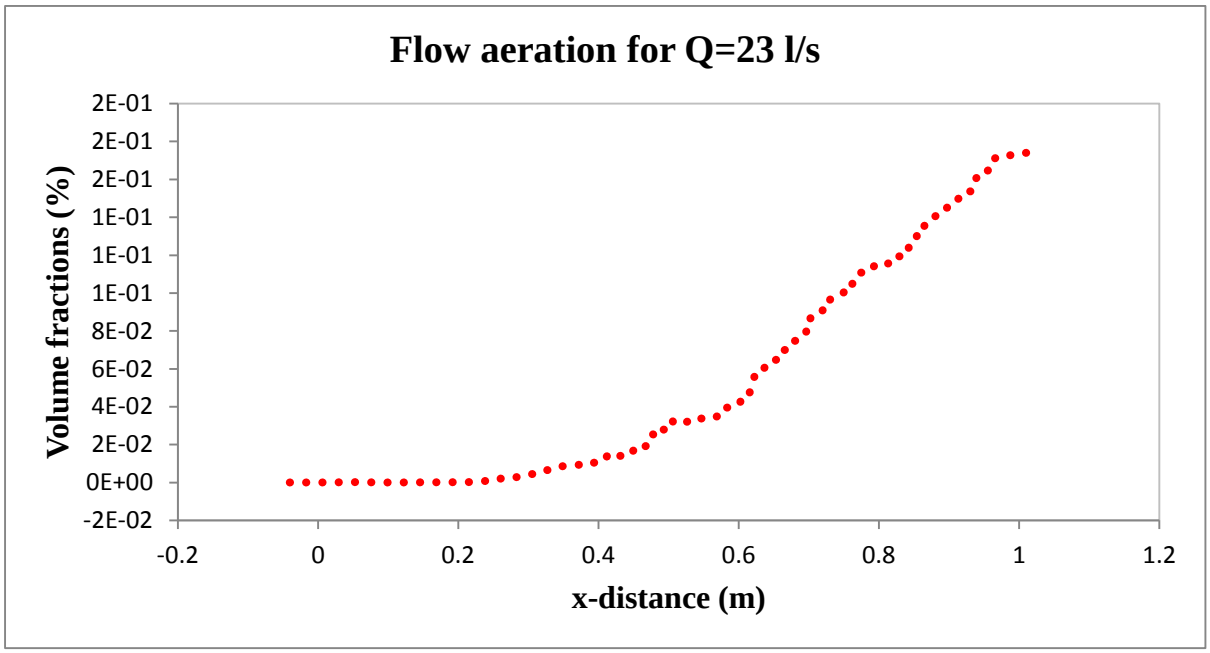

Figure 4-14: Aeration of Flow over ogee spillway model (Case-1) for Q=23 l/s

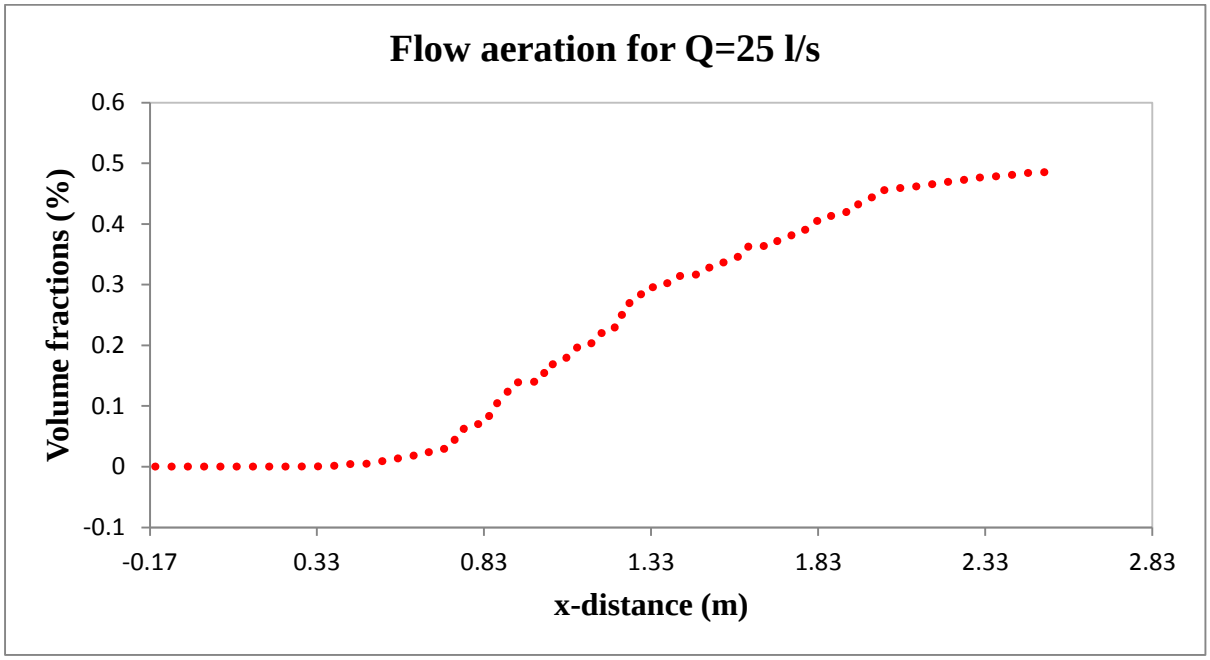

Figure 4-15: Aeration of Flow over ogee spillway model (Case-2) for Q=25 l/s

Figure 4-14 and Figure 4-15 present the rate of volume fraction of air in the flow of 23 l/s and 25 l/s for Case-1 and Case-2, respectively. They provide a better representation of the self-aeration of the flow as discussed in the section 2.3.5.

They also confirm the reason attributed to the pressure fluctuations in section 3.7.1.1 and 3.7.1.2. The pressure sensors located upstream exhibit a steady trend in pressure reading while those located downstream show fluctuations in the pressure readings.

4.2.3.2 Water levels (Surcharge)

Since the general purpose of the multiphase model include capturing flow behaviour and phase interaction, the interface between two phases played a capital role in surface flow determination. The flow levels were measured along the spillway crest by plotting the middle of phase interface, that is, at 0.5 volume fraction. The water surface was plotted at the centreline to eliminate any influence from the boundary walls.

The measurements of water free surfaces acquired form steady and fully hydrodynamic state tests produced the same water free surfaces. However, to make a fully satisfied decision on the accuracy of numerical water surcharge, the results obtained from CFD models were compared to results from physical modelling as a validation process. Figure 4-16 and Figure 4-17 present a sample of a graphical representation of water free surfaces obtained from CFD model of Case-1 and Case-2.

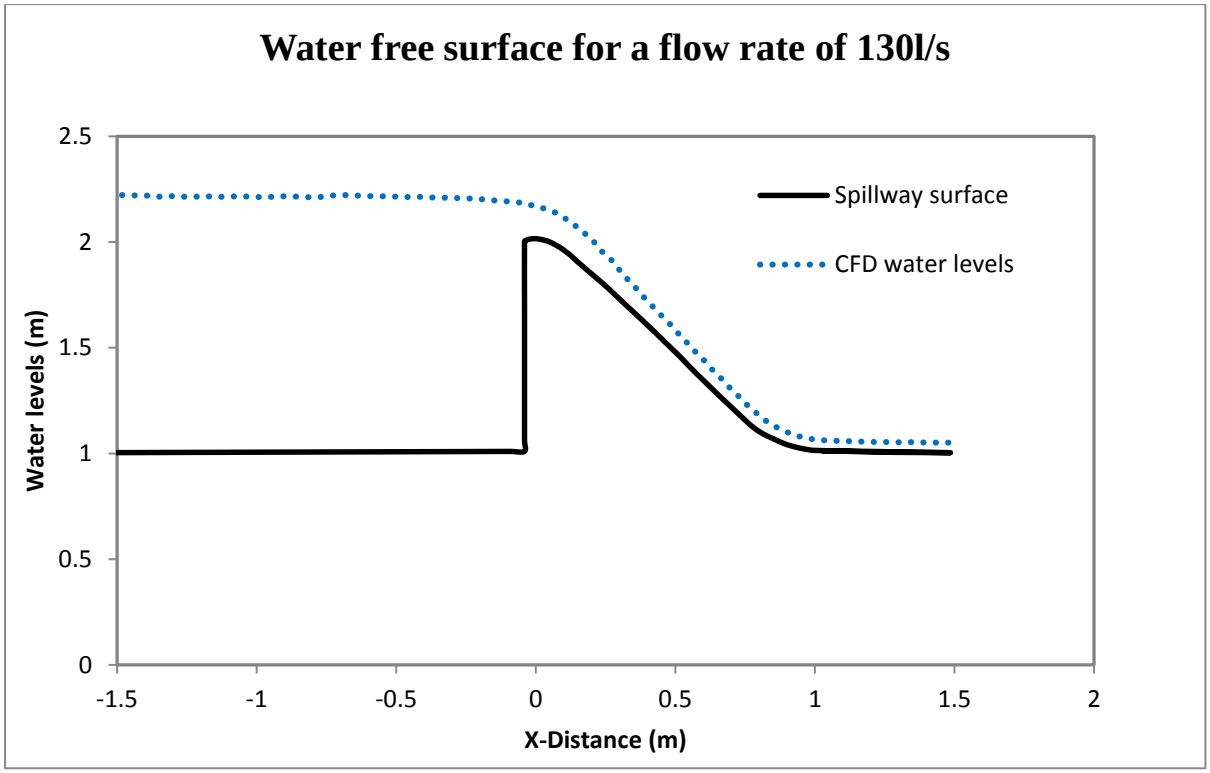

Figure 4-16: Water free surface over Case-1 spillway model for 130 l/s

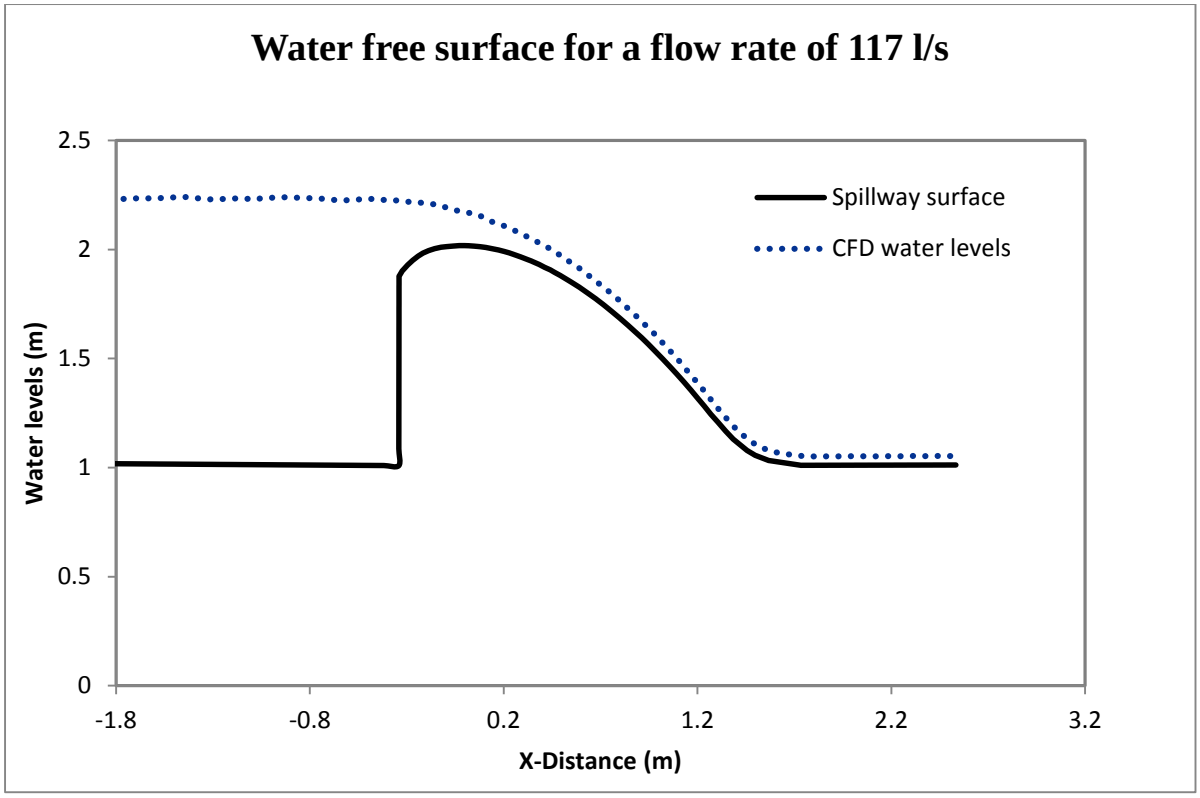

Figure 4-17: Water free surface over Case-2 spillway model for 117 l/s

Figure 4-16 and Figure 4-17 show that at the spillway crest, water levels are slightly higher than those found in the downstream area. This shows that two actions simultaneously happen in the flow over the crest, that is, the formation and gradual thickening of the turbulent boundary layer along the spillway profile, and a continuous increase in the velocity and decrease in the depth of the main flow. As displayed in the graphical representation of velocity contours in Figure 4-18 and Figure 4-19, in the upstream part, a low approach velocity corresponds to higher water depths whereas in downstream part, the supercritical conditions lead to high velocity magnitude. Using Equation 3-1 the Froude number (Fr) was determined to grasp the flow characteristics.

As demonstrated by the results, the Froude number remains subcritical at the upstream part and develops into supercritical state gradually after the crest. After entering the spillway, the flow drops at a critical depth thereby developing into supercritical depths along the chute. The CFD model indicated the location of the critical flow section (Froude number = 1) near the spillway crest. In addition, the intensity of turbulence can be assessed along the spillway by determining the Reynolds number as stated in equation (4-4).

$$Re = \frac{\rho RV}{\mu} \tag{4-4}$$

Where

$Re =$ Reynolds number $(Dimensionless\ quantity)$

$\rho =$ Density (kg/m^3)

$R =$ Hydraulic diameter (m)

$\mu =$ Kinetic viscosity (m^2/s)

At the downstream part of the spillway, the Reynolds number is above 2000 which proves, therefore, a turbulent flow. As seen from the figures (Figure 4-18 and Figure 4-19) depicting the velocity contours, it is quite evident that the velocities become higher at the downstream portion of the spillway. Special energy dissipaters should be provided at this portion of spillway so as to protect the structure from scour due to high velocities.

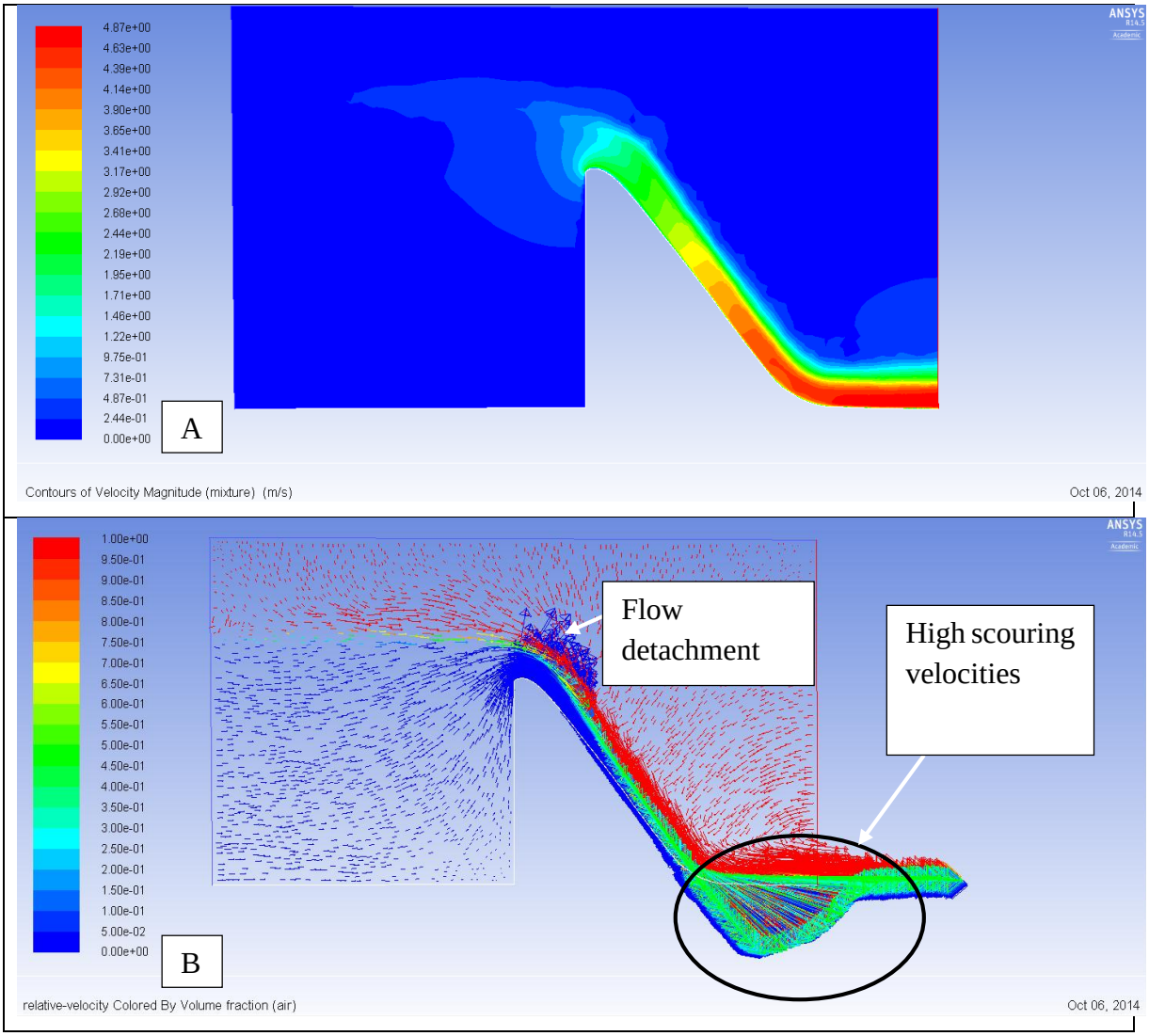

Figure 4-18: Velocity distribution along the spillway model (Case-1) for 130 l/s. A: Density contours, B: Velocity vector contours

As can be seen in Figure 4-18, air (dark red colour) is entrained in the water at the crest. The velocity vectors (dark blue colour) show that water has a tendency to pull away from the crest thereby reattaching to the spillway face downstream. This phenomenon was encountered in physical modelling as it is depicted in Figure 3-20.

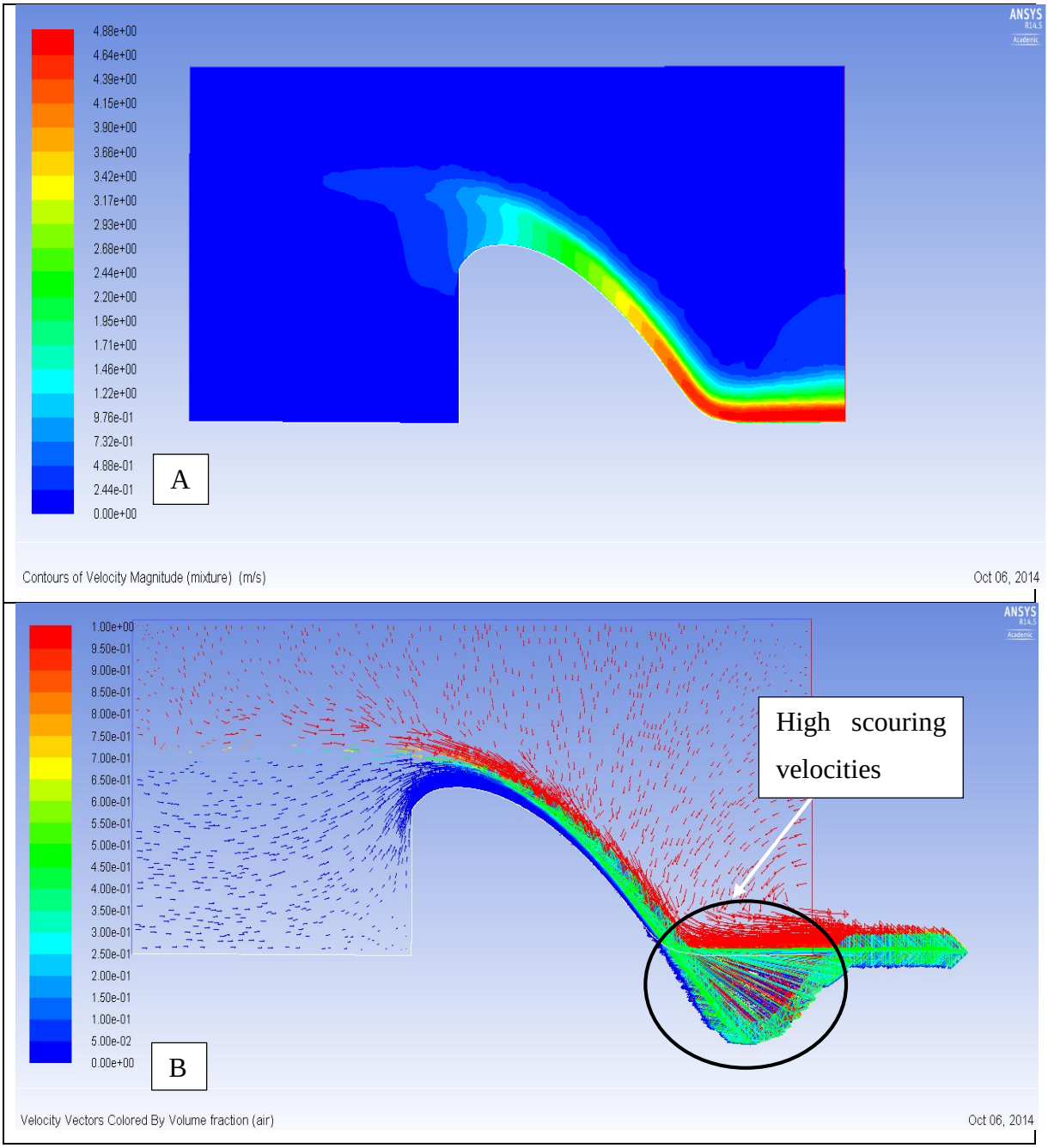

Figure 4-19: Velocity distribution along the spillway model (Case-2) for 117 l/s. A: Density contours, B: Velocity vector contours

4.2.3.3 Pressure results

In this section, the steady and fully hydrodynamic pressures extracted from 2D and 3D models for eight flow rates are presented. For each spillway case, a comparison was made in form of graphical representation of the results obtained for each discharge tested.

For each case, a sample of the results of one flow rate is presented while the rest of the results are found in Appendix C and D.

i. Case-1

The steady state pressure results at each of the 7 recording locations were determined through the average pressures recorded for 2500 iterations, while the average fully hydrodynamic pressure results were determined by averaging of the simulated pressures recorded over the run time of twenty seconds. Table 4-2 and Table 4-3 present the results produced by the 2D-numerical model for steady and unsteady states respectively.

Table 4-2: CFD simulated steady state pressure results for 2D model

Flow rate (l/s)	**Sensor 1**	**Sensor 2**	**Sensor 3**	**Sensor 4**	**Sensor 5**	**Sensor 6**	**Sensor 7**
	CFD modelling: Average Sensor pressure (m)						
23	0.026	0.009	0.017	0.007	-0.005	-0.027	0.003
35	0.020	0.007	0.020	0.011	-0.005	-0.033	0.006
41	0.015	0.005	0.020	0.014	-0.004	-0.035	0.008
56	0.013	0.003	0.023	0.021	-0.001	-0.037	0.012
71	0.000	-0.004	0.021	0.028	0.002	-0.037	0.018
89	-0.013	-0.012	0.018	0.036	0.006	-0.037	0.023
108	-0.053	-0.019	0.015	0.039	0.011	-0.033	0.029
130	-0.119	-0.035	0.008	0.042	0.016	-0.030	0.036

Table 4-3: CFD simulated fully hydrodynamic pressure results for 2D model

Flow rate (l/s)	**Sensor 1**	**Sensor 2**	**Sensor 3**	**Sensor 4**	**Sensor 5**	**Sensor 6**	**Sensor 7**
	CFD modelling: Average Sensor pressure (m)						
23	0.021	0.008	0.015	0.005	-0.006	-0.028	0.002
35	0.016	0.007	0.018	0.009	-0.004	-0.032	0.005
41	0.011	0.006	0.020	0.011	-0.003	-0.034	0.007
56	-0.003	0.002	0.021	0.016	0.000	-0.035	0.012
71	-0.023	-0.005	0.020	0.022	-0.003	-0.036	0.017
89	-0.049	-0.013	0.018	0.028	0.007	-0.034	0.022
108	-0.081	-0.022	0.014	0.035	0.011	-0.032	0.029
130	-0.121	-0.035	0.008	0.041	0.016	-0.028	0.036

Table 4-2 and Table 4-3 present the average pressure readings of the fully hydrodynamic and steady state which indicate a close similarity in the results. Most of the results achieved in both states are equal or close to each other. This model offered a advantage of testing flow rates greater than the design discharge.

In this context, the performance of a spillway for the head that is less, equal and/or greater than the design head has been assessed. For the flow rates less than the design discharge (41 l/s), the hydrodynamic conditions exhibit a positive pressure reading, while for the discharges other than 41 l/s the pressures become negative with the increase of discharge which proves the theoretical principles reviewed in **section 2.3.5**.

An illustrative graph comparison between steady and fully hydrodynamic results for a flow rate of 130 l/s is presented in Figure 4-20.

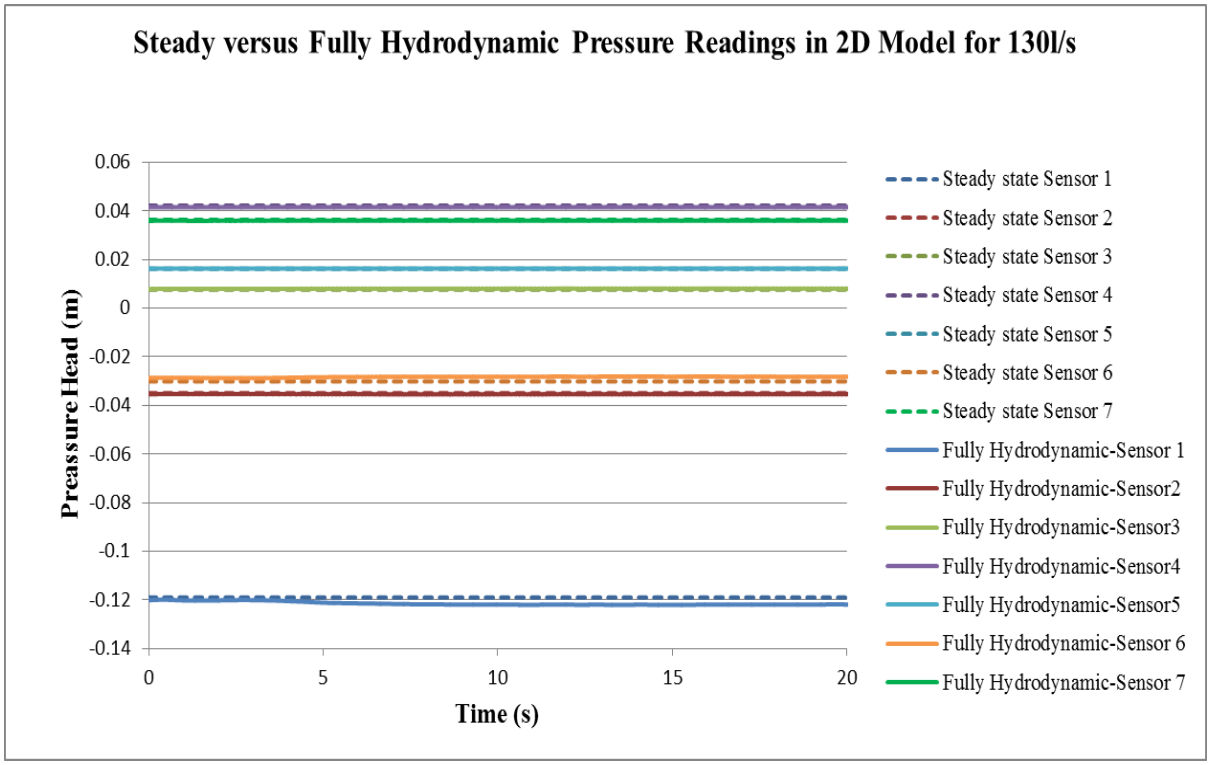

Figure 4-20: Comparison between 2D-simulated steady and fully hydrodynamic state models for a discharge of 130l/s (Case-1)

Figure 4-20 shows that for a flow rate of 130 l/s the steady state and fully hydrodynamic state readings correlate well.

For the 3D model, the average pressures recorded in both steady and fully hydrodynamic tests are shown in Table 4-4 and Table 4-5.

Table 4-4: CFD simulated steady state pressure results for 3D model

Flow rate (l/s)	Sensor 1	Sensor 2	Sensor 3	Sensor 4	Sensor 5	Sensor 6	Sensor 7
	CFD modelling: Average Sensor pressure (m)						
23	0.022	0.003	0.014	0.010	0.008	-0.003	0.010
35	0.020	0.003	0.018	0.015	0.010	-0.005	0.014
41	0.017	0.001	0.019	0.017	0.012	-0.005	0.016
56	0.007	-0.004	0.021	0.023	0.015	-0.007	0.021
71	-0.024	-0.018	0.019	0.035	0.022	-0.007	0.032
89	-0.024	-0.018	0.019	0.035	0.022	-0.007	0.032
108	-0.047	-0.028	0.017	0.041	0.027	-0.006	0.039
130	-0.072	-0.039	0.013	0.047	0.031	-0.003	0.045

Table 4-5: CFD simulated fully hydrodynamic pressure results for 3D model

Flow rate (l/s)	Sensor 1	Sensor 2	Sensor 3	Sensor 4	Sensor 5	Sensor 6	Sensor 7
	CFD modelling: Average Sensor pressure (m)						
23	0.021	0.005	0.014	0.013	0.012	0.000	0.011
35	0.017	0.004	0.018	0.016	0.015	0.000	0.015
41	0.014	0.003	0.020	0.017	0.015	-0.002	0.017
56	0.004	-0.002	0.021	0.023	0.017	-0.005	0.021
71	-0.011	-0.008	0.021	0.029	0.020	-0.005	0.026
89	-0.029	-0.016	0.020	0.036	0.023	-0.005	0.032
108	-0.051	-0.025	0.017	0.042	0.028	-0.004	0.039
130	-0.074	-0.035	0.013	0.048	0.032	-0.002	0.045

Pressure results recapitulated in Table 4-4 and Table 4-5 are similar with a negative reading at the first two sensors for the discharges greater than the design discharges. The sixth sensor indicates the negative pressure reading for steady and fully hydrodynamic state, which is also found in the 2D model.

Figure 4-21 presents a comparison between steady and fully hydrodynamic results for a flow rate of 130l/s.

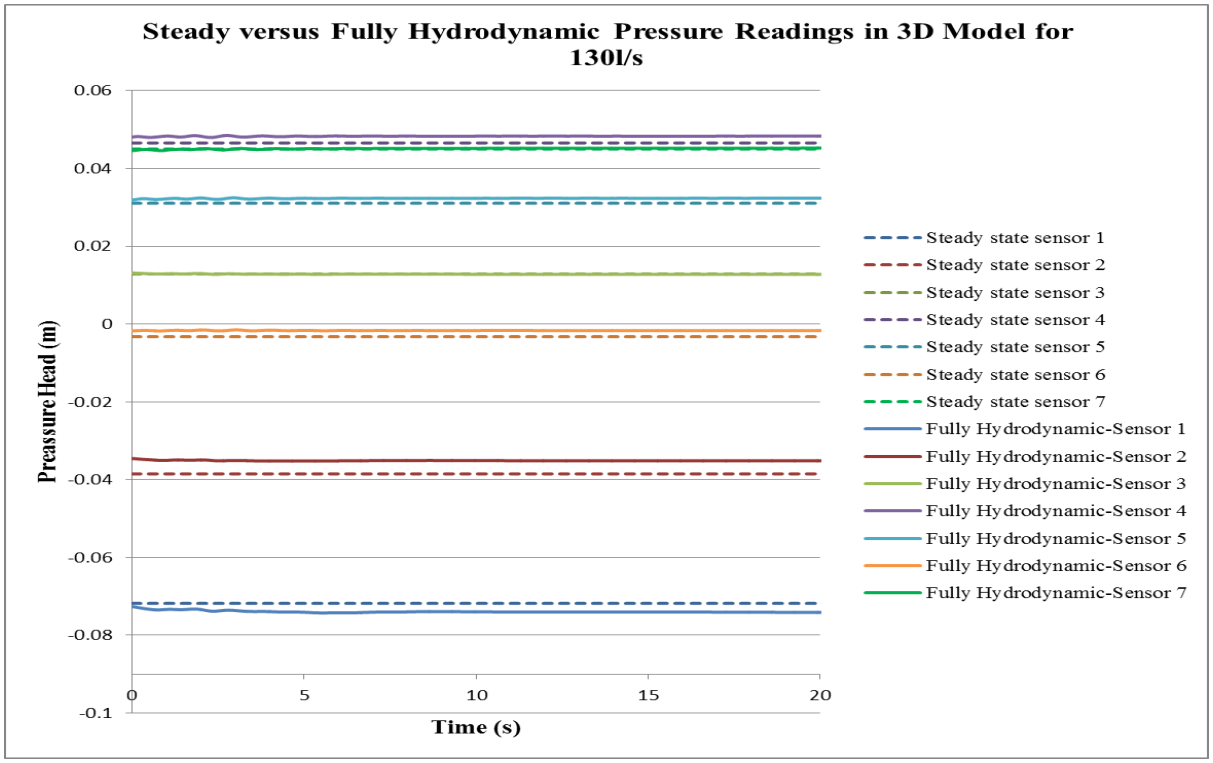

Figure 4-21: Comparison between 3D-simulated steady and fully hydrodynamic state models for a discharge of 130 l/s (Case-1)

ii. Case -2

The hydrodynamic aspects attained from this case scenario have been presented below, in both tabular and graphical forms. Table 4-6 and Table 4-7 present the results produced by the 2D-numerical model for both steady and unsteady states.

Table 4-6: CFD simulated steady state pressure results for 2D model

Flow rate (l/s)	Sensor 1	Sensor 2	Sensor 3	Sensor 4	Sensor 5	Sensor 6	Sensor 7
	CFD modelling: Average Sensor pressure (m)						
25	0.097	0.054	0.026	0.003	-0.012	0.013	0.053
37	0.118	0.070	0.036	0.007	-0.014	0.016	0.070
44	0.127	0.077	0.040	0.009	-0.014	0.017	0.077
51	0.138	0.085	0.045	0.011	-0.014	0.019	0.083
76	0.157	0.101	0.056	0.017	-0.013	0.022	0.097
85	0.160	0.103	0.058	0.018	-0.013	0.023	0.100
95	0.167	0.110	0.062	0.020	-0.012	0.024	0.105
117	0.180	0.120	0.069	0.024	-0.012	0.027	0.116

Table 4-7: CFD simulated fully hydrodynamic pressure results for 2D model

Flow rate (l/s)	Sensor 1	Sensor 2	Sensor 3	Sensor 4	Sensor 5	Sensor 6	Sensor 7
	CFD modelling: Average Sensor pressure (m)						
25	0.094	0.052	0.025	0.003	-0.012	0.013	0.053
37	0.115	0.067	0.034	0.007	-0.014	0.017	0.070
44	0.127	0.076	0.040	0.009	-0.014	0.018	0.077
51	0.136	0.083	0.044	0.011	-0.014	0.019	0.083
76	0.157	0.101	0.056	0.017	-0.013	0.023	0.097
85	0.160	0.103	0.059	0.018	-0.013	0.024	0.101
95	0.166	0.108	0.062	0.019	-0.013	0.025	0.105
117	0.177	0.117	0.069	0.023	-0.011	0.028	0.114

As can be seen from Table 4-6 and Table 4-7, the average pressure results produced by steady and fully hydrodynamic tests exhibit a great similarity. The average results from the steady and the fully hydrodynamic state simulations illustrate the success of CFD modelling. The highest difference encountered for all sensors is equal to 0.003 m pressure head at the first and second sensor for a flow rate of 37 l/s and 117 l/s. A sample of a graphic comparison between steady and fully hydrodynamic results for a flow rate of 117 l/s is presented in Figure 4-22.

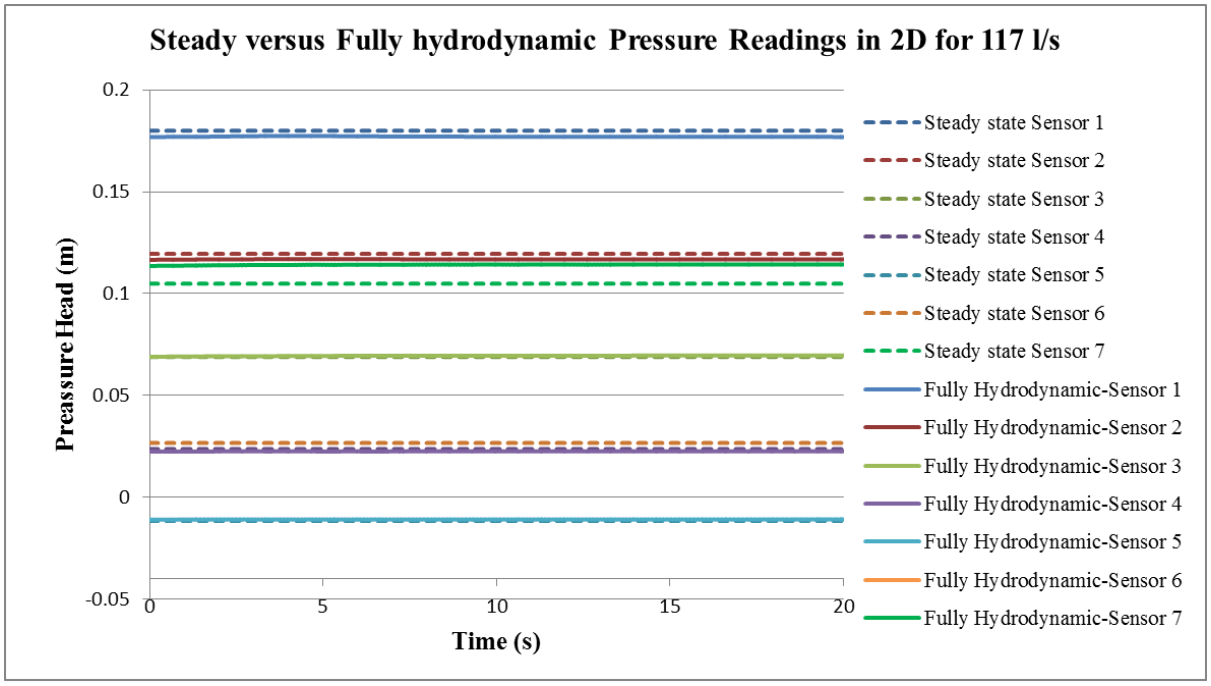

Figure 4-22: Comparison between 2D-simulated steady and fully hydrodynamic state models for a discharge of 117l/s (Case-2)

Figure 4-22 indicates the differences between steady and fully hydrodynamic state simulation results in graphical form for a flow rate of 117 l/s. The fully hydrodynamic pressure readings recorded for a period of 20 seconds correlate to the results produced by steady tests. To confirm the results accuracy as obtained in 2D-modelling, the same tests were performed in 3D modelling, as presented in Table 4-8 and Table 4-9.

Table 4-8: CFD simulated steady state pressure results for 3D model

Flow rate (l/s)	**Sensor 1**	**Sensor 2**	**Sensor 3**	**Sensor 4**	**Sensor 5**	**Sensor 6**	**Sensor 7**
	CFD modelling: Average Sensor pressure (m)						
25	0.086	0.047	0.016	0.008	0.003	0.005	0.019
37	0.106	0.064	0.025	0.012	0.003	0.007	0.029
44	0.115	0.071	0.030	0.014	0.003	0.008	0.033
51	0.132	0.080	0.040	0.018	0.004	0.010	0.037
76	0.143	0.094	0.044	0.022	0.005	0.012	0.051
85	0.149	0.099	0.048	0.023	0.005	0.012	0.056
95	0.154	0.104	0.051	0.025	0.005	0.013	0.059
117	0.167	0.115	0.058	0.029	0.006	0.015	0.069

Table 4-9: CFD simulated fully hydrodynamic pressure results for 3D model

Flow rate (l/s)	Sensor 1	Sensor 2	Sensor 3	Sensor 4	Sensor 5	Sensor 6	Sensor 7
	CFD modelling: Average Sensor pressure (m)						
25	0.083	0.044	0.018	0.009	0.005	0.003	0.018
37	0.102	0.059	0.027	0.013	0.007	0.004	0.028
44	0.119	0.073	0.036	0.018	0.008	0.006	0.037
51	0.119	0.073	0.036	0.018	0.008	0.005	0.037
76	0.139	0.090	0.047	0.025	0.010	0.007	0.051
85	0.145	0.095	0.050	0.027	0.010	0.008	0.055
95	0.153	0.103	0.050	0.025	0.005	0.013	0.059
117	0.163	0.110	0.060	0.033	0.012	0.010	0.068

In Table 4-8 and Table 4-9, above, the average steady and fully hydrodynamic results simulated in three dimensions, have been found to be equal or close to each other for all seven sensors.

The largest difference realised was 0.013 m pressure head at sensor 1 for a flow rate of 51 l/s, which is not a significant difference. For the same discharge as in the 2D-modelling, an illustrative comparison in graphical form is presented in Figure 4-23 so as to compare the steady and fully hydrodynamic results.

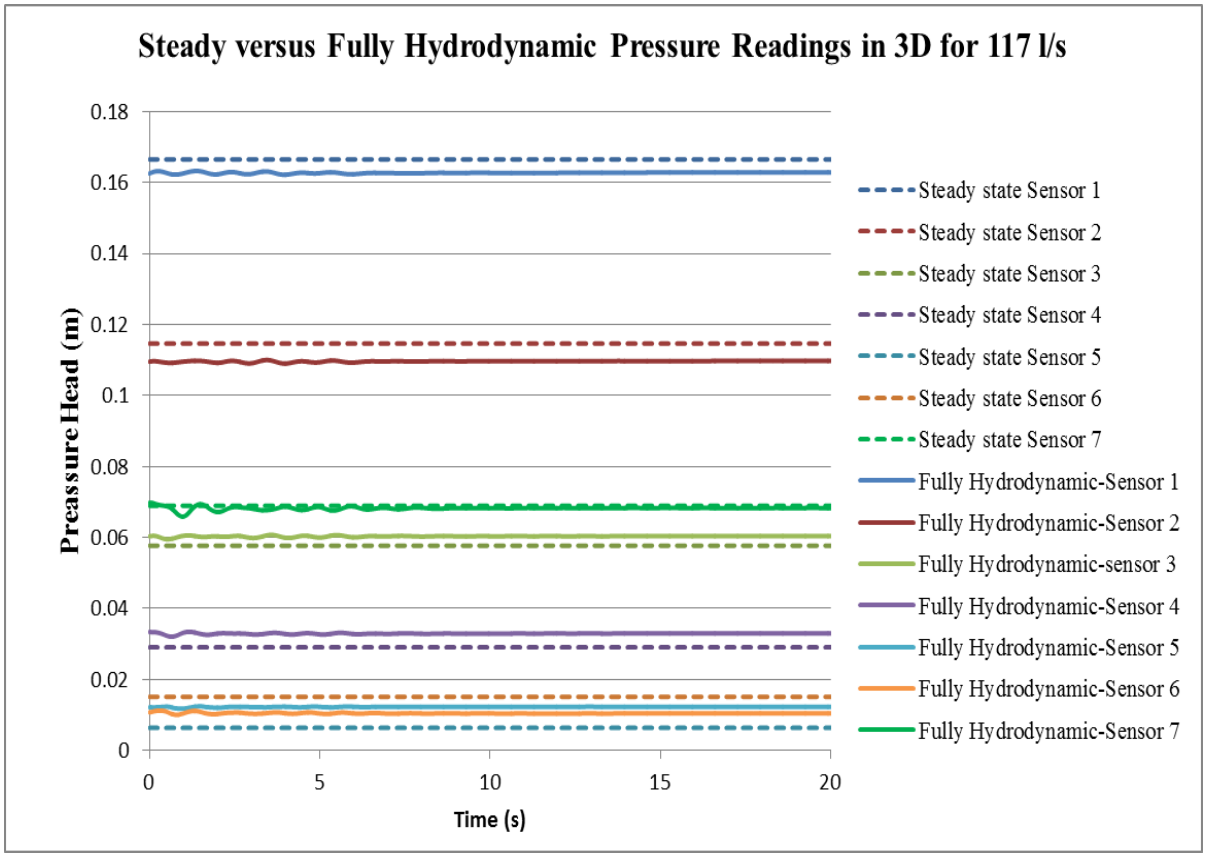

Figure 4-23: Comparison between 3D-simulated steady and fully hydrodynamic state models for a discharge of 117 l/s (Case-2)

Figure 4-23 shows that the two states produced a significant correlation, with sensor 7 producing the best results correlation for both simulation states.

As can be seen, the fully hydrodynamic simulations produced pressure readings which oscillated slightly within the first five seconds and became stable afterwards. This phenomenon is attributed to the instability in the flow at the beginning of the simulation. The same phenomenon was noticed during physical modelling, whereby the modeller would wait 5 to 7 minutes in order to record more accurate results.

For Case-2, it was not possible to test discharge greater than the design discharge since the flume channel was limited to 0.25 m above the crest.

However, the tests did not encounter sub-atmospheric pressures at the crest, all the pressure readings recorded were positive.

4.3 Discussion of numerical model results

After analysing CFD results obtained from two spillway cases, the following remarks can be drawn:

- The steady state simulations remain a near constant from the beginning untill the end whilst the fully hydrodynamic simulations produced, at the beginning, unstable pressure readings which oscillated slightly for 5 to 7 seconds.
- From the comparison between two and three dimension modelling, no significant variation in pressure reading was encountered. The pressures obtained from 2D and 3D-CFD numerical models are in close agreement at all the recording locations on the spillway face. However, the discrepancy between these models and the degree to which they are accurate will be determined in validation process.

CHAPTER 5: COMPARISON OF PHYSICAL AND CFD MODEL RESULTS

The investigations conducted in the physical and numerical modelling were centred on the surcharge and hydrodynamic effects of flow as discussed in the preceding chapters. This chapter focuses on the validation of CFD modelling through a comparison of results obtained for equivalent flow rates from the physical modelling discussed in the preceding chapter. However, there are a number of factors, known and unknown, which might have affected the comparison between numerical and physical modelling results. In the Appendix D, the source of these factors called errors and uncertainties are discussed.

5.1 Comparison between Physical and CFD Model Results

The following section is devoted to the validation of the CFD results achieved in this study by comparing the CFD model results with the physical model results.

5.1.1 Water surcharge

The results of surcharge presented in this section are divided into two main parts: (1) Flow surcharge upstream of the spillway and (2) the water surface along the entire spillway model.

5.1.1.1 Upstream water surcharge

The flow surcharge upstream of the crest (at 5H) was an important key consideration during the CFD modelling as it showed the quality of the CFD set-up and confirmed that the flow was behaving similar to the physical modelling.

Table 5-1 and Figure 5-1 compare the physical and CFD modelling water surcharge that were obtained from Case-1.

Table 5-1: CFD and physical modelling water surcharge for ogee spillway (Case-1)

SN°	Discharge (Q/l)	(1) Physical model water surcharge (mm)	(2) CFD water surcharge (mm)	(3) = (2) - (1) Difference (mm)
1	0	0	0	0
2	23	70	78	8
3	35	86	97	11
4	41	98	106	8
5	56	120	125	5
6	71	137	149	12
7	89	156	169	13
8	108	175	187	12
9	130	197	211	14

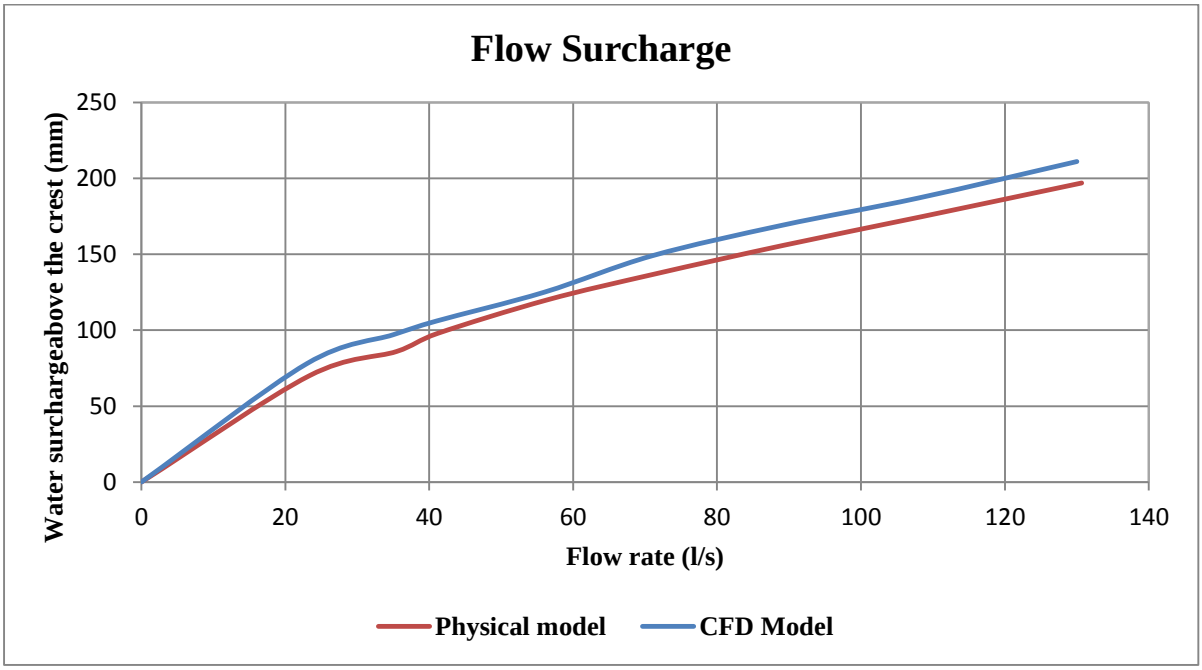

Figure 5-1: Physical modelling and CFD surcharge measured at 5H upstream of Case-1

The flow surcharge results, shown in Table 5-1 and Figure 5-1, include the surcharge measurements obtained through CFD modelling and physical modelling. As can be observed from the differences, CFD model simulations exhibit a great similarity between the physical model and CFD surcharge measurements. The maximum difference which was found corresponds to 14 mm.

Using the same methodology, Table 5-2 and Figure 5-2 present the water surcharge measurements obtained from Case-2.

Table 5-2: CFD and physical modelling water surcharge for ogee spillway (Case-2)

SN°	Discharge (l/s)	(1) Physical model water surcharge (mm)	(2) CFD water surcharge (mm)	(3) = (2) - (1) Difference (mm)
1	0	0	0	0
2	25	79	82	3
3	37	104	112	8
4	45	118	125	7
5	51	128	137	9
6	77	166	171	5
7	85	179	187	8
8	95	192	203	11
9	117	218	223	5

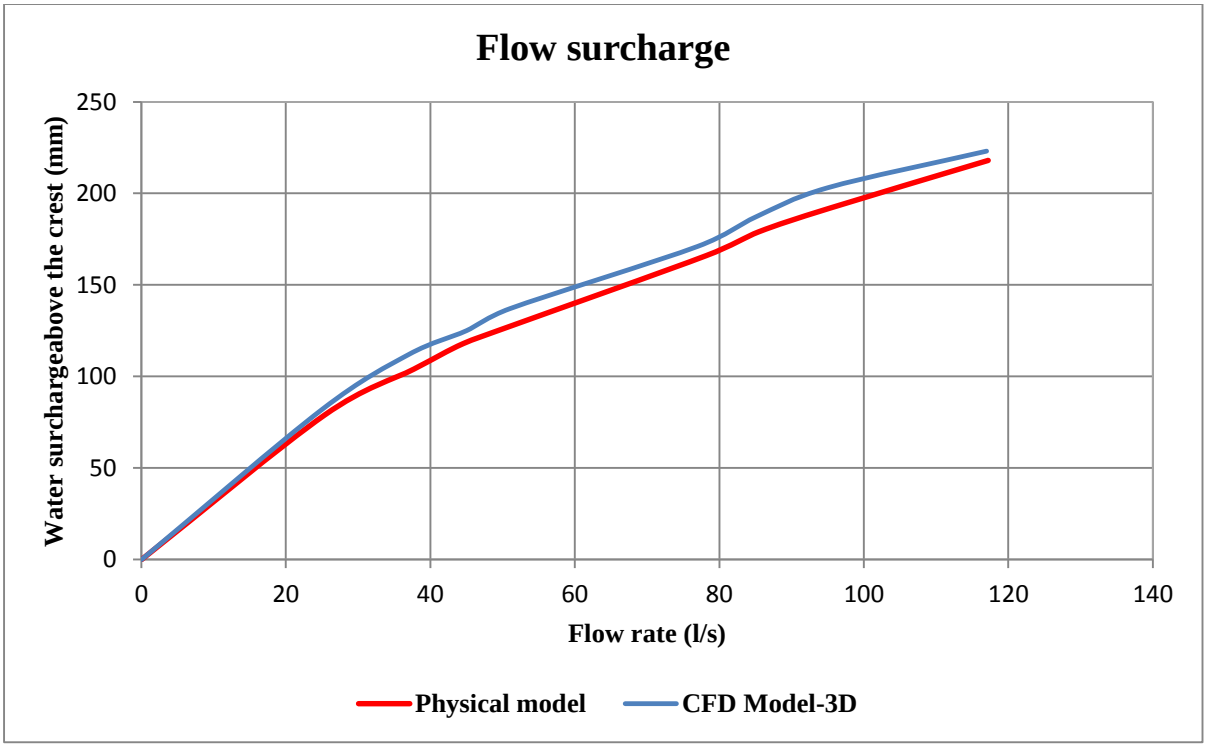

Figure 5-2: Physical modelling and CFD surcharge measured at 5H upstream of Case-2

From Table 5-2 and Figure 5-2, it is observed that the results simulated by CFD models indicate a strong correlation to those measured through physical modelling. The maximum difference obtained from physical modelling was 11 mm.

5.1.1.2 Water surface profiles

In both spillway models the water surface profiles were investigated along the spillway chute from upstream to downstream of the spillway. The study of the flow surcharge at different flow rates indicated that the water surface profiles obtained from CFD modelling are similar to those of the physical model. It should be noted that the water surface profiles obtained along the spillway refer to the flow depth measured perpendicular to the spillway face. A sample of profiles of 130 l/s and 117l/s tested in case-1 and Case-2 are presented in Figure 5-3 and Figure 5-4 respectively. The other profiles plotted for the remaining flow rates are presented in Appendix D.

The water free surfaces, as shown in Figure 5-3 and Figure 5-4, include the surcharge readings obtained through CFD modelling and physical modelling.

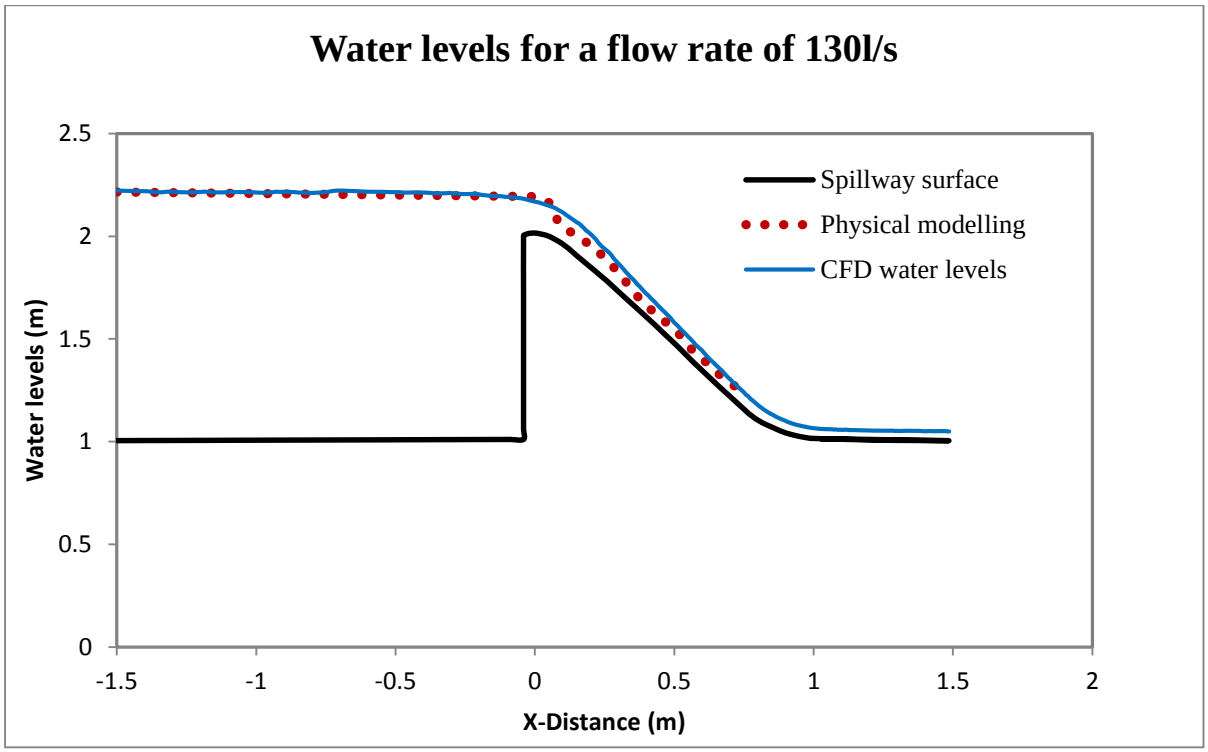

Figure 5-3: The comparison of CFD and experimental free surfaces for 130l/s (case-1)

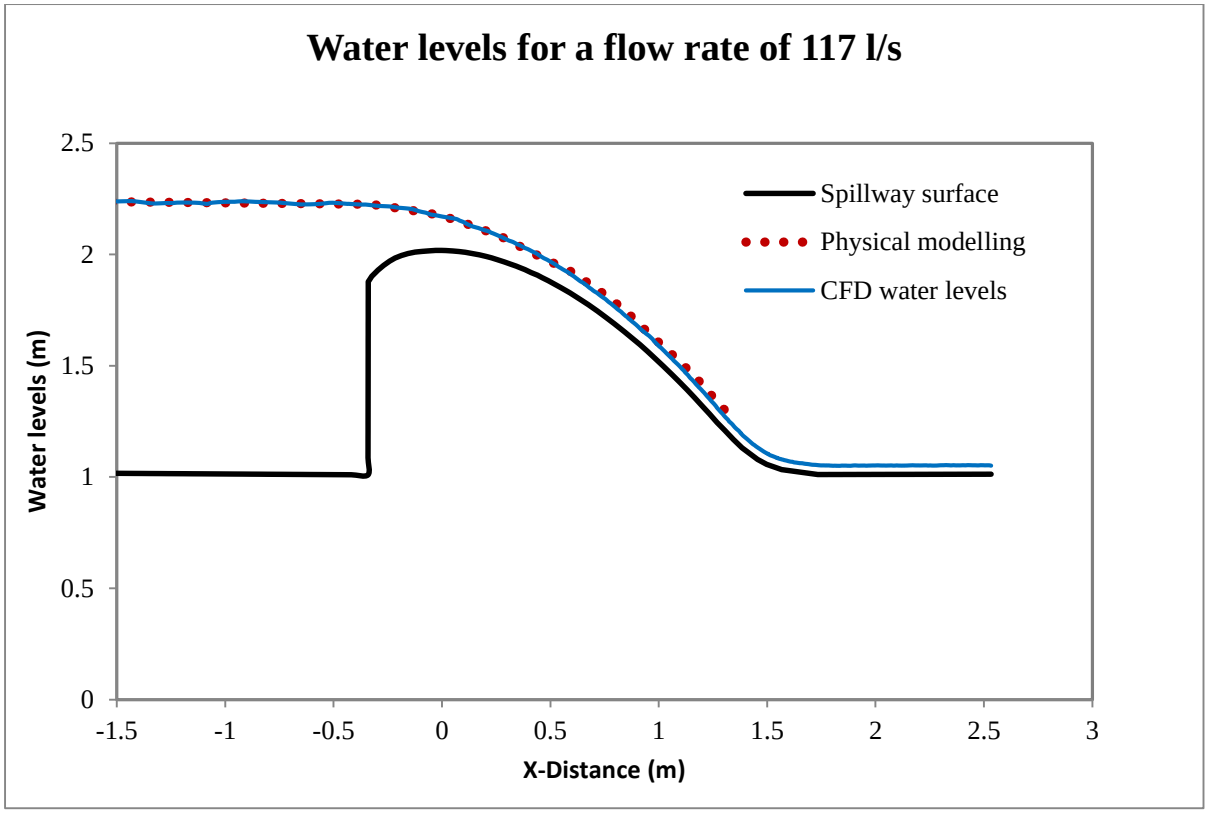

Figure 5-4: The comparison of CFD and experimental free surfaces for 117l/s (case-2)

From Figure 5-3 and Figure 5-4, it can be seen that the water free surfaces simulated by CFD models are in good agreement with those measured in physical modelling. It should be noted that the CFD models can simulate the surcharge of flow for ogee spillways consistently.

5.1.2 Pressure results

The average pressure results obtained from CFD and physical modelling are compared in this section to determine the accuracy of CFD models. As discussed in **section 4.5.3,** the comparison of steady and fully hydrodynamic pressure readings indicated a close similarity in all states. However, both steady and fully hydrodynamic pressures were compared to the physical modelling results in this section. Figure 5-5 compares CFD and physical model average pressure for a discharge of 130l/s.

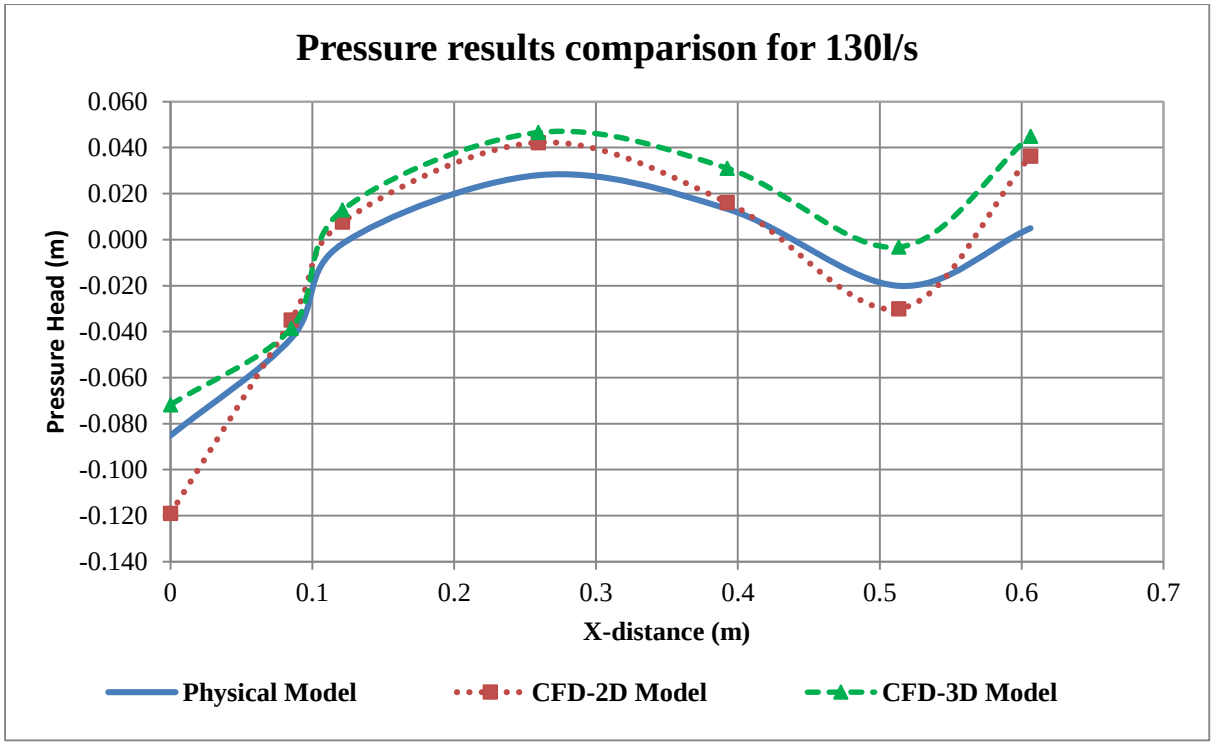

Figure 5-5: Comparison of CFD model and average Physical model results for 130 l/s (Case-1)

As can be seen in Figure 5-5, the pressure results presented for 2D and 3D models produced the reasonable agreement. The graphical comparison indicates a great agreement between CFD and physical model results. By observing all the results in Appendix D, it can be seen that a better correlation was achieved for higher flow rate.

To compare CFD with physical modelling results, the differences between the steady state pressures and the physical model average pressures were calculated. These differences were calculated in order to determine the accuracy of the CFD model results.). For positive figures, it means that the CFD model overestimates the physical model pressures and vice versa.

Table 5-3 and Table 5-4 present the differences of 2D and 3D steady state with physical model average pressures from Case-1 and Case-2 respectively.

Table 5-3: Differences between 2D-steady state simulated gauge pressures and physical model average gauge pressure readings (Case-1)

Flow rate (l/s)	**Difference between 2D steady State Over mean Physical Model Pressures (m)**						
Sensor	**1**	**2**	**3**	**4**	**5**	**6**	**7**
23	0.004	0.003	0.007	0.003	0.013	0.008	0.020
35	-0.015	0.002	0.007	0.008	0.010	0.004	0.021
41	-0.016	0.001	0.008	0.009	0.011	0.004	0.022
56	-0.003	0.004	0.007	0.013	0.008	0.005	0.023
71	0.001	0.002	0.006	0.016	0.006	-0.004	0.025
89	0.011	0.004	0.006	0.019	0.006	-0.006	0.027
108	-0.003	0.007	0.010	0.017	0.005	-0.005	0.029
130	-0.034	0.008	0.009	0.014	0.003	-0.010	0.031

Table 5-4: Differences between 3D-steady state simulated gauge pressures and physical model average gauge pressure readings (Case-1)

Flow rate (l/s)	**Difference between 3D steady State Over mean Physical Model Pressures (m)**						
Sensor	**1**	**2**	**3**	**4**	**5**	**6**	**7**
23	0.000	-0.003	0.004	0.006	0.027	0.032	0.028
35	-0.016	-0.002	0.005	0.012	0.026	0.032	0.030
41	-0.014	-0.002	0.007	0.013	0.026	0.033	0.031
56	-0.009	-0.003	0.006	0.015	0.024	0.035	0.031
71	-0.023	-0.012	0.004	0.023	0.026	0.027	0.040
89	0.000	-0.002	0.008	0.017	0.022	0.024	0.036
108	0.003	-0.001	0.011	0.019	0.020	0.022	0.039
130	0.013	0.004	0.015	0.019	0.018	0.017	0.040

Table 5-3 and Table 5-4 present the difference of gauge pressures between CFD model and the physical model results. The differences calculated for all sensors proved a good correlation between the observed and simulated pressures. The results presented above compared the average pressures. To confirm their accuracy, however, 2D and 3D-CFD pressure readings have been compared with those obtained from physical modelling.

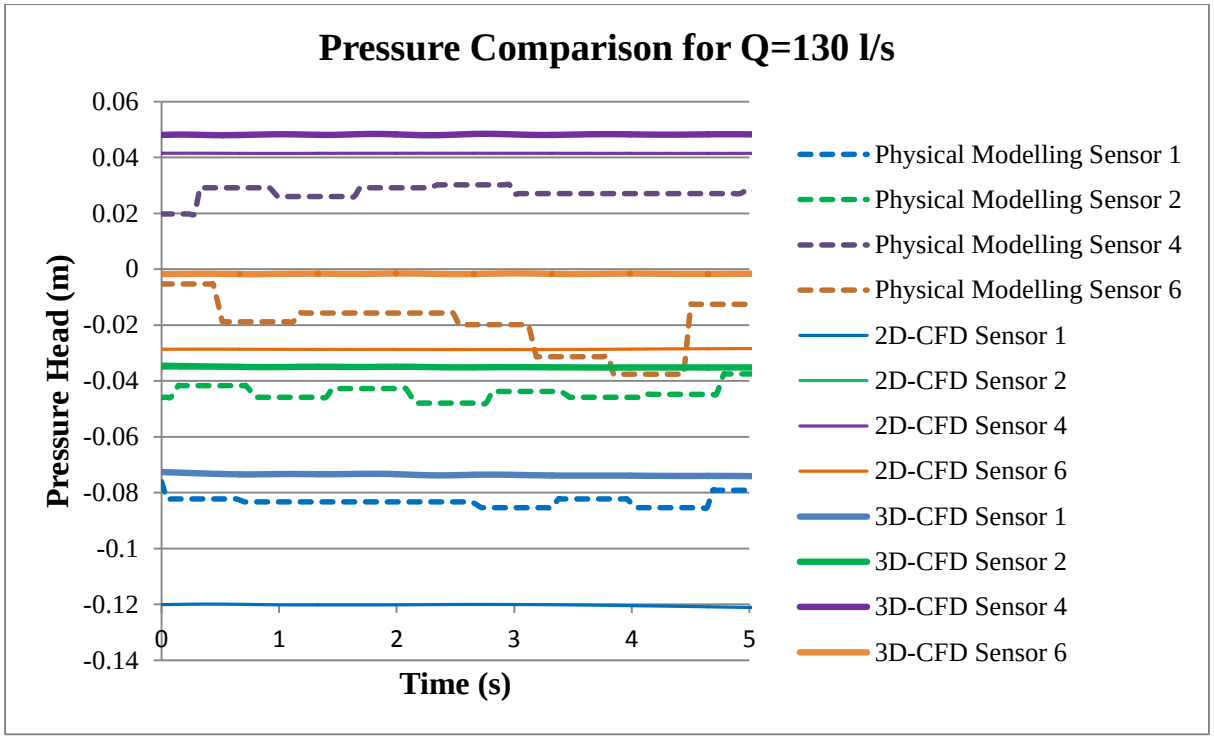

Figure 5-6: Physical modelling, 2D and 3D CFD fully hydrodynamic state pressure readings for 130 l/s, for sensor 1, 2, 4 and 6; Compared for Case-1

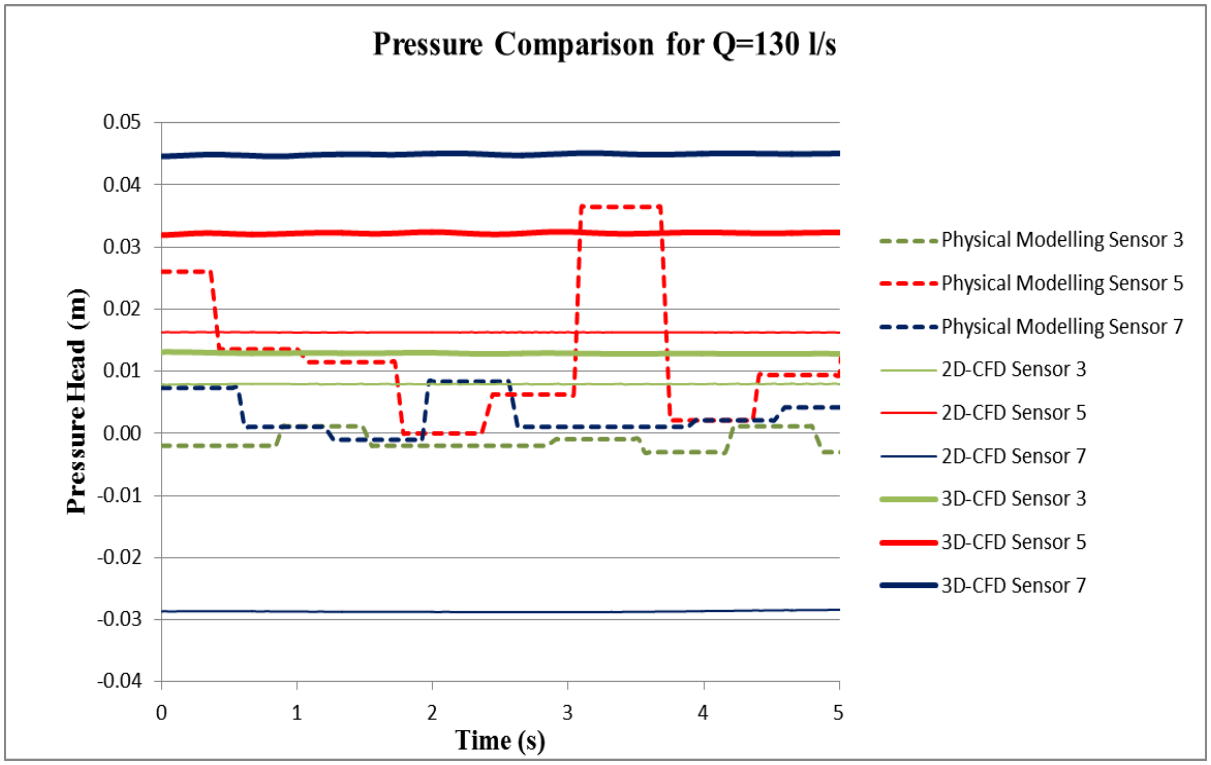

Figure 5-7: Physical modelling, 2D and 3D CFD fully hydrodynamic state pressure readings for 130 l/s, for sensor 3, 5 and 7; Compared for Case-1

For Figure 5-6 and Figure 5-7, all the sensors exhibit a great correlation between physical modelling and CFD-fully hydrodynamic pressure readings. Only sensor 7 indicates a large difference between the simulated pressure readings and those obtained from the physical modelling.

In addition, CFD pressure readings indicate a steady trend in the results while physical modelling results fluctuate within a constant range. This shows that CFD models do not accurately simulate the fluctuations in pressure.

To display the variation in physical model and 3D-CFD model results, the box plot was a convenient way of graphically depicting the pressure fluctuations. The two dimensional model results were not plotted since the variations in pressure are insignificant.

Figure 5-8, presents the variation in pressure per sensor for a flow rate of 130 l/s.

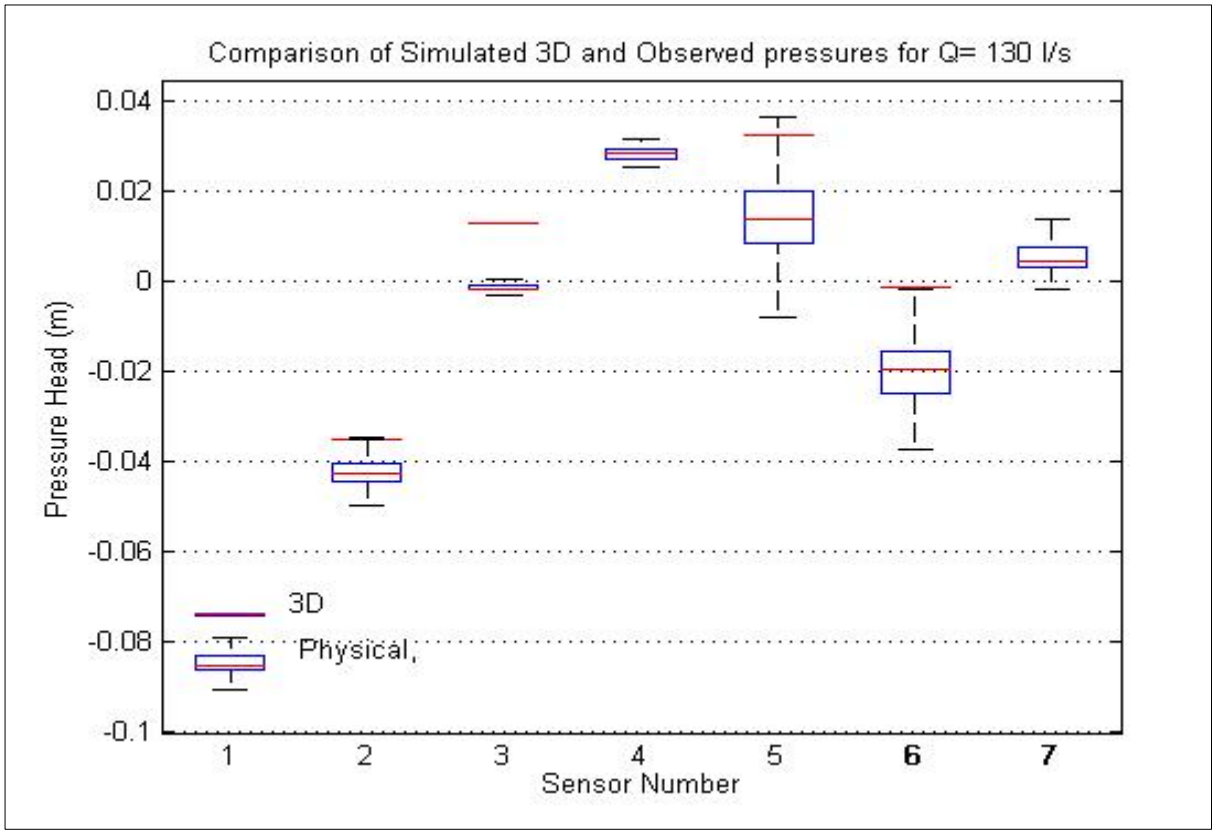

Figure 5-8: Box plot for the comparison of the simulated and observed pressure readings (Case-1)

Figure 5-8, is the box plot of pressure variation for a flow rate of 130 l/s and for all sensors. As observed clearly from graphical representation, the physical model pressures fluctuate more than the CFD model pressures.

As well as for Case-2, the steady state pressure results were compared with physical model results in Figure 5-9 to analyse the accuracy of CFD results. Figure 5-9 presents a validation of the average pressure results for 117 l/s while Table 5-5 and Table 5-6 present the differences that were calculated with regard to determine the degree of accuracy of 2D and 3D CFD steady state results.

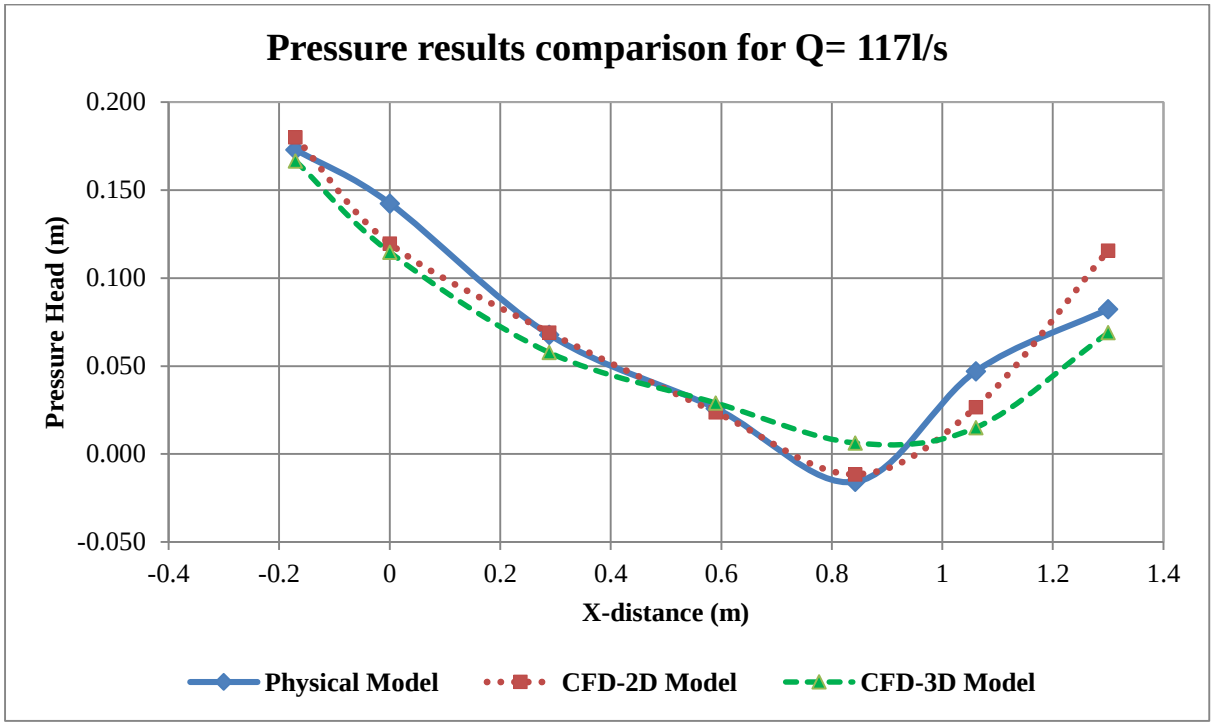

Figure 5-9: Comparison of CFD model and average Physical model results for 117 l/s (Case-2)

Figure 5-9 presents the average pressure readings for a discharge of 117l/s. The results produced by 2D and 3D models indicate a close agreement between CFD and physical models. As found in Appendix D, the trend of the graphs of all the discharges simulated looks similar in this case, since all the discharges tested were below the design discharge.

Table 5-5: Differences between 2D-steady state gauge pressures and physical model gauge pressure readings (Case-2)

Flow rate (l/s)	**Difference between 2D steady State mean Over Physical Model Pressures (m)**						
Sensor	**1**	**2**	**3**	**4**	**5**	**6**	**7**
23	0.007	-0.009	0.001	-0.002	0.005	-0.025	-0.015
35	0.012	-0.013	0.006	0.004	0.010	-0.021	0.000
41	0.012	-0.014	0.004	0.005	0.024	-0.020	0.005
56	0.015	-0.012	0.005	0.006	0.030	-0.020	0.010
71	0.012	-0.016	-0.032	0.003	0.041	-0.020	0.021
89	0.008	-0.020	0.000	0.000	0.005	-0.019	0.024
108	0.008	-0.020	0.000	-0.001	0.005	-0.021	0.027
130	0.007	-0.023	0.001	-0.002	0.004	-0.020	0.033

Table 5-6: Differences between 3D-steady state gauge pressures and physical model gauge pressures readings (Case-2)

Flow rate (l/s)	**Difference between 3D steady State Over mean Physical Model Pressures (m)**						
Sensor	**1**	**2**	**3**	**4**	**5**	**6**	**7**
23	-0.004	-0.015	-0.009	0.003	0.020	-0.032	-0.049
35	0.000	-0.019	-0.004	0.009	0.027	-0.030	-0.042
41	0.000	-0.020	-0.007	0.010	0.041	-0.029	-0.039
56	0.010	-0.017	0.000	0.012	0.048	-0.028	-0.036
71	-0.001	-0.022	-0.004	0.007	0.058	-0.030	-0.024
89	-0.003	-0.023	-0.010	0.006	0.023	-0.029	-0.021
108	-0.006	-0.026	-0.011	0.004	0.023	-0.032	-0.019
130	-0.006	-0.028	-0.010	0.003	0.022	-0.032	-0.013

The differences presented in Table 5-5 and Table 5-6 indicate a close agreement between CFD steady state and physical model average pressure results. To confirm the accuracy the pressure readings were compared. Figure 5-10 and Figure 5-11 present a sample of a graphical representation of pressure readings simulated by CFD fully hydrodynamic models and those obtained from physical modelling.

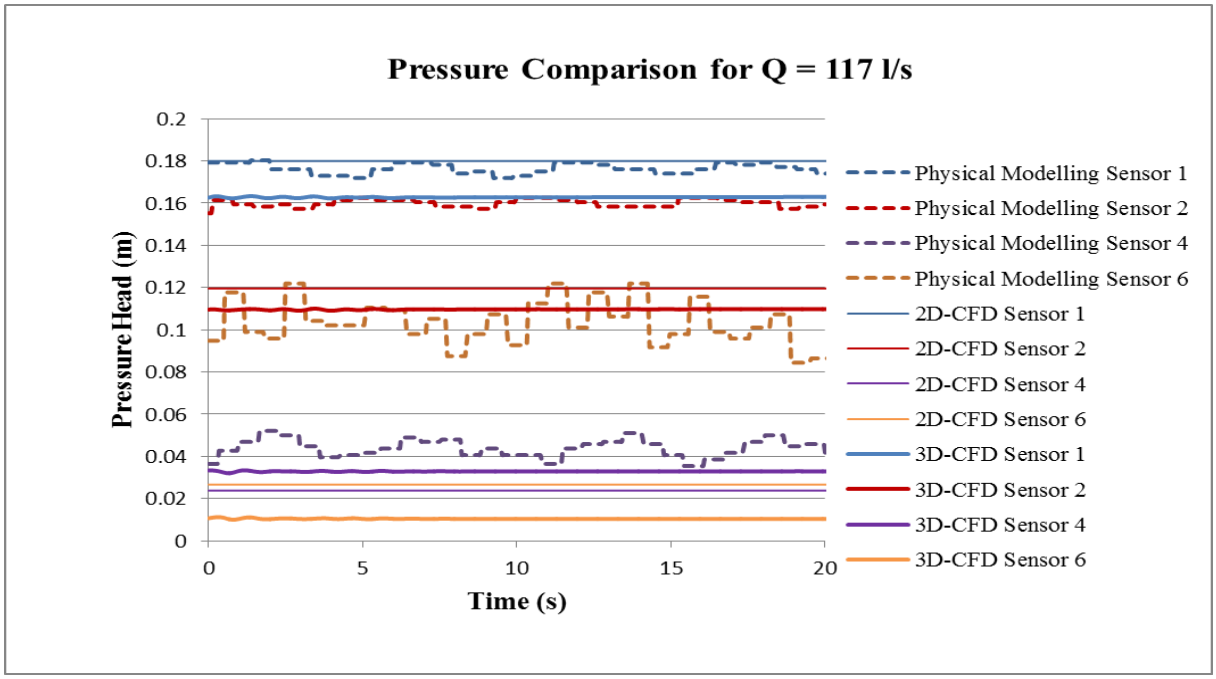

Figure 5-10: Physical modelling, 2D and 3D CFD fully hydrodynamic state pressure readings for 117 l/s for sensor 1, 2, 4 and 6; compared for Case-2

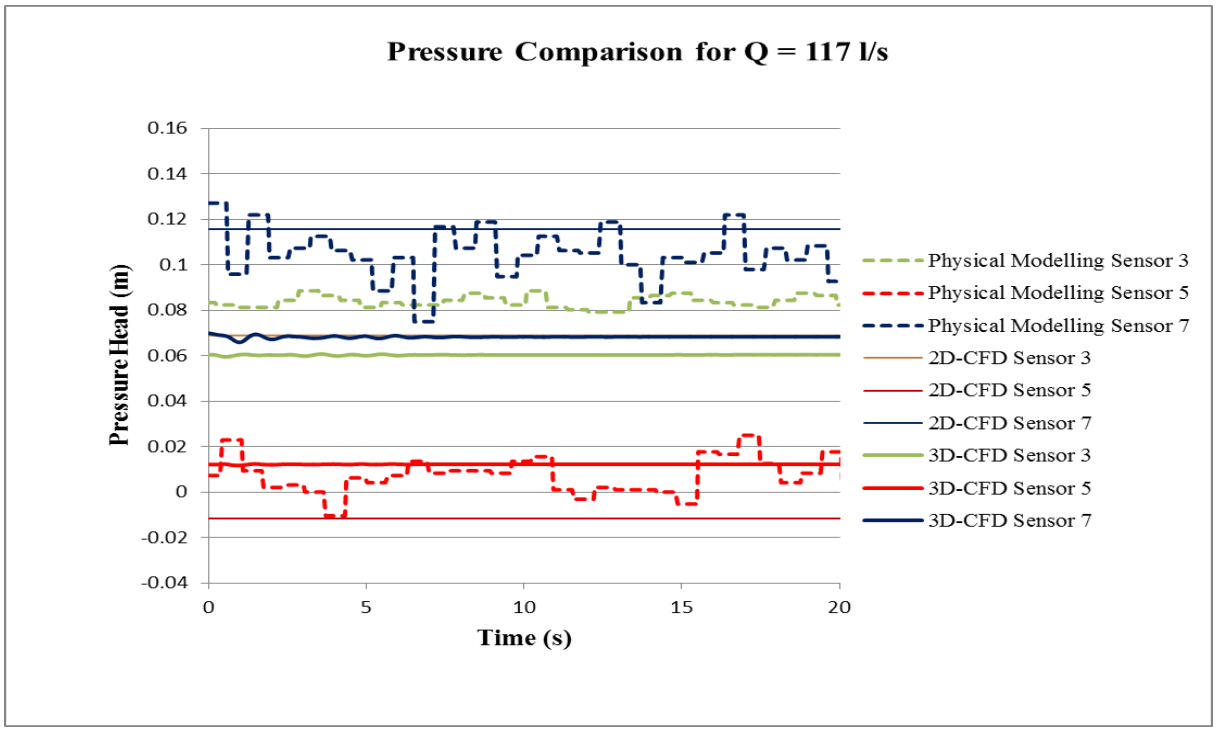

Figure 5-11: Physical modelling, 2D and 3D CFD fully hydrodynamic state pressure readings for 117 l/s for sensor 3, 5 and 7; compared for Case-2

As well as for Case-2, the box plot displaying the variation in pressure for physical model and CFD model is presented here below in Figure 5-12.

As can be seen in the representation below, the fluctuations in pressures are insignificant for 3D-CFD model.

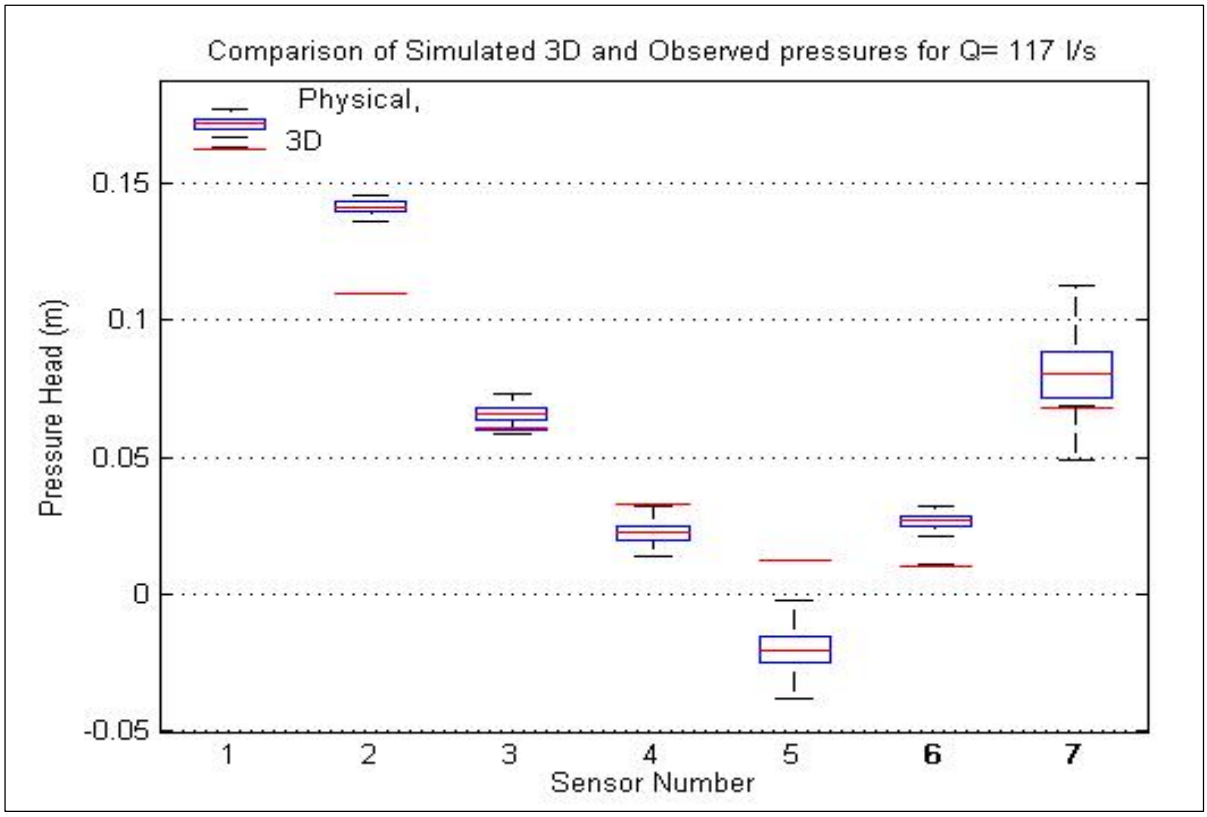

Figure 5-12: Box plot for the comparison of the simulated and observed pressure reading (Case-2)

5.2 Final remarks

Based on the validation process of ogee spillway hydraulics conducted this chapter, the following remarks can be highlighted:

- The physical modelling results were used as benchmarks for the water surcharge and free surfaces, for different flow rates measured. The values produced by a CFD model predicted free surface results that reflect the general flow characteristics over ogee spillways.
- The pressure results obtained from physical and CFD modelling show similar pressure distribution patterns on the spillway face and the pressures are in reasonable agreement. For Case-2, both 2D and 3D models produced significantly accurate results. However, CFD models did not simulate the pressure fluctuations as observed in the physical model pressures.

CHAPTER 6: CONCLUSIONS AND RECOMMENDATIONS

6.1 Introduction

Based on the results obtained from both physical and CFD models, conclusions are presented and recommendations for further research are proposed in this chapter.

6.2 Conclusions

Mathematical modelling plays a capital role in the design and analysis of hydraulic structures. However, this often necessitates physical models, considered as the most established form of hydraulic modelling, to ensure reasonable accuracy of the results. This study was devoted to carrying out a CFD validation of ogee spillway hydraulics. To achieve this objective, two distinct ogee spillway models were adopted in this study and the most established method (physical modelling) was chosen as comparison baseline.

The findings in this thesis can be summarised as follows:

- In physical modelling, pressures for eight discharges were recorded over a recording period of five minutes. Measurements of the water surcharge along the crest and upstream of the crest at a distance equal to 5H were taken.
- The pressure readings obtained from Case-1, a negative pressure reading was encountered for the discharges greater than the design discharges with a clear flow separation from the crest. In addition, an accentuated sub-atmospheric pressure appeared, especially for heads which are greater than $1.33H_o$.
- For Case-2 (having a design head equal to 1.0 m), it was not possible to test the discharges greater than the design discharge as the channel height of the flume was limited to 0.25 m from the spillway crest.
- A reasonable agreement was achieved between physical modelling and CFD water surcharge, with a maximum difference of 14 and 11 mm for Case-1 and Case-2, respectively.
- For CFD modelling, the model domain was developed with the same dimensions as the physical model with regard to minimising errors as much as possible.

Triangle mesh in 2D was selected and cutcell meshing was used for 3D modelling where the minimum grid size in 2D and 3D models was 4mm and 20mm respectively. The trend towards mesh independence was observed by comparing the pressure reading obtained for different grid sizes.

- 3D models have proved to be more accurate than 2D models since 3D-fully hydrodynamic pressures, when compared to the physical modelling results, displayed slightly the pressure fluctuations.
- The Volume of Fluid (VOF) and the Realisable "$k - \varepsilon$" models chosen for this study to model the multiphase flow and turbulence, respectively, simulated successfully the flow over an ogee spillway. The investigations proved that CFD models were able to develop a flow surcharge and simulate the pressures similar to the physical model test results. However, they were unable to accurately determine the pressure fluctuations similar to those obtained from physical modelling.

Concerning the comparison between physical and CFD modelling, it is clear that physical modelling still proves to be the more established of the two methods. Although CFD tools still have limitations (including grid resolution, run times and numerical instabilities to name a few), there are many instances where they may offer an increased accuracy over the designs and provide an insight into the required application. CFD models can provide more detail about velocity and turbulence than a physical model can and may be more economical in some cases.

6.3 Recommendations

The current study has provided an insight into the CFD modelling of ogee spillways. Based on these concluding remarks, the following recommendations are made:

- This study attempted to validate the uncontrolled ogee spillway hydraulics with Ansys-Fluent software. The same validation is recommended for a controlled ogee spillway to assess the use of this software in the design and testing processes of this particular type.
- Other types of turbulence models, apart from Realisable $k - \varepsilon$ and Volume of Fluid model (VOF) within Ansys-Fluent should be assessed to determine their capabilities for turbulence and multiphase modelling.
- Ansys-Fluent takes a very long time to produce results. Normally, a five minutes test length in physical modelling would take more than one month to provide results for a single discharge scenario. Therefore, methods should be developed to reduce simulation periods e.g. by means of computer clusters.

References

AIAA, 1998. Guide for the Verification of Computational Fluid Dynamics Simulations. *s.1: AIAAG-077-1988*.

Berger, C. R., & Winant, E.H. (1991). One dimensional Finite Element Model for Spillway. *Hydraulic Engineering, Proceedings 1991*. Nashville: National Conference , ASCE.

Bhajantri, M. E., & Deolalikar, P. (2006). Hydrodynamic modelling of flow over a spillway using a two-dimensional finite volume-based numerical model. *Sadhana*, 743-754.

Blight, G. E., Robinson, M. J., & Diering, J. A. (1981). The Flow of Slurry from a breached tailings dams. *Journal of The South African Institute of Mining and Metallurgy*, Johannesburg.

Bradley, J. N. (1945.). *Studies of flow characteristics, discharge and pressures relative to submerged dams.* Hydraulic Laboratory Rep No. 182, Denver.

Brater, F. E., King, W. H., Lindell, J., & Wei, Y. C. (1996). *Handbook of Hydraulics.* New York: MC Graw - Hill.

Brown, K. W., Savage, B., & Paxson, S. G. (2012). Revisiting Spillway discharge coefficients for several weir shape. *32nd Annual USSD conference: Innovative Dam and Levee Design and Construction for Sustainble water Management* (pp. 1317-1335). New Orleans, Lousiana: United States Society on Dams (USSD).

Cain, P., & Wood, I. (1981). Measurements of Self-aerated Flow on a Spill way. *JI. Hyd. Div., ASCE, 107, HY11*, 1425-1444.

Causon, D., Mingham, C., & Ingram, D. (1999). Advances in Calculation methods for super-critical flow in spillway channels. *Journal of Hydraulic Engineering 125 (10)*, 1039-1050.

Chadwick, A., Morfett, J., & Borthwick, M. (2004). *Hydraulics in Civil and Environmental Engineering.* New York: Spon Press.

Chanson, H. (2002). *The Hydraulics of stepped chutes and spillways.* Lisse, Netherlands: Balkema.

Chanson, H. (2004). Air-water flows in water engineering and hydraulic structures. Basic processes and metrology. *Proceedings of the international conference on hydraulics of dams and River structures*, (pp. 3-21). Tehran - Iran.

Chanson, H. (2004). *The Hydraulics of Open Channel Flow : An Introduction. Second Edition.* Oxford: Elsevier"s Science & Technology.

Chatila, J., & Tabbara, M. (2004). Finite Analytic Method in Flows and Heat Transfer. *Computers and Structures 82*, 1805-1812.

Chow, V. T. (1959). *Open-Channel Hydraulics.* New York: McGraw Hill Book Company INC.

Chung, T. (2002). Computational fluid dynamics. *The press syndicate of the University of Cambridge*, 1036.

Cloete, S., Olsen, J., & Skjetne, P. (2009). CFD modelling of plume and free surface behavior resulting from a sub sea gas release. *Applied Ocean Research 31(3)*, 220-225.

Daneshkhah, A., & Vosoughifar. (2012). Solution of Flow Field Equations to investigate the Best Turbulent Model of Flow over a Standard Ogee Spillway in Finite Volume Method. *The First International Conference on Dams & Hydropower.*

Darvas, L. (1971). Performance and design of labyrinth weirs. *Journal of Hydraulic Engineering ASCE*, Issue 97(8), pp. 1246-125.

Falvey, H. (2003). *Hydraulic Design of Labyrinth Weirs.* Virginia: ASCE Press.

Ferzieger, J., & Peric, M. (1996). *Computational Methods for Fluid Dynamic.* Heidelberg: Springer-Verlag.

Fluent. (2008). *Ansys Fluent 6.3 User's guide.* Ansys Inc.

Fluent. (2009). *Ansys Fluet 12.0 Theory Guide, S.1.* Ansys Inc.

Franz, D. D., & Melching, S. C. (1997). *Full equation (FEQ) Model for the Solution of Dynamic equations of motion for one-dimensional Unsteady Flow in open channels and through control structures.* Mountain View-California, Urbana-Illnois: U.S. Geological Survey.

Gessler, D. (2005). CFD Modelling of Spillway performance, EWRI 2005: Impacts of global climate change. *In Proceedings of the World Water and Environmental Resources Congress.* Anchorage, Alaska: American Society of Civil Engineers.

Ghare, A., Wadhai, P., Mistry, N., & Porey, P. (2008). Hydraulic and Environmental Aspects of Long Crested Weirs. *Global Journal of Environmental Research 2 (3),* 122-125.

Ghosh, S. (2014). *Flood Control and drainage Engineering, Fourth Edition.* London, UK: CRC Press/Balkema.

Guo, Y., Wen, X., & Wu, C. F. (1998). Numerical Modelling of Spillway Flow with Free Drop and Initially Unknown Discharge. *J. Hydr. Res. 36(5).* , 785-801.

Hattingh, L. N. (2012). Lessons learned from Dam Safety Incidents in South Africa. Kyoto, Japan: ICOLD.

Henderson, F. (1996). *Open Channel Flow.* Prentice-Hall Inc.

Hirt, C. W., & Nicholas, B. (1981). Volume of Fluid Method (VOF) for the Dynamics of Free Boundaries. *J.Comp. Physics, Vol. 39,* 201-205.

Horton, E. R. (1907). *Weir experiments, coefficients and formula.* Watshington: Government printing Office.

Houston, K. (1983). *Hydraulic Model Study of Hyrum Dam Auxilliary Spillway.* Denver: Bureau of Reclamation Division of Research Hydraulics Branch.

ICOLD. (2001). Risk of Dangerous occurences: Lessons learnt from practical experiences. *Bulletin of Tailings Dams*.

ICOLD. (2001). Tailings Dams- Risk of dangerous occurences, lessons learnt from practical experiences. *ICOLD Comittee on Tailings Dam and Waste Lagoons* (p. Bulletin 121). Paris: United Nations Environmental Programme (UNEP), Division of Technology, Industry and Economics (DTIE) and International Commission on Large Dams (ICOLD).

ICOLD. (2012). Complementary Use of Physical and Numerical Modelling Techniques in Spillway Design Refinement. *ICOLD, 24th Congress* (pp. 55-76). Kyoto: ICOLD.

Johnson, M., & Savage, M. B. (2006). Physical And Numerical Comparison of Flow Over Ogee Spillway in the Presence of Tailwater. *Journal of Hydraulic Engineering, Vol. 132, No.12*.

Keller, R. (1972). *Field Measurement of Self-Aerated High Speed Open Channel Flow*. Dept. of Civil Eng., Univ. of Canterbury, New Zealand.

Khatsuria, R. (2005). *Hydraulics of Spillways and Energy disspators.* New York: Marcel Dekker.

Kim, G. D., & Park, H. J. (2005). Analysis of Flow Structure overOgee - Spillway in consideration of Scale and Roughness Effects by using CFD Model. *KSCE Journal of Civil Engineering*, PP 161-169.

Kjellesvig, H. (1996). Numerical Modelling of Flow over a Spillway. *Hydroinformatics- 96*.

Kositgittiwong, D. (2012). *Validation of numerical model of flow behaviour through smooth and stepped spillways using Large - Scale Physical model.* Thon Buri: King Mongkut's University of Technology Thon Buri.

Lihe, J., Mazin, E., Natalya, S., Dudley, R., & Sukumar, A. (2011). Ruskin Dam spillway shocrete assessed. *Concrete Internationwithpermission of American Concrete Institute*, 7.

Loftin, M. (1999). *Water Resources Engineering",.* The McGraw-Hill Companies, Inc.

Maynord, T. S. (1985). *General Spillway investigation.* Washington D.C: Department of The Army - Waterways Experiment STation-Corps of Engineers.

Mays, W. L. (1999). *Hydraulic Design Handbook.* Tempe, Arizona: McGraw. Hill Companies.

Moin, P., & Kim, J. (1997). Tackling turbulence with supercomputers. *Scientific American 1*, 276.

Murphy, T. (1973, Dec.). Spillway Crest Design. Viscksburg, Vicksburg, U.S.A: U.S Army Engineer Waterways Experiment Station .

Murrone, A., & Villedieu, P. (2011). Numerical Modeling of Dispersed Two-Phase Flows. *Aerospace Lab*.

Nikseresht, A., Alishahi, M., & Emdad, H. (2008). Complete Flow Field Computation around an ACV (Air Cushion Vehicle) Using 3-D VOF with Lagrangian Propagation in Computational Domain. *Computer and structures Vol. 86, ,* No7-8.

Oberkampf, l., Deland, M., Rutherford, M. B., Diegert, V. K., & Alvin, F. K. (2001). Error and Uncertainty in modelling and Simulation. *Reliability Engineering & System Safety*, 333-357.

Panton, R. (1984). Incompressible flow. *John Wiley and Sons*, 675.

Parviz, M., & John, K. (1997). Tackling Turbulence with Supercomputers . *Scientific American I, 276*.

Perez, R. (2008). *Uncertainty Analysis of Computational Fluid Dynamics Via Polynomial.* Blacksburg: sn.

SANCOLD. (2011). *Guidelines on Freeboard for Dams, Volume II.* Pretoria: SA Water Research Commission.

Savage, B., Frizell, K., & Crowder, J. (2004). *Brains versus Brawn: The Changing World of Hydraulic Model Studies*.[Online] Available at: http://www.usbr.gov/pmts/hydraulics_lab/pubs/PAP/PAP-0933.pdf [Accessed 09 05 2014]

Savage, M., & Johnson, M. (2001). Flow over Ogee Spillway: Physical and Numerical model Case Study. *Journal of Hydraulic Engineering 127(8)* , 640-649.

Şentrürk, F. (1994). *Hydraulics of Dams and reservoirs.* Toulouse: Water ressources publications.

Shih, T., Liou, W. S., & Zhu, J. (1995). A new k-[epsilon] eddy viscosity model for high reynolds number turbulent flows. *Computers & Fluids 24(3)*, 227-238.

Song, C., & Zhou, F. (1999). Simulation of Free Surface Flow over Spillway. *Journal of hydraulic Engineering 125(9)*, 959-967.

Strydom, J., & Willams, A. (1999). A review of important and interesting technical findings regarding the tailing dam failure at Merriespruit. *Journal of the South African Institution of CIvil Engineering: Fourth Quarter 1999: 41, 4: ProQuest Science Journals*.

Takasu, J., & Yamaguchi, S. (1988). *Principals for selecting types of spillway for flood control dams in Japan.* San Francisco, USA: Proceeding of the 16th Congress of the international commission on large dams, 13-16 June.

U.S.B.R. (1948). *Crests of overfall Dams.* Boulder Canyon Project - Final Report.

U.S.B.R. (1973). *Design of Small Dams.* United States Department of Interior - Bureau of Reclamation.

U.S.B.R. (1987). *Design of Small Dams.* United States Department of Interior - Bureau of Reclamation.

USACE. (1990). *Hydraulic design of spillways.* Washington: Department of the U.S Army corps of Engineers.

Veersteg, H., & Malalasekera, W. (1995). *An Introduction to Computational Fluid Dynamics.* Harlow: Longman Group Ltd.

Versteeg, H., & Malalasekera, W. (2007). *An introduction to Computational Fluid Dynamics: The finite volume method.* England: Prentice Hall.

Wanot, J. (1996). *Computational fluid dynamics methods in ship design.* Germany.: R&D projects (1996).

Wendet, F. J. (2009). *Computational Fluid Dynamics: An Introduction, 3rd Edition.* Eagle River, WI, USA: Springer.

WIKA. (2013). [Online] *Available at :http://www.wika.co.za/publish/download_datasheets_PE_en_co.aspx?ActiveID=14267*. [Accessed 10 09 2014]

Winant, R., & Berge, E. (1991). One dimensional finite element model for spillway flow. *National Conference on Hydraulic Engineering.* New York: ASCE.

Appendix A: Physical Modelling Results

A.1. Pressure Conversion

As the pressure transducer transforms an excitation caused by the flow into an electrical current, the initial reading is a value in ampere. This is converted to volt according to Ohm's law which states that the potential difference is equal to the current multiplied by the resistance as shown in the equation (A.1-1)

$$V = I\ X\ R \qquad \text{(A.1-1)}$$

where

V= Potential difference (V)

I = Current (A)

R = Resistance (with R= 120 Ω)

The average voltage pressure obtained was converted to pressure head by calibrating the sensor pressure reader using the range of different pressures as shown in the Figure A-1: below. This calibration yielded a way of converting the readings into a pressure head as presented in equation (A.1-2):

$$Y = 0.125x - 1.5 \qquad \text{(A.1-2)}$$

where

Y = The pressure head (m)

x = The current measured (A)

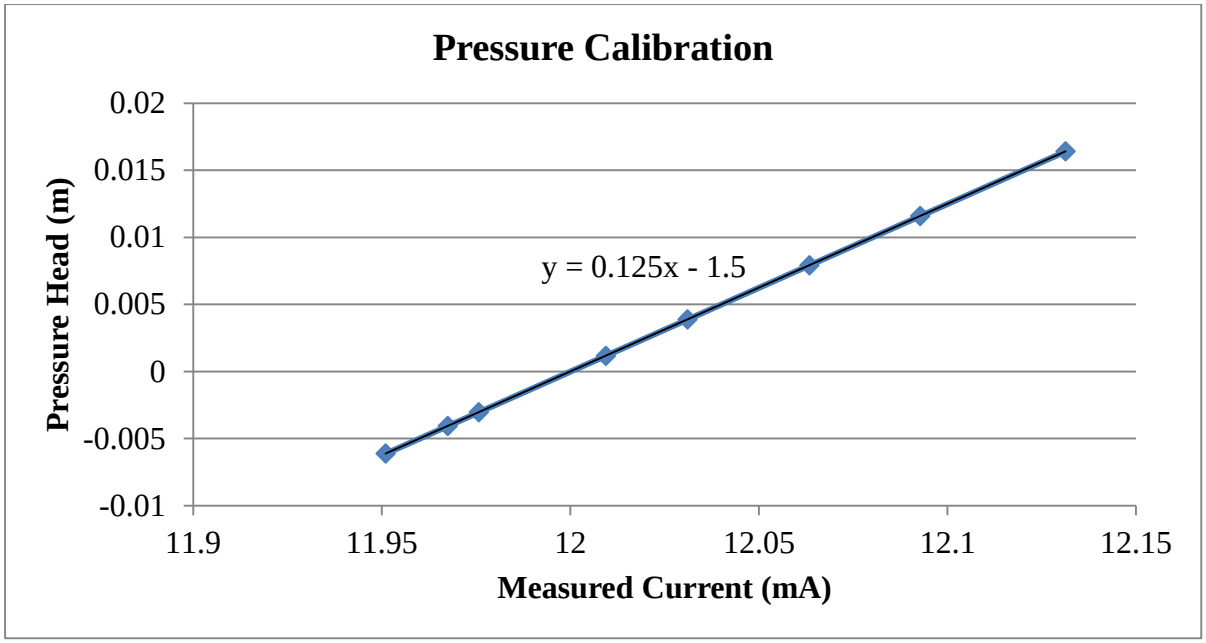

Figure A- 1: Pressure results calibration

A.2. Pressure results

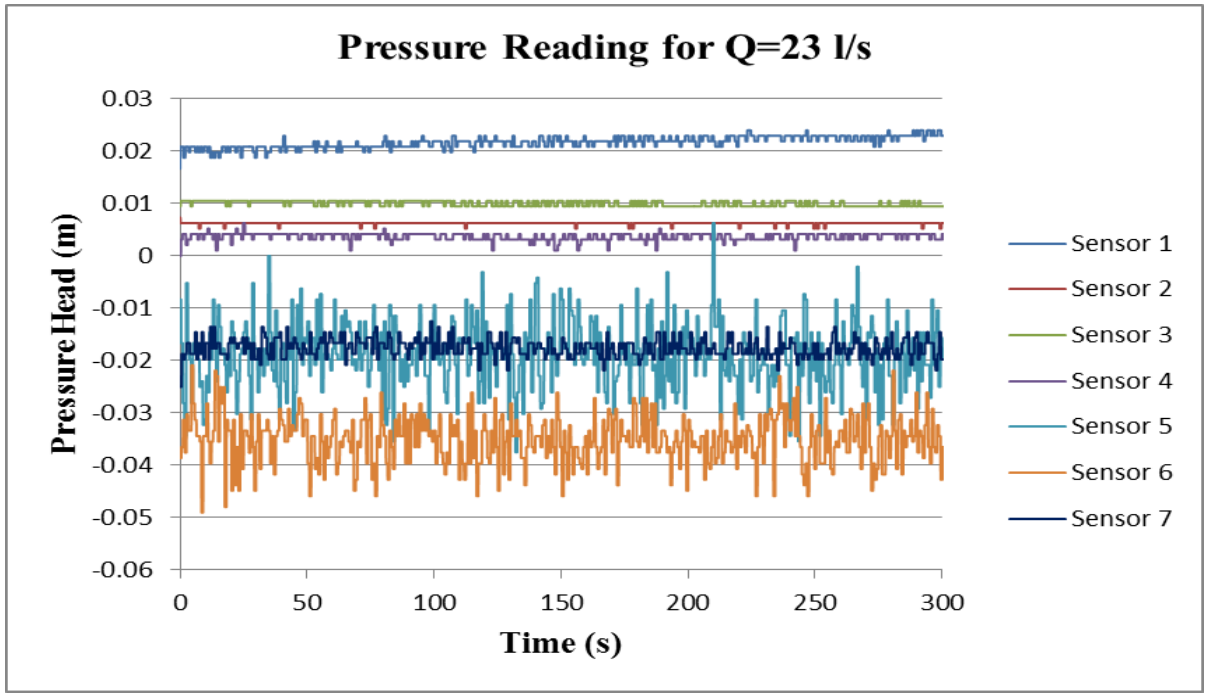

Figure A- 2: Pressure results for 23 l/s: case - 1

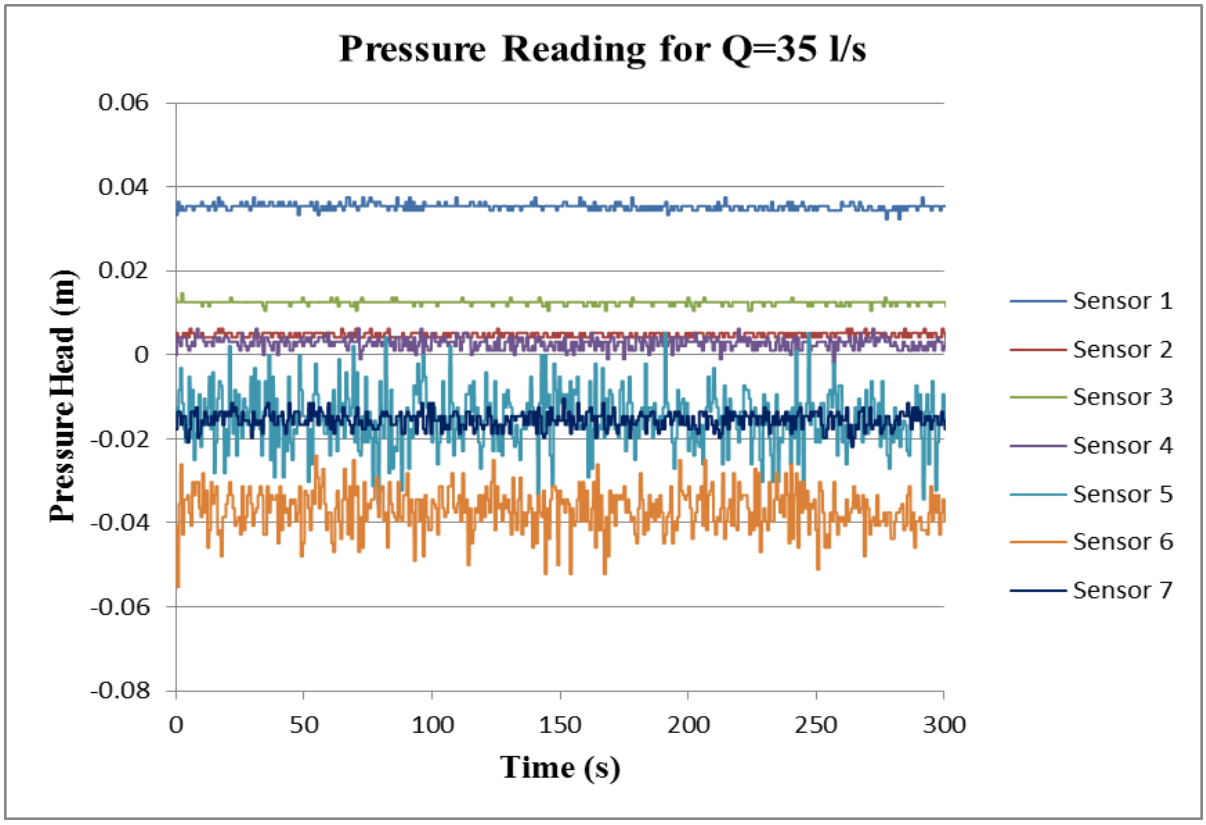

Figure A- 3: Pressure results for 35 l/s: case - 1

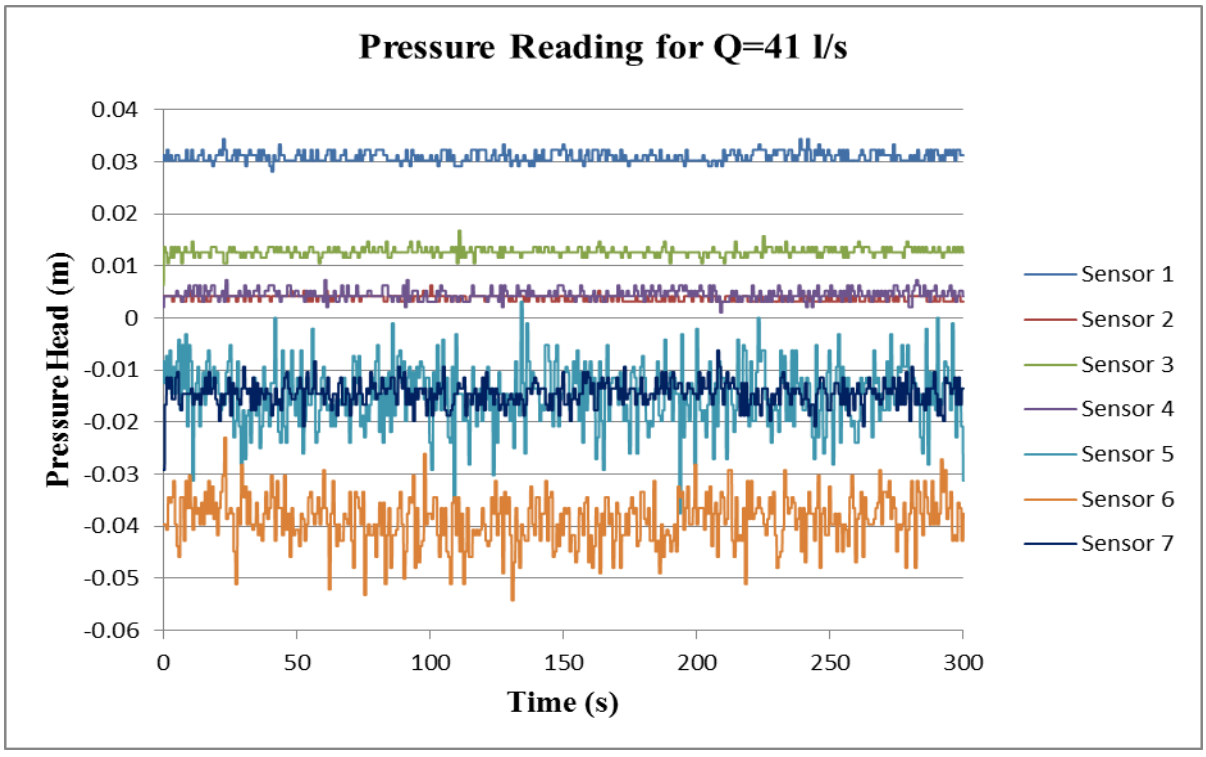

Figure A- 4: Pressure results for 41 l/s: case - 1

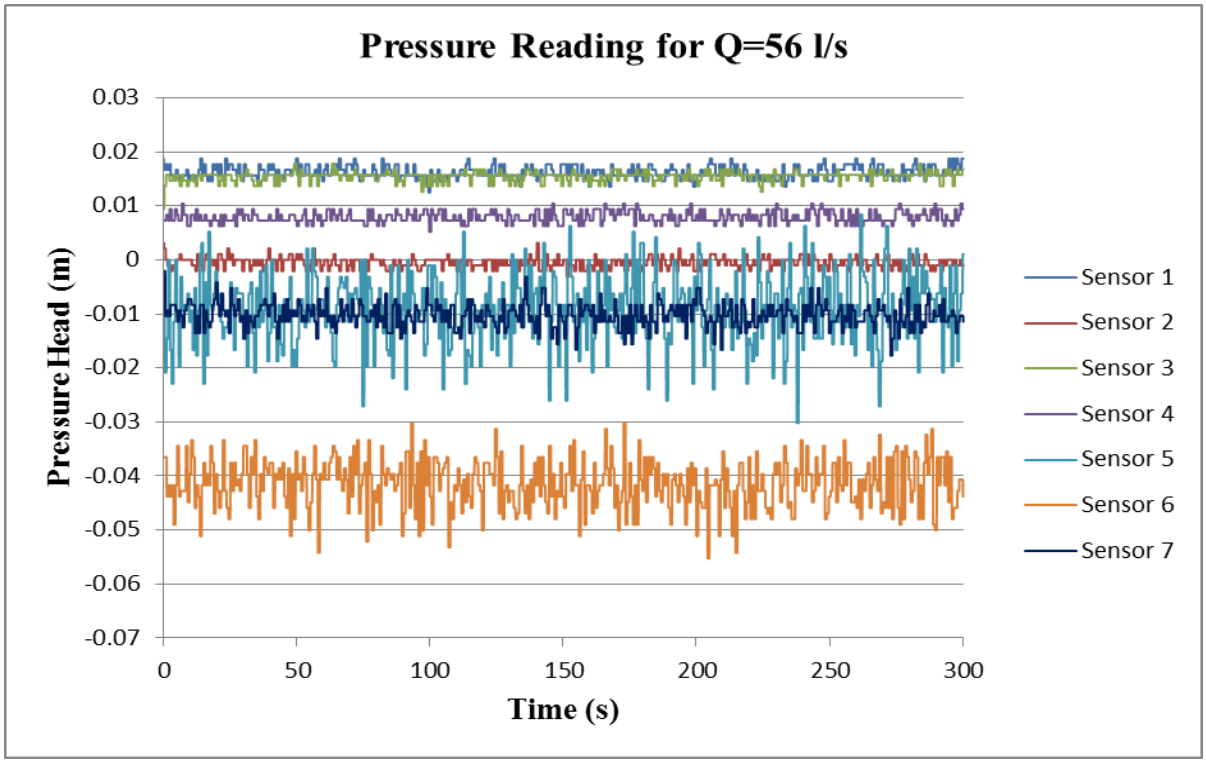

Figure A- 5: Pressure results for 56 l/s: case - 1

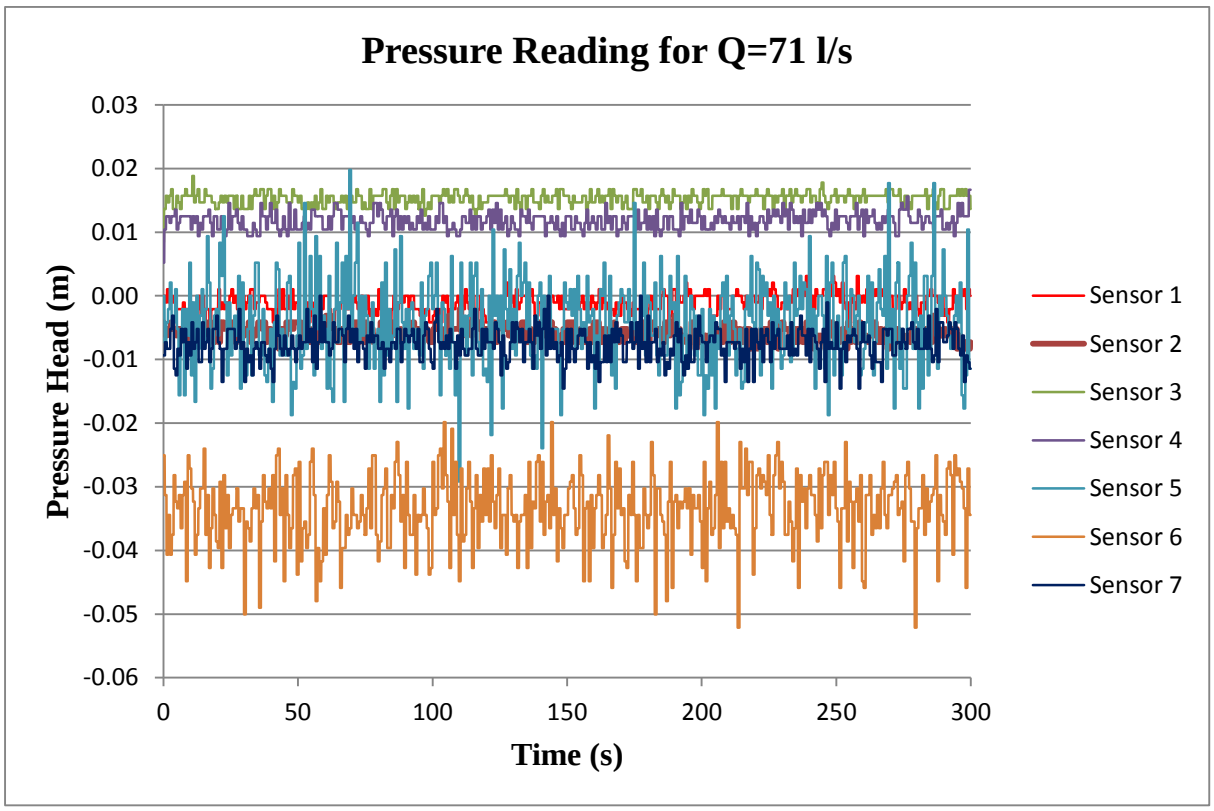

Figure A- 6: Pressure results for 71 l/s: case – 1

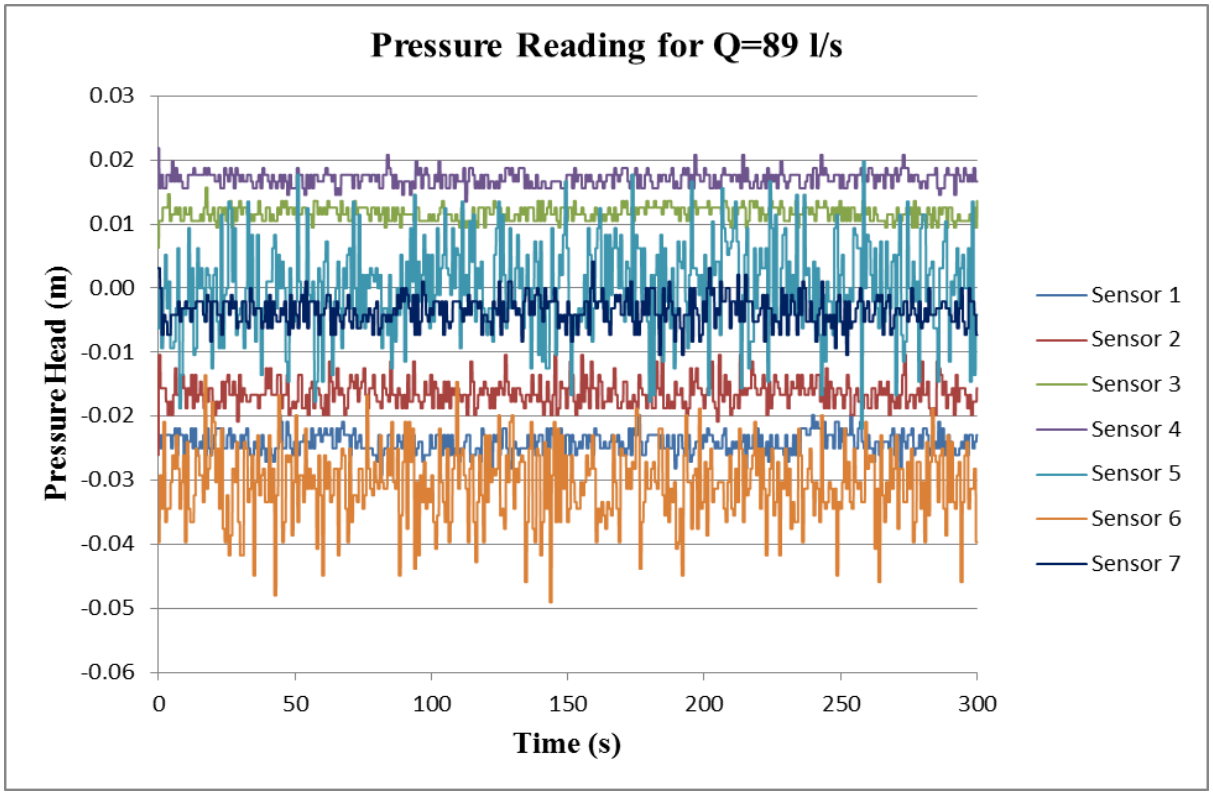

Figure A- 7: Pressure results for 89 l/s: case – 1

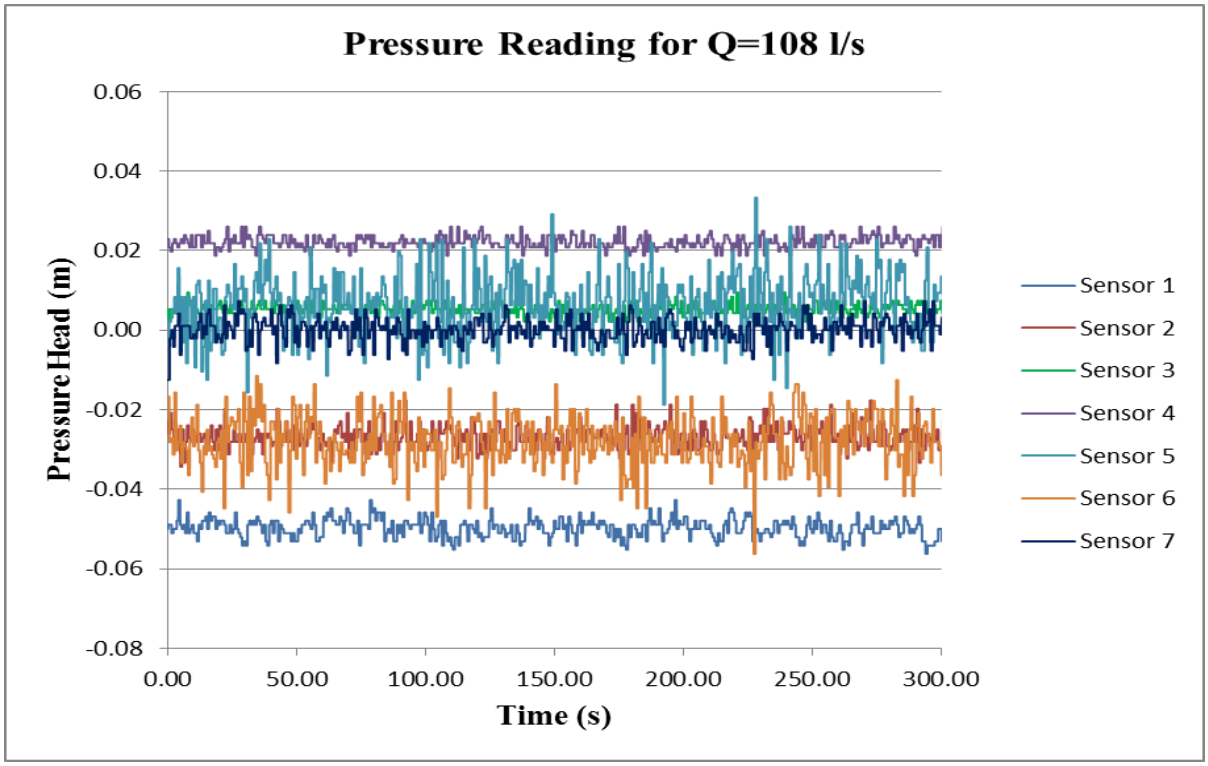

Figure A- 8: Pressure results for 108 l/s: case – 1

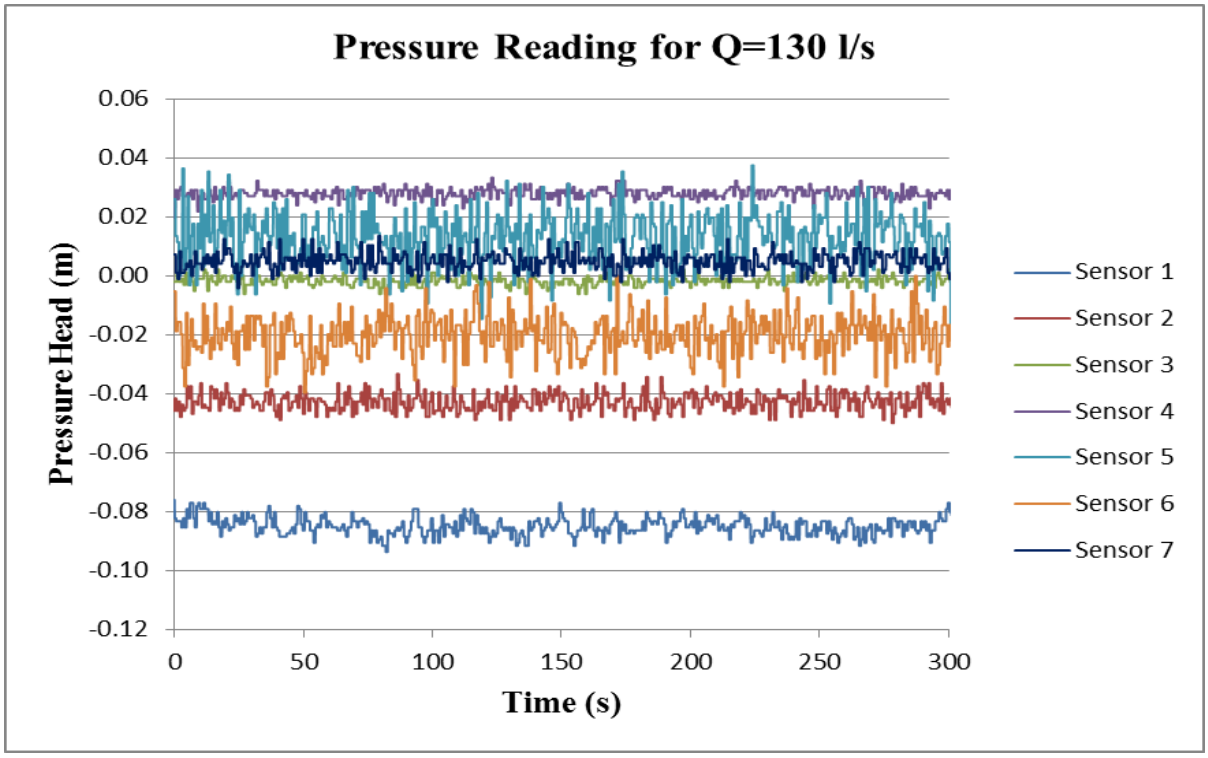

Figure A- 9: Pressure results for 130 l/s: case – 1

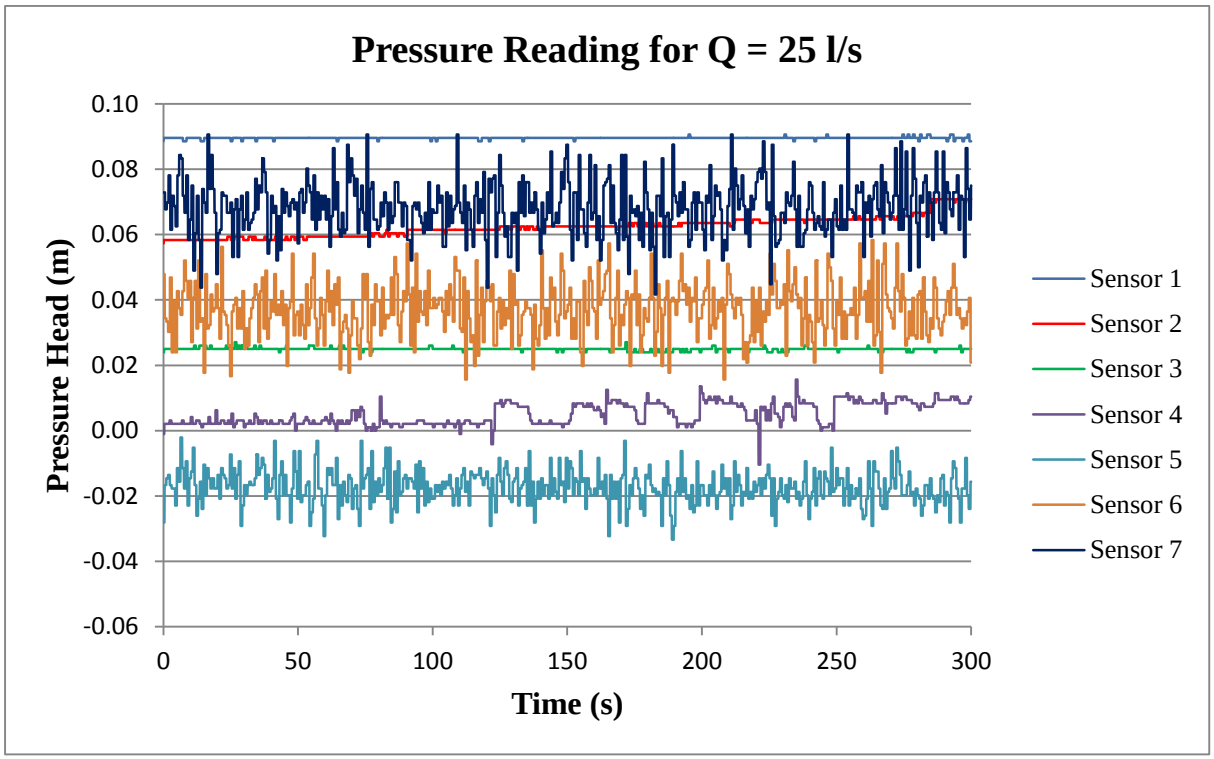

Figure A- 10: Pressure results for 25 l/s: case – 2

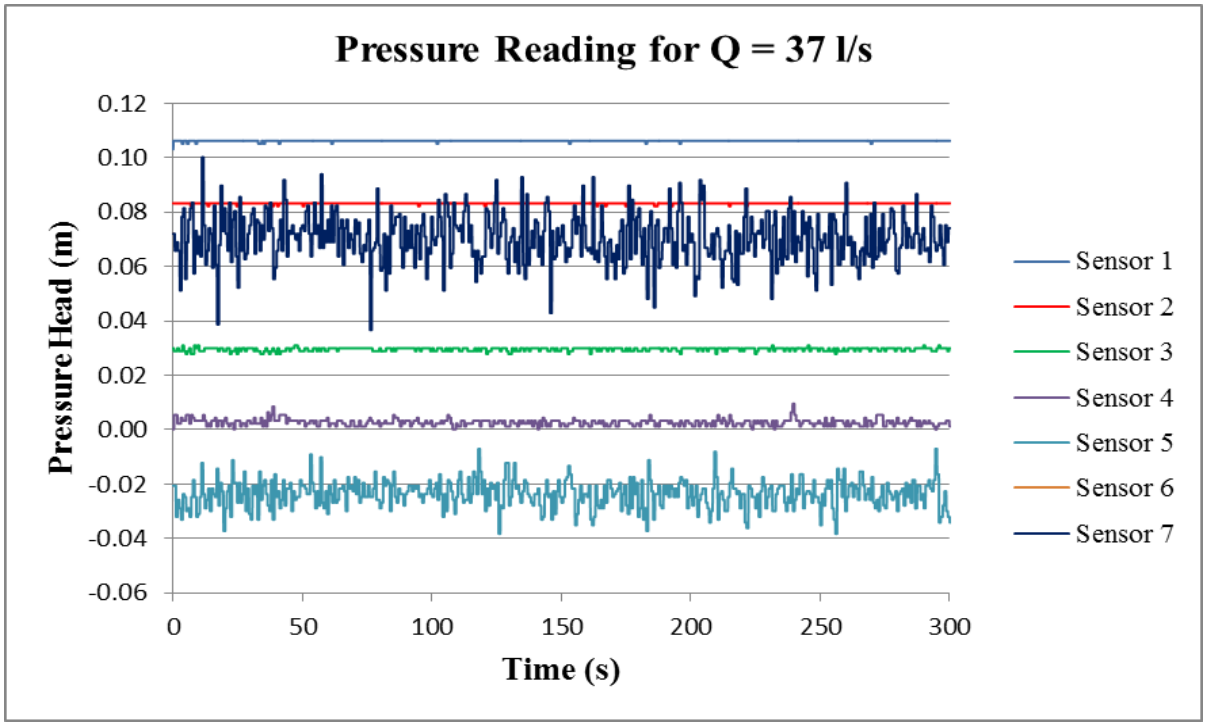

Figure A- 11: Pressure results for 37 l/s: case – 2

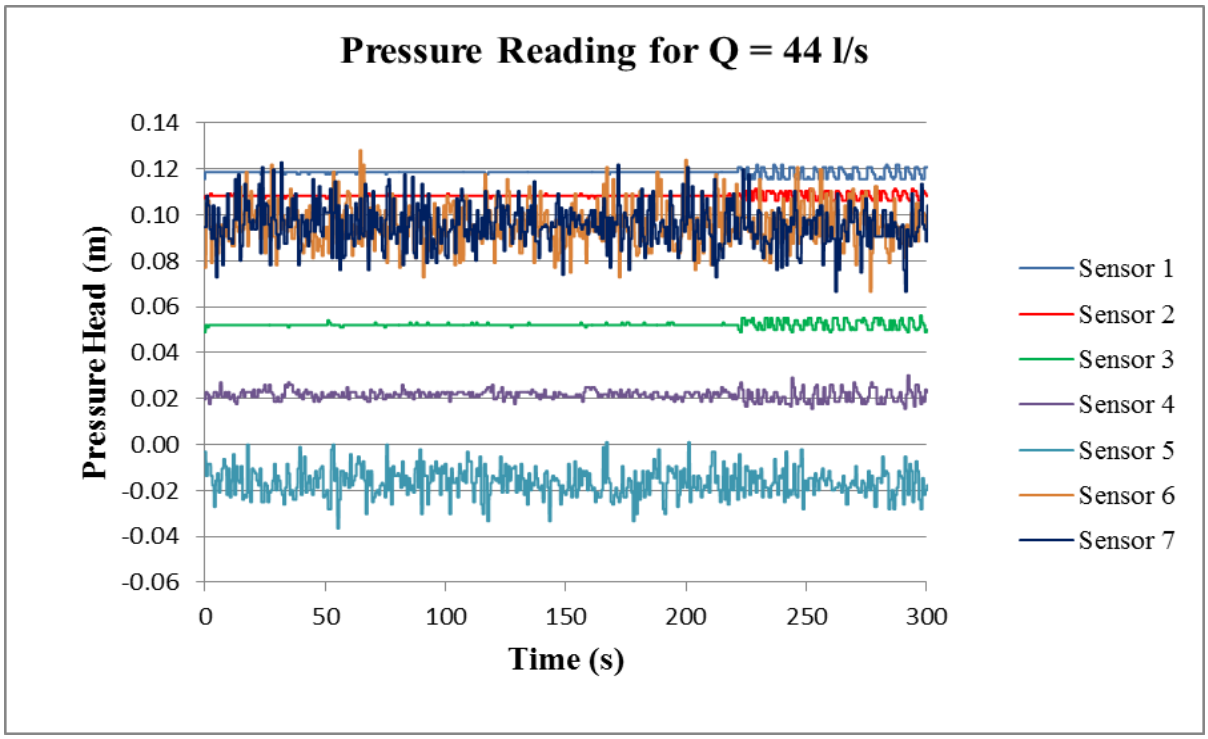

Figure A- 12: Pressure results for 44 l/s: case – 2

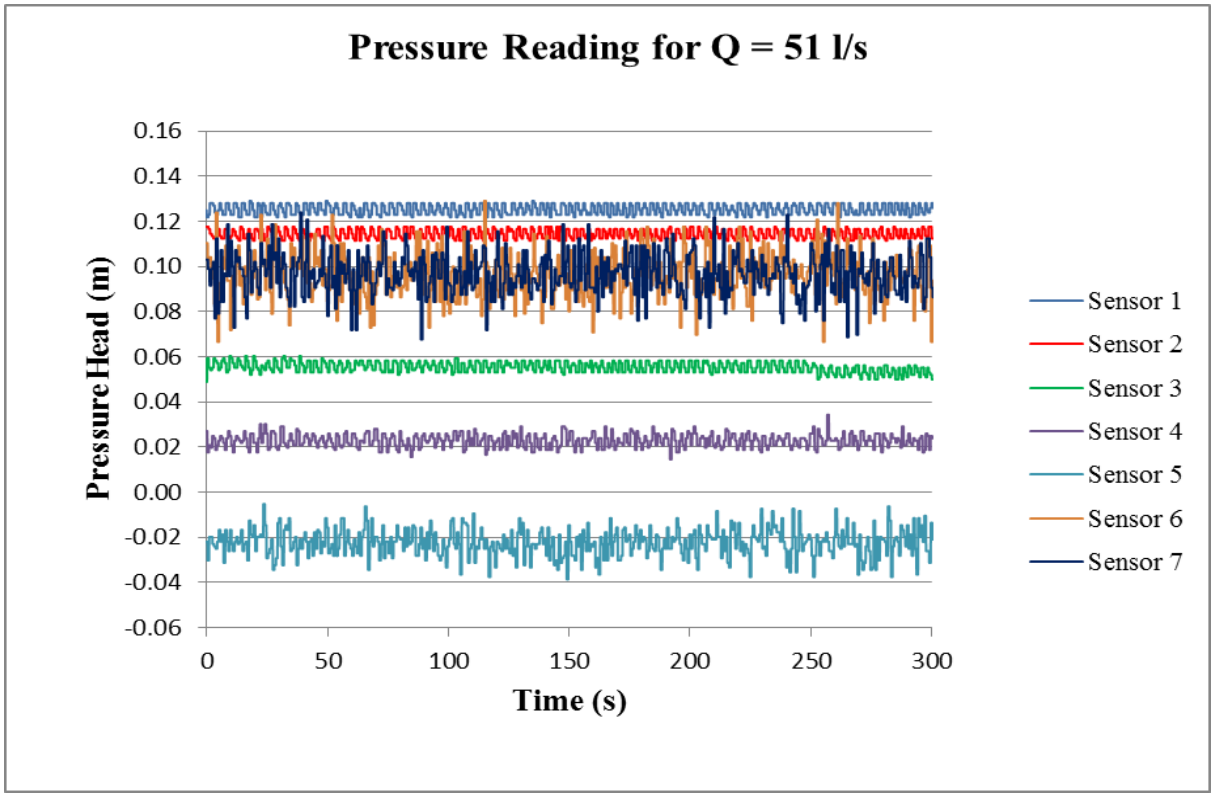

Figure A- 13: Pressure results for 51 l/s: case – 2

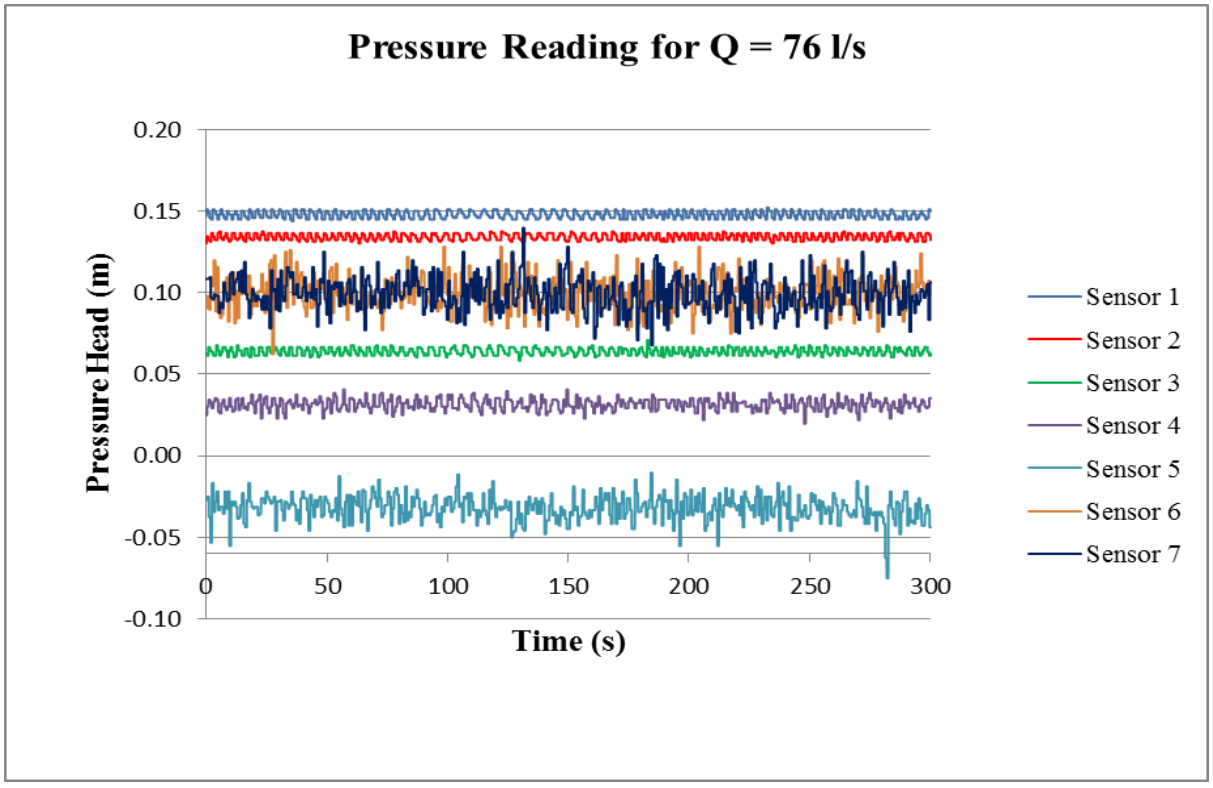

Figure A- 14: Pressure results for 76 l/s: case – 2

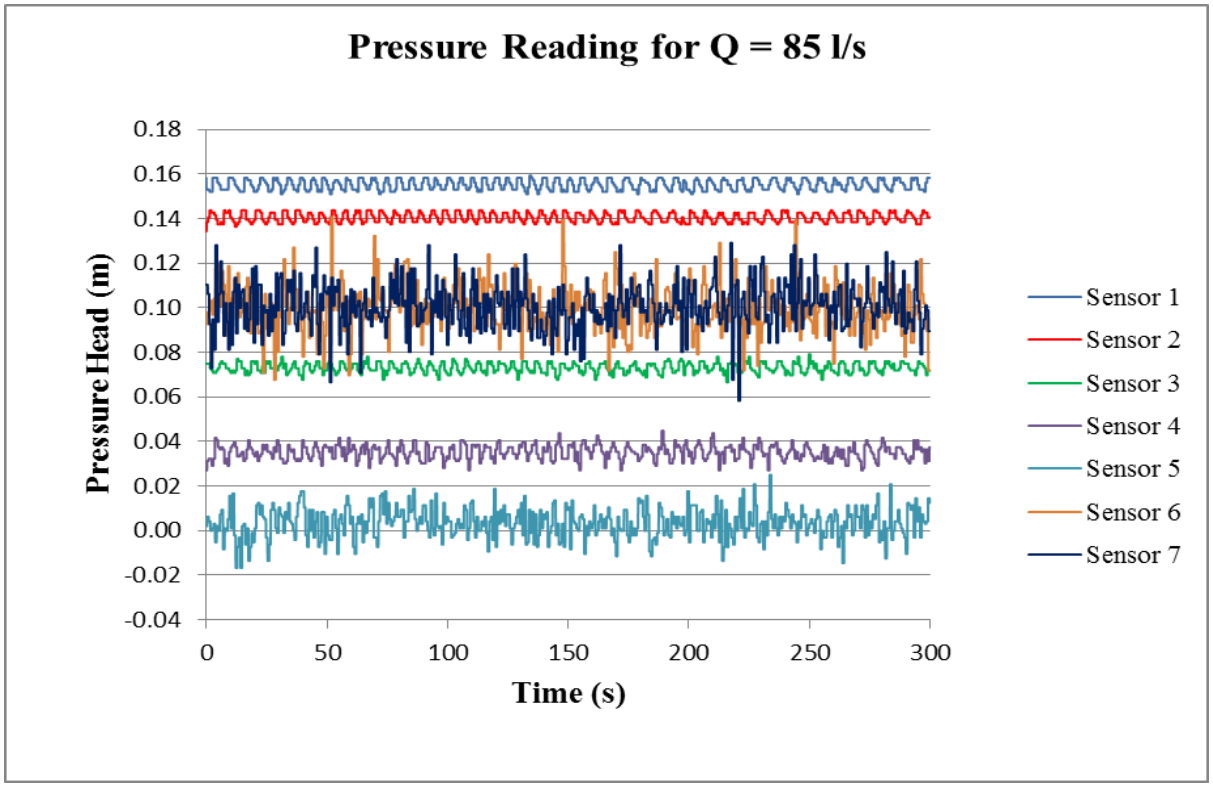

Figure A- 15: Pressure results for 85 l/s: case – 2

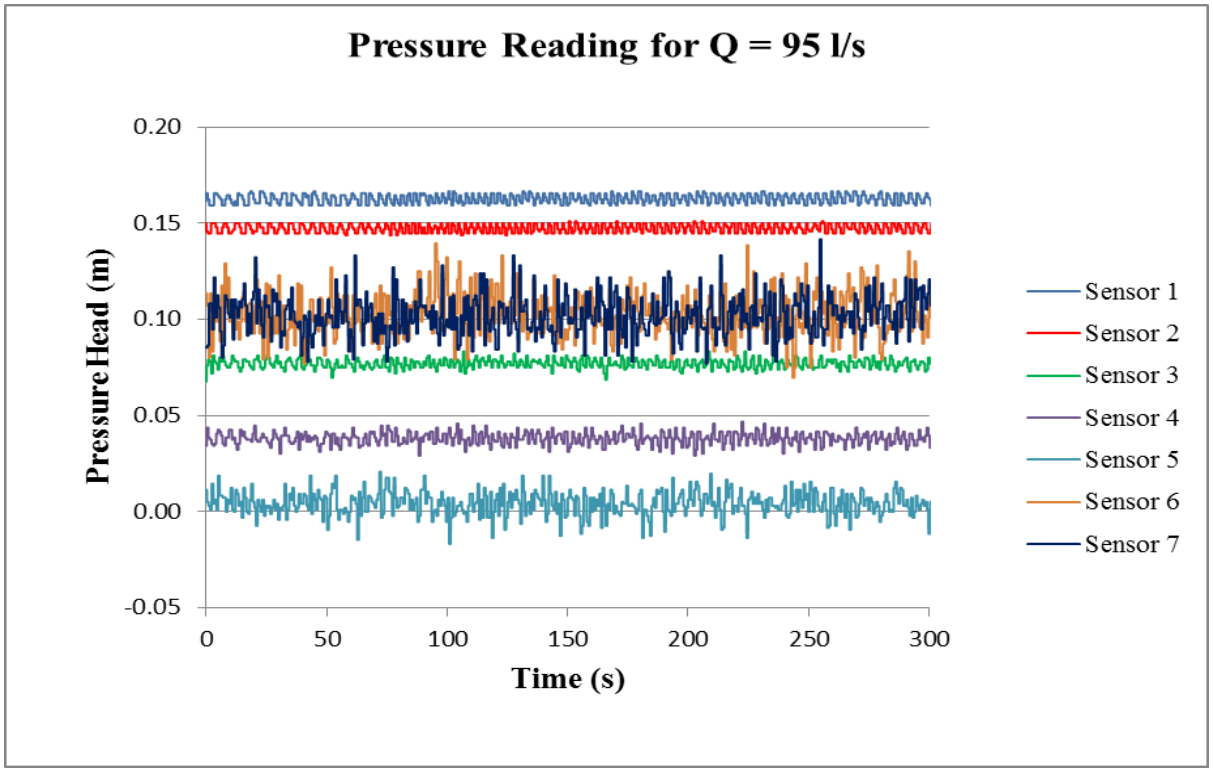

Figure A- 16: Pressure results for 95 l/s: case – 2

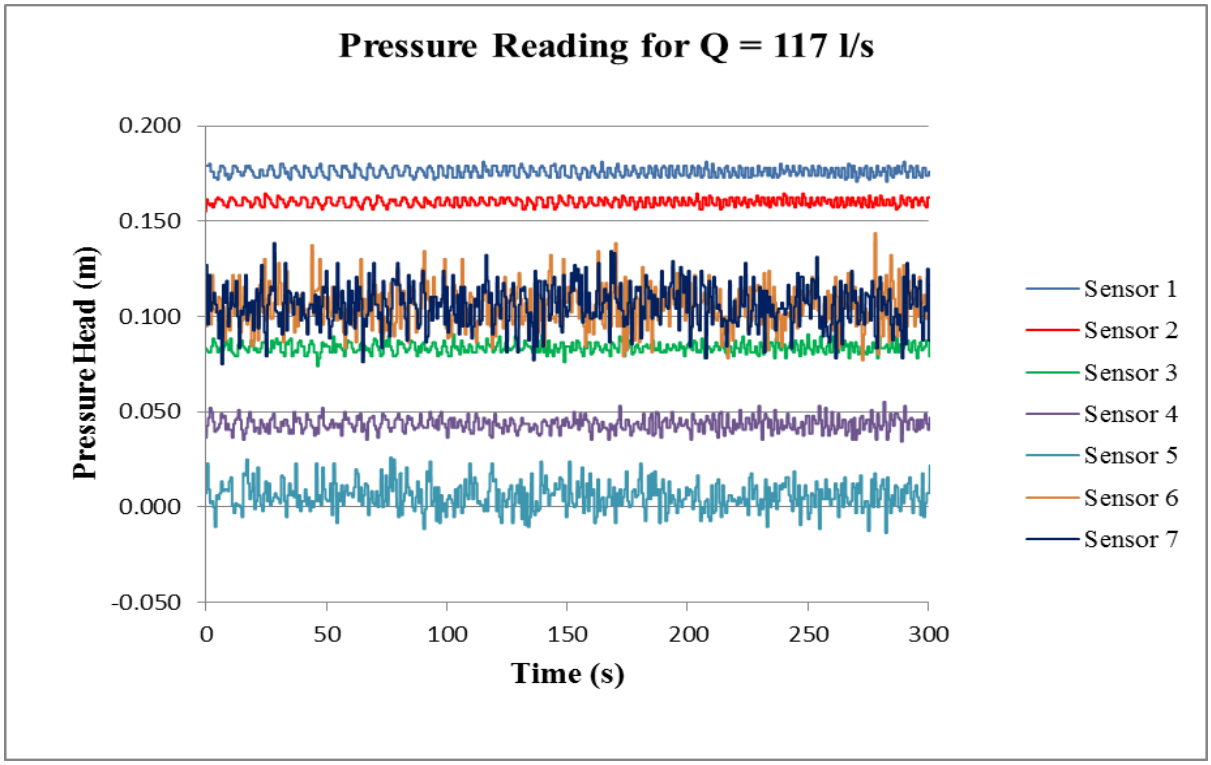

Figure A- 17: Pressure results for 117 l/s: case – 2

A.3. Water surcharge

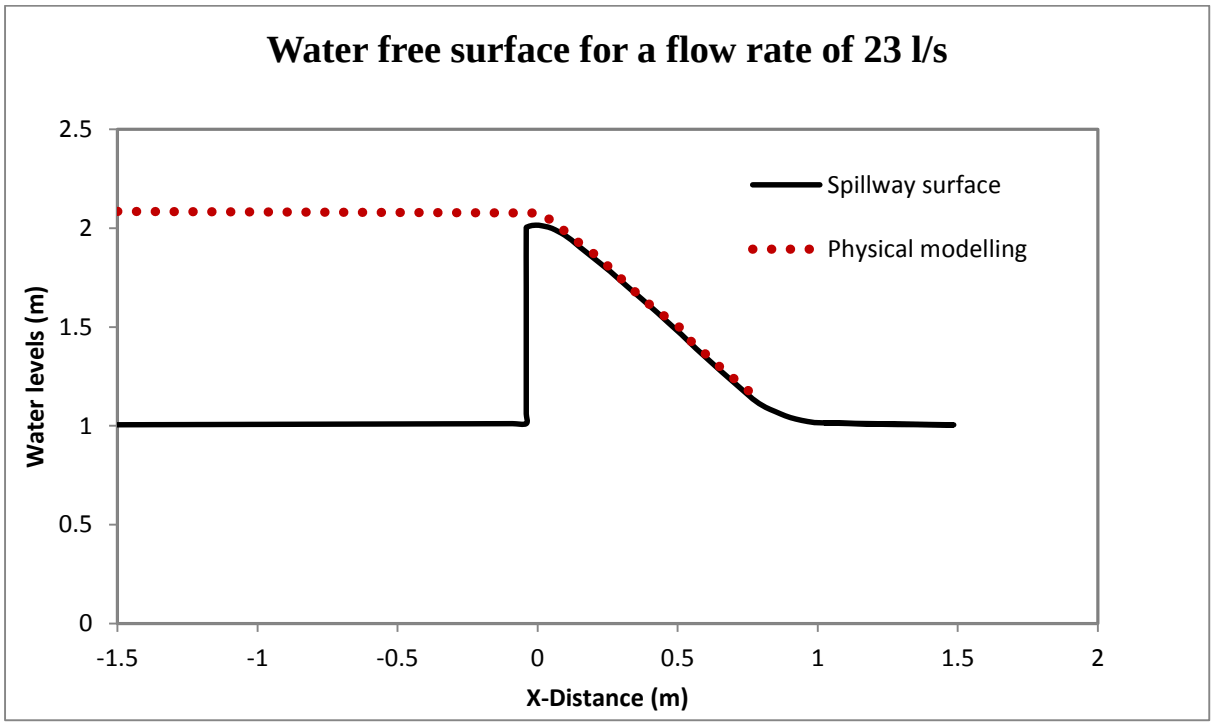

Figure A- 18: Water free surface over Case-1 for 23 l/s

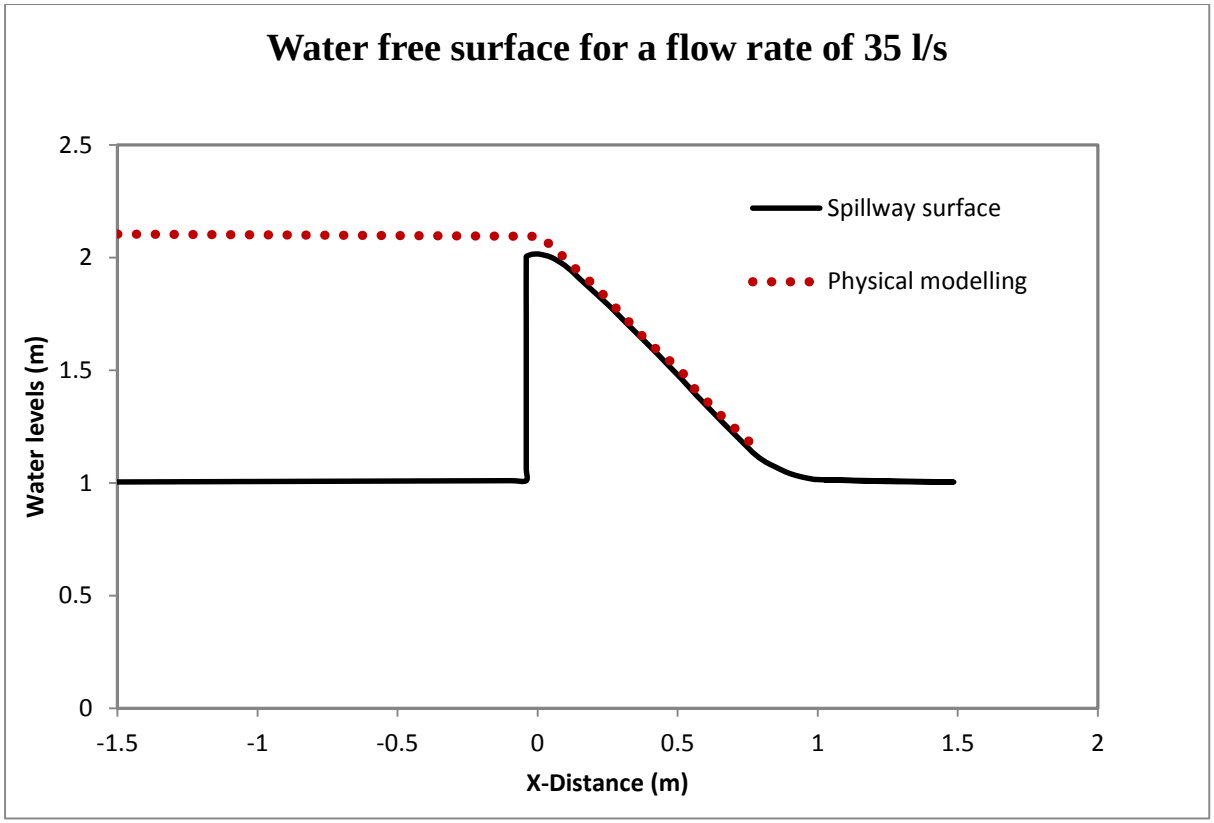

Figure A- 19: Water free surface over Case-1 spillway model for 35 l/s

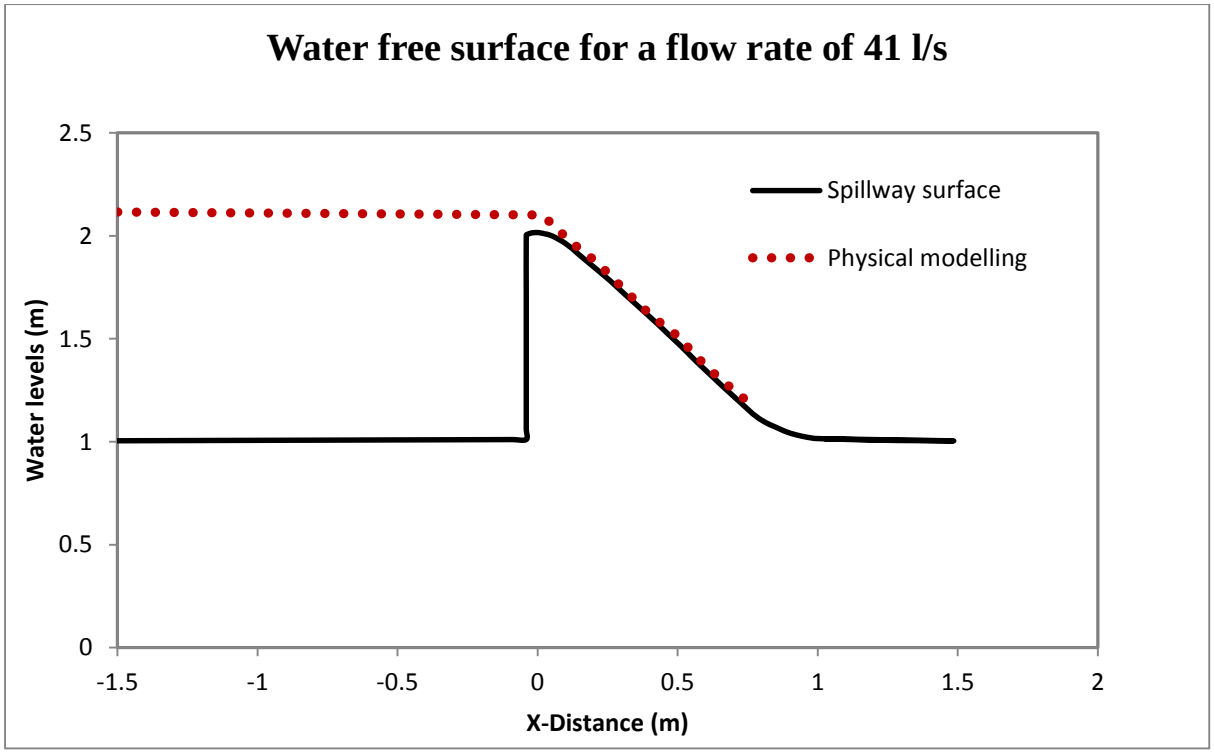

Figure A- 20: Water free surface over Case-1 spillway model for 41 l/s

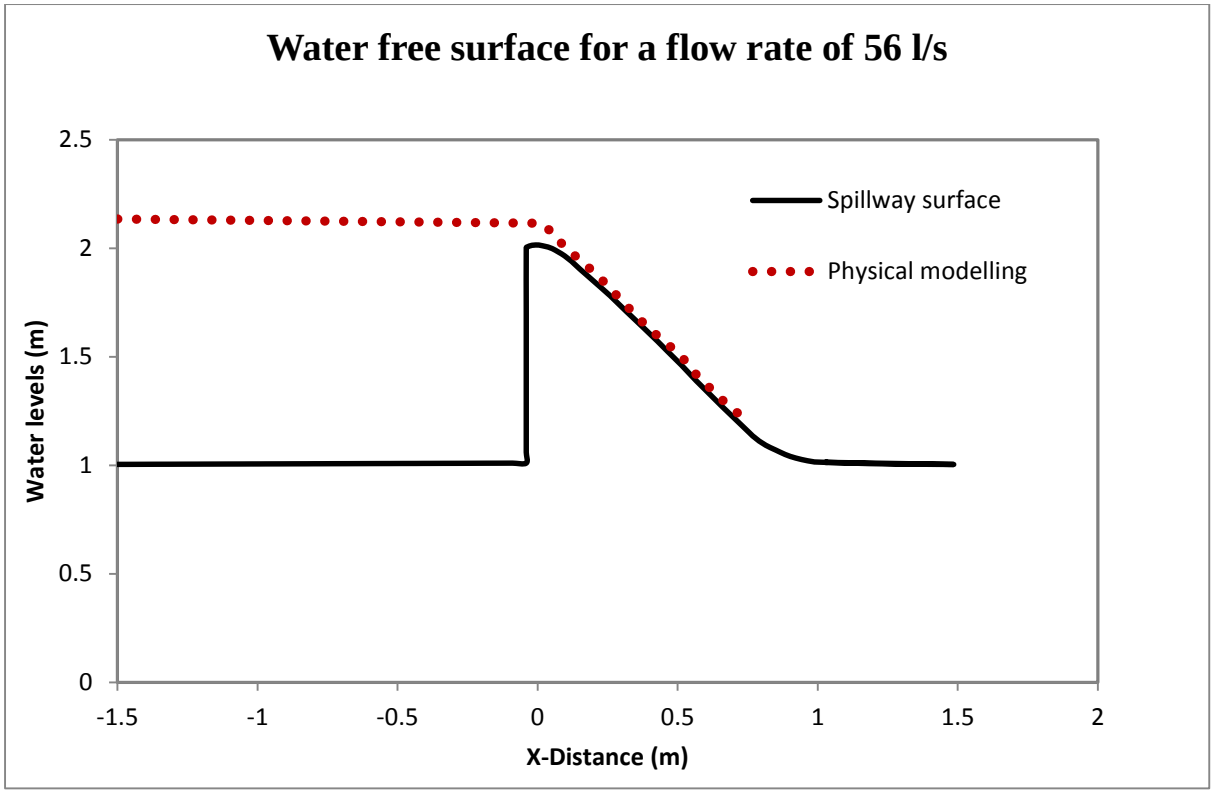

Figure A- 21: Water free surface over Case-1 spillway model for 56 l/s

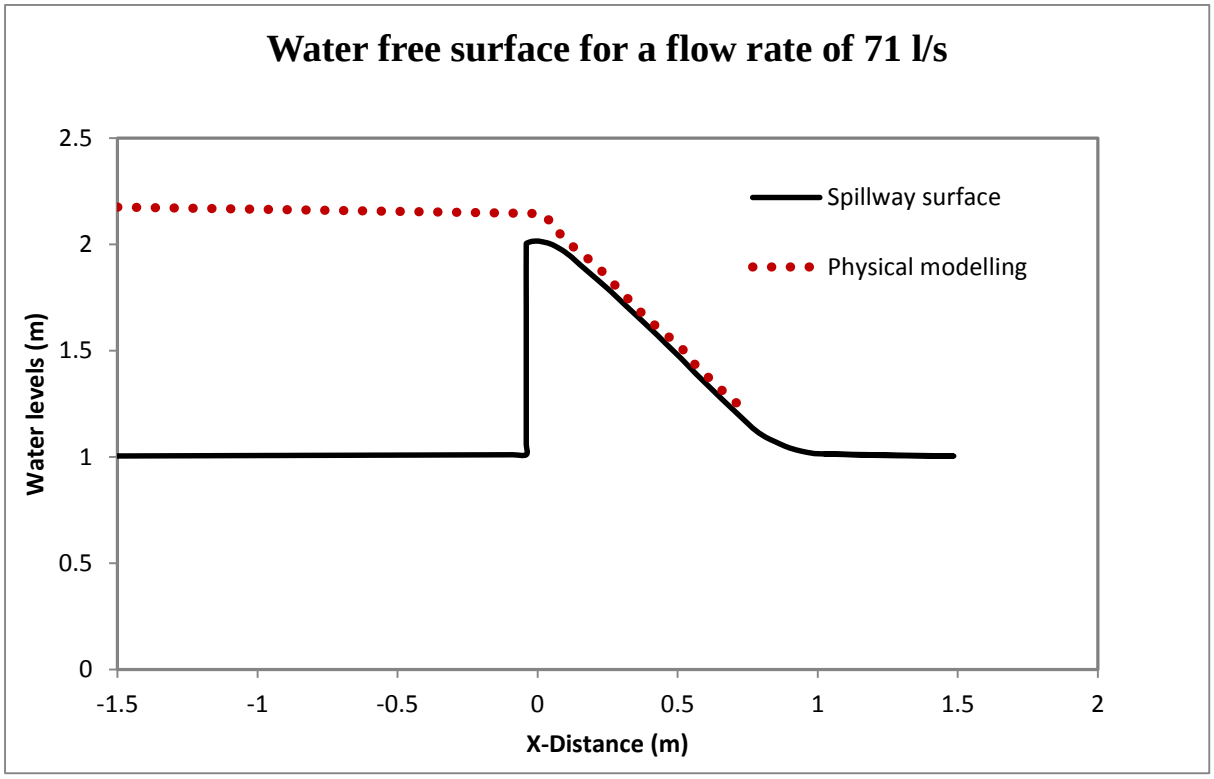

Figure A- 22: Water free surface over Case-1 spillway model for 71 l/s

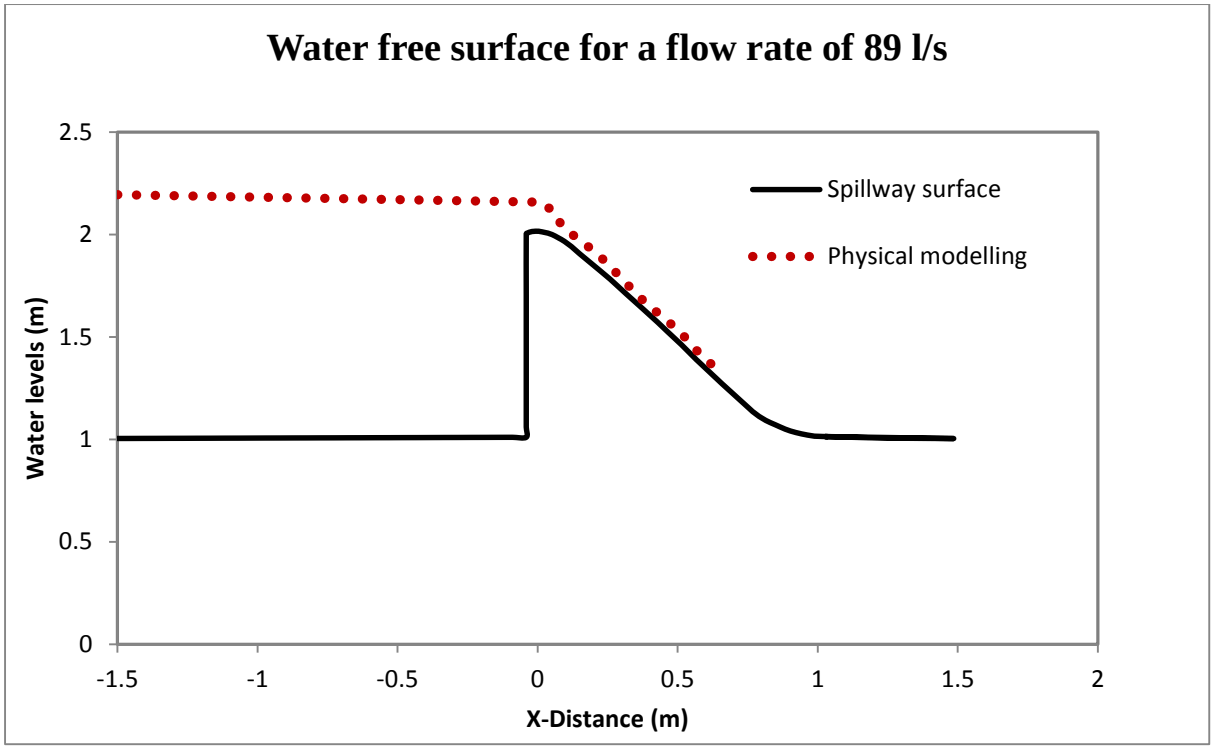

Figure A- 23: Water free surface over Case-1 spillway model for 89 l/s

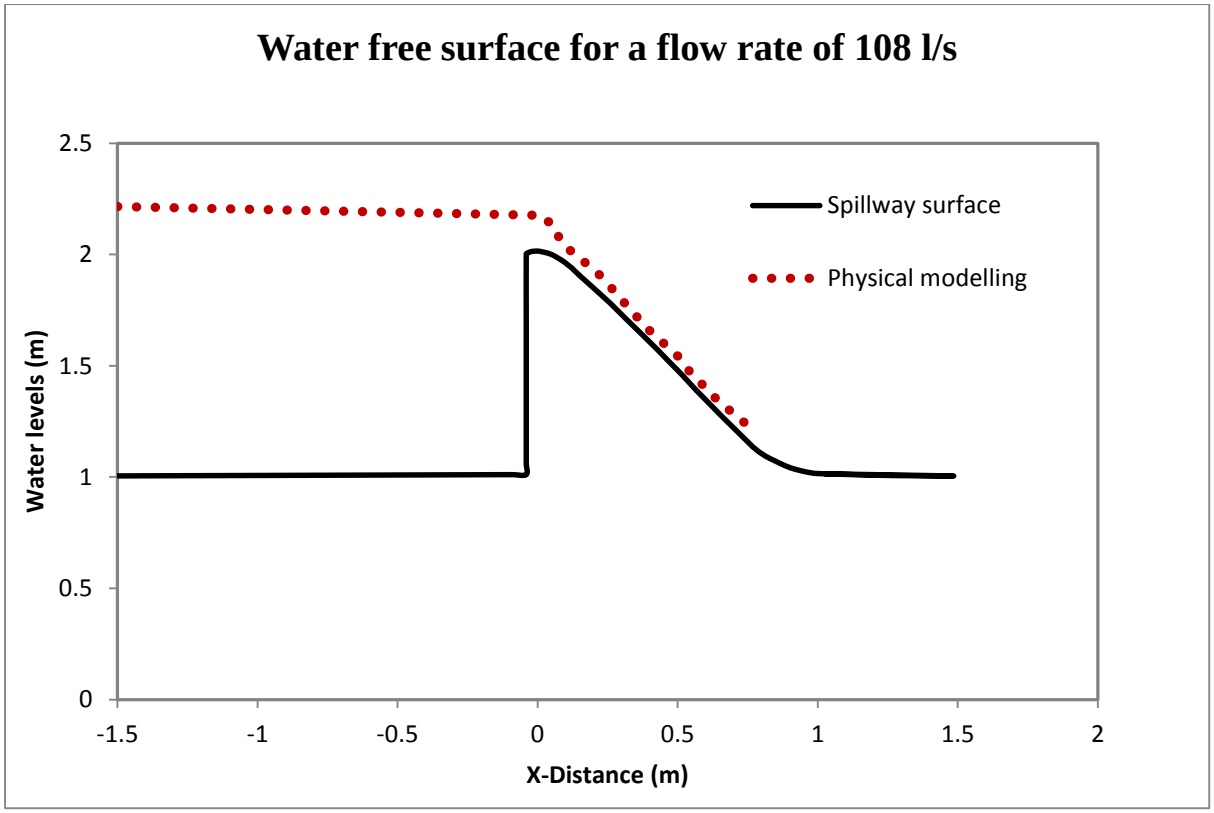

Figure A- 24: Water free surface over Case-1 spillway model for 108 l/s

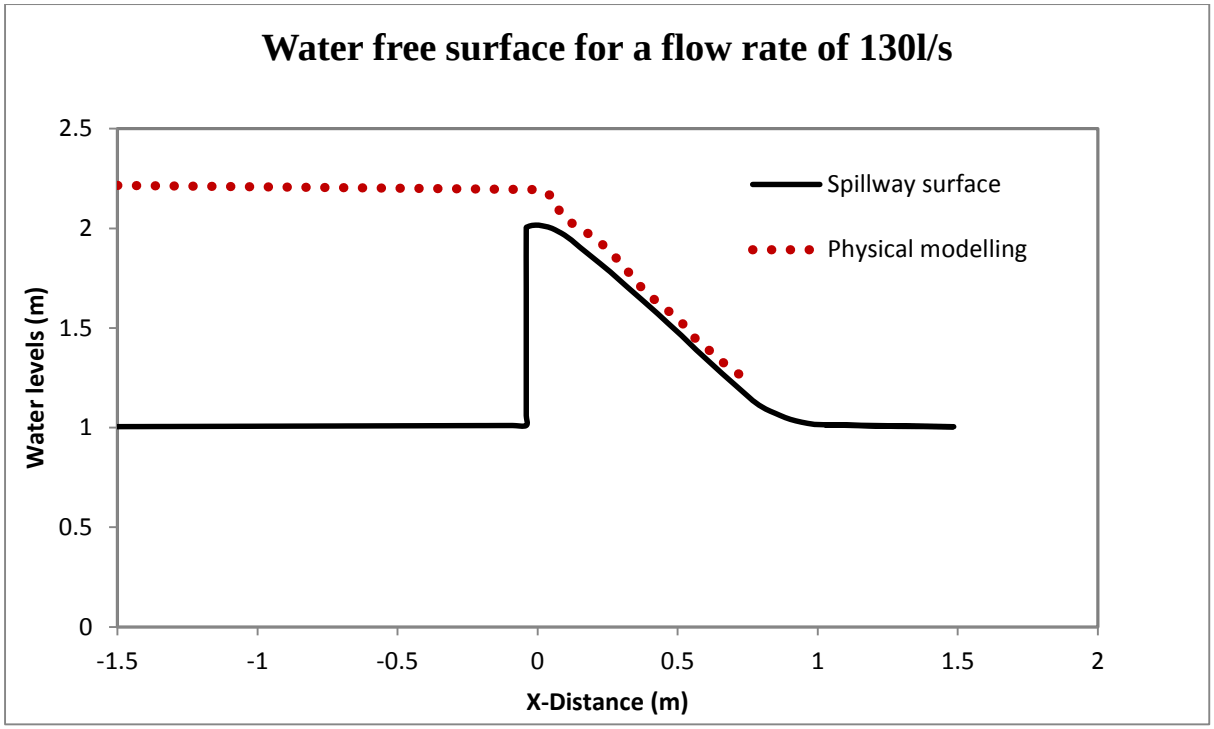

Figure A- 25: Water free surface over Case-1 spillway model for 130 l/s

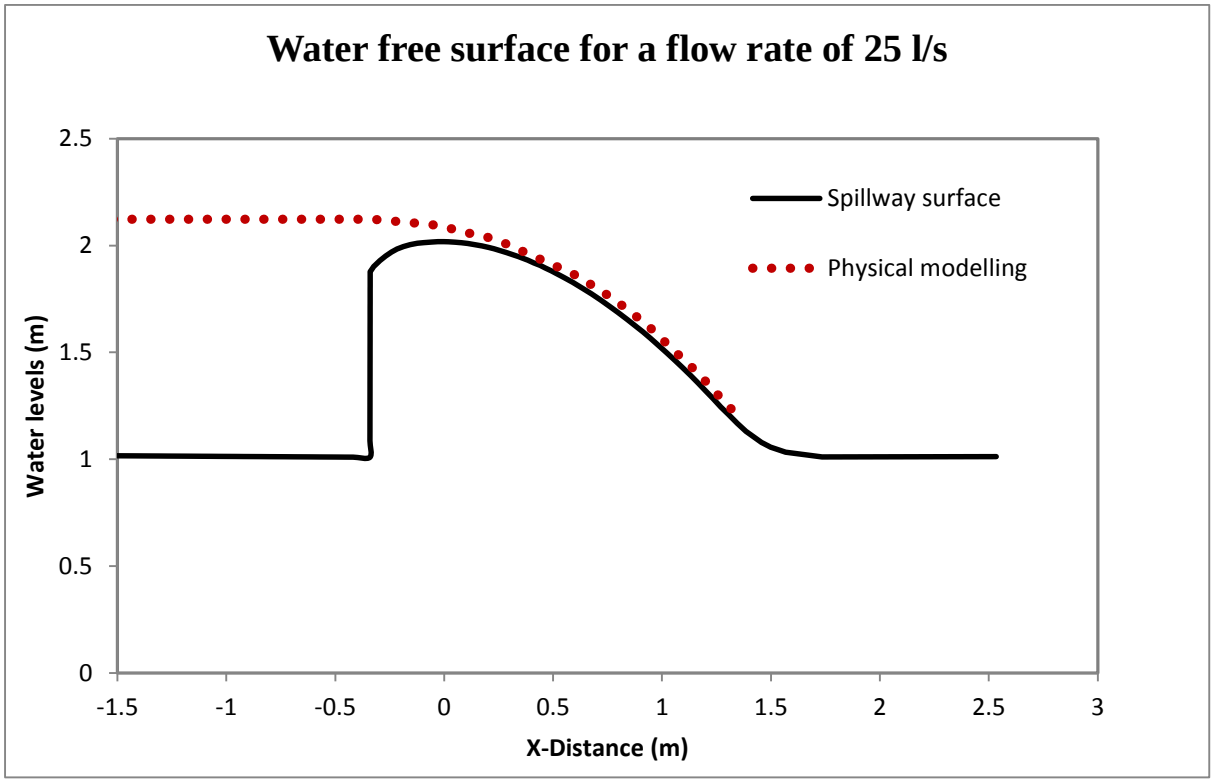

Figure A- 26: Water free surface over Case-2 spillway model for 23 l/s

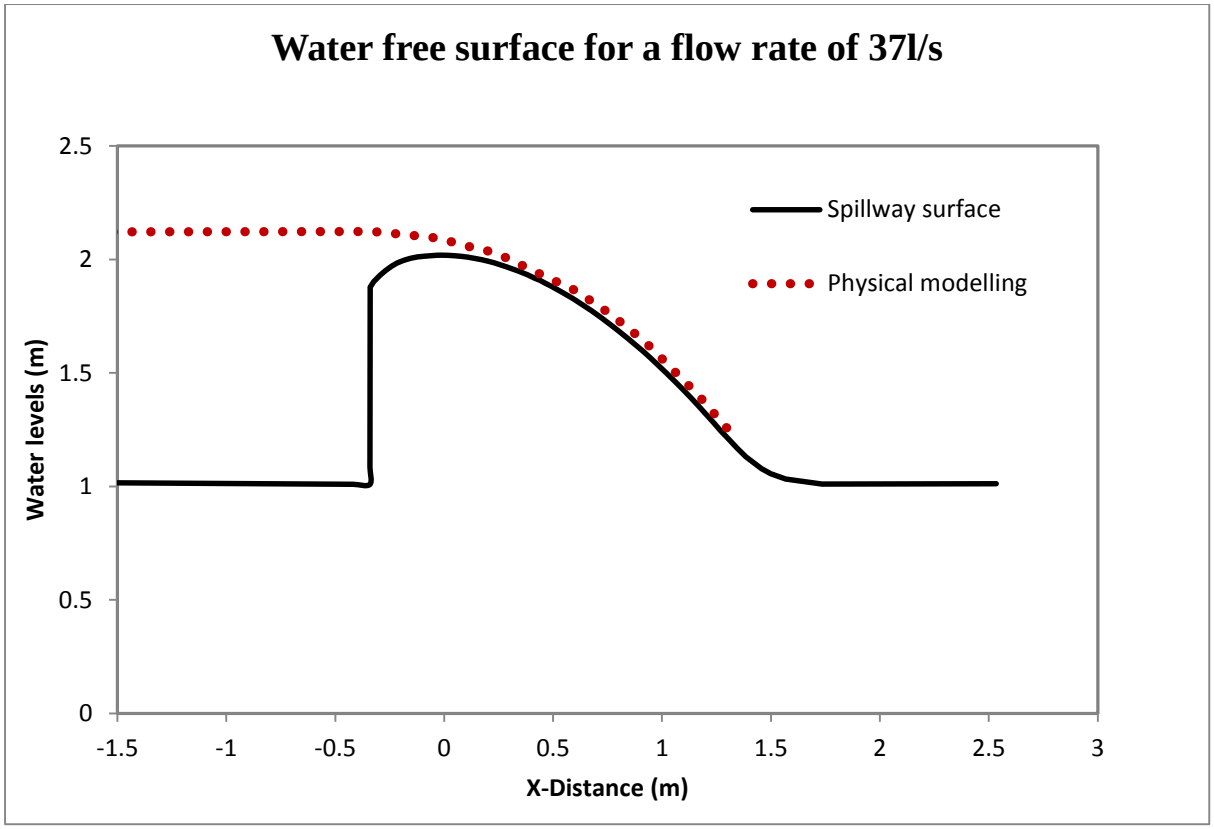

Figure A- 27: Water free surface over Case-2 spillway model for 37 l/s

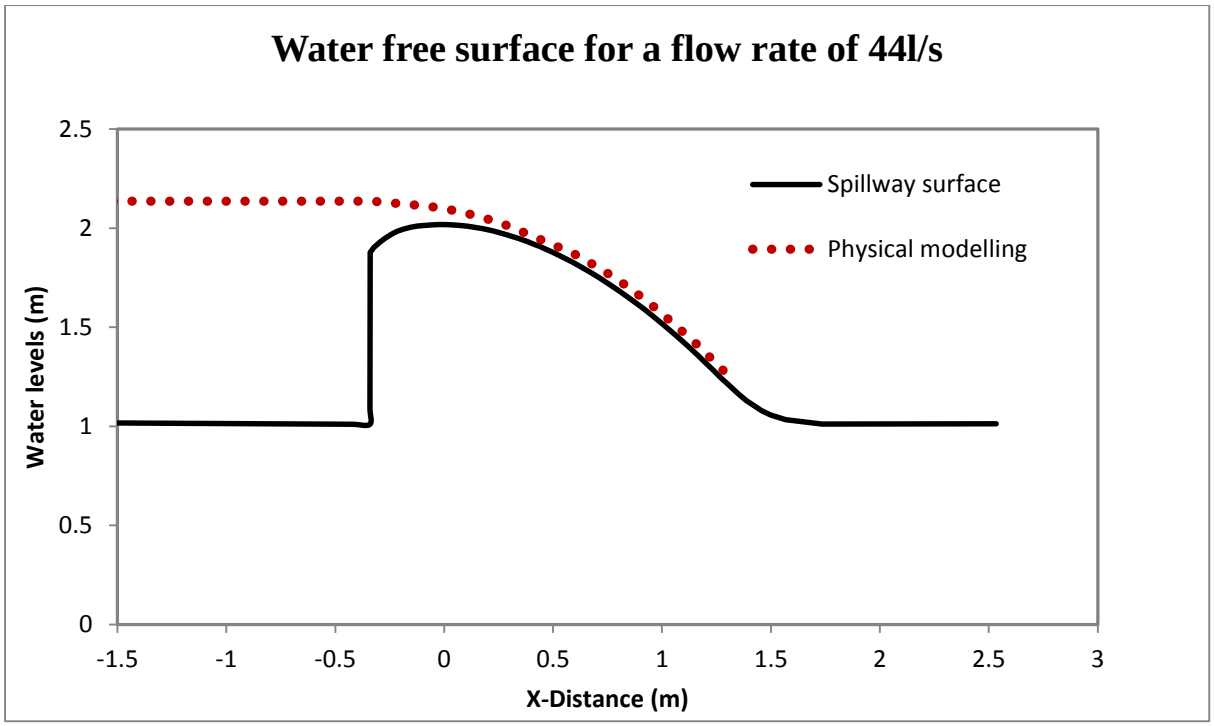

Figure A- 28: Water free surface over Case-2 spillway model for 44 l/s

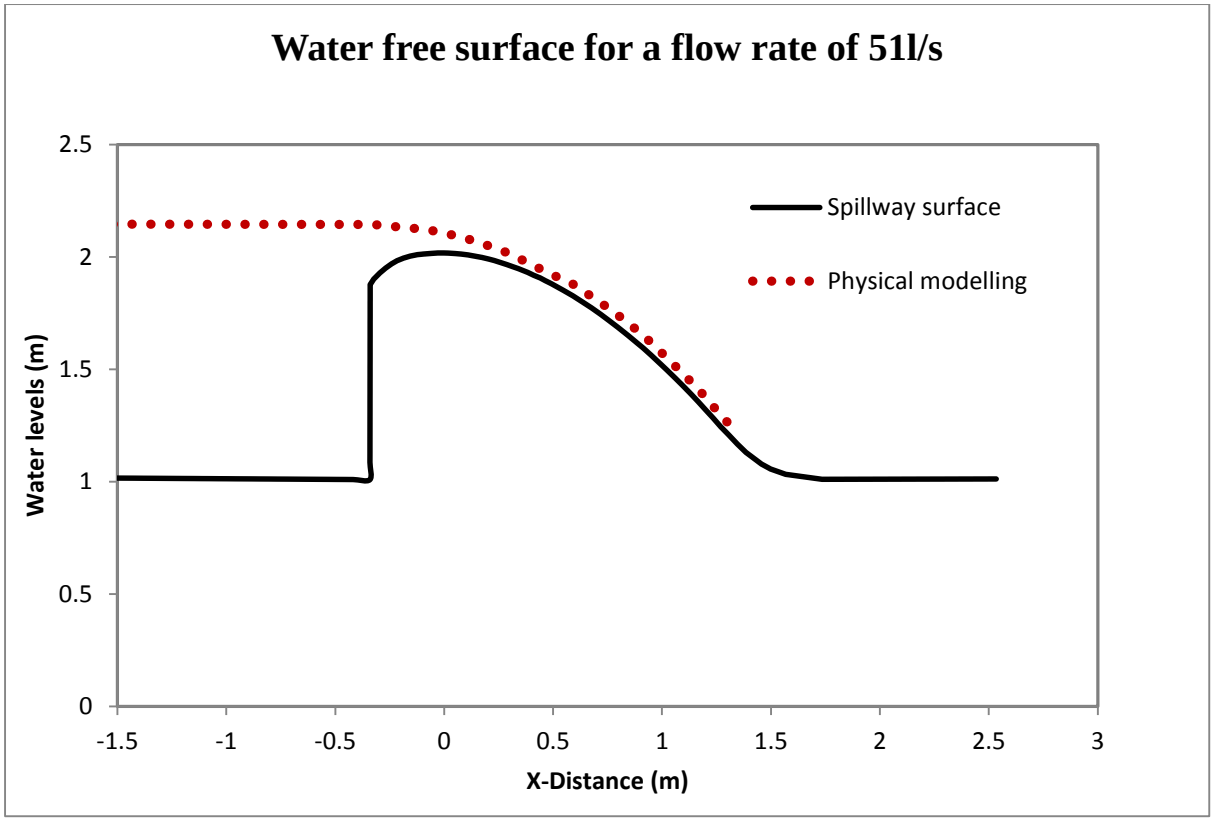

Figure A- 29: Water free surface over Case-2 spillway model for 51 l/s

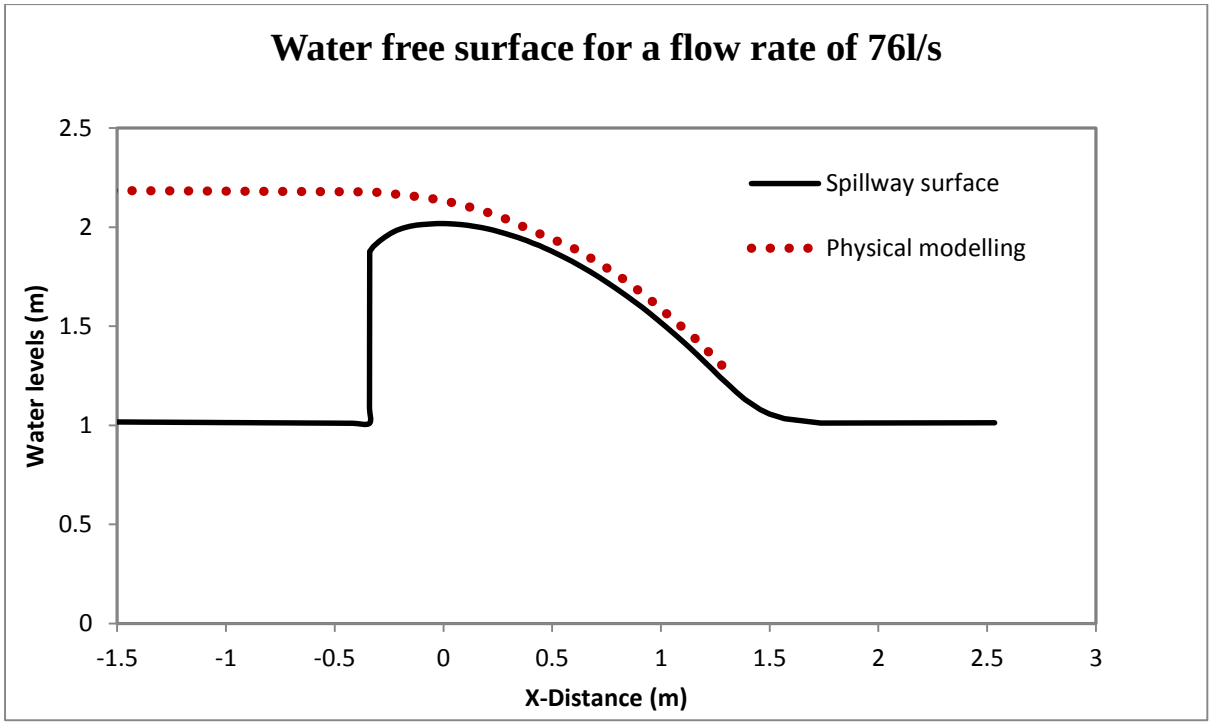

Figure A- 30: Water free surface over Case-2 spillway model for 76 l/s

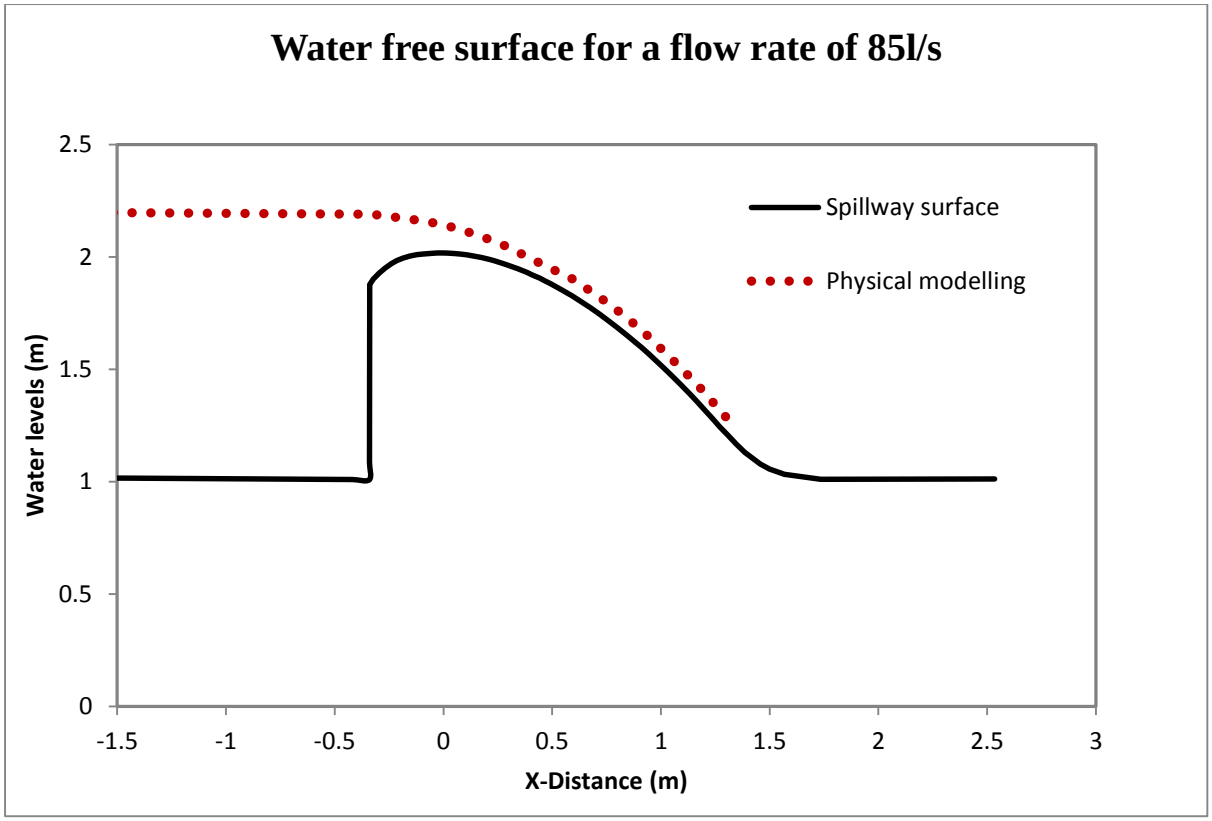

Figure A- 31: Water free surface over Case-2 spillway model for 85 l/s

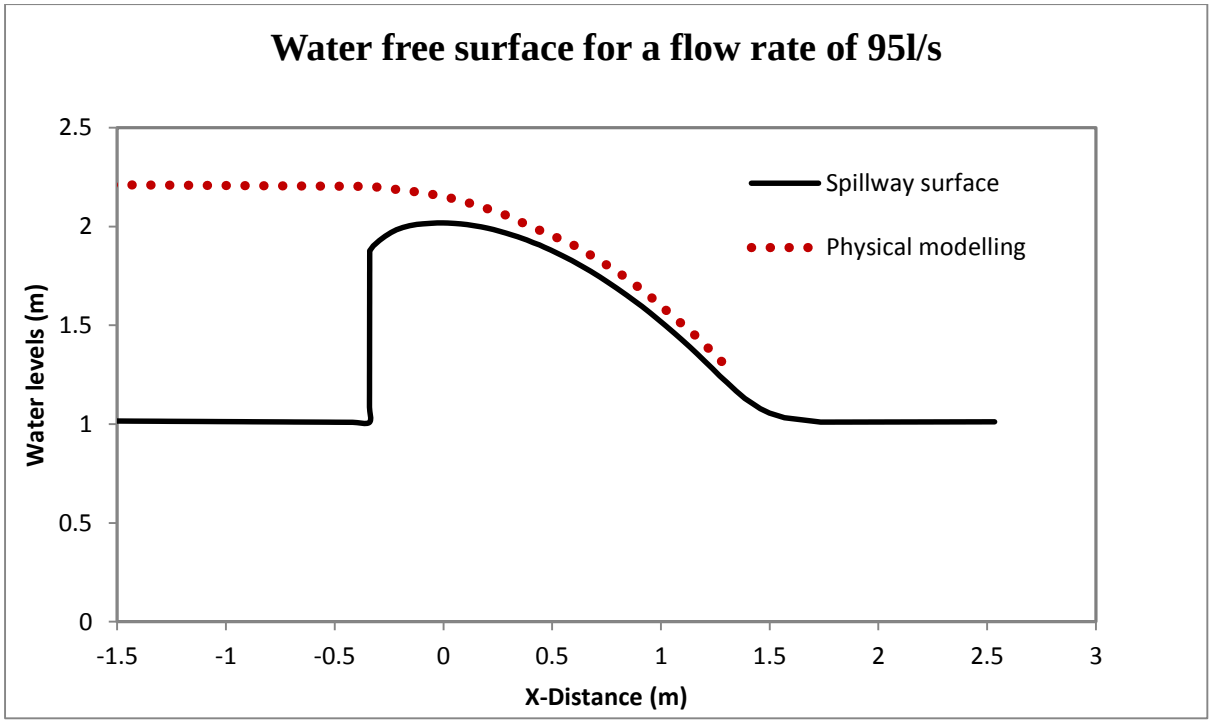

Figure A- 32: Water free surface over Case-2 spillway model for 95 l/s

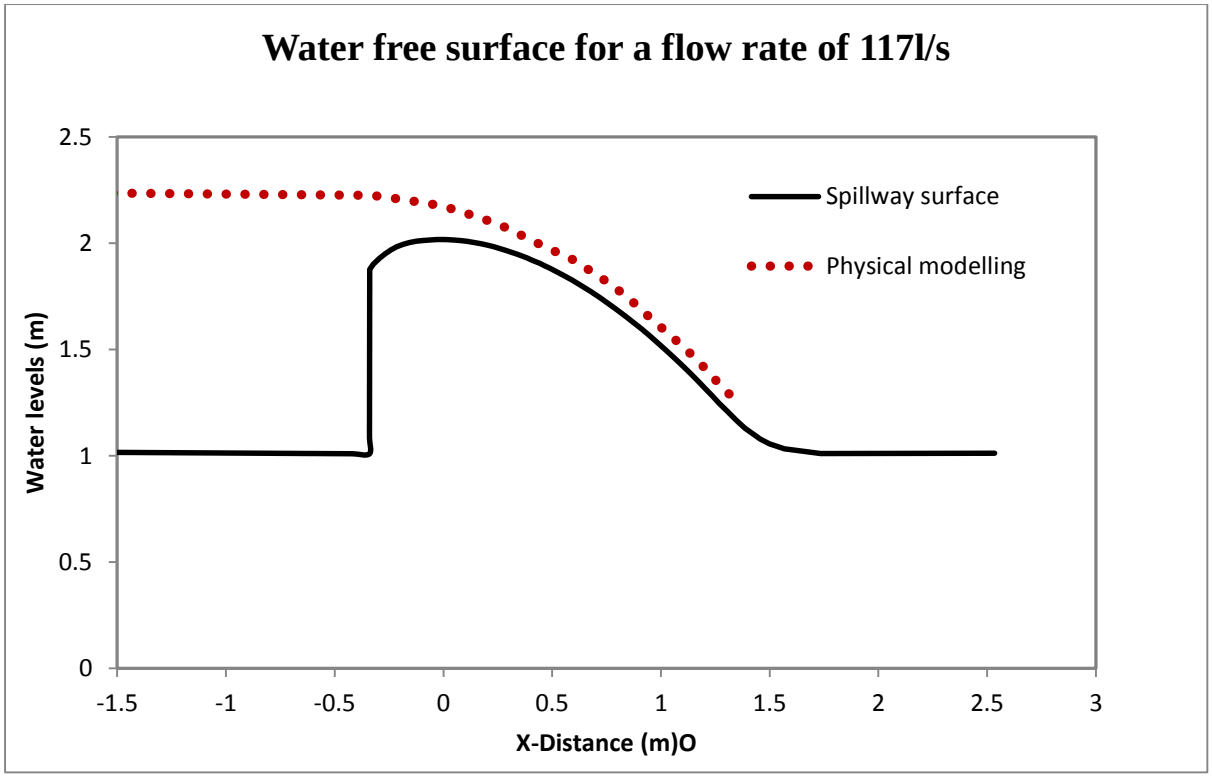

Figure A- 33: Water free surface over Case-2 spillway model for 117 l/s

Appendix B: Photographs of Physical Modelling

Figure B- 1: Physical model set up and instruments

Figure B- 2: Physical model (Case-1) viewed aside showing prexiglass windows and pressure sensor wiring

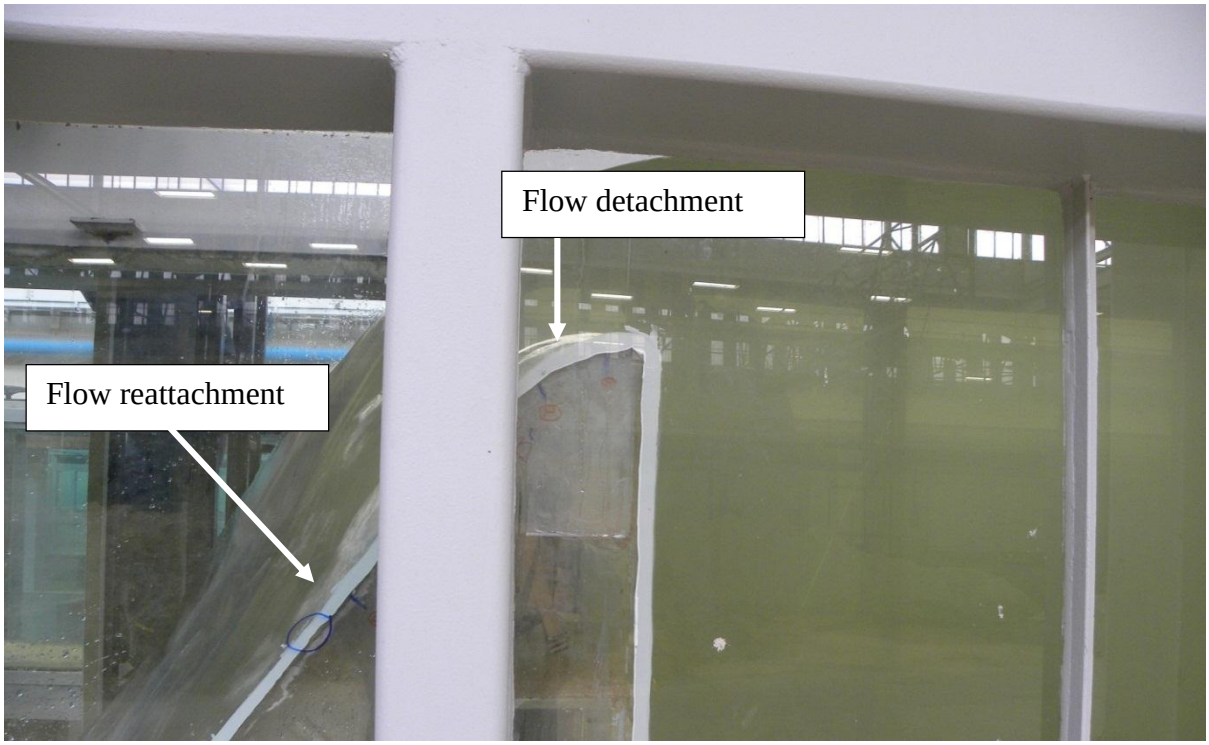

Figure B- 3: Flow detachment and reattachment on the spillway model (case-1)

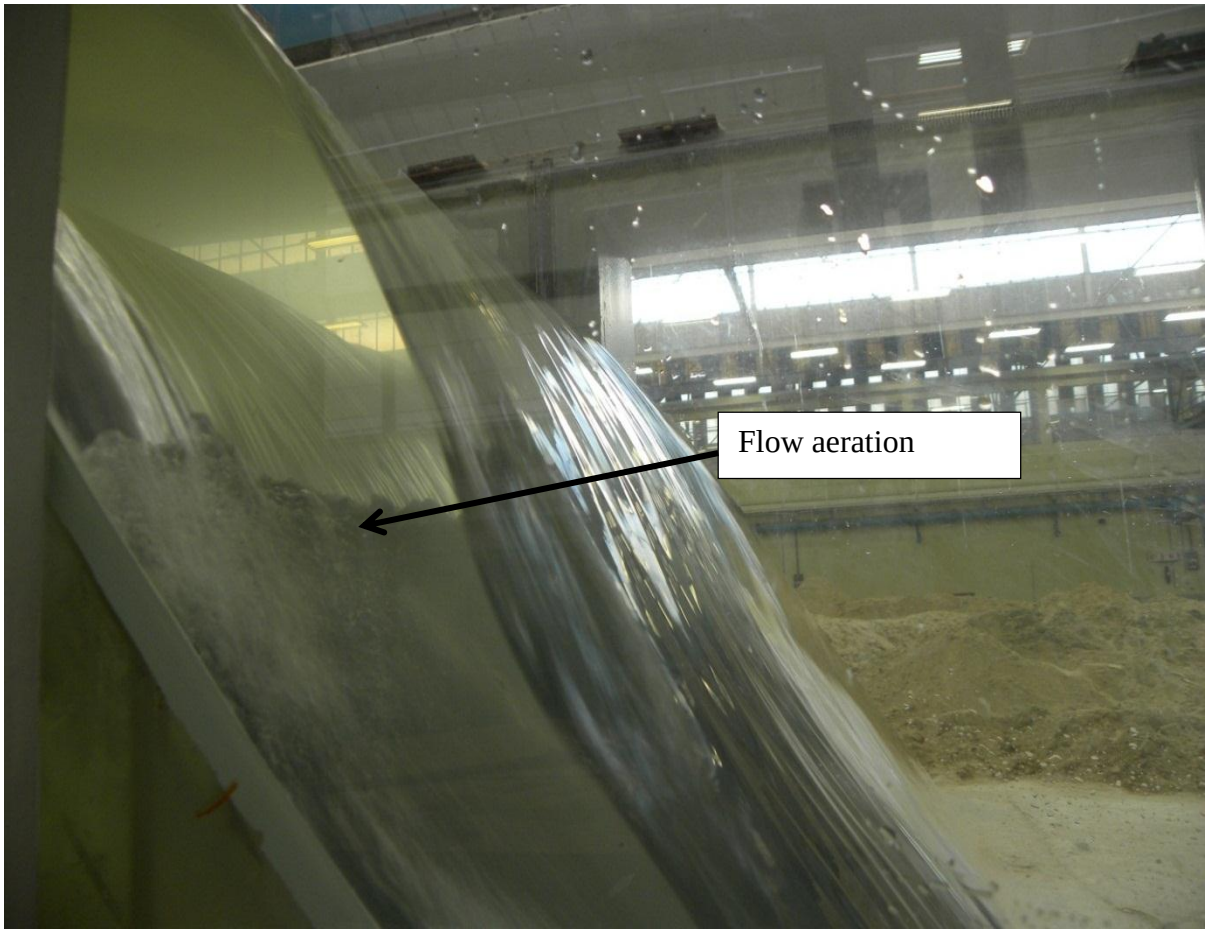

Figure B- 4: Ogee spillway model (Case-1) viewed from aside under high flow conditions, showing aeration patterns

Figure B- 5: Physical model (Case-2) viewed aside showing prexiglass windows and pressure sensor wiring

Figure B- 6: Water flowing over ogee spillway model (Case-2)

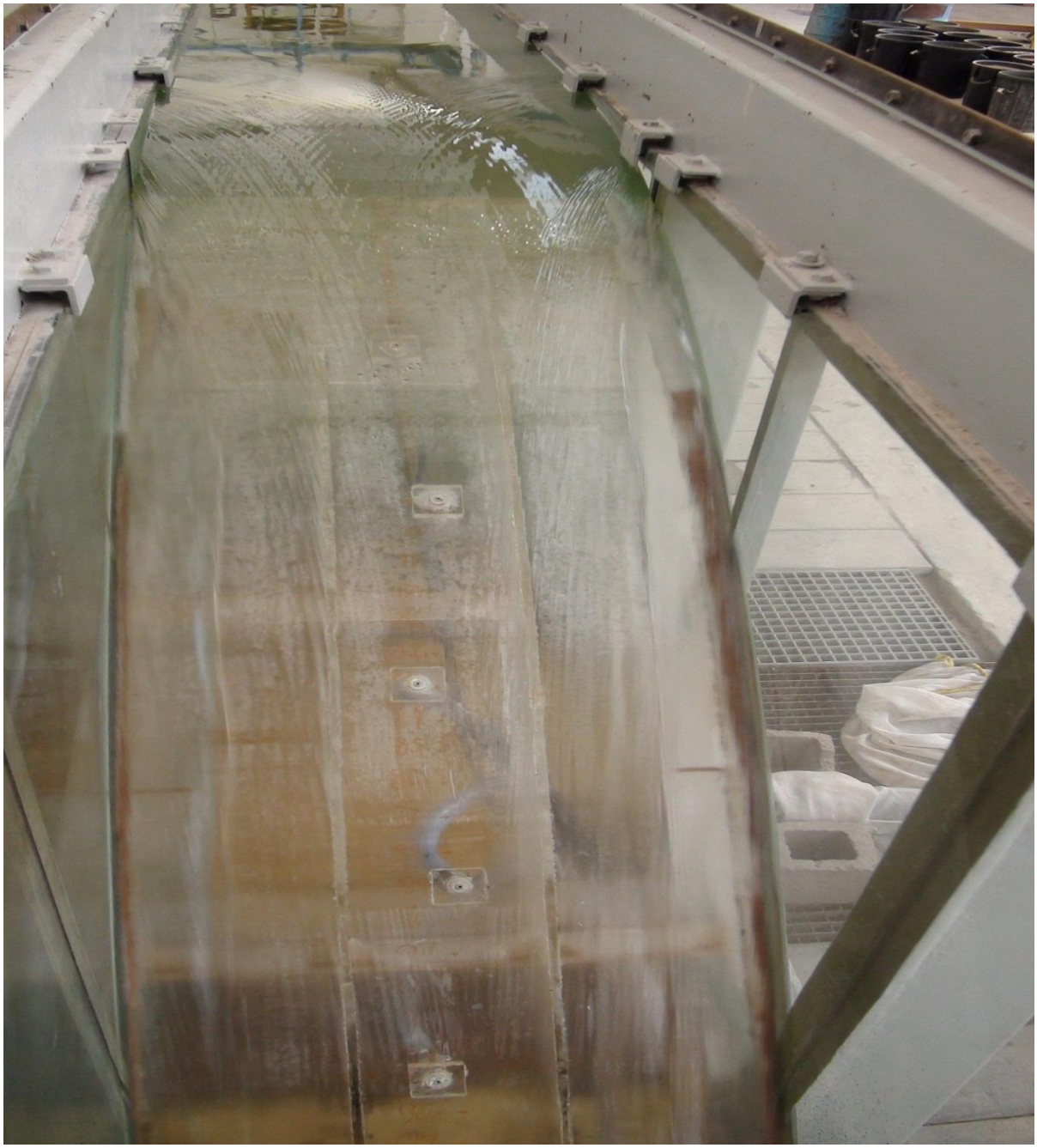

Figure B- 7: Ogee Spillway model (Case-2) viewed from the front under low flow conditions, showing flume side walls and flow behaviour downstream of the weir

Appendix C: CFD Modelling Results

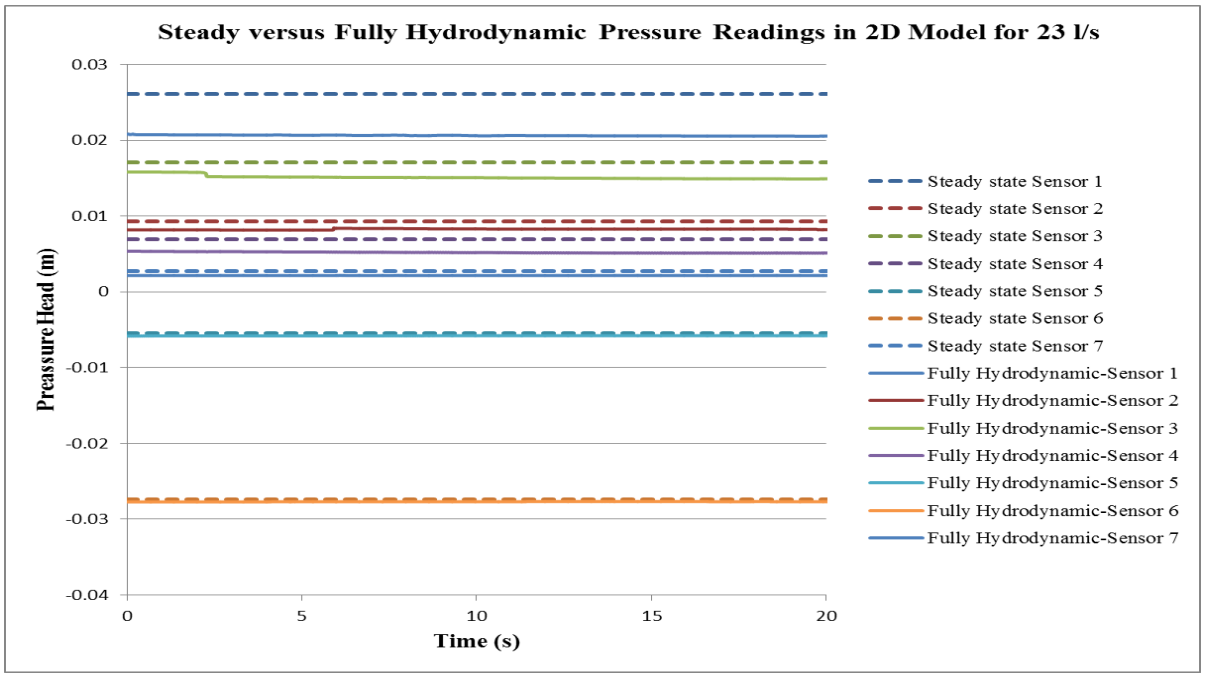

Figure C- 1: Comparison between 2D-simulated steady and fully hydrodynamic state models for a discharge of 23 l/s (Case-1)

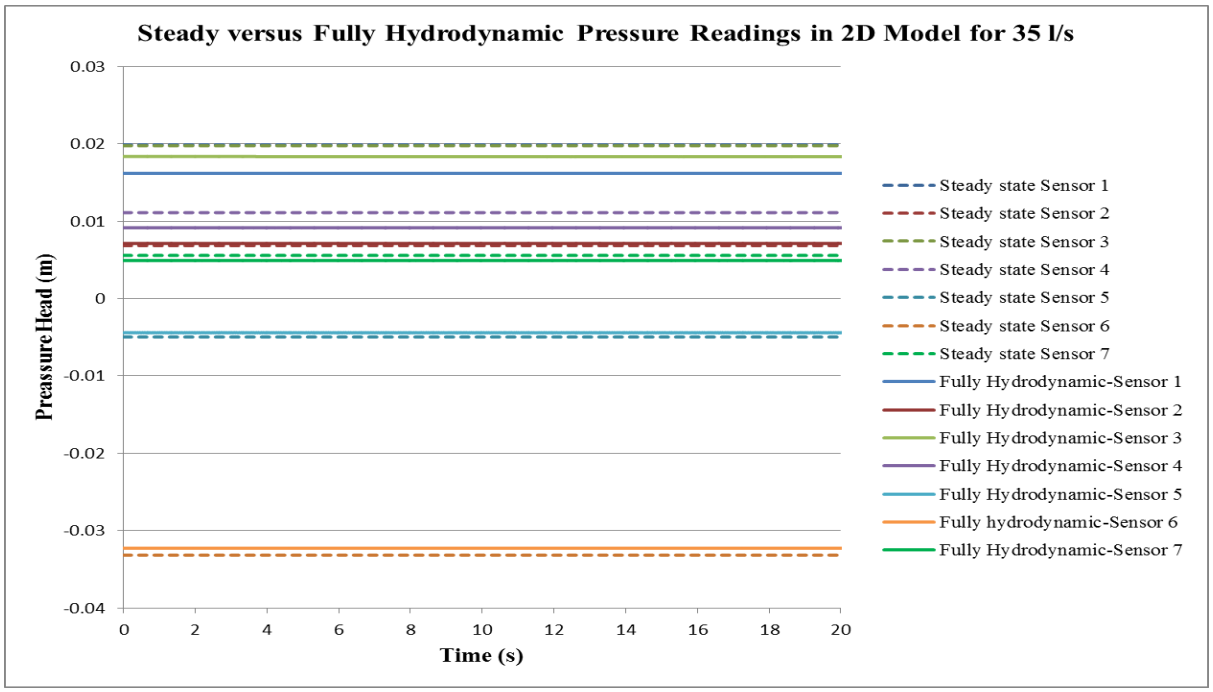

Figure C- 2: Comparison between 2D-simulated steady and fully hydrodynamic state models for a discharge of 35 l/s (Case-1)

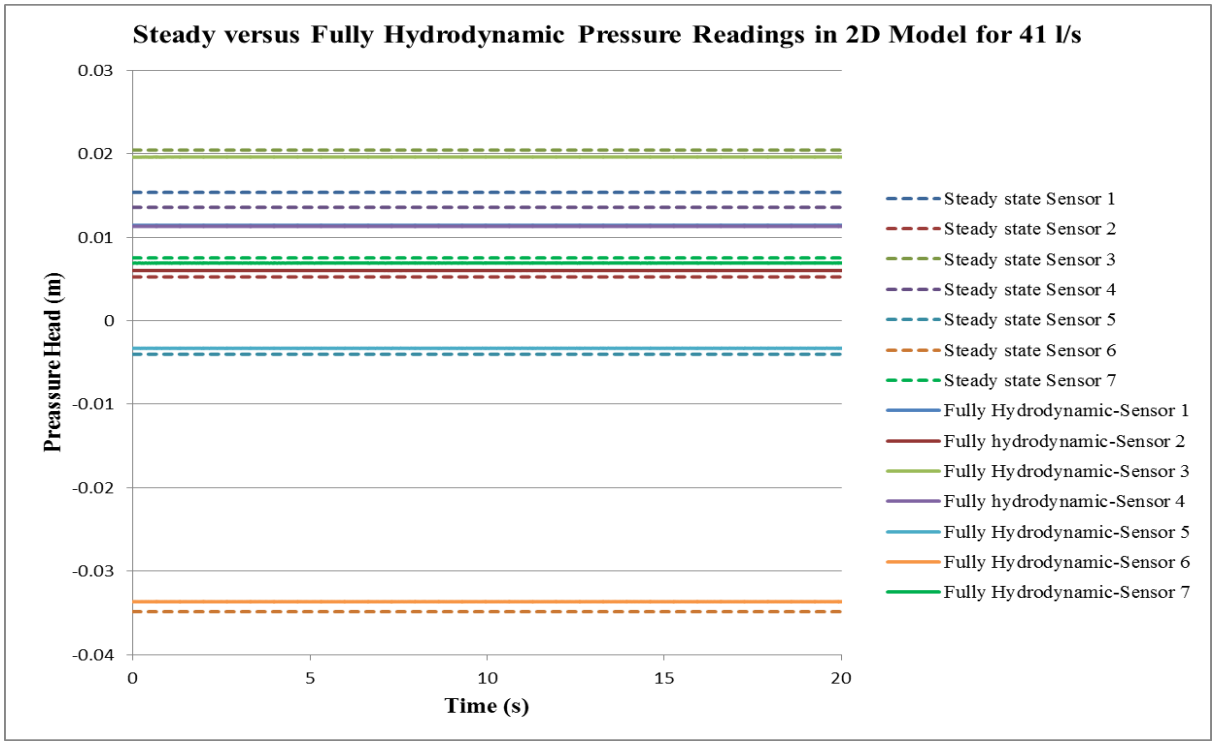

Figure C- 3: Comparison between 2D-simulated steady and fully hydrodynamic state models for a discharge of 41 l/s (Case-1)

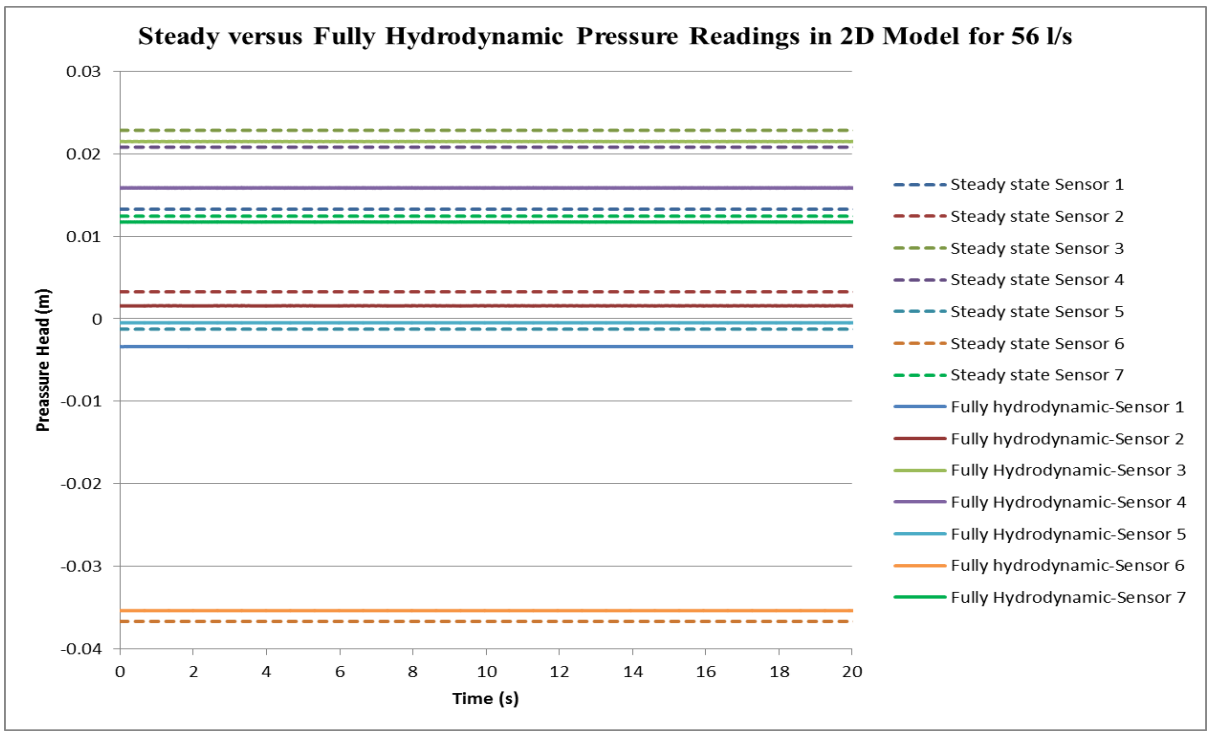

Figure C- 4: Comparison between 2D-simulated steady and fully hydrodynamic state models for a discharge of 56 l/s (Case-1)

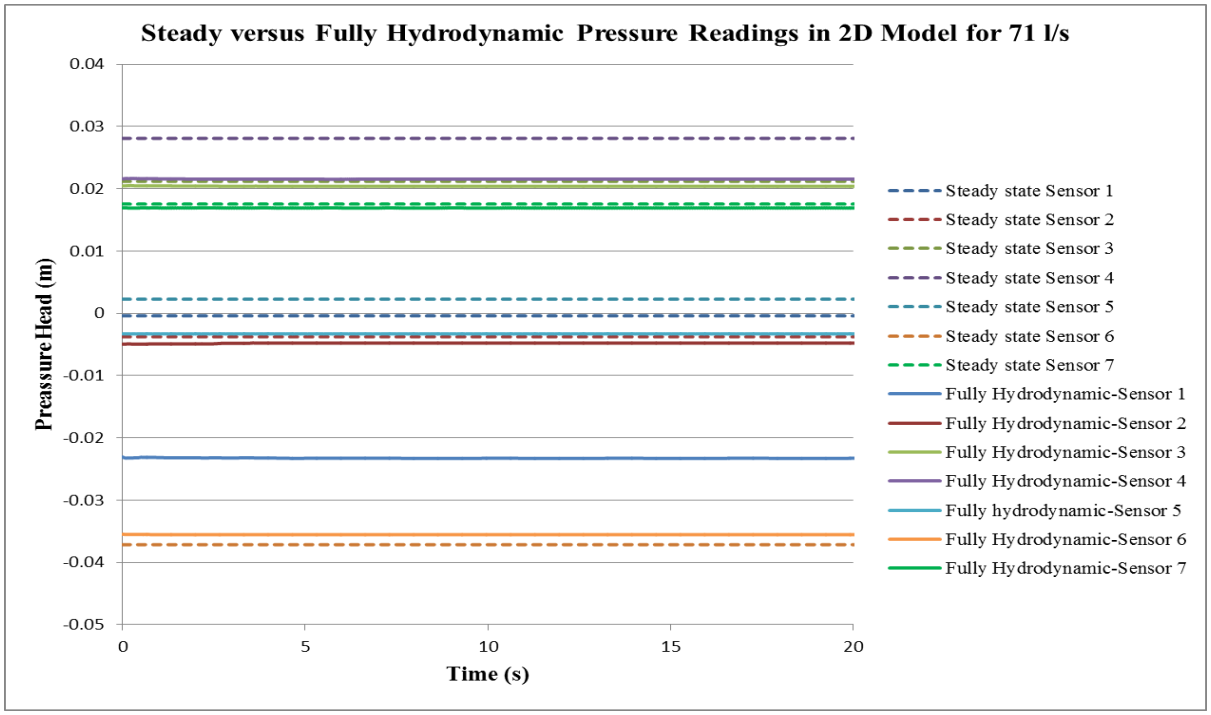

Figure C- 5: Comparison between 2D-simulated steady and fully hydrodynamic state models for a discharge of 71 l/s (Case-1)

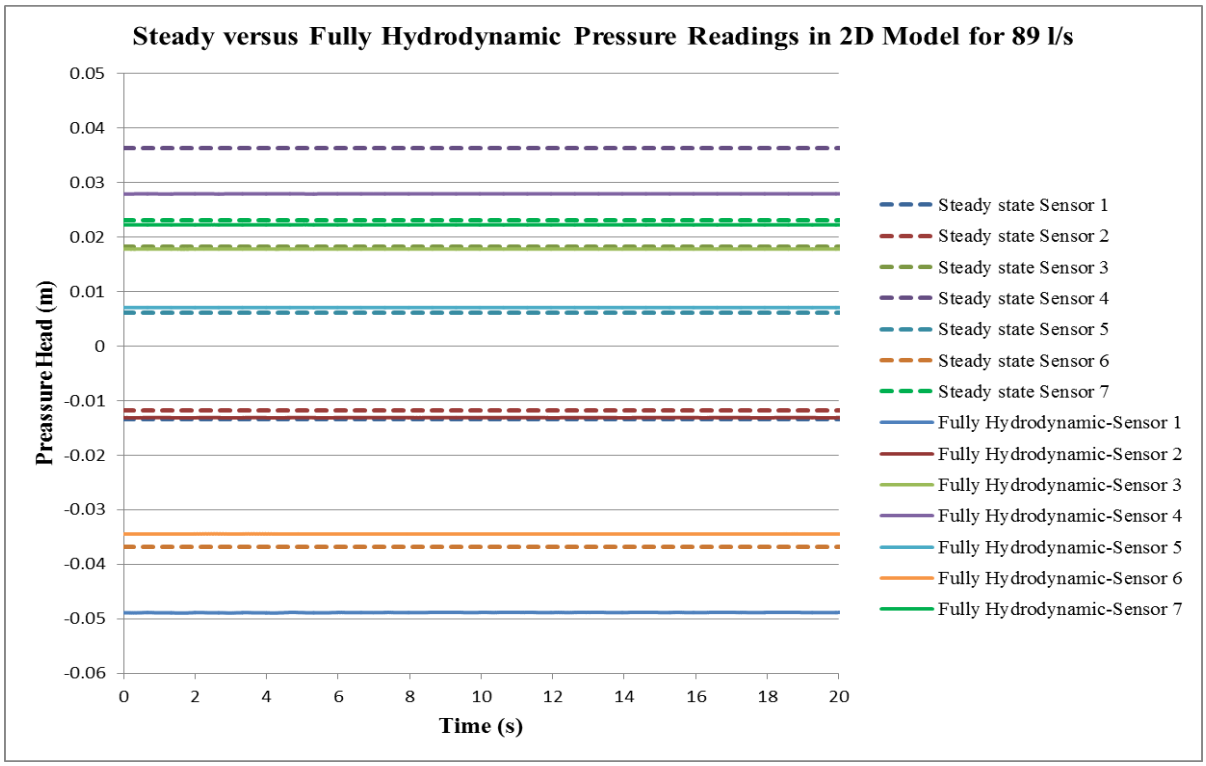

Figure C- 6: Comparison between 2D-simulated steady and fully hydrodynamic state models for a discharge of 89 l/s (Case-1)

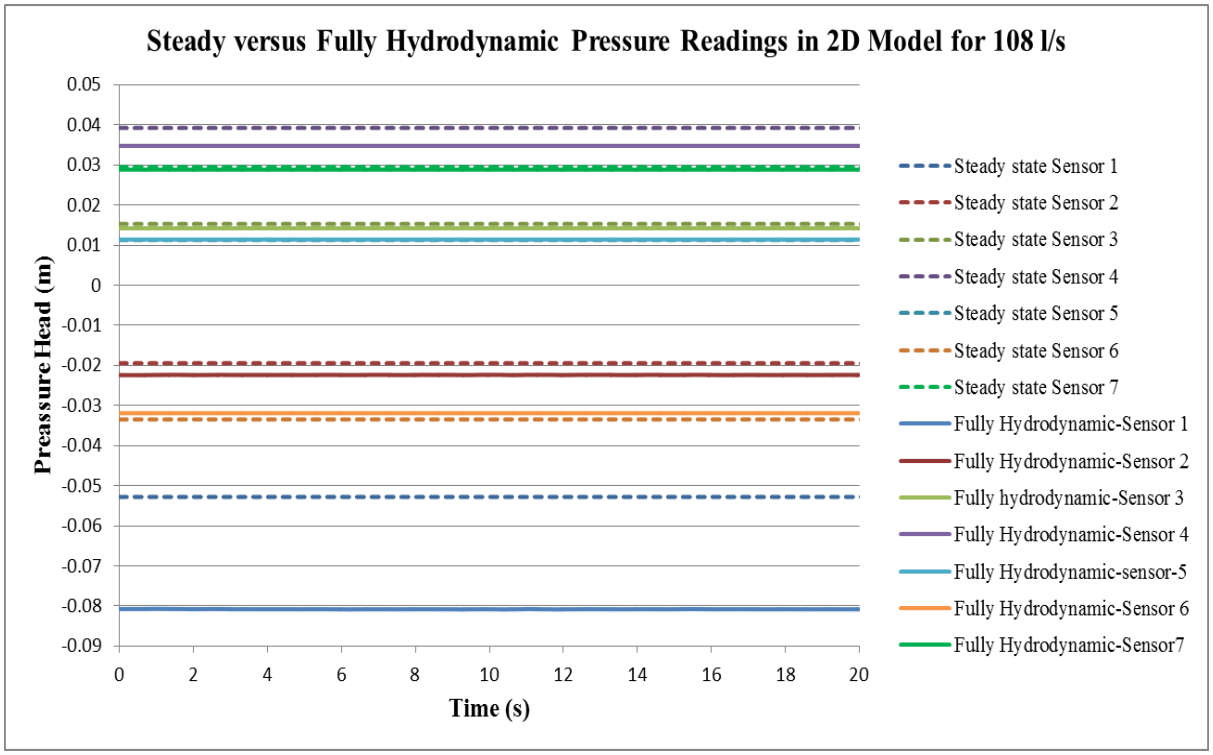

Figure C- 7: Comparison between 2D-simulated steady and fully hydrodynamic state models for a discharge of 108 l/s (Case-1)

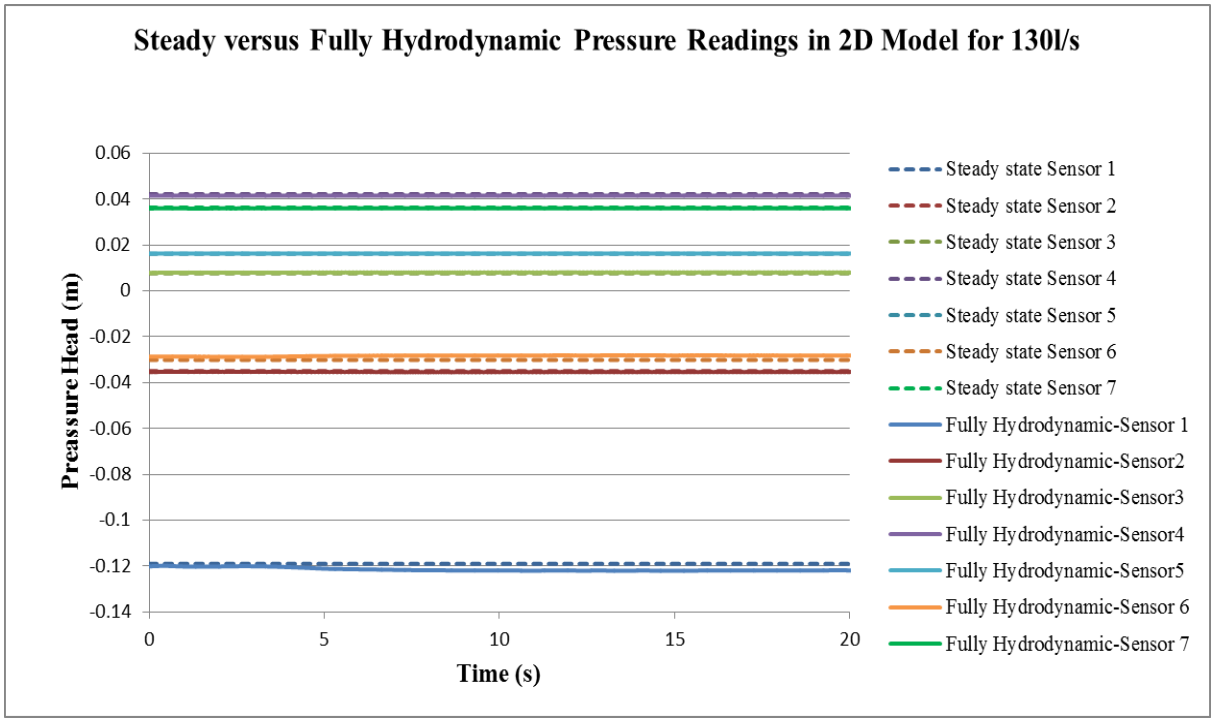

Figure C- 8: Comparison between 2D-simulated steady and fully hydrodynamic state models for a discharge of 130 l/s (Case-1)

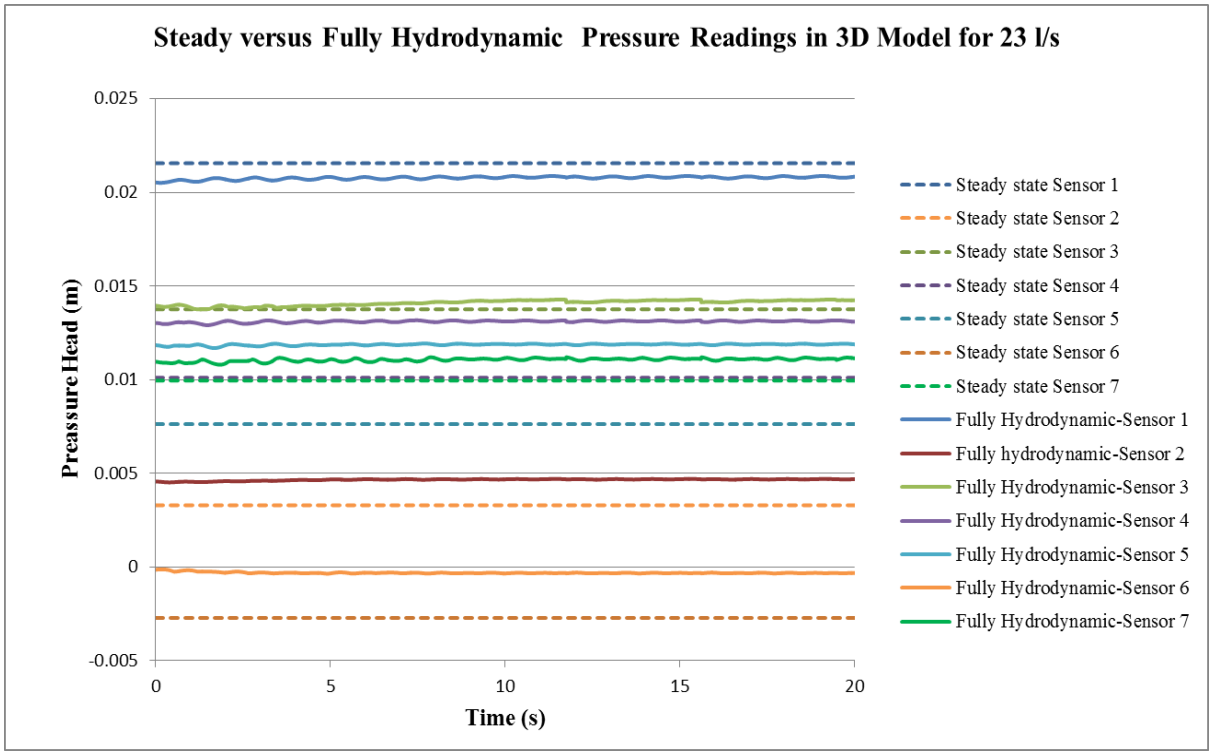

Figure C- 9: Comparison between 3D-simulated steady and fully hydrodynamic state models for a discharge of 23 l/s (Case-1)

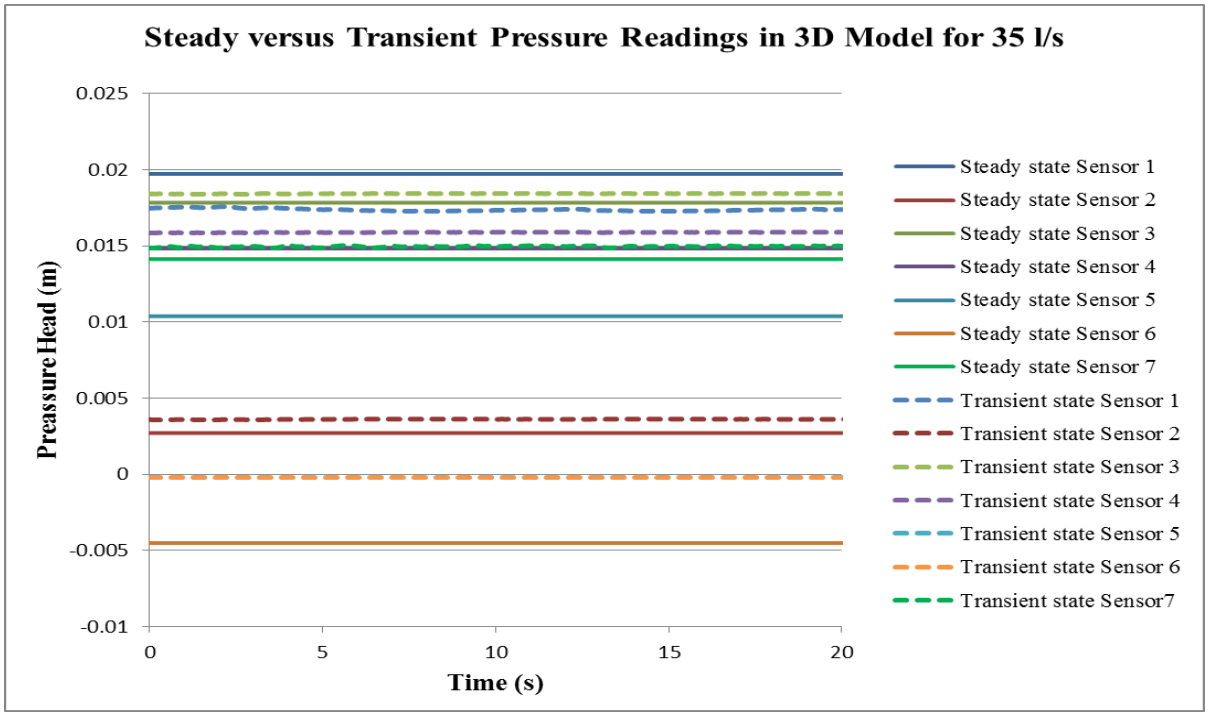

Figure C- 10: Comparison between 3D-simulated steady and fully hydrodynamic state models for a discharge of 35 l/s (Case-1)

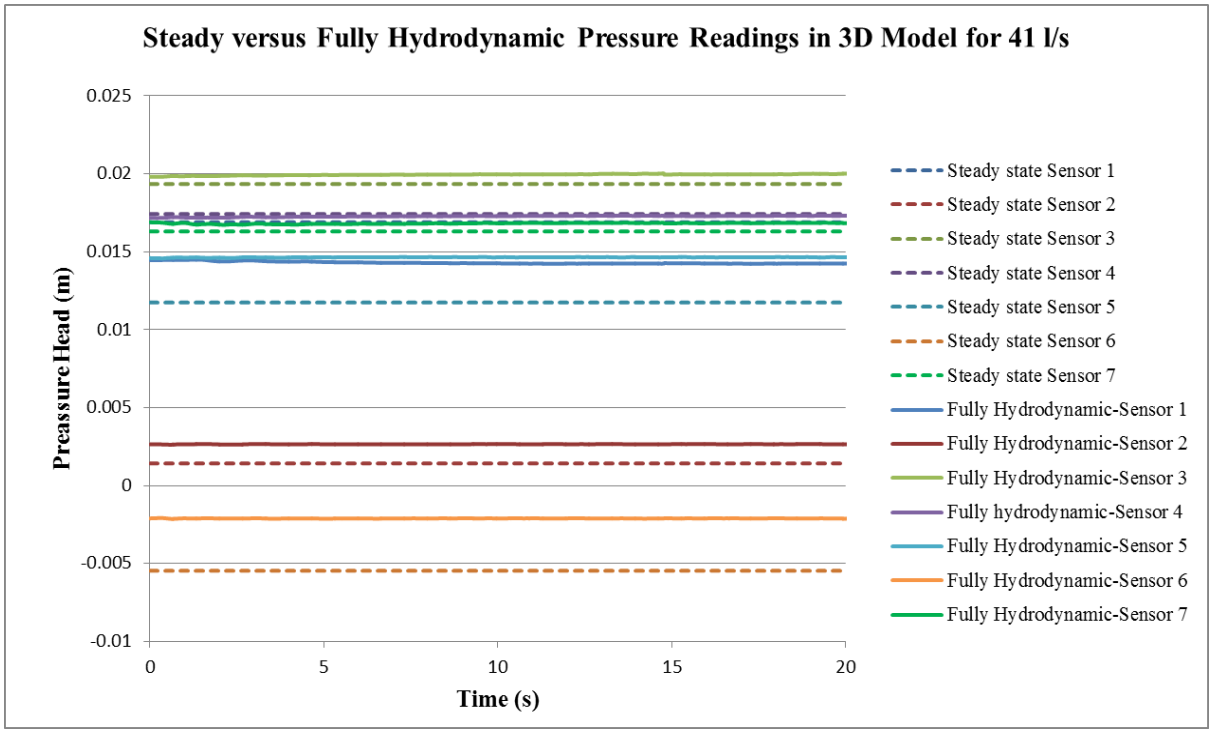

Figure C- 11: Comparison between 3D-simulated steady and fully hydrodynamic state models for a discharge of 41 l/s (Case-1)

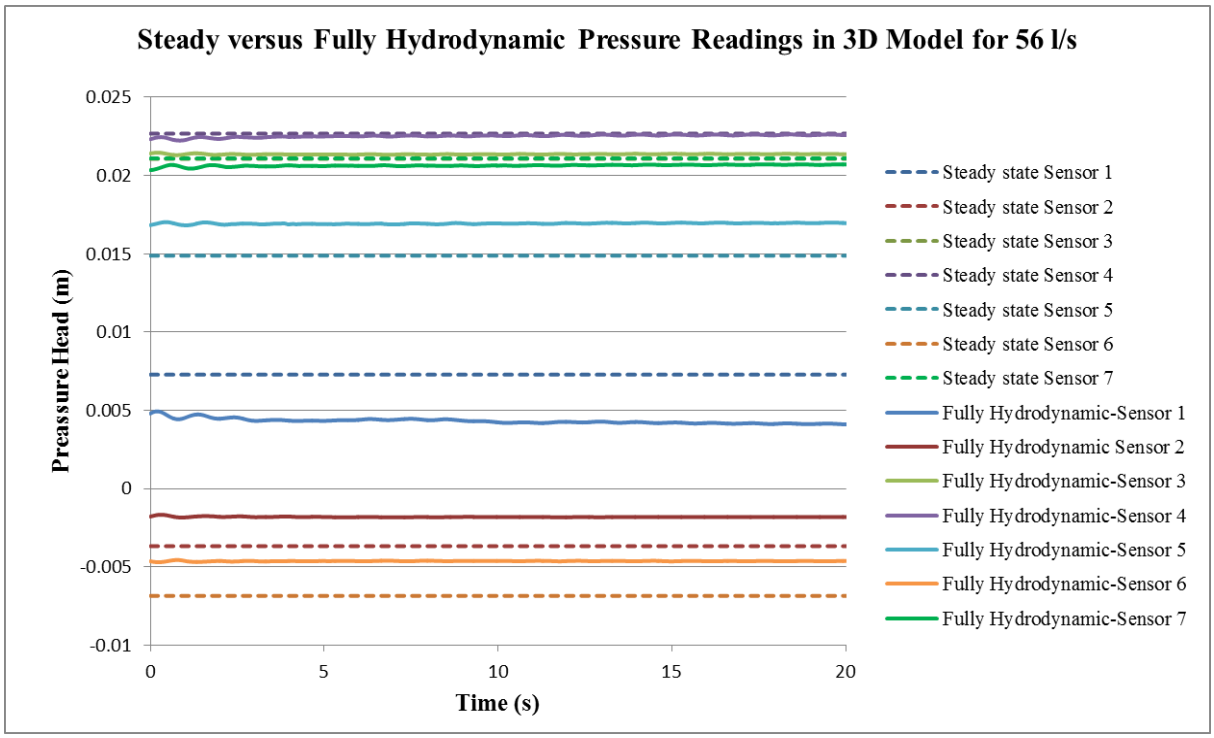

Figure C- 12: Comparison between 3D-simulated steady and fully hydrodynamic state models for a discharge of 56 l/s (Case-1)

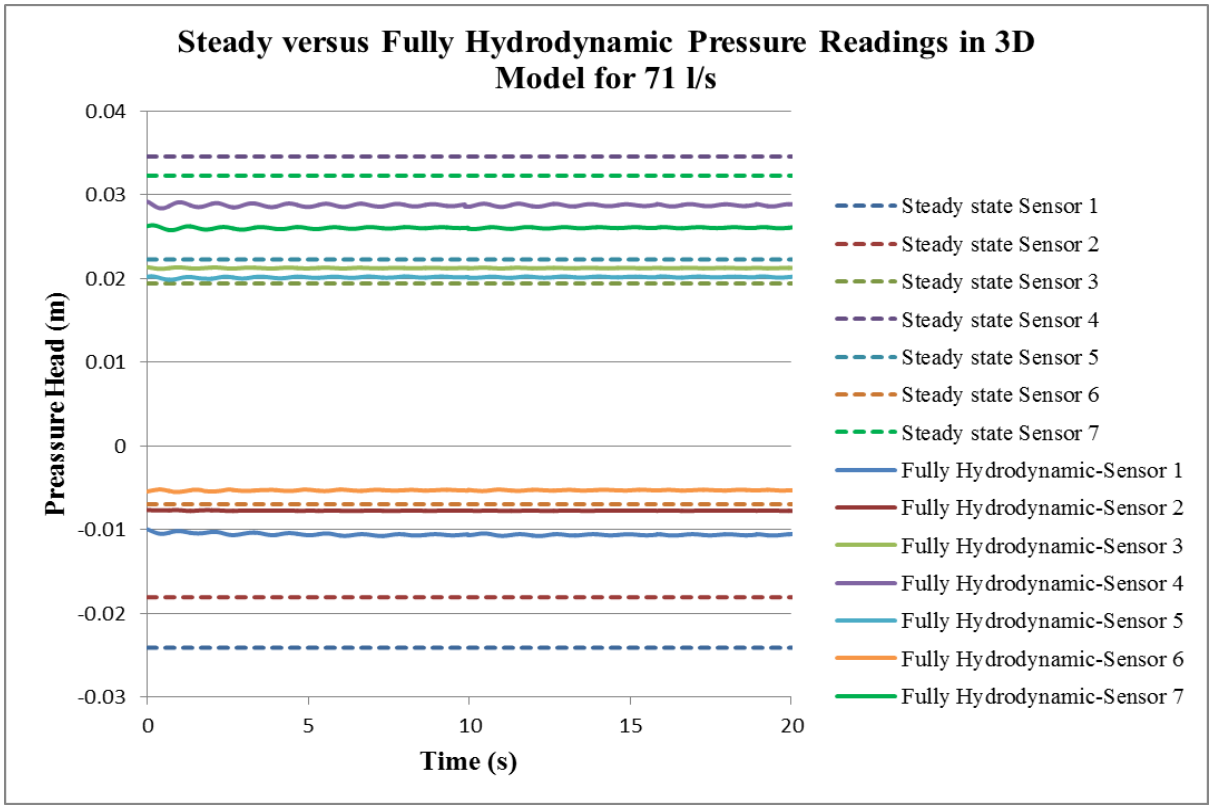

Figure C- 13: Comparison between 3D-simulated steady and fully hydrodynamic state models for a discharge of 71 l/s (Case-1)

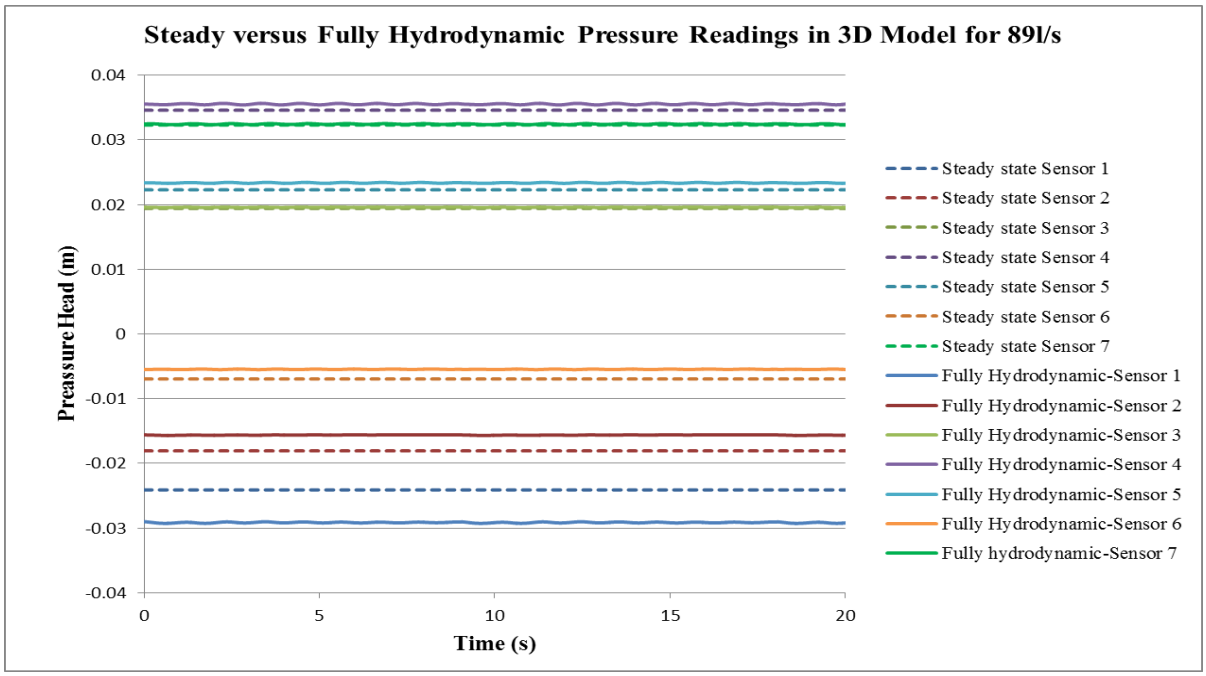

Figure C- 14: Comparison between 3D-simulated steady and fully hydrodynamic state models for a discharge of 89 l/s (Case-1)

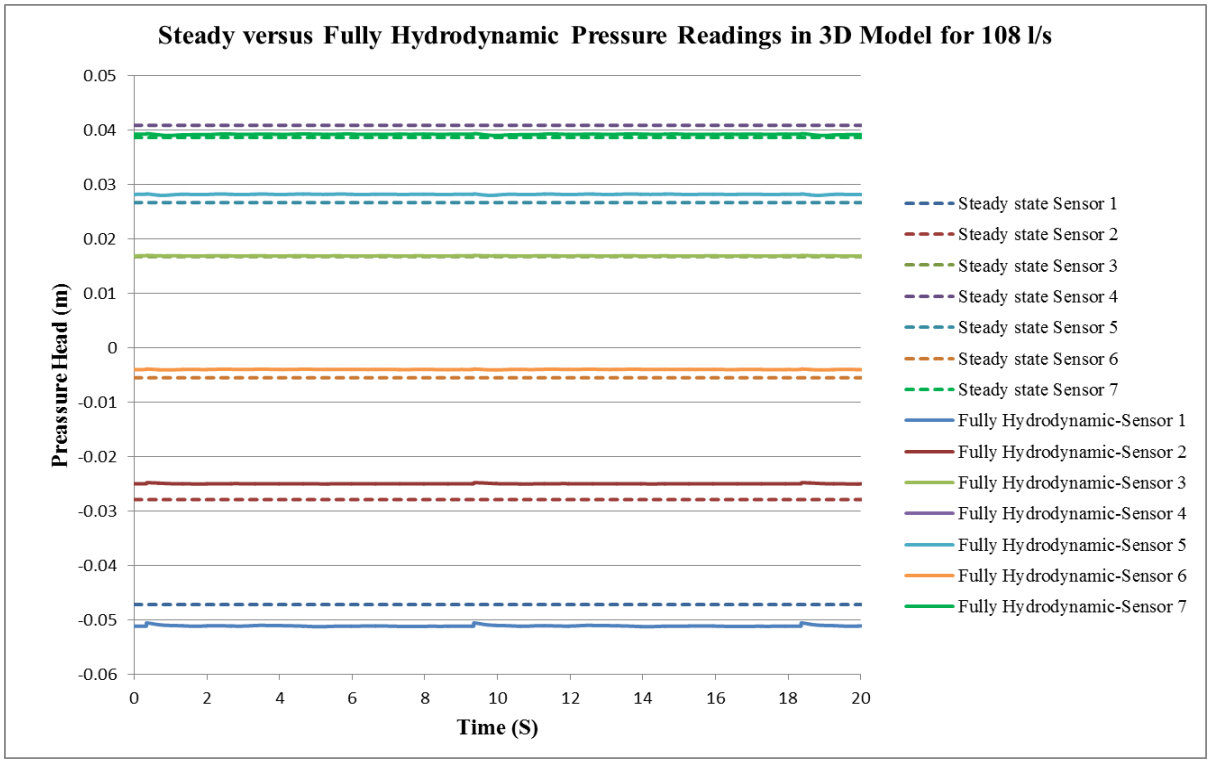

Figure C- 15: Comparison between 3D-simulated steady and fully hydrodynamic state models for a discharge of 108 l/s (Case-1)

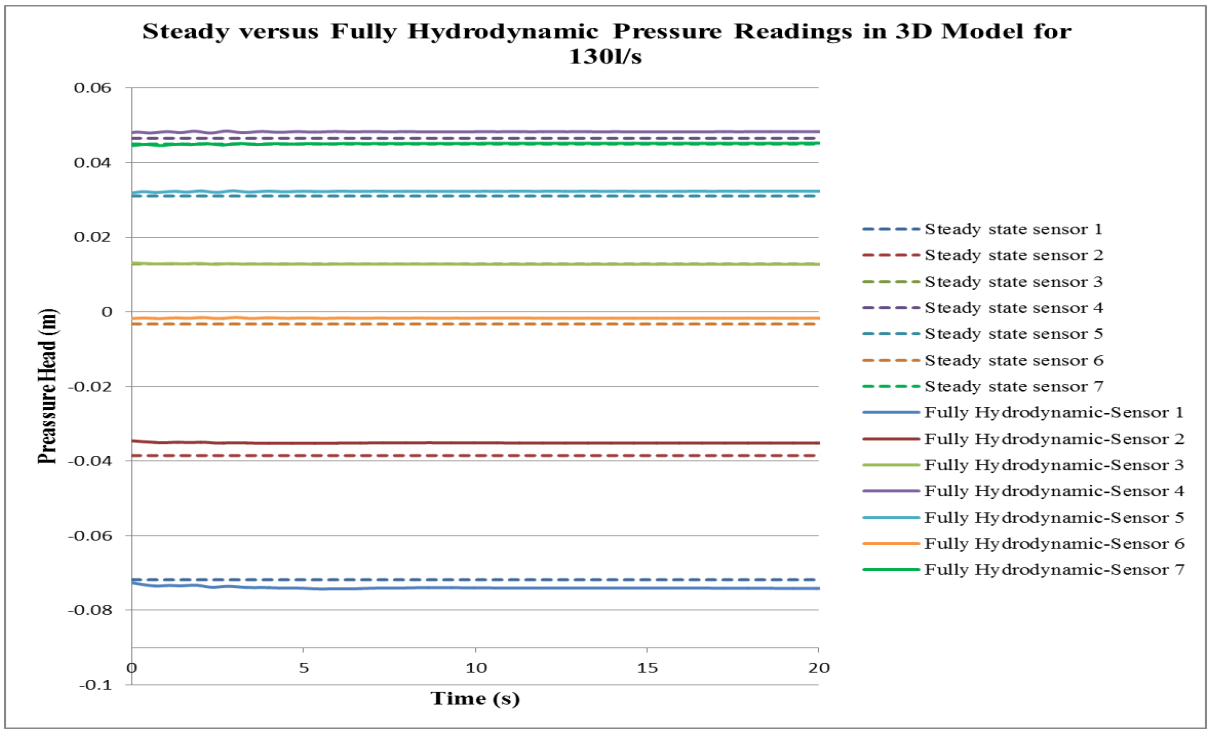

Figure C- 16: Comparison between 3D-simulated steady and fully hydrodynamic state models for a discharge of 130 l/s (Case-1)

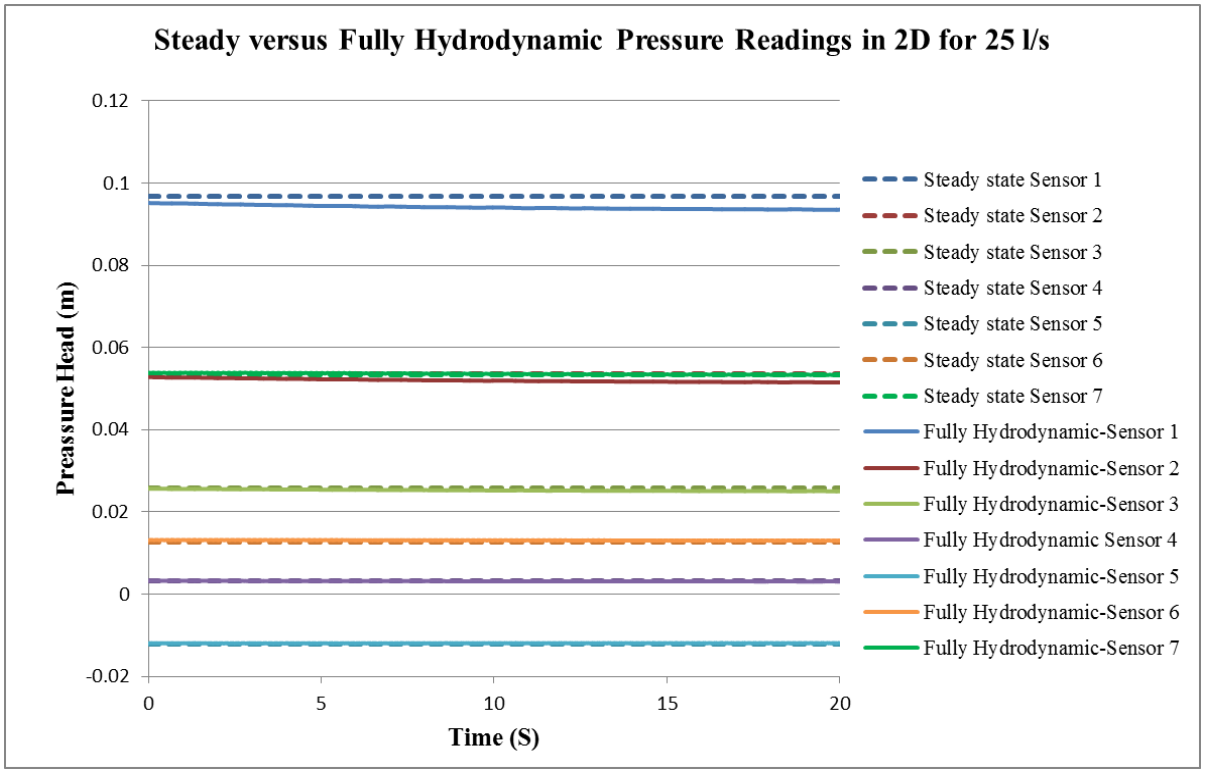

Figure C- 17: Comparison between 2D-simulated steady and fully hydrodynamic state models for a discharge of 25 l/s (Case-2)

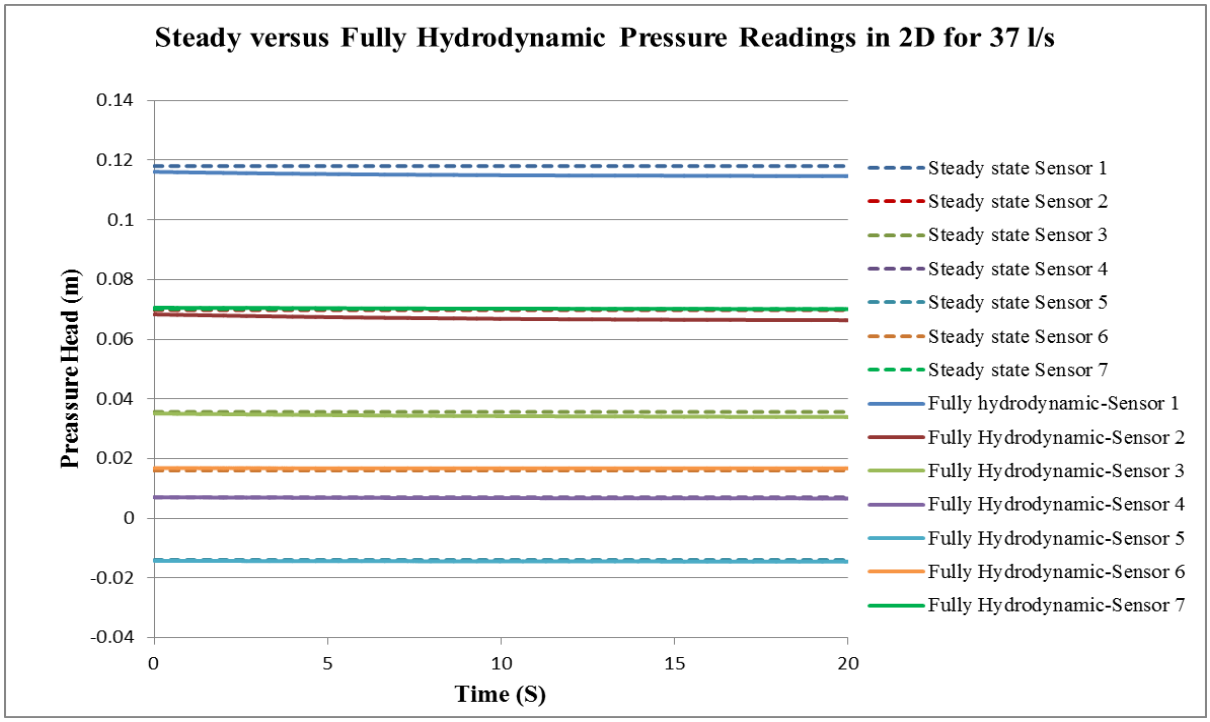

Figure C- 18: Comparison between 2D-simulated steady and fully hydrodynamic state models for a discharge of 37 l/s (Case-2)

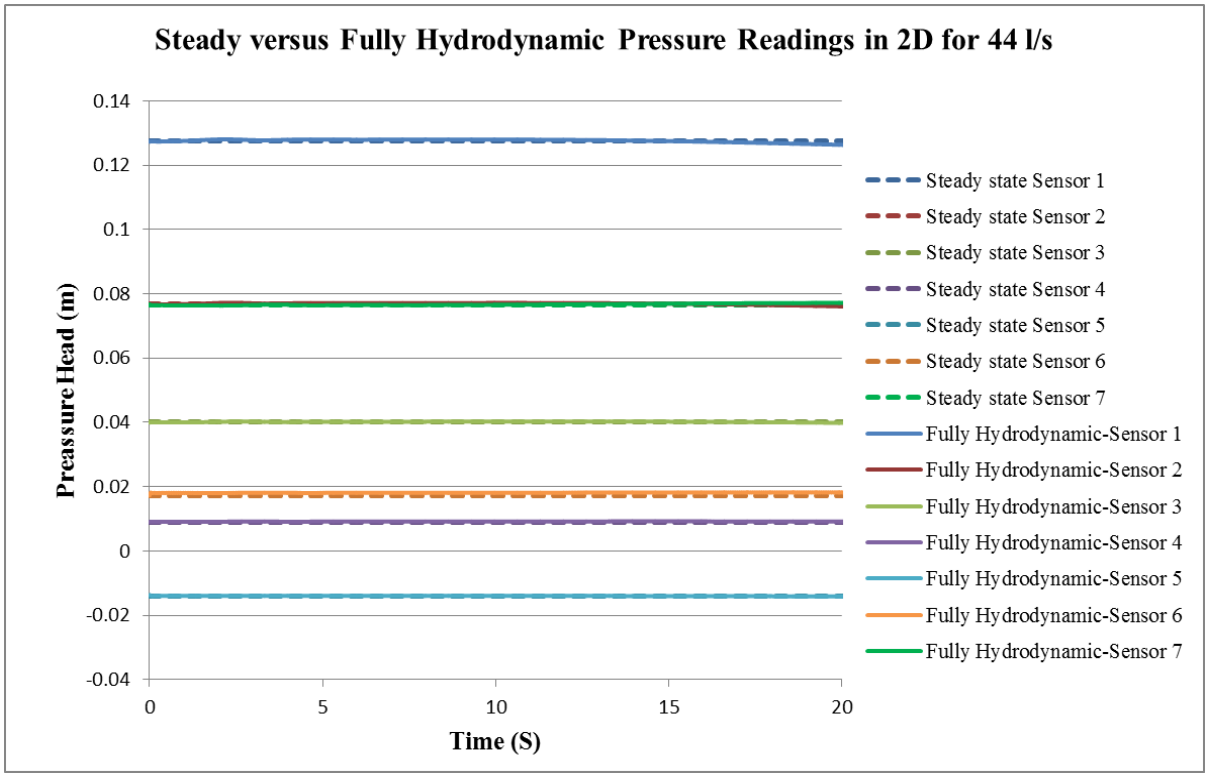

Figure C- 19: Comparison between 2D-simulated steady and fully hydrodynamic state models for a discharge of 44 l/s (Case-2)

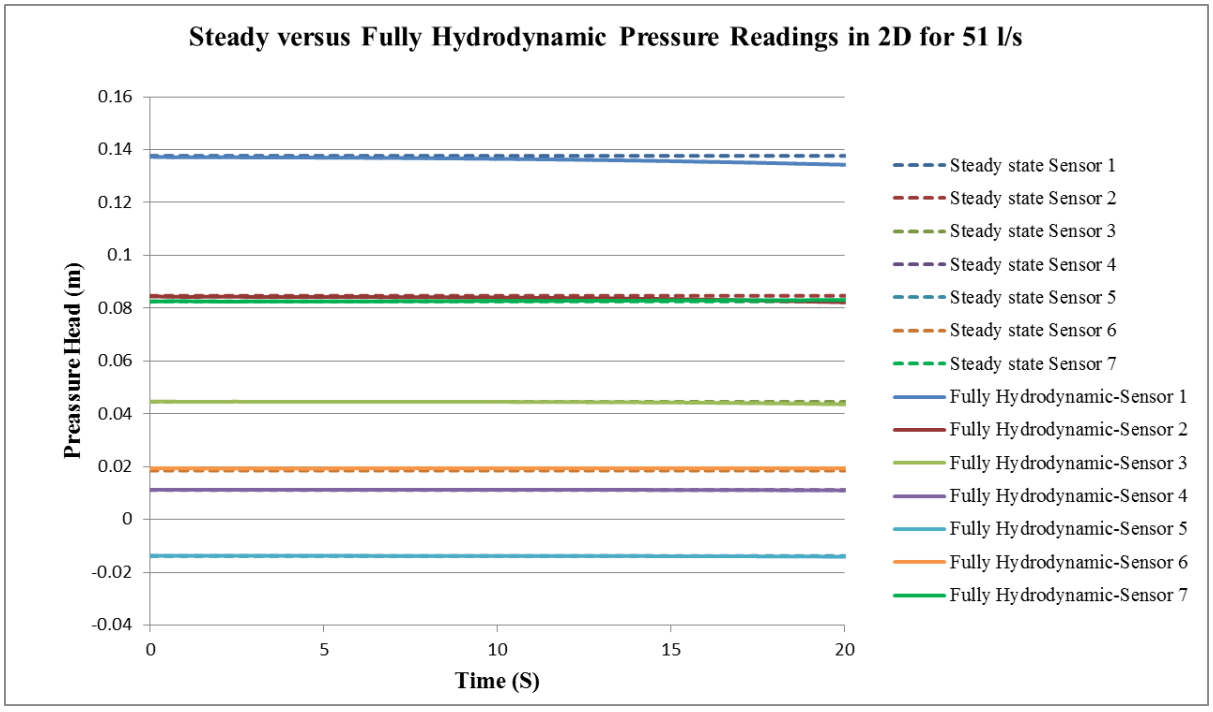

Figure C- 20: Comparison between 2D-simulated steady and fully hydrodynamic state models for a discharge of 51 l/s (Case-2)

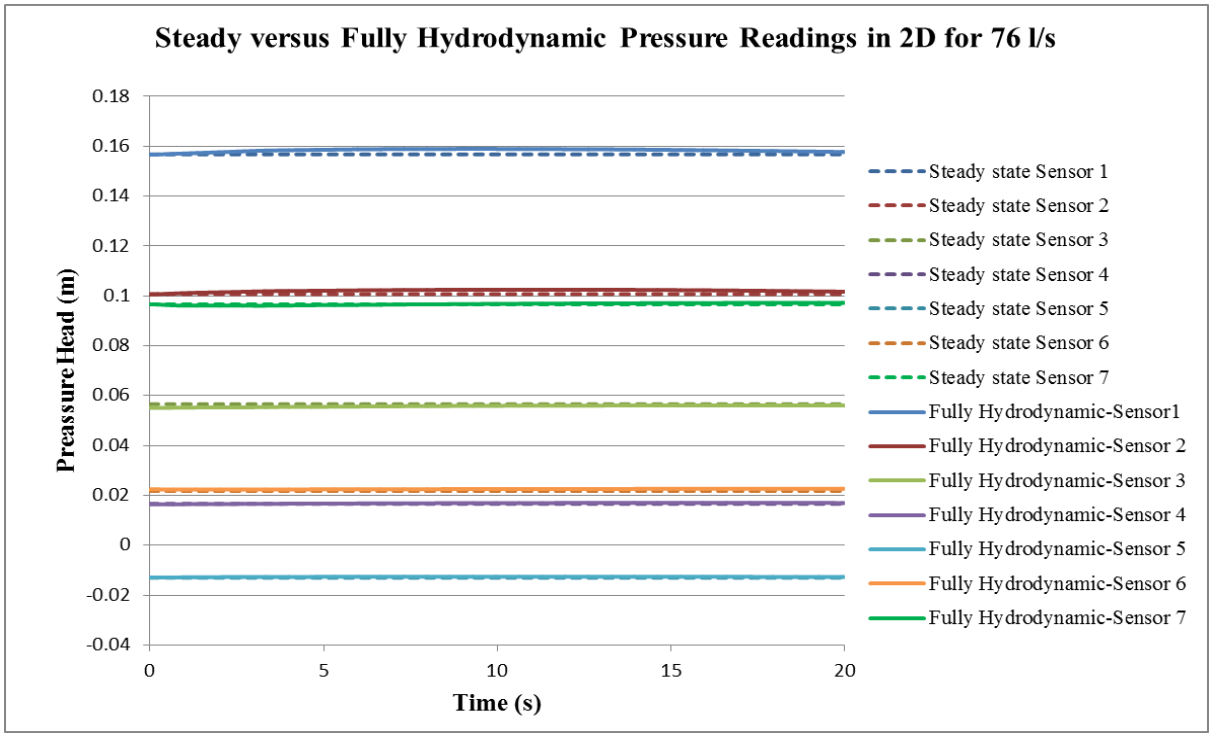

Figure C- 21: Comparison between 2D-simulated steady and fully hydrodynamic state models for a discharge of 76 l/s (Case-2)

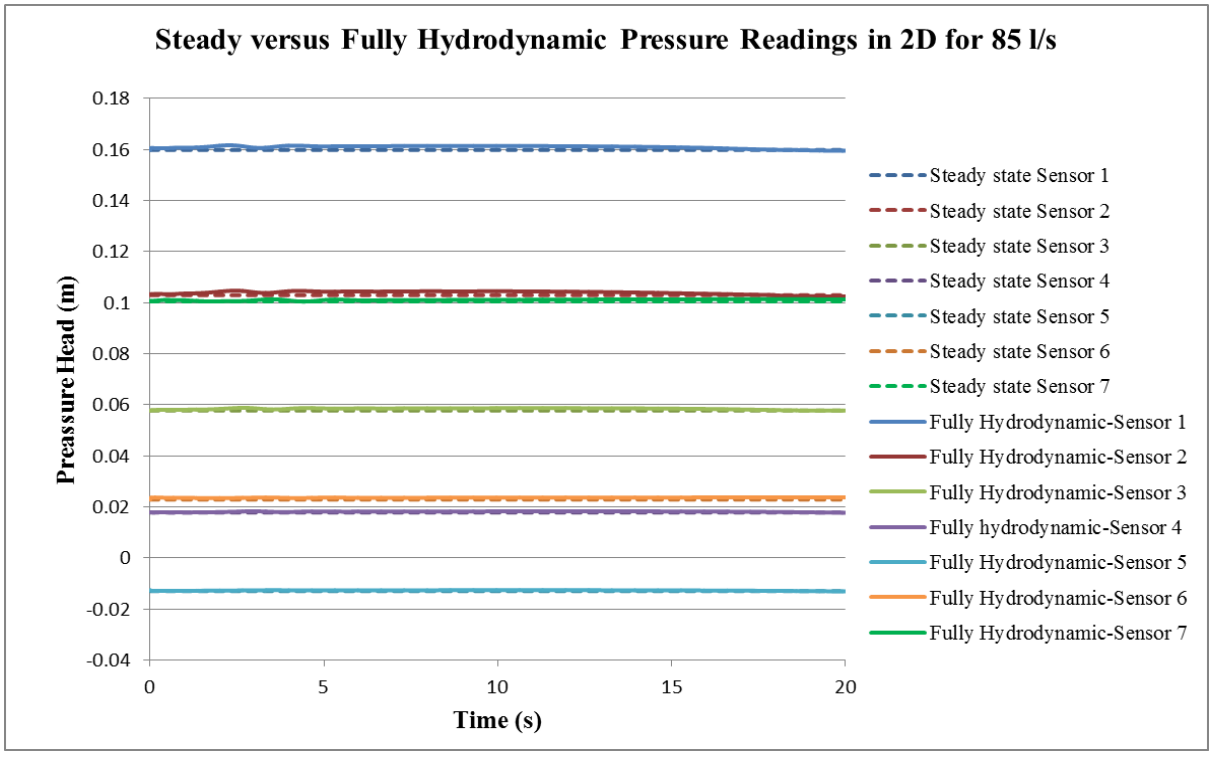

Figure C- 22: Comparison between 2D-simulated steady and fully hydrodynamic state models for a discharge of 85 l/s (Case-2)

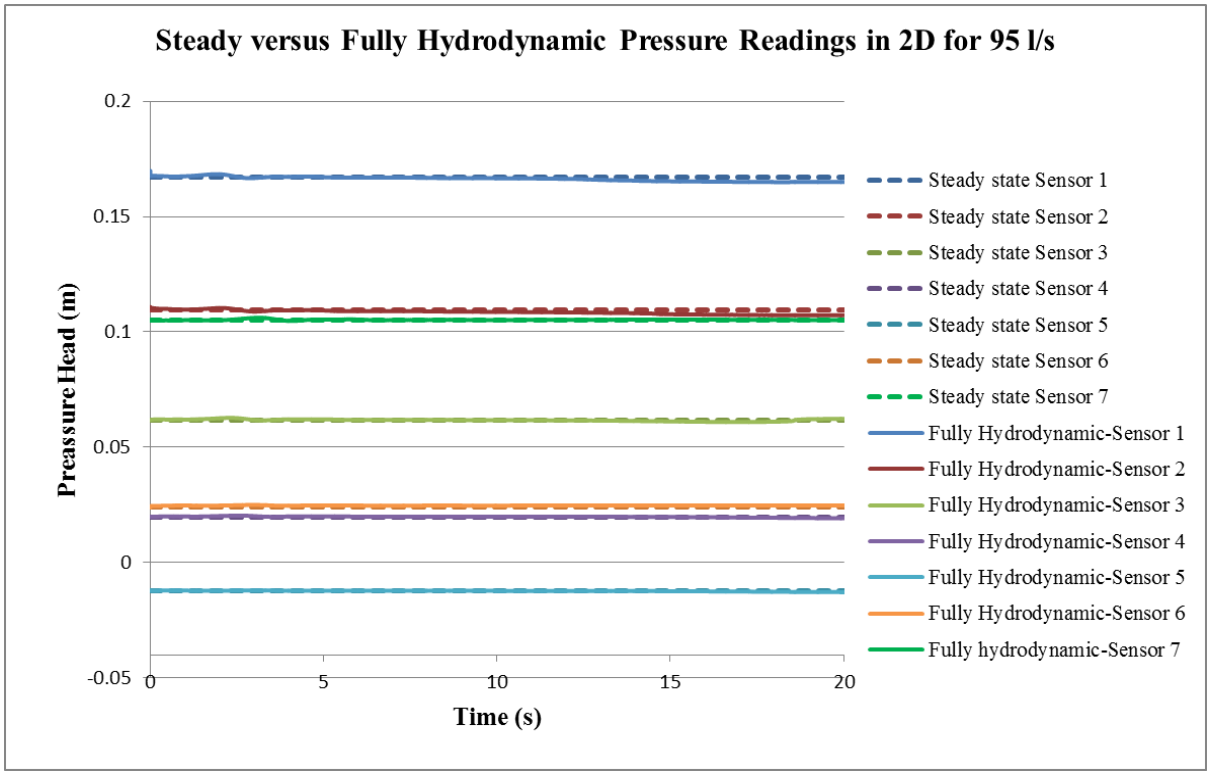

Figure C- 23: Appendix C-7: Comparison between 2D-simulated steady and fully hydrodynamic state models for a discharge of 95 l/s (Case-2)

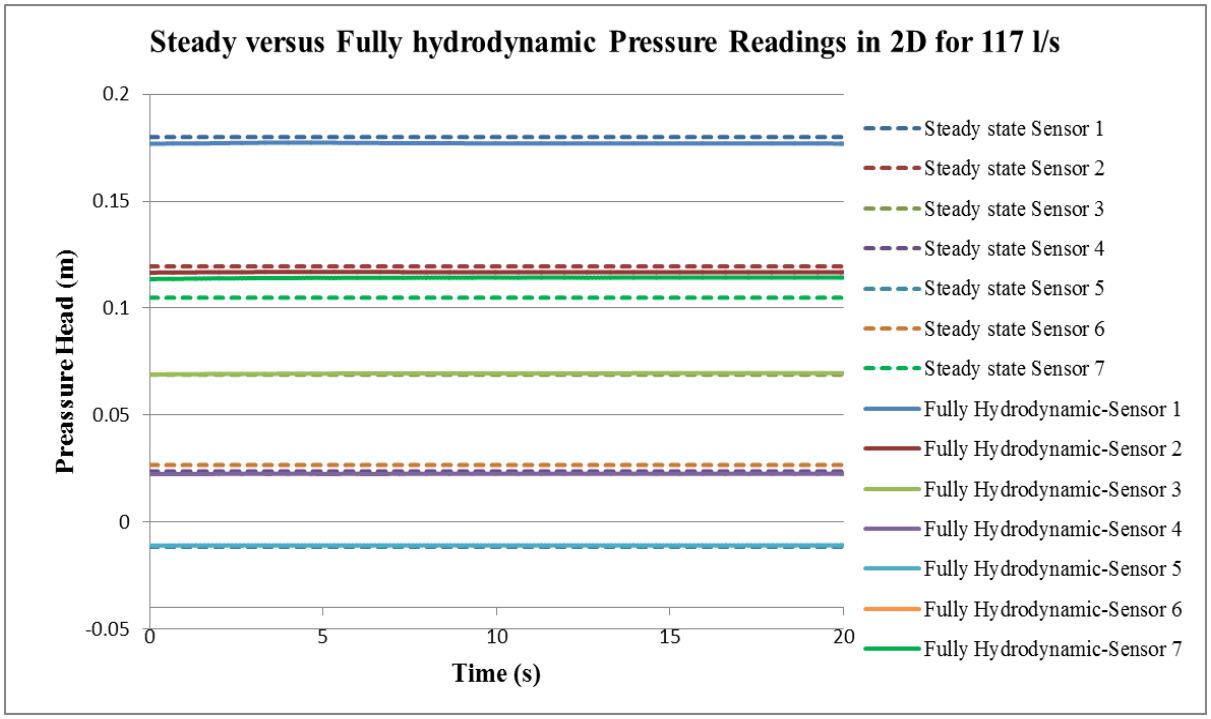

Figure C- 24: Comparison between 2D-simulated steady and fully hydrodynamic state models for a discharge of 117 l/s (Case-2)

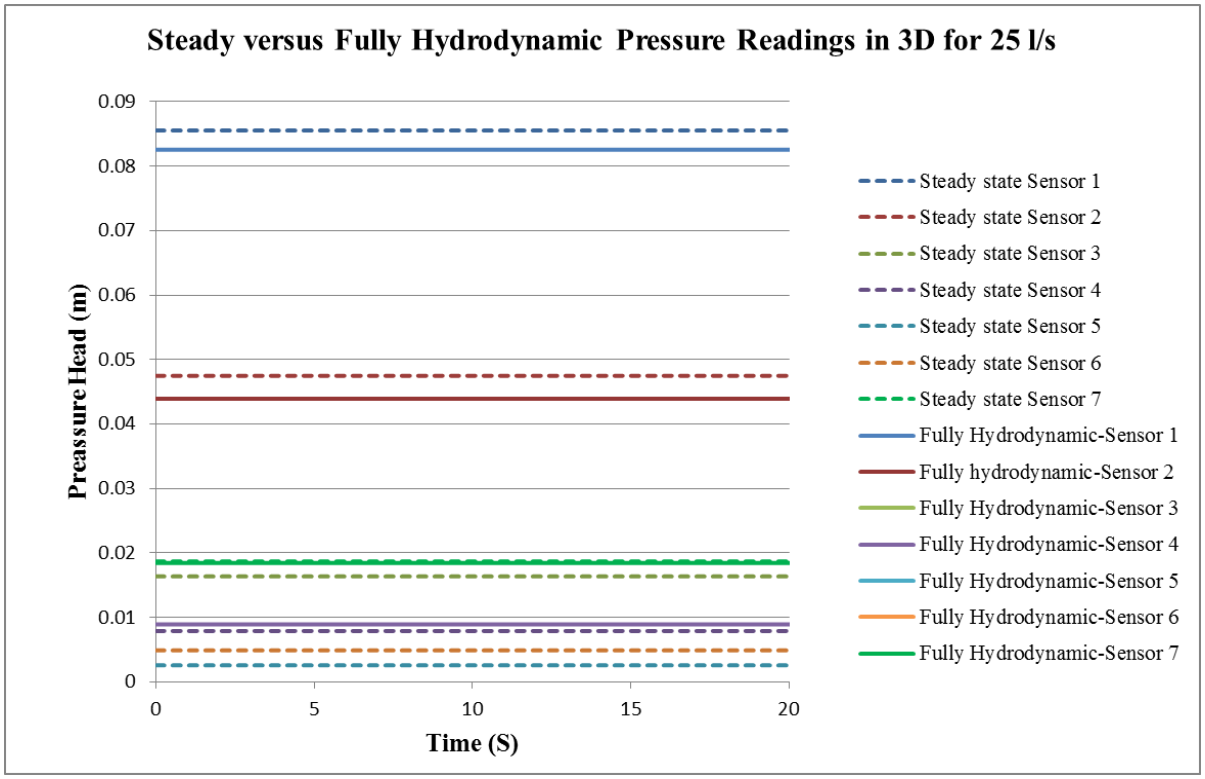

Figure C- 25: Comparison between 3D-simulated steady and fully hydrodynamic state models for a discharge of 25 l/s (Case-1)

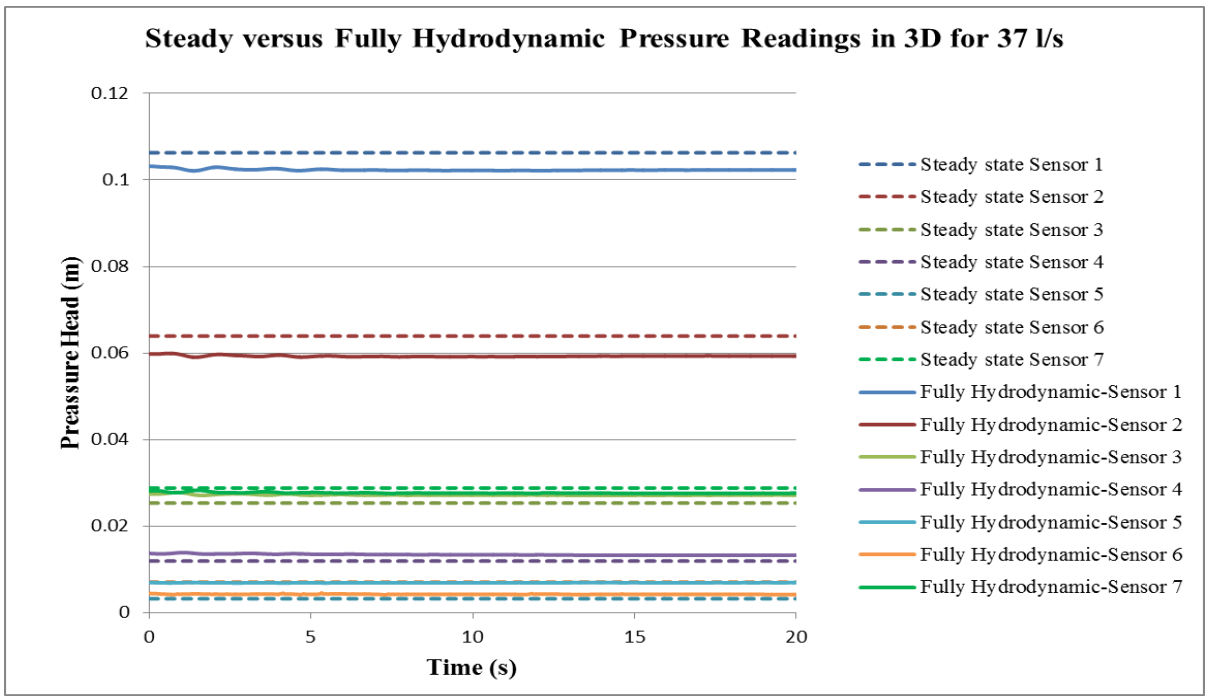

Figure C- 26: Comparison between 3D-simulated steady and fully hydrodynamic state models for a discharge of 37 l/s (Case-2)

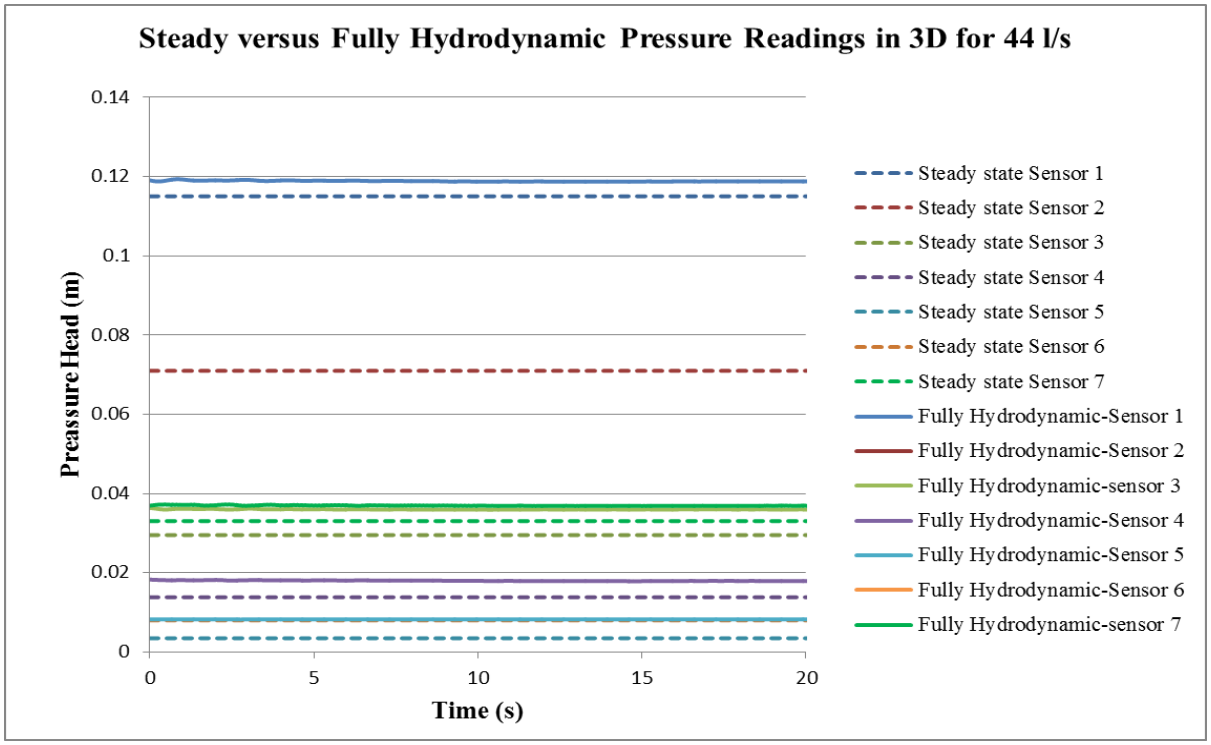

Figure C- 27: Comparison between 3D-simulated steady and fully hydrodynamic state models for a discharge of 44 l/s (Case-2)

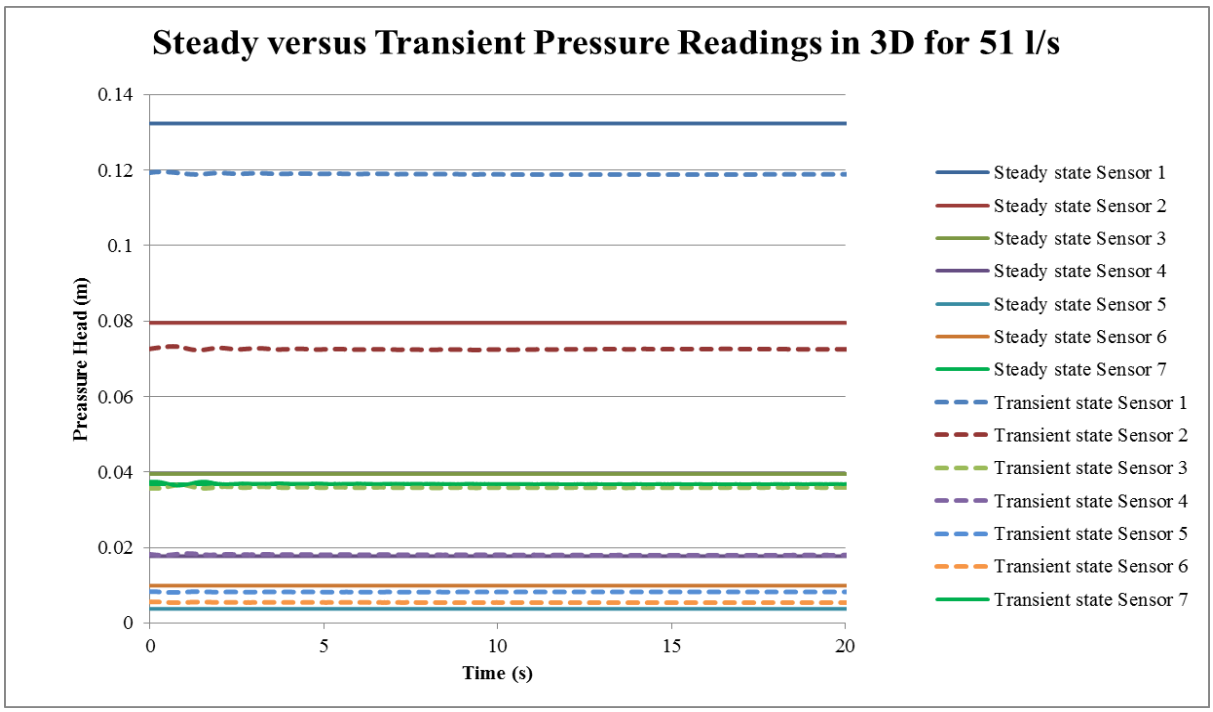

Figure C- 28: Comparison between 3D-simulated steady and fully hydrodynamic state models for a discharge of 51 l/s (Case-2)

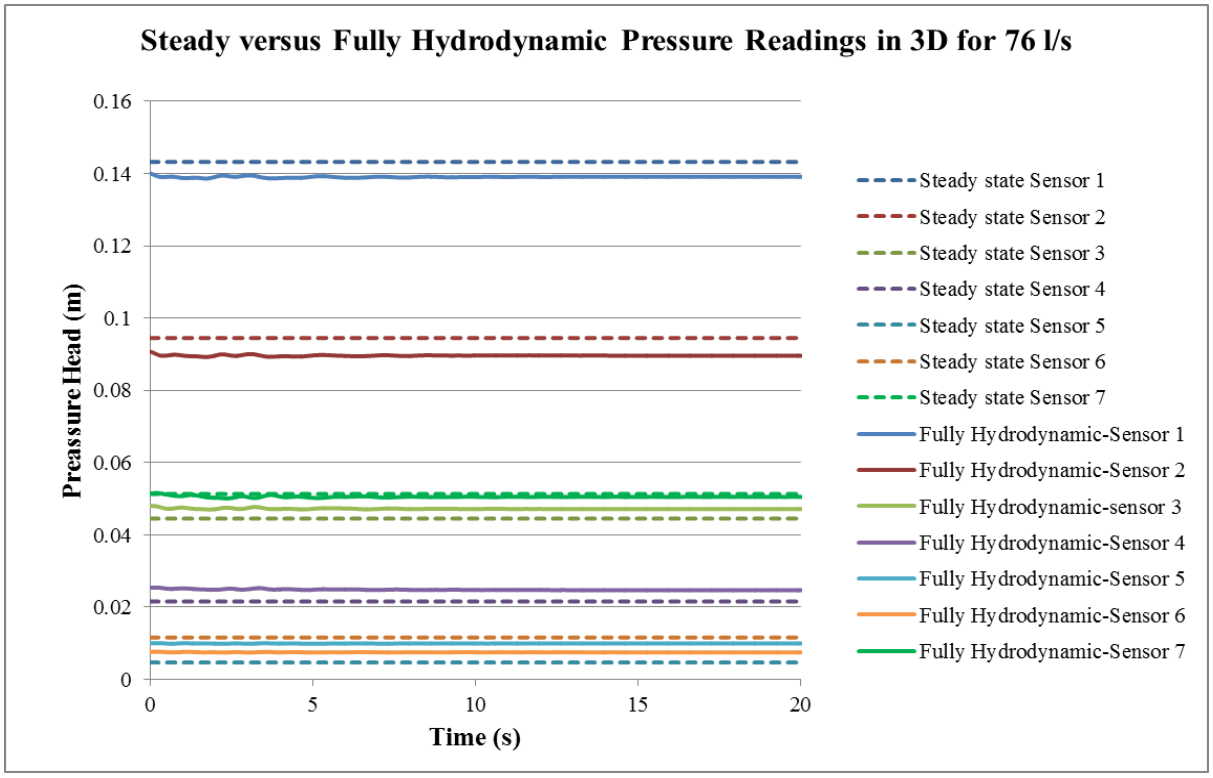

Figure C- 29: Comparison between 3D-simulated steady and fully hydrodynamic state models for a discharge of 76 l/s (Case-2)

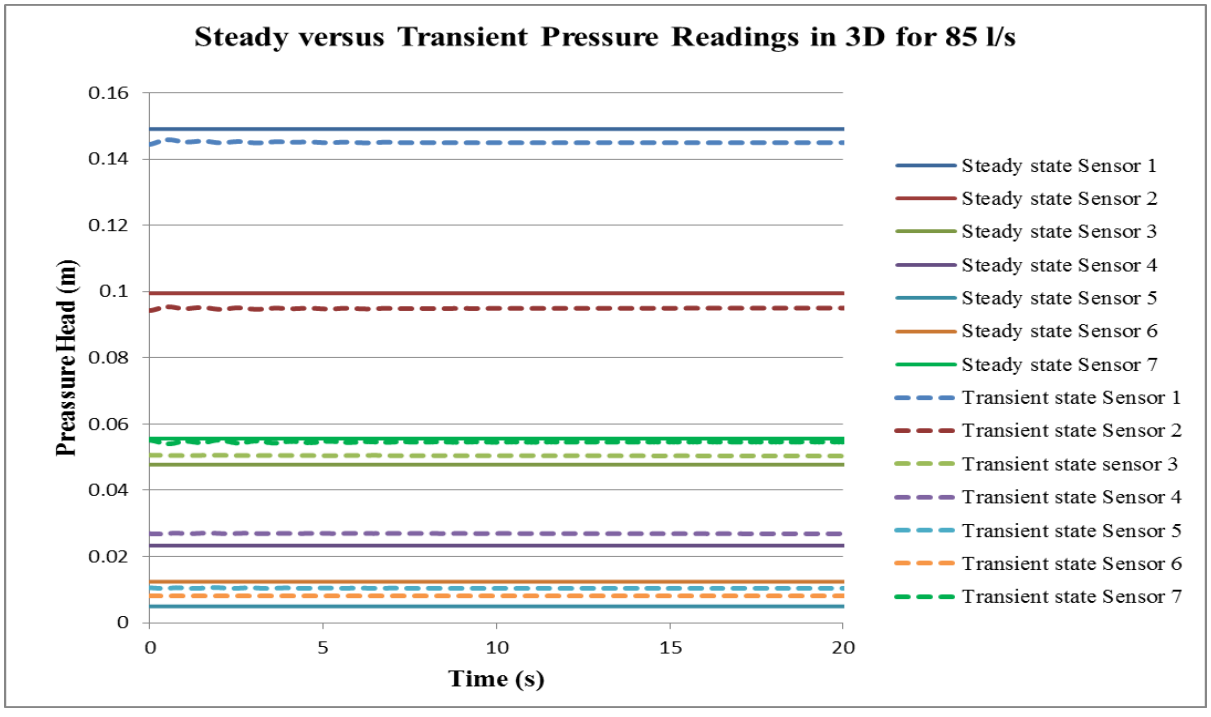

Figure C- 30: Comparison between 3D-simulated steady and fully hydrodynamic state models for a discharge of 85 l/s (Case-2)

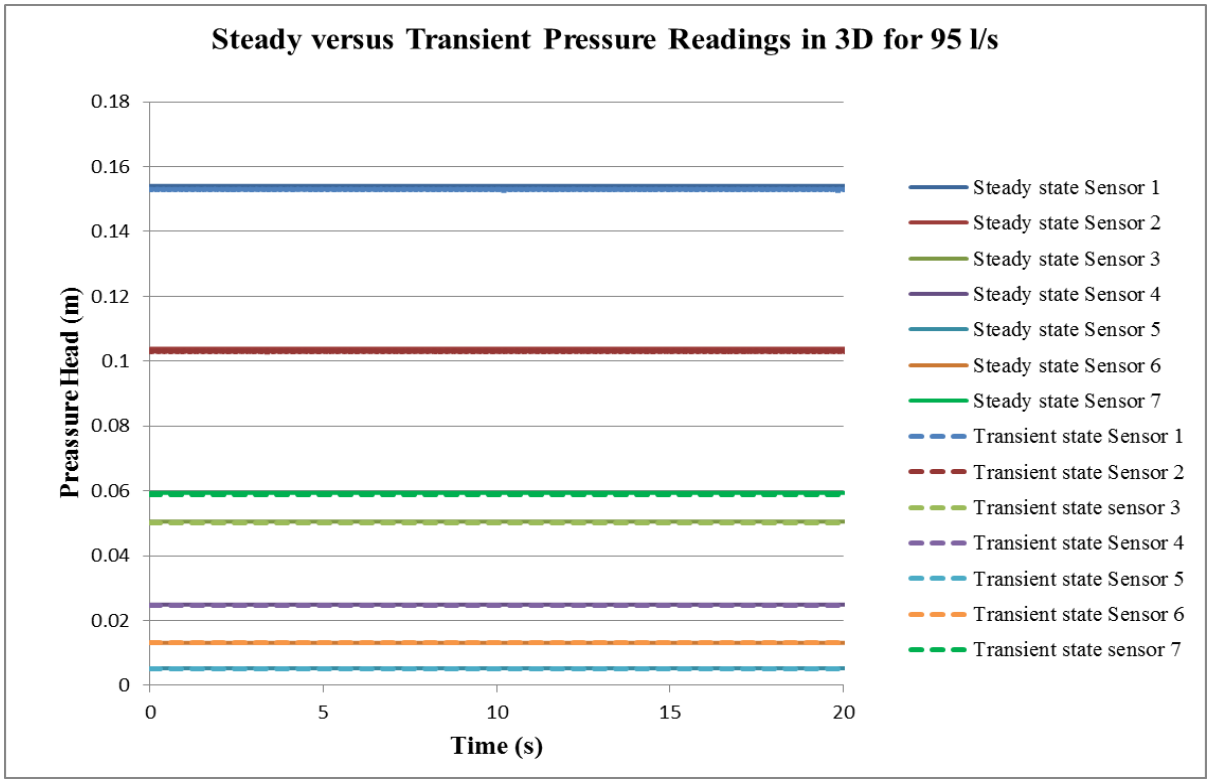

Figure C- 31: Comparison between 3D-simulated steady and fully hydrodynamic state models for a discharge of 95 l/s (Case-2)

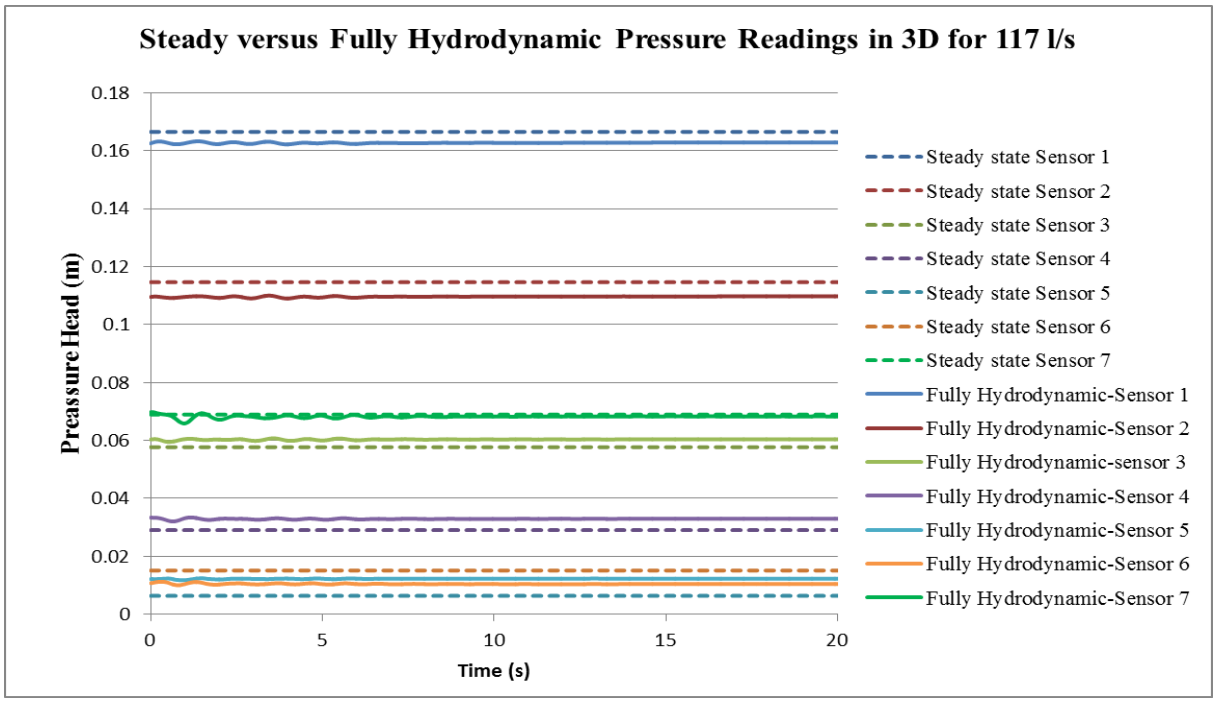

Figure C- 32: Comparison between 3D-simulated steady and fully hydrodynamic state models for a discharge of 117 l/s (Case-2)

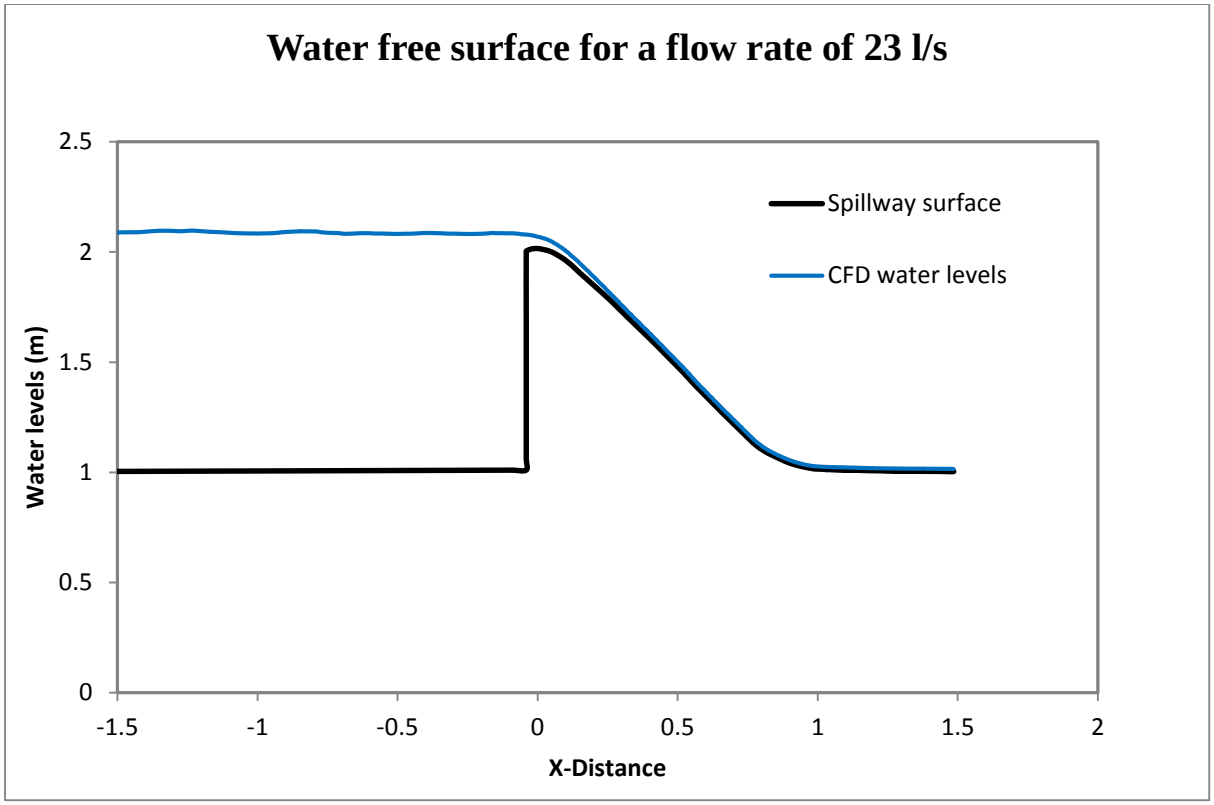

Figure C- 33: CFD Water free surface for Q= 23 l/s (Case-1)

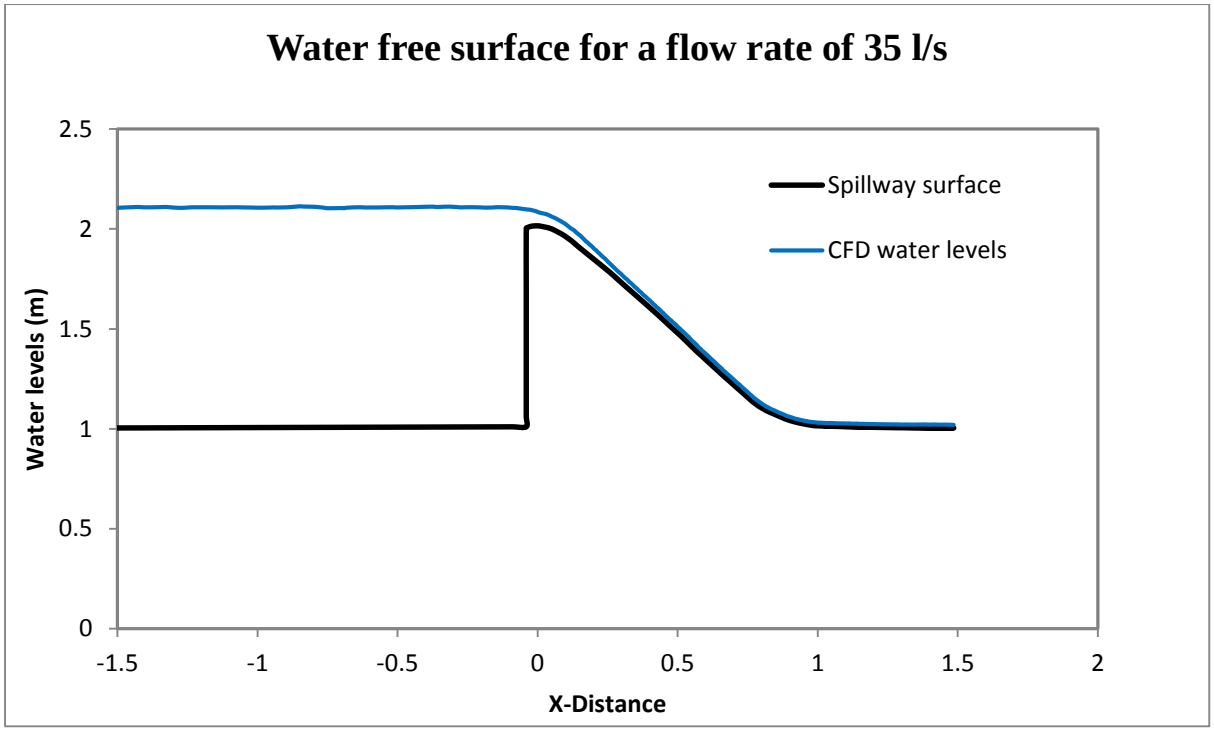

Figure C- 34: CFD Water free surface for Q= 35 l/s (Case-1)

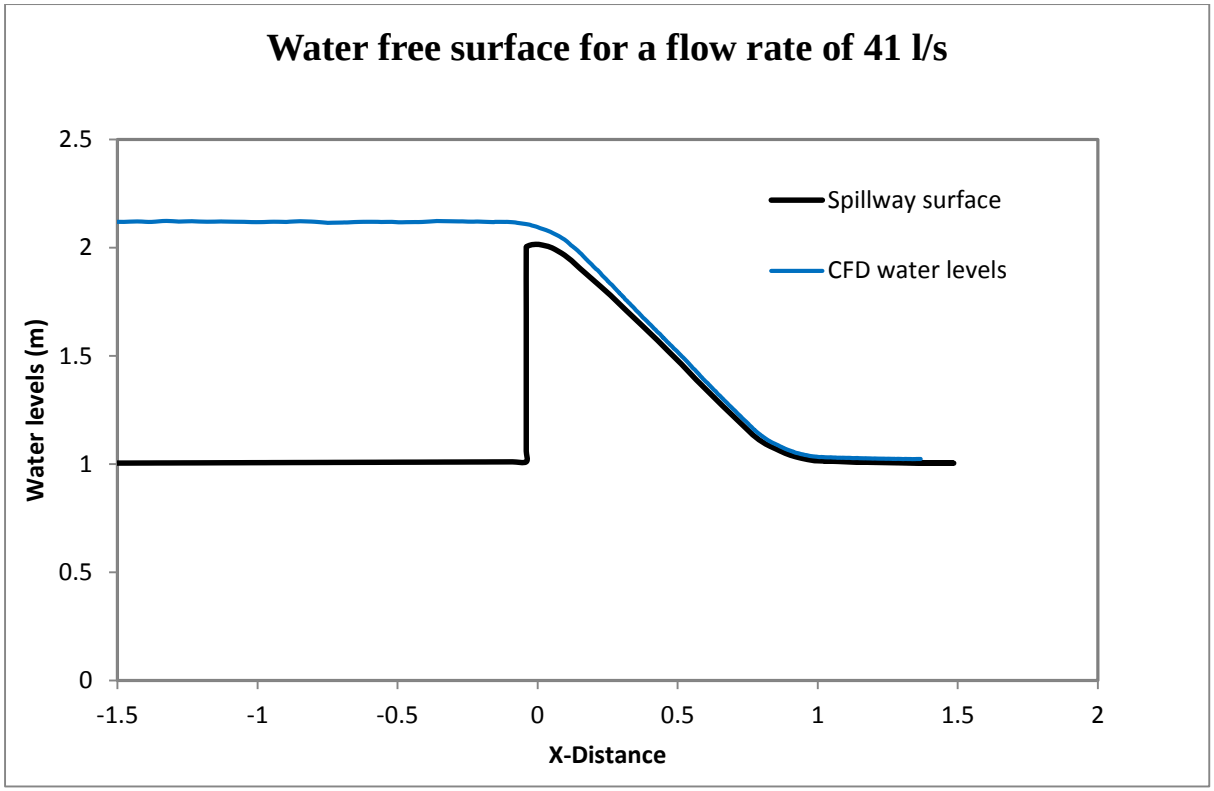

Figure C- 35: CFD Water free surface for Q= 41 l/s (Case-1)

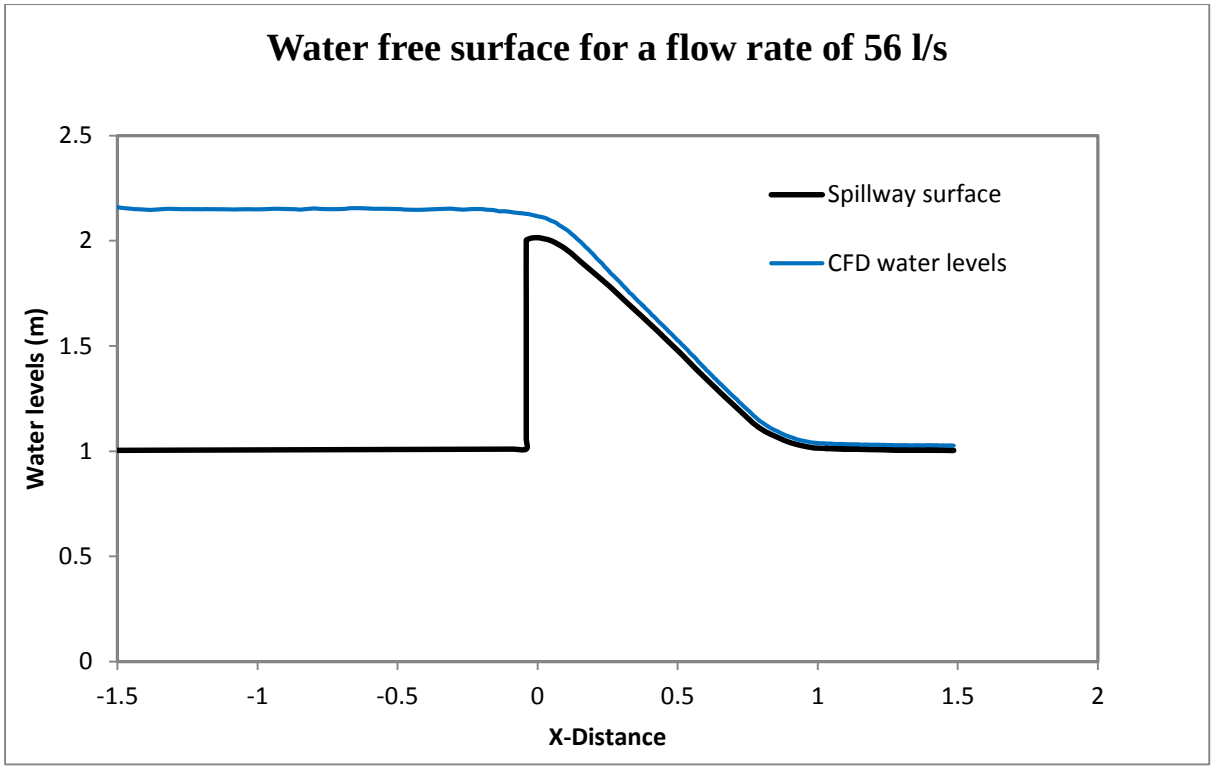

Figure C- 36: CFD Water free surface for Q= 56 l/s (Case-1)

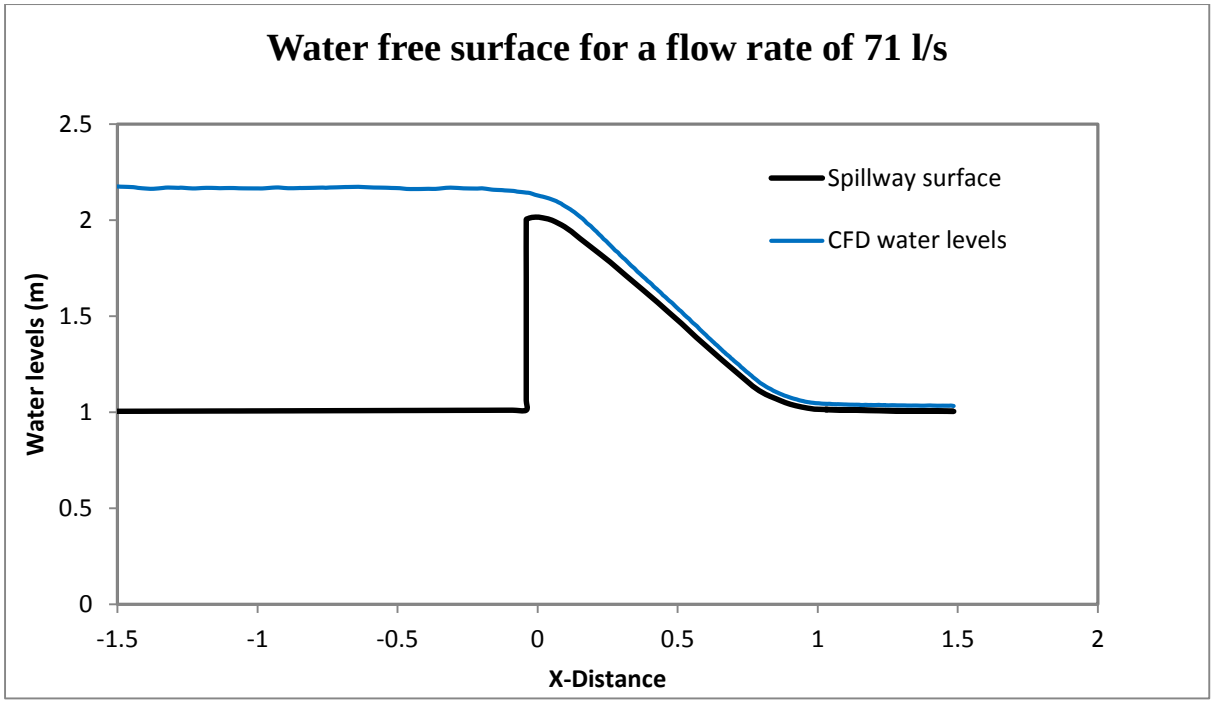

Figure C- 37: CFD Water free surface for Q= 71 l/s (Case-1)

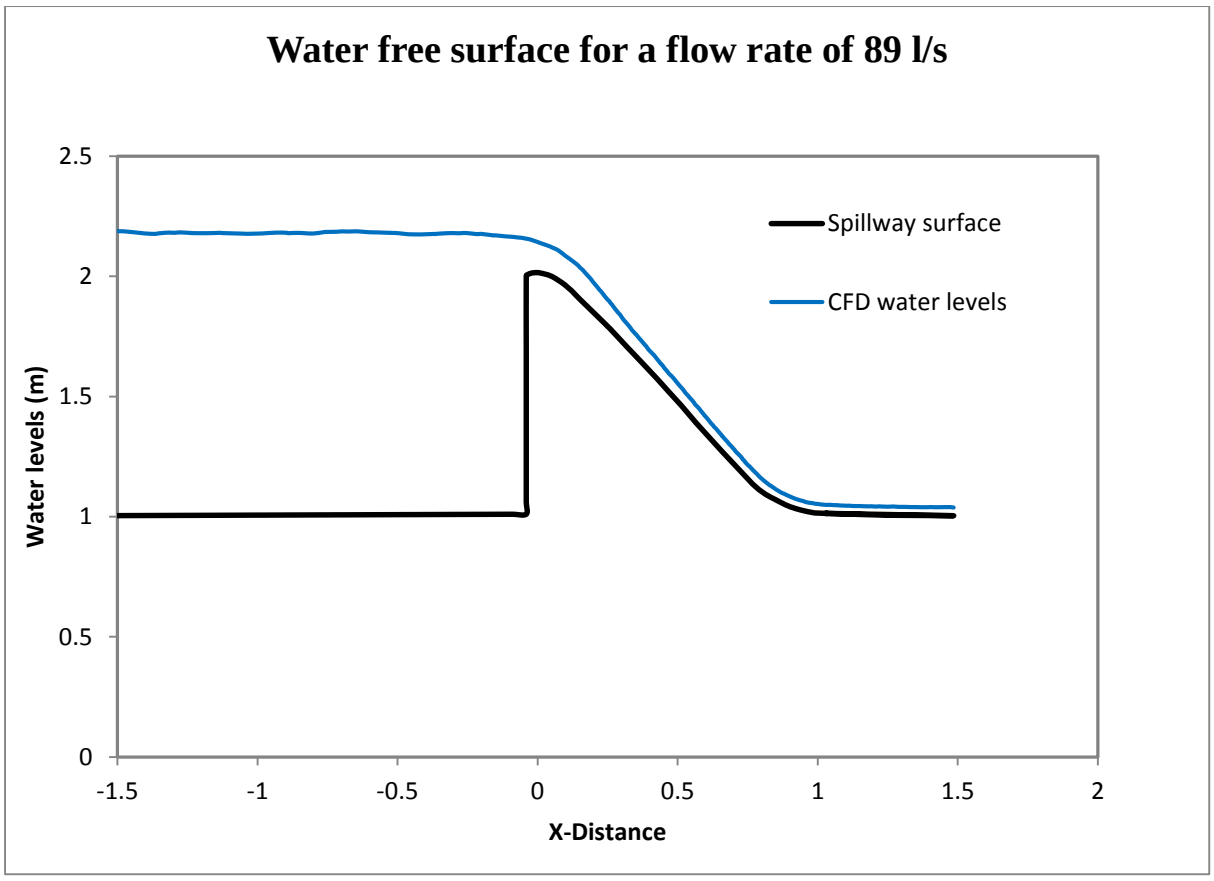

Figure C- 38: CFD Water free surface for Q= 89 l/s (Case-1)

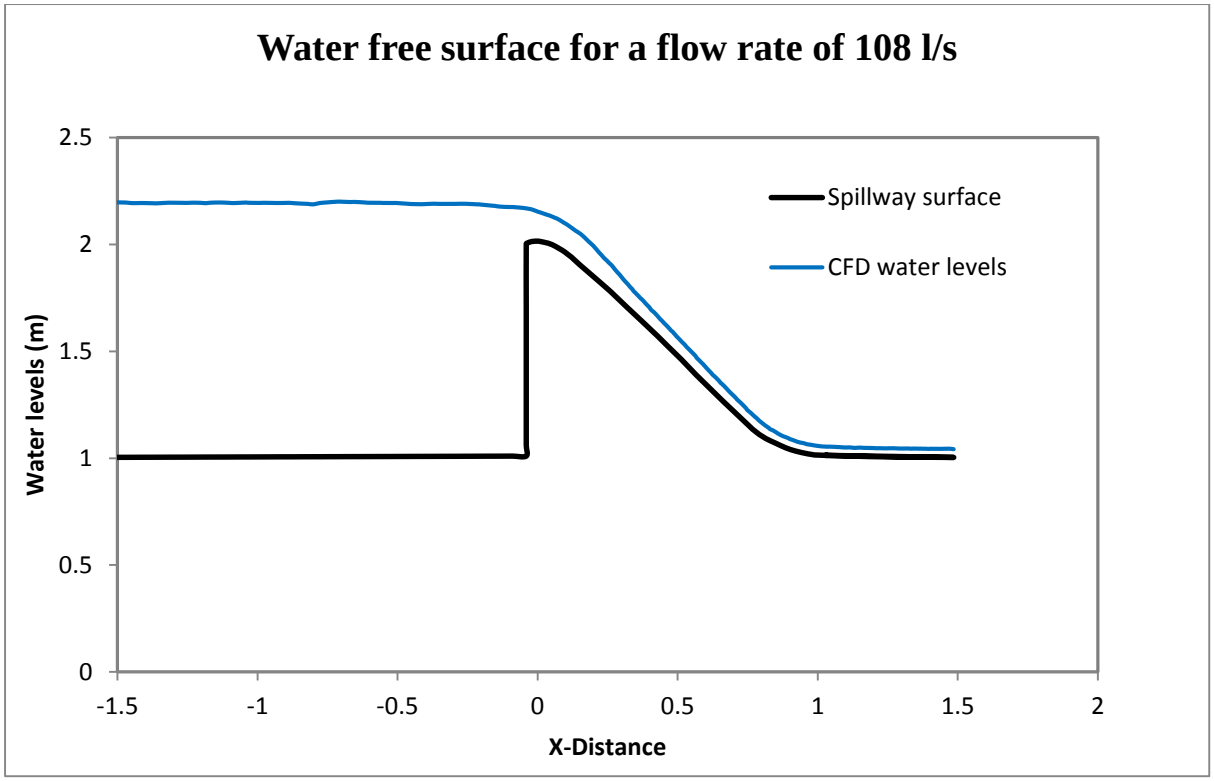

Figure C- 39: CFD Water free surface for Q= 108 l/s (Case-1)

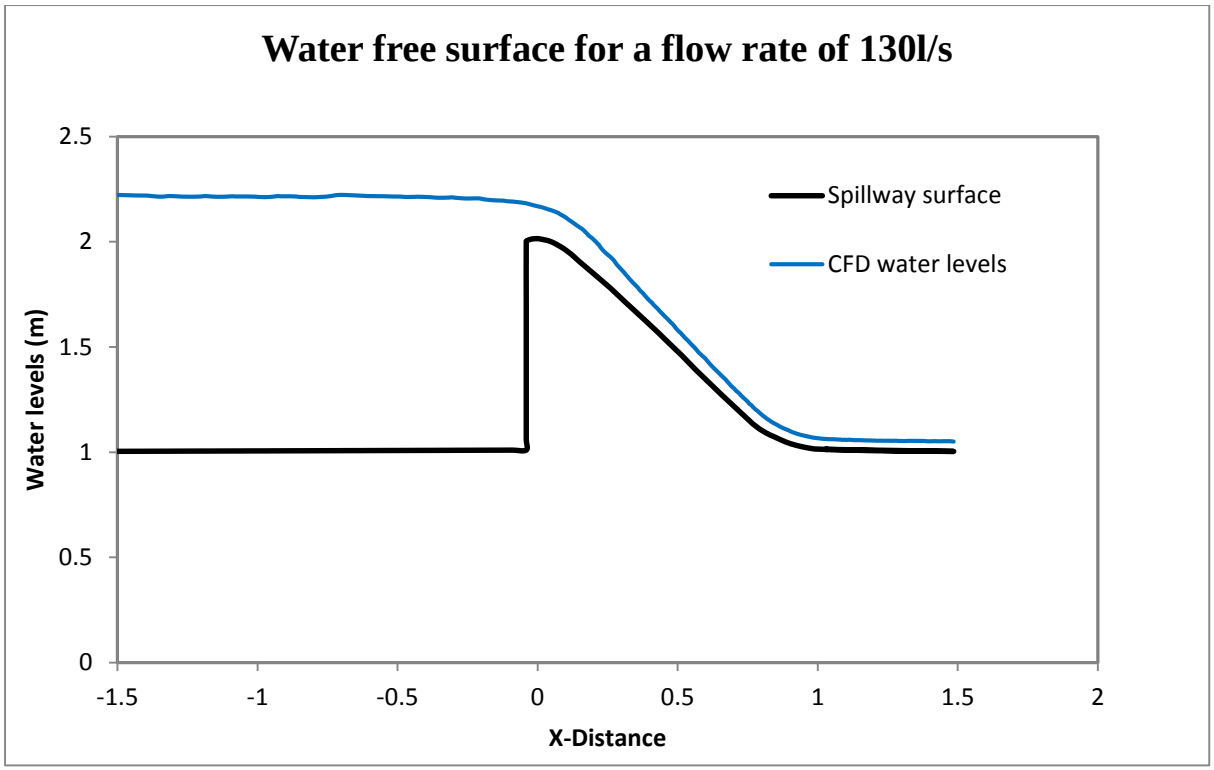

Figure C- 40: CFD Water free surface for Q= 130 l/s (Case-1)

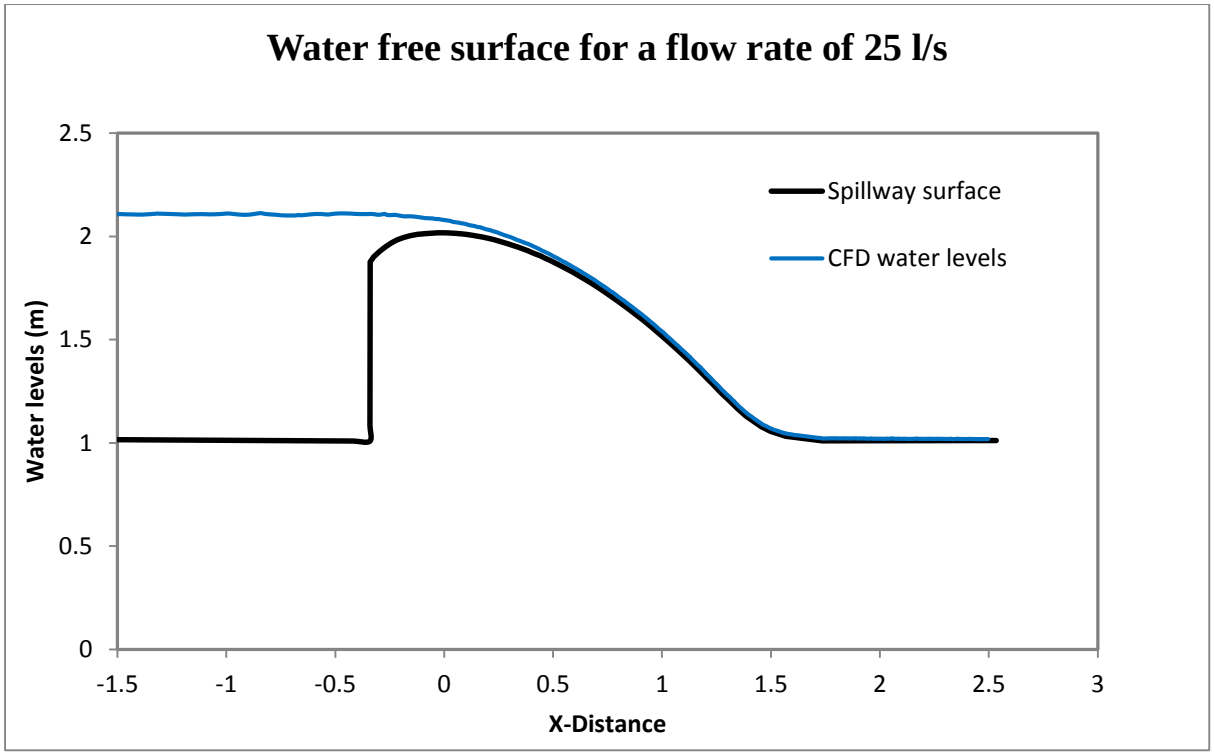

Figure C- 41: Water free surface for Q= 25 l/s (Case-2)

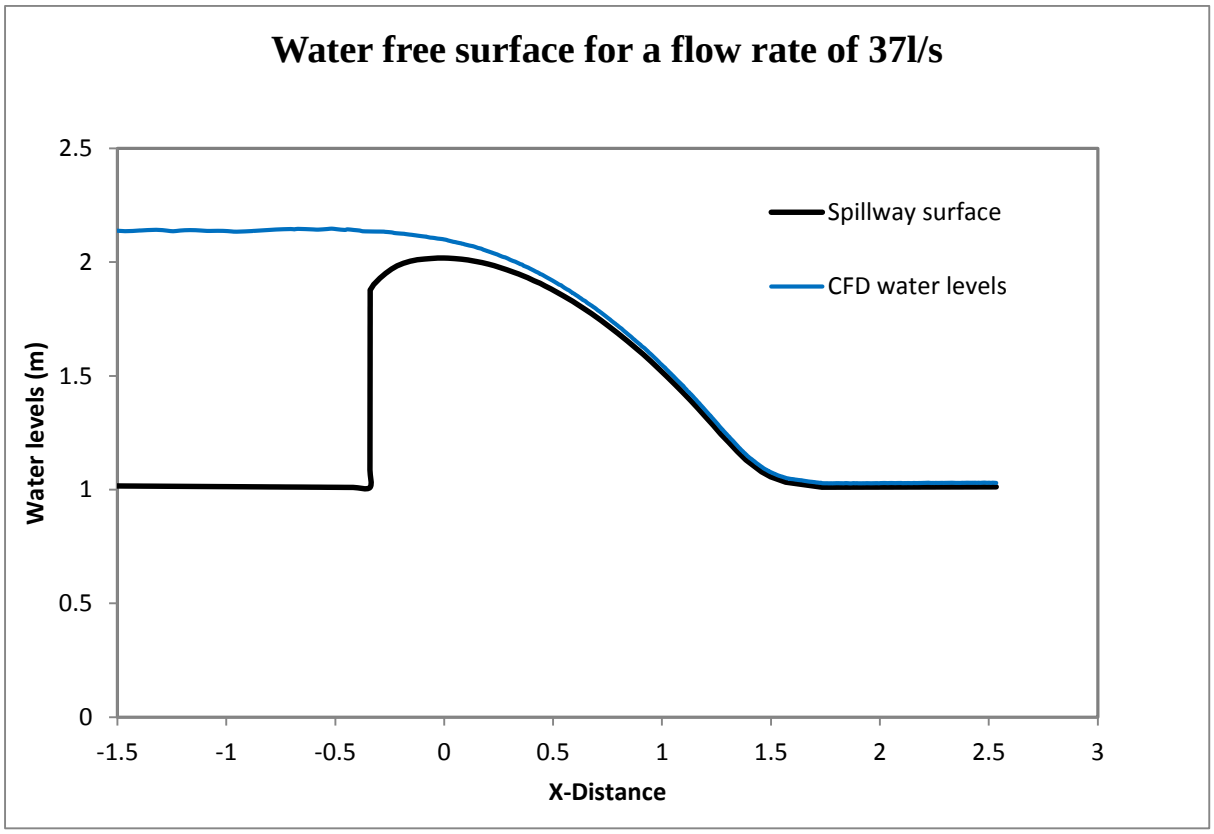

Figure C- 42: CFD Water free surface for Q= 37 l/s (Case-2)

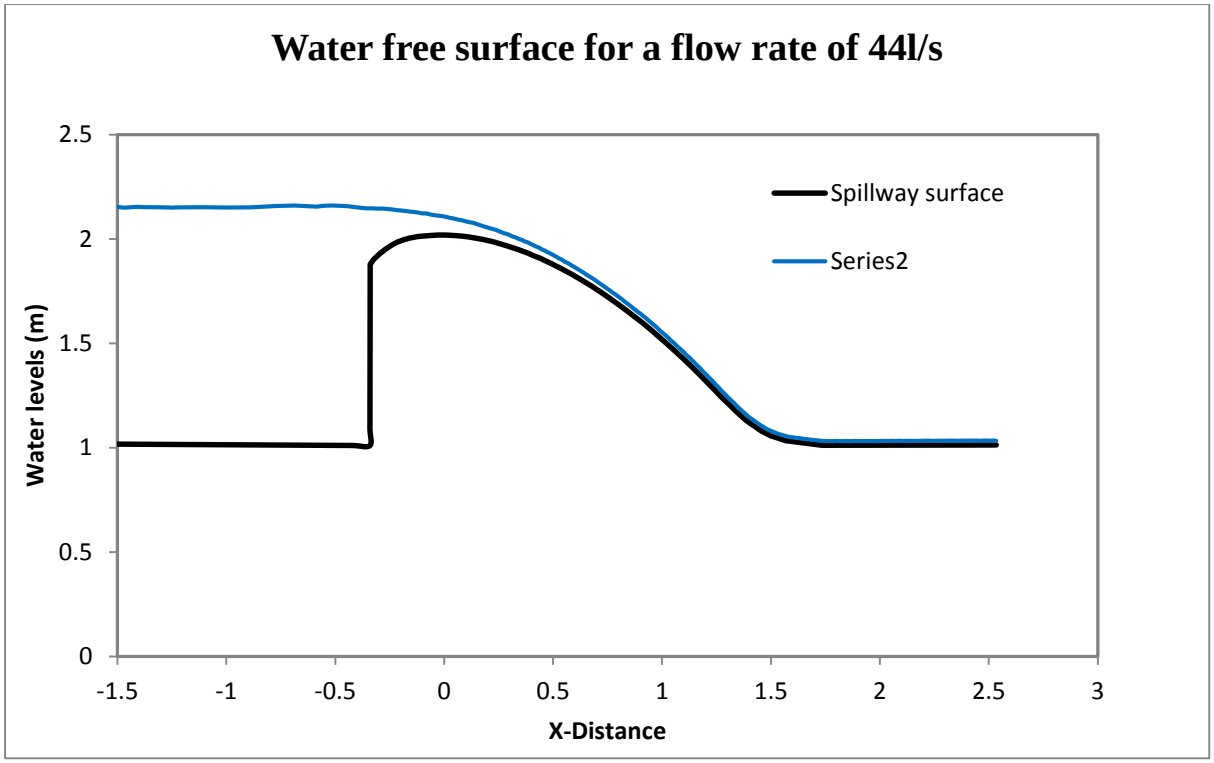

Figure C- 43: CFD Water free surface for Q= 44 l/s (Case-2)

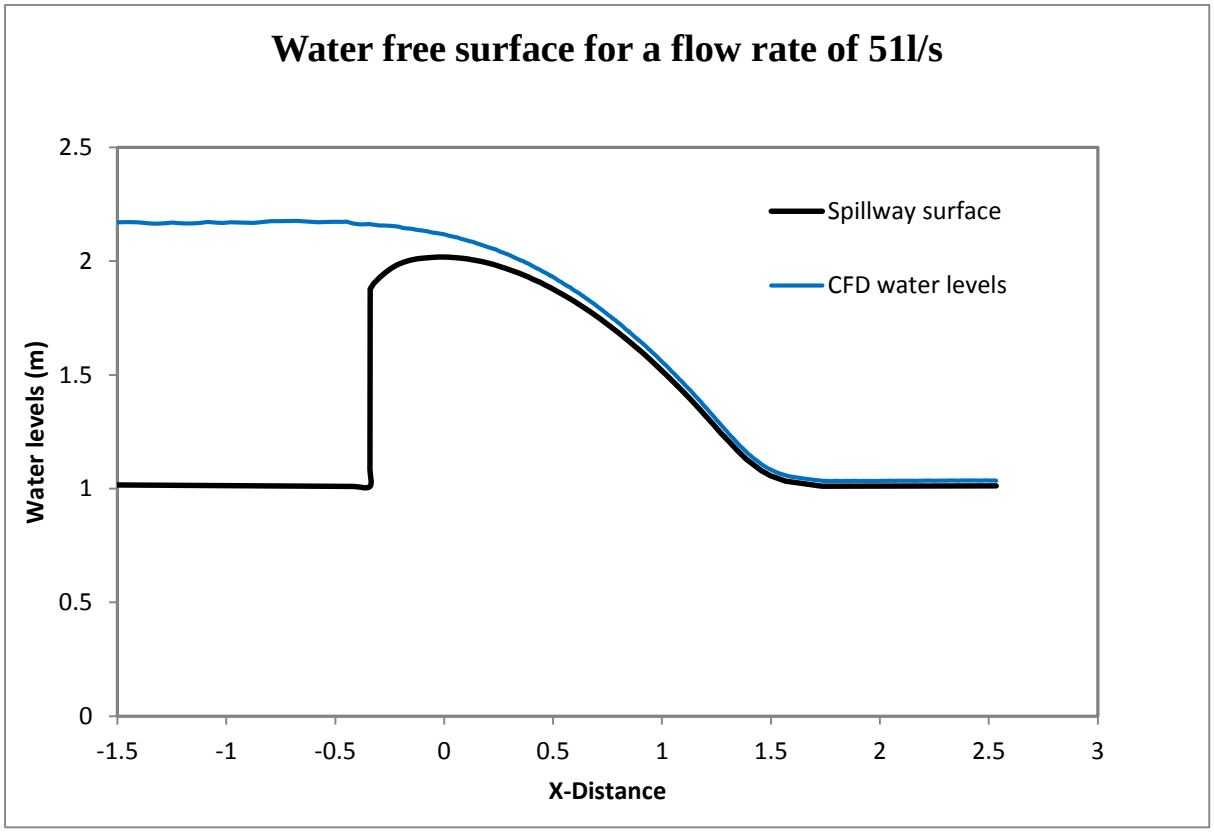

Figure C- 44: CFD Water free surface for Q= 51 l/s (Case-2)

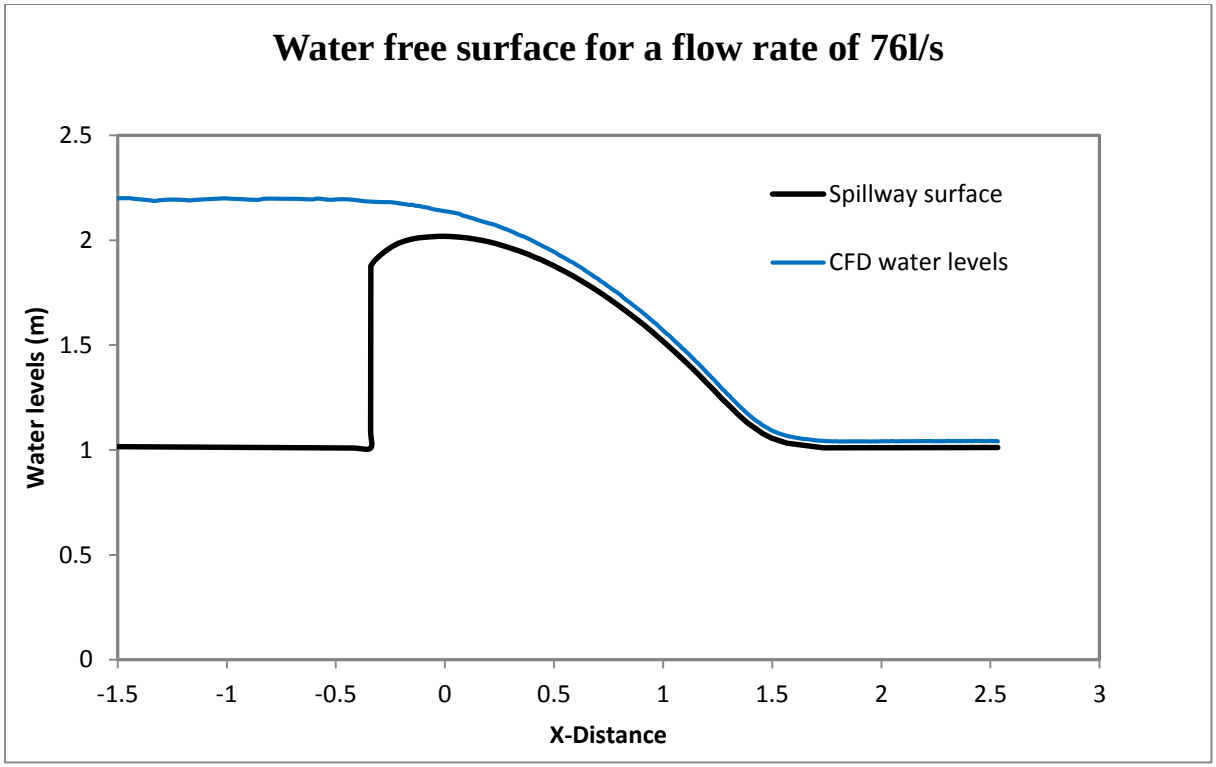

Figure C- 45: CFD Water free surface for Q= 76 l/s (Case-2)

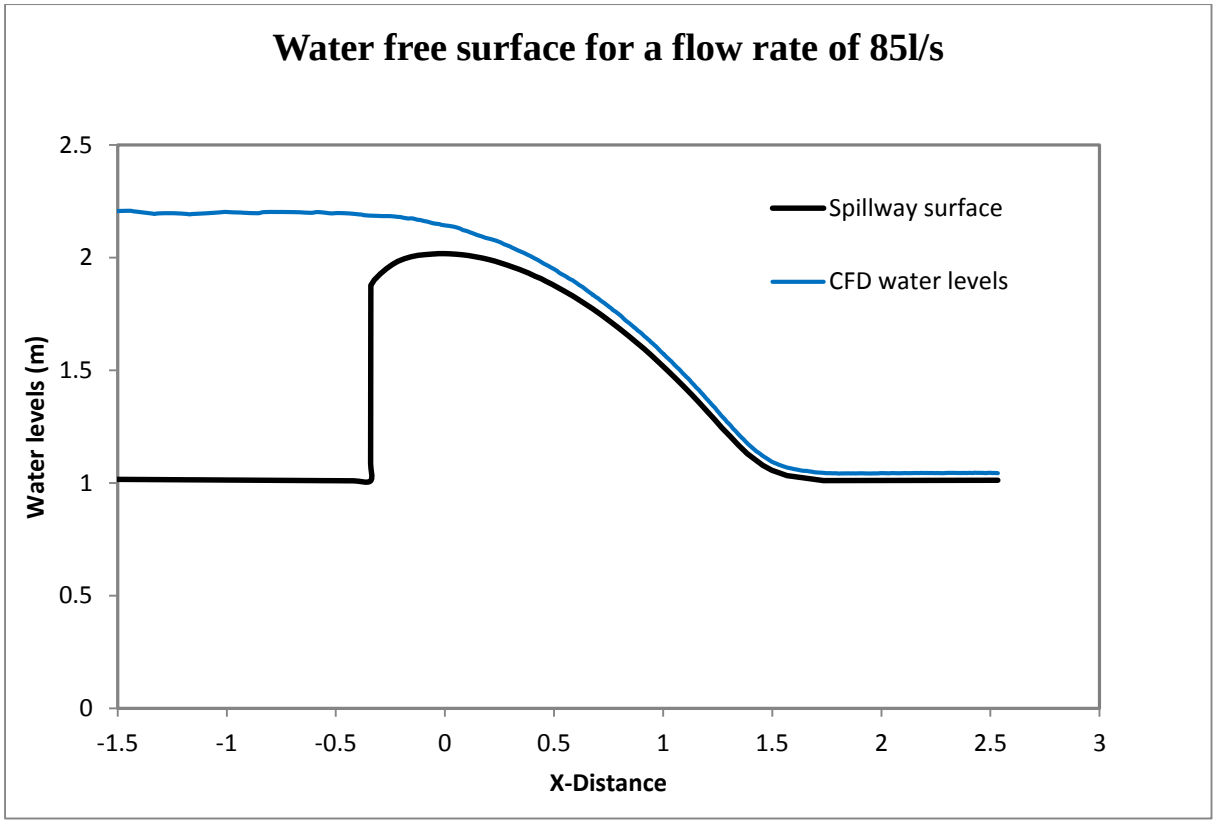

Figure C- 46: CFD Water free surface for Q= 85 l/s (Case-2)

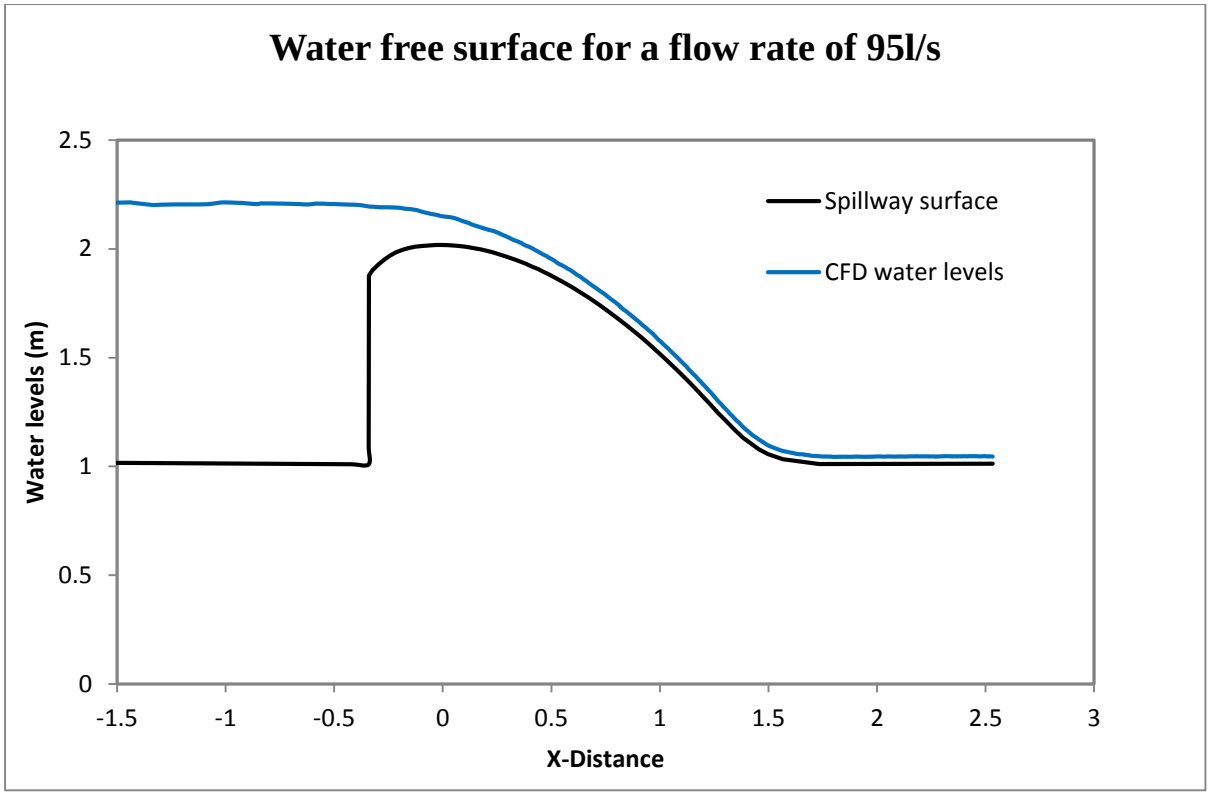

Figure C- 47: CFD Water free surface for Q= 95 l/s (Case-2)

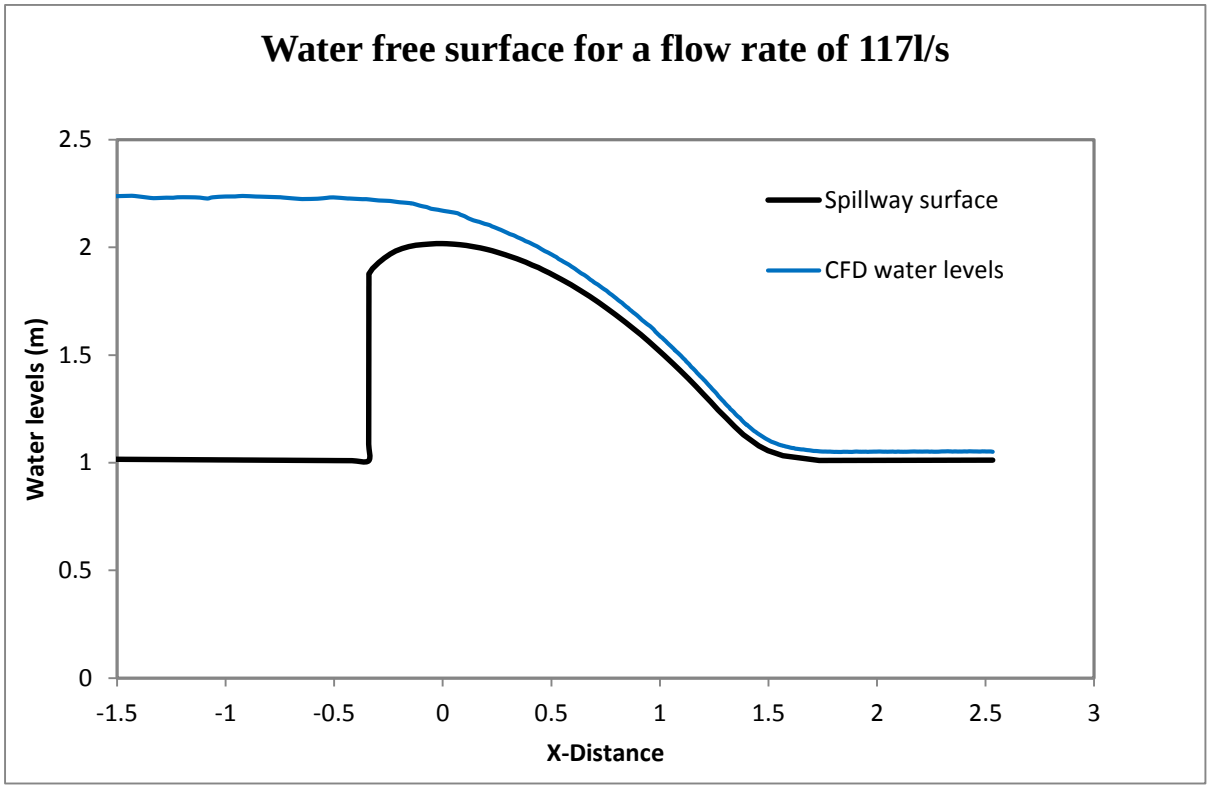

Figure C- 48: CFD Water free surface for Q= 44 l/s (Case-2)

Appendix D: Comparison of CFD and physical model results

D.1. Errors and Uncertainty

D.1.1. Definitions

According to Oberkampf, *et., al* (2001) & AIAA (1998),

- **Uncertainty "***is defined as a potential deficiency in any activity or phase of the modelling process that is due to the lack of knowledge*", whereas,
- **Error** "*is known as a recognizable deficiency in any phase or activity of modelling and simulation that is not due to lack of knowledge*".

The difference between the definitions of error and uncertainty is based on "the *lack of knowledge".* Although these errors and uncertainties cannot be completely avoided, the modeller attempts to reduce them as much as possible. Before drawing a final conclusion regarding the physical and numerical modelling accuracy, the results must be thoroughly analysed, once they are found inaccurate the set-up should be revised so as to yield a better solution accuracy.

For physical modelling, some major errors and uncertainties include systematic errors, instrumental errors and physical uncertainties. In numerical modelling, the limiting factors leading to inaccurate solution are mostly related to the conception and set-up phase of the model. These are uncertainty in model set-up, physical approximation, numerical errors and code errors. The subsequent section discusses the errors and uncertainties commonly found in physical modelling and Computational Fluid Dynamics modelling.

D.1.2. Physical Modelling Errors and Uncertainty

D.1.2.1. Systematic errors

Basically, systematic errors include scale effects and operation errors. The scale effects in physical modelling have a great impact on the accuracy of the results and they may lead to a severe increase as the ratio of prototype to model size increases. To minimise these effects, much attention should be given to the geometric, kinematic (time and velocity) and dynamic (force) similarity between the prototype and the model. In this study, there are no scale effects involved as the CFD modelling considered a1:1 scale of the physical modelling.

On the other hand, the operational method can affect the solution accuracy. During the laboratory testing, each test run was performed after setting a discharge over the model and allowing it to stabilise before recording the measurements. Nevertheless, with this continuous inflow, the flow surface elevation never remains the same. There are some fluctuations in water surchargesince the model continues to be supplied, which imply an increment and declining in the reservoir.

Falvery (2003) expresses an equation to represent this phenomenon by computing the difference between the outflow and inflow discharges of the flume or any other reservoir.

$$d\left(\frac{tQ_o}{A_r h_o}\right) = \frac{1}{1-\left(\frac{h}{h_o}\right)^{1.5}} d\left(\frac{h}{h_o}\right) \qquad \text{(D.1-1)}$$

Where:

$Q_o =$ The inflow discharge (m^3/s);

$A_r =$ The reservoir area (m^2);

$h =$ The head at any time (m);

$h_o =$ The head over the weir crest at steady state (m); and

$t =$ The time (s)

D.1.2.2 Instrumentation Errors

i. Pressure sensors

The pressure transducers used for pressure recordings during the physical modelling were WIKA S-10.

These transmitters are used for general applications including hydraulics and pneumatics, vacuum, test equipment, liquid level measurement, pressure control, compressor control, pump protection etc. They have an accuracy of ±0.25% for a full measuring span of 1m (WIKA, 2013) which implies that a maximum error of ± 2.5mm could be associated with the determination of the pressure readings.

The straight line depicted in Figure D-1 below represents ideal, linear output readings. In reality, the errors are produced by various transmitter components into the output signal. The quantity of error produced refers to the deviation from the ideal straight line (WIKA, 2013).

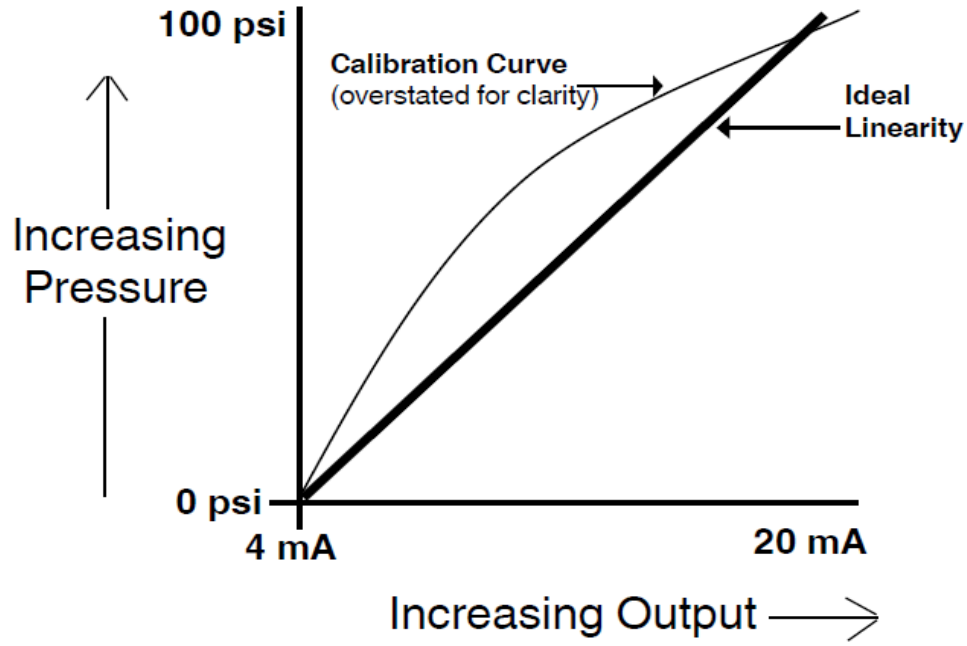

Figure D- 1: Accuracy representation of pressure transducers (WIKA, 2013)

ii. Flow gauge

The water flow discharge (Q) for each test run was measured with an electromagnetic flow meter (SAFMAG). This flow gauge type model has an accuracy of 0.5% of the flow rate.

The lowest and highest flow rates measured during testing were 23 l/s and 130 l/s respectively which mean that the accuracy of the flow meter ranges from ± 0.115 *l*/s to ± 0.65 *l*/s.

iii. Needle (point) gauge

To measure the water surcharge, a needle gauge was adopted in physical modelling. The accuracy in measurement was ± 0.001m.

D.1.2.3. Physical Modelling Uncertainty

During physical modelling, there were some leaks and losses throughout the system. This was not an easy task to avoid them totally or to quantify them. They were assumed negligible and less than 1%.

D.1.3. CFD Modelling Errors and Uncertainty

D.1.3.1. Human Error

This category of error is the result of the modeller's errors made while performing simulations by the incorrect operation of the tools available. In addition, human error can result from the incorrect analysis of the solution provided by CFD packages. This type of errors can be avoided by improving the understanding of the parameters in modelling.

D.1.3.2. Coding errors

Coding errors involve mistakes in Computer packages. These errors are made during the development of these packages and they are very difficult to discover as they are the most insidious forms of error.

D.1.3.3. Numerical errors

The process of solving partial differential equations through cells can result in three different categories of error, namely discretisation and solution errors, round off errors and iterative convergence errors.

i. **Discretisation errors**: They are generated from the use of numerical algebraic expressions to represent partial differential equations (Perez, 2008). These errors are associated with neglected contributions due to the higher-order terms, which give rise to errors in CFD results (Versteeg & Malalasekera, 2007).
   It is possible to reduce the discretised error until it becomes negligible by reducing the size of the time step and refining the mesh cells.

ii. **Round off errors**: These types of errors are generated from the representation of a real number to a finite number of significant digits. Round off errors contribute to numerical errors at a small scale and they are considered insignificant since computers can store numbers with 16, 32 or 64 bits.

iii. **Iterative convergence errors**: In the CFD modelling process, the solution of flow problem entails iterative steps until convergence is reached. The final solution must satisfy the discretised flow equations within the numerical domain. The difference between the final solution of the coupled set of discretised flow equations and the current solution is the error associated with iterative convergence.

D.1.3.4. Model set-up uncertainty

i. **Domain geometry:** While building computational geometry, the modeller is required to specify the shape and size of the region of concern correctly. However, it is gaugely impossible to build a CAD model to its design specification. This problem generates some differences between the CAD geometry and the real model.

ii. **Boundary conditions:** It is quite impossible to obtain a high degree of accuracy to the input boundary values such as pressure, temperature and velocity which leads to imperfect behaviour. Most of the time, the modeller is obliged to select the boundary condition values pre-set in the CFD package or to make general assumptions which can be approximately true.

iii. **Fluid properties:** Normally, the fluid properties depend on the temperature and pressure of the environment within which the fluid is flowing. In most cases, these parameters are assumed constant, which reduces, the convergence thereby producing an error if the assumption is not correct.

iv. **Physical representation uncertainty:** Physical model uncertainty is referred to as the representation failure of the real life flow in CFD modelling due to the lack of knowledge of physical and/or chemical processes.

D.2. Comparison of Physical model and CFD model results

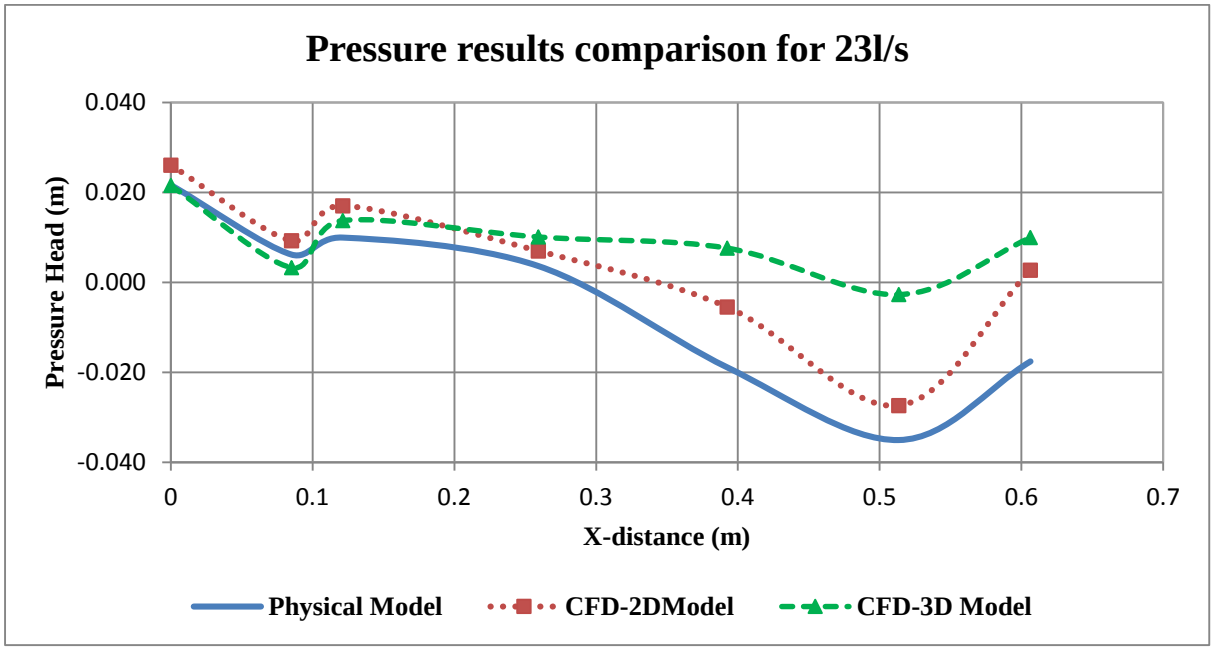

Figure D- 2: Comparison of CFD steady and average Physical model pressures for Q= 23 l/s (Case-1)

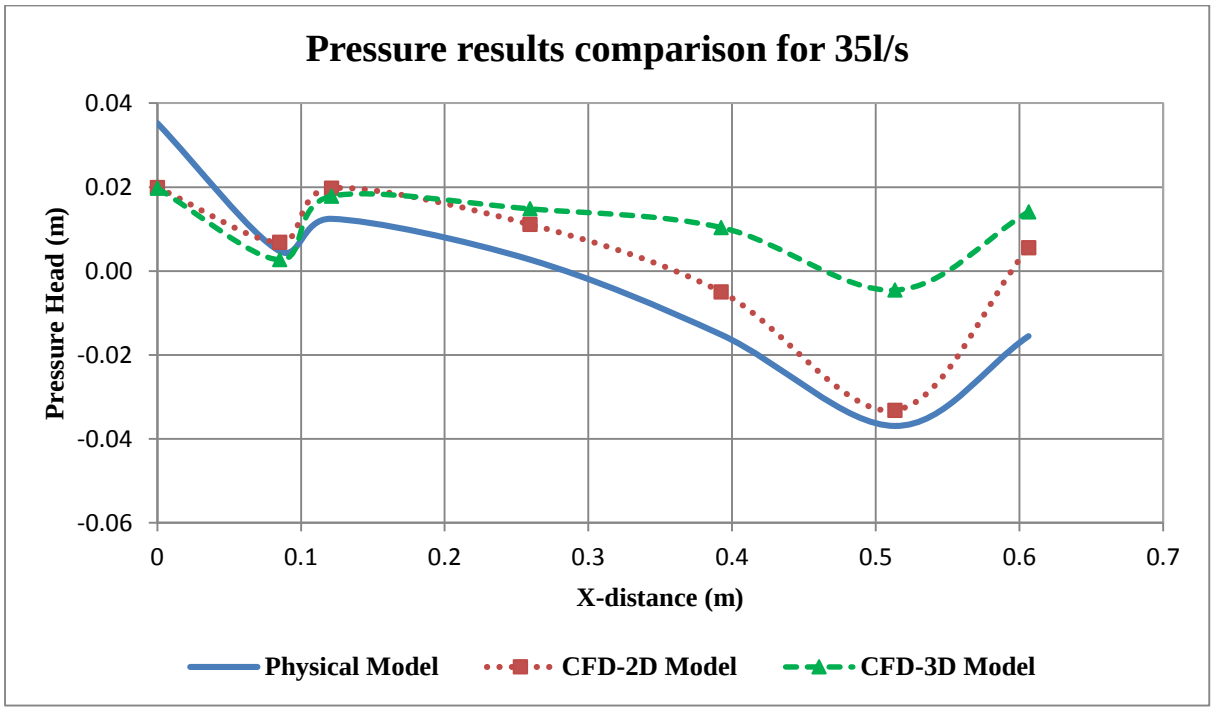

Figure D- 3: Comparison of steady-CFD and average Physical model pressures for Q= 35 l/s (Case-1)

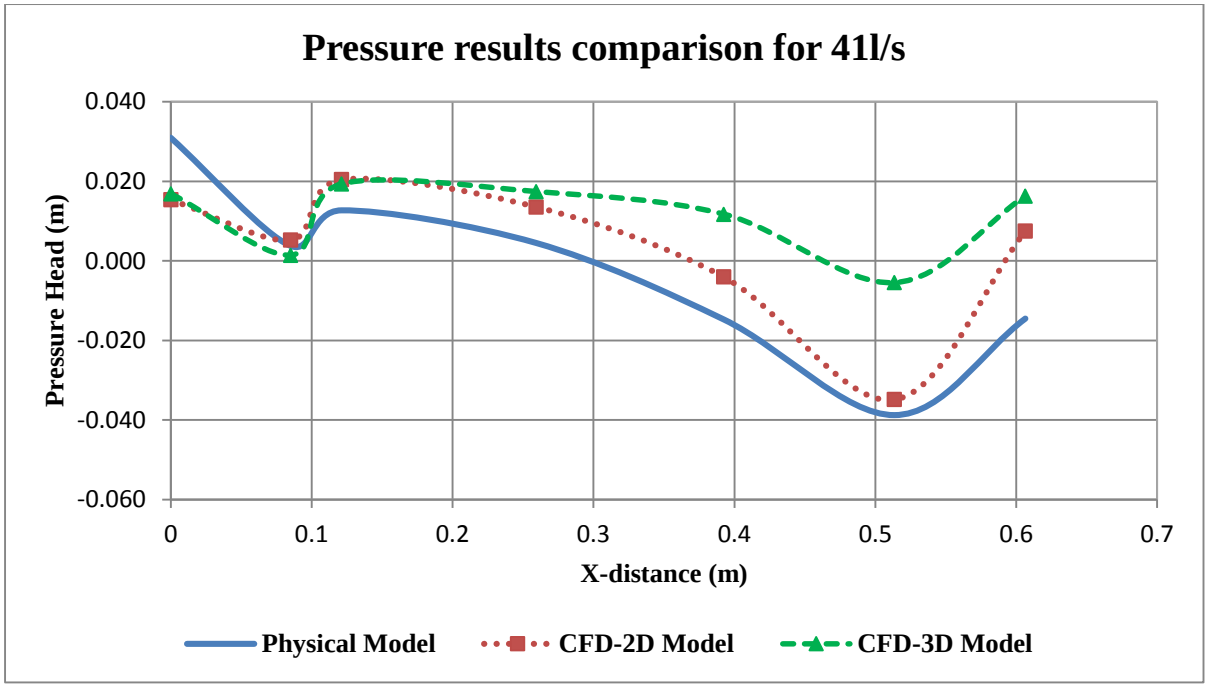

Figure D- 4: Comparison of steady-CFD and average Physical model pressures for Q= 41 l/s (Case-1)

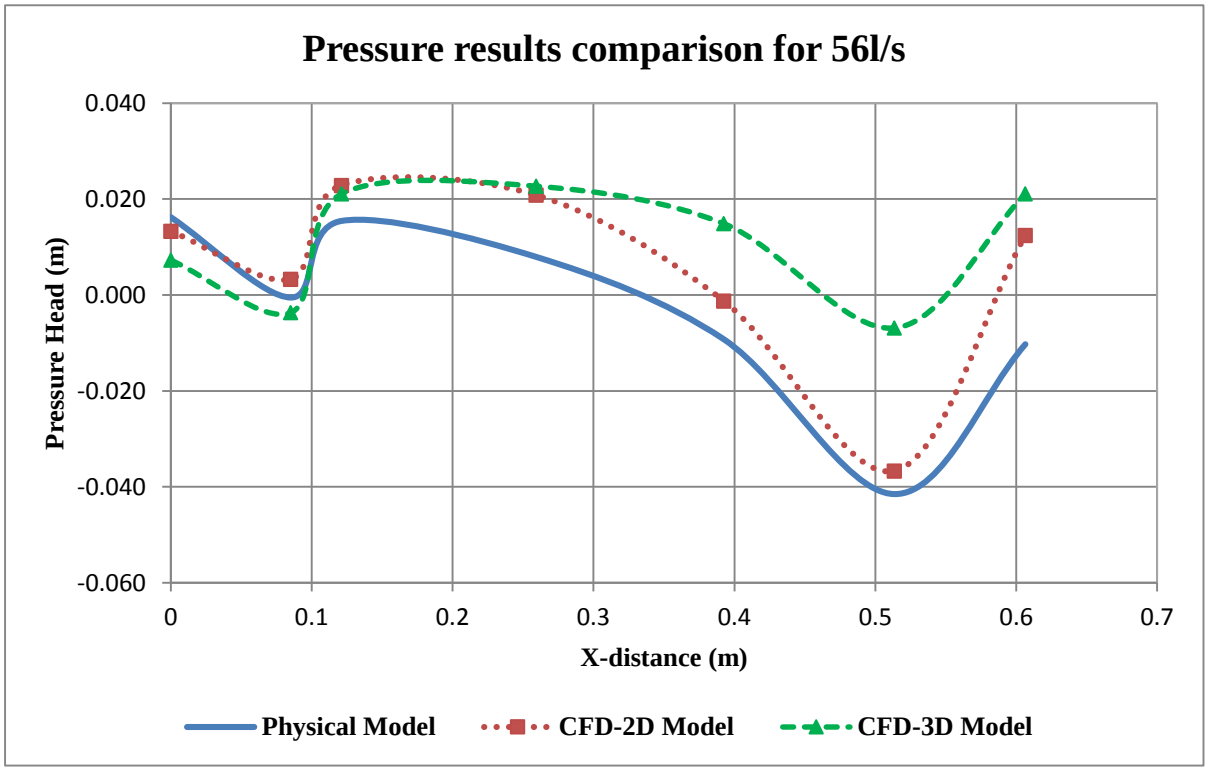

Figure D- 5: Comparison of steady-CFD and average Physical model pressures for Q= 56 l/s (Case-1)

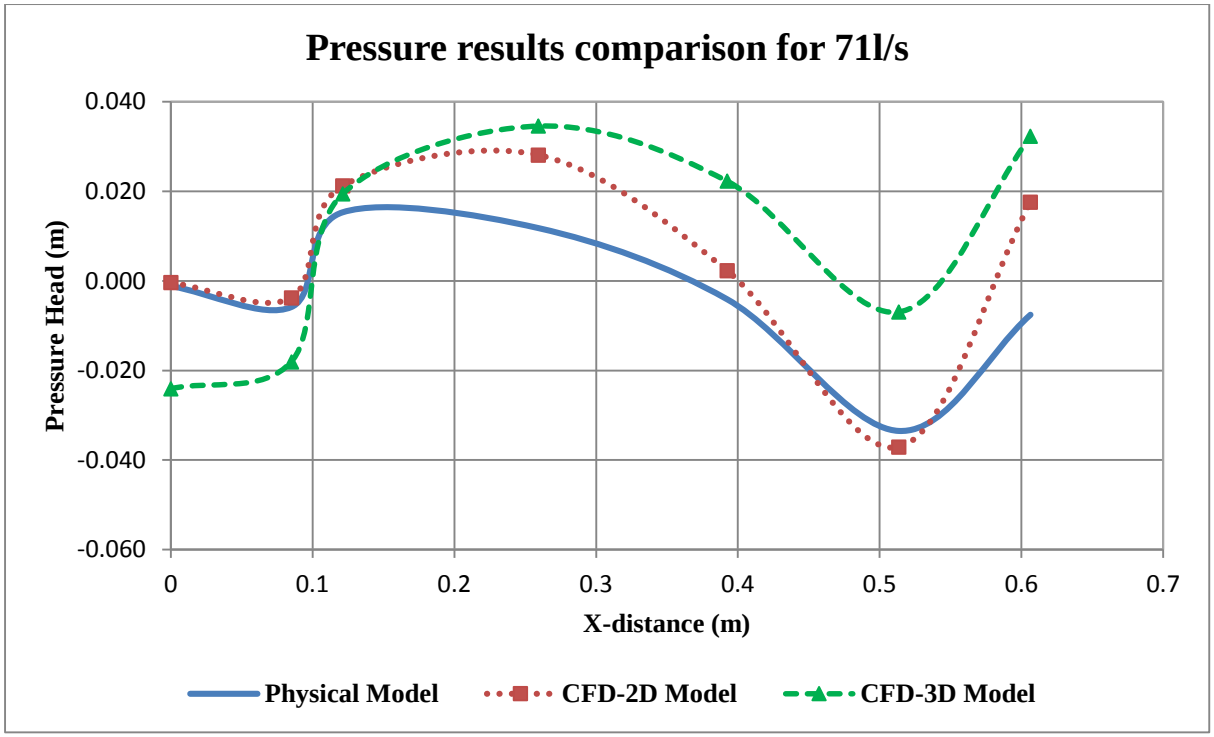

Figure D- 6: Comparison of stead CFD and average Physical model pressures for Q= 71 l/s (Case-1)

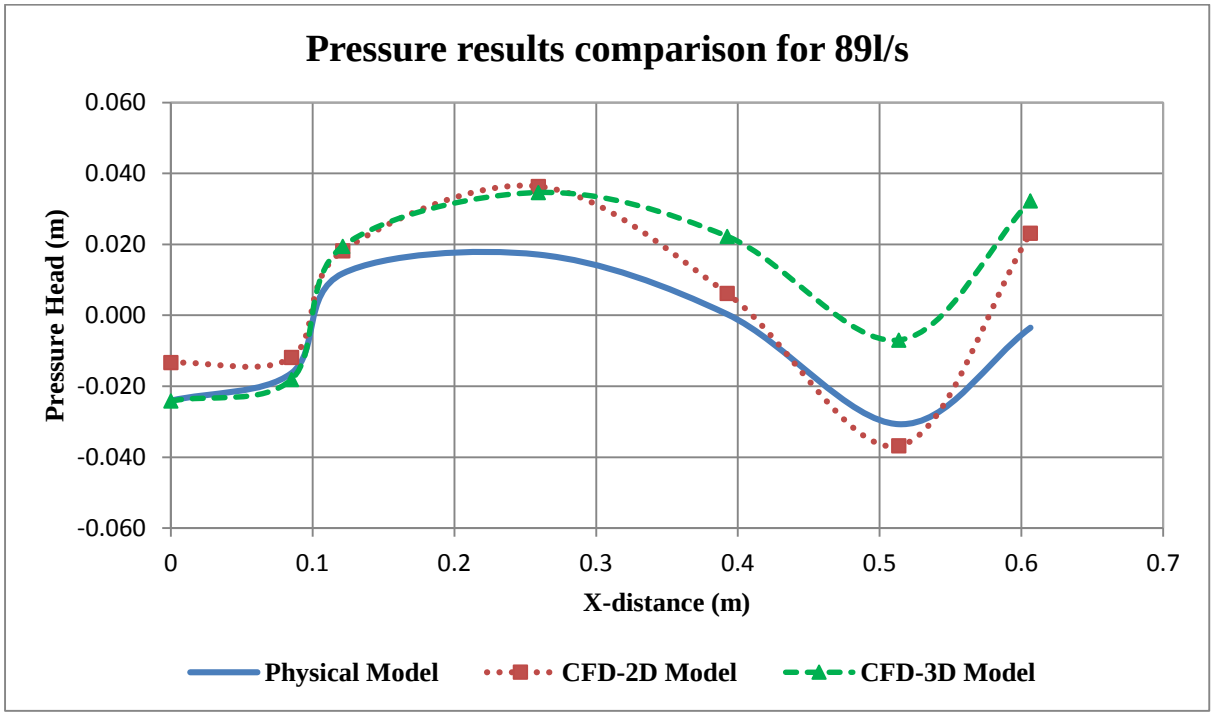

Figure D- 7: Comparison of stead CFD and average Physical model pressures for Q= 89 /s (Case-1)

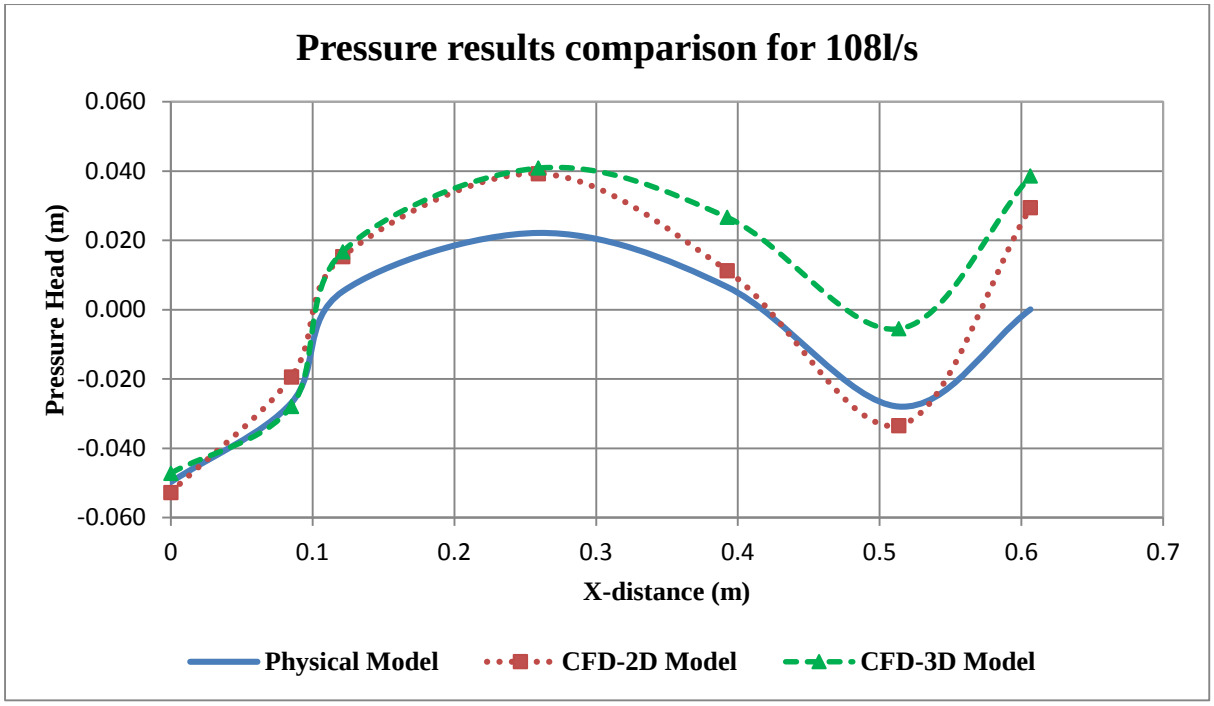

Figure D- 8: Comparison of average CFD and average Physical model pressures for Q= 108l/s (Case-1)

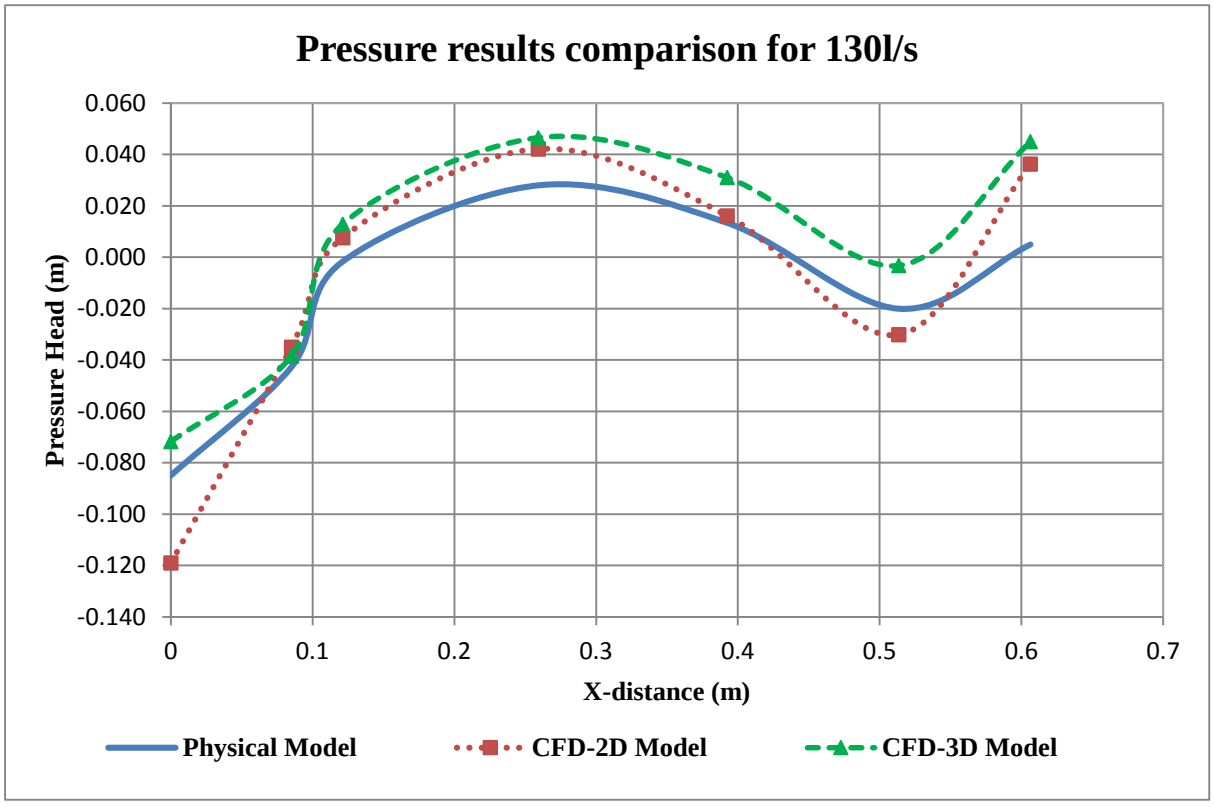

Figure D- 9: Comparison of stead CFD and average Physical model pressures for Q= 130 l/s (Case-1)

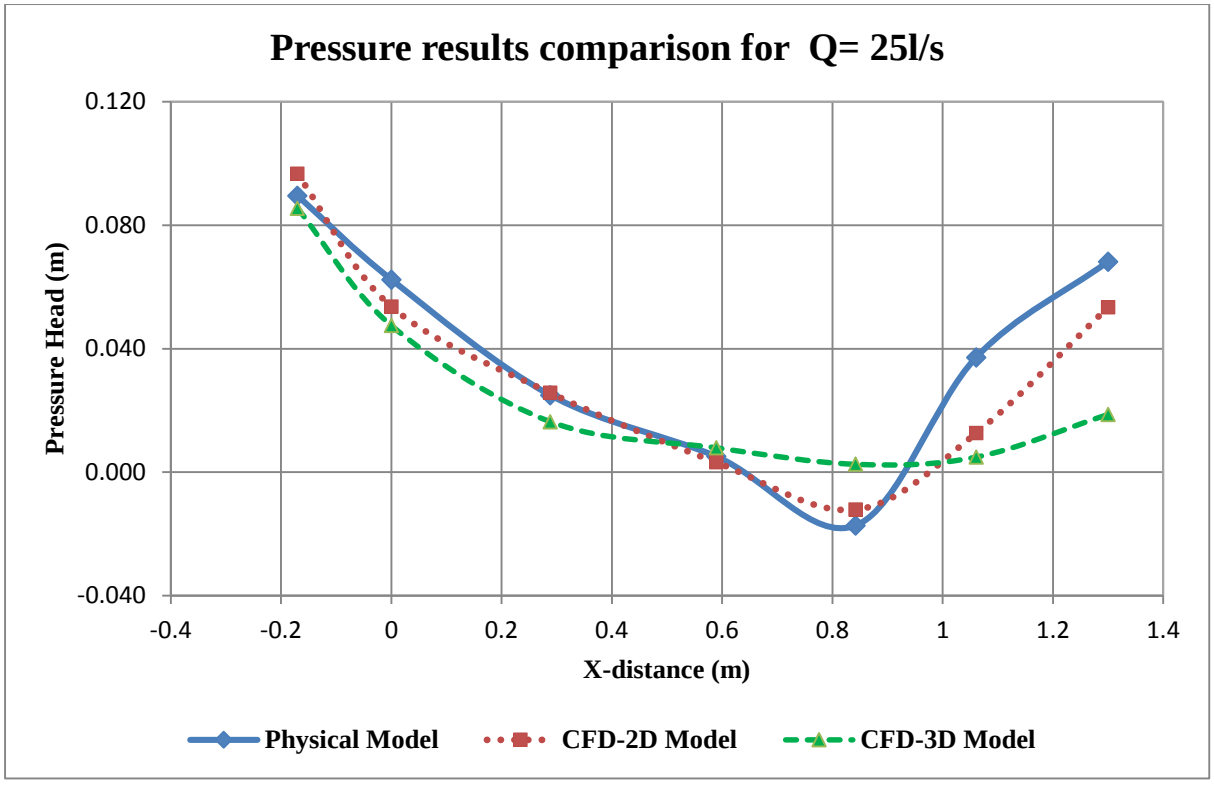

Figure D- 10: Comparison of stead CFD and average Physical model pressures for Q= 25 l/s (Case-2)

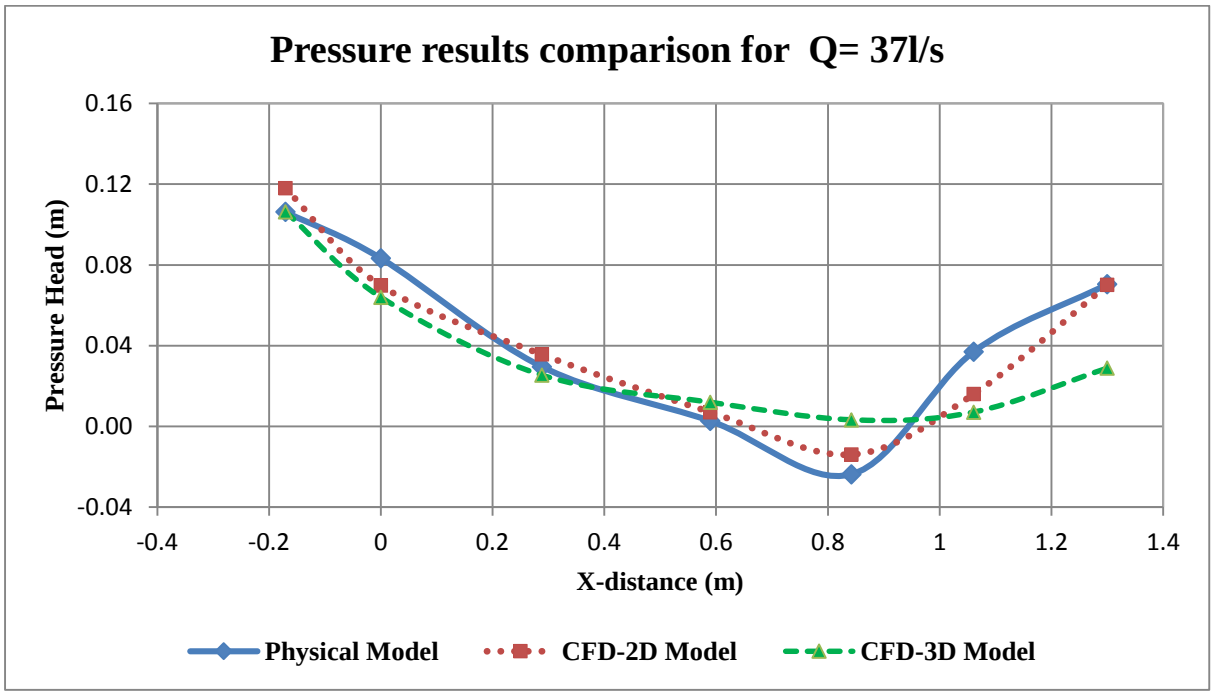

Figure D- 11: Comparison of stead CFD and average Physical model pressures for Q= 37 l/s (Case-2)

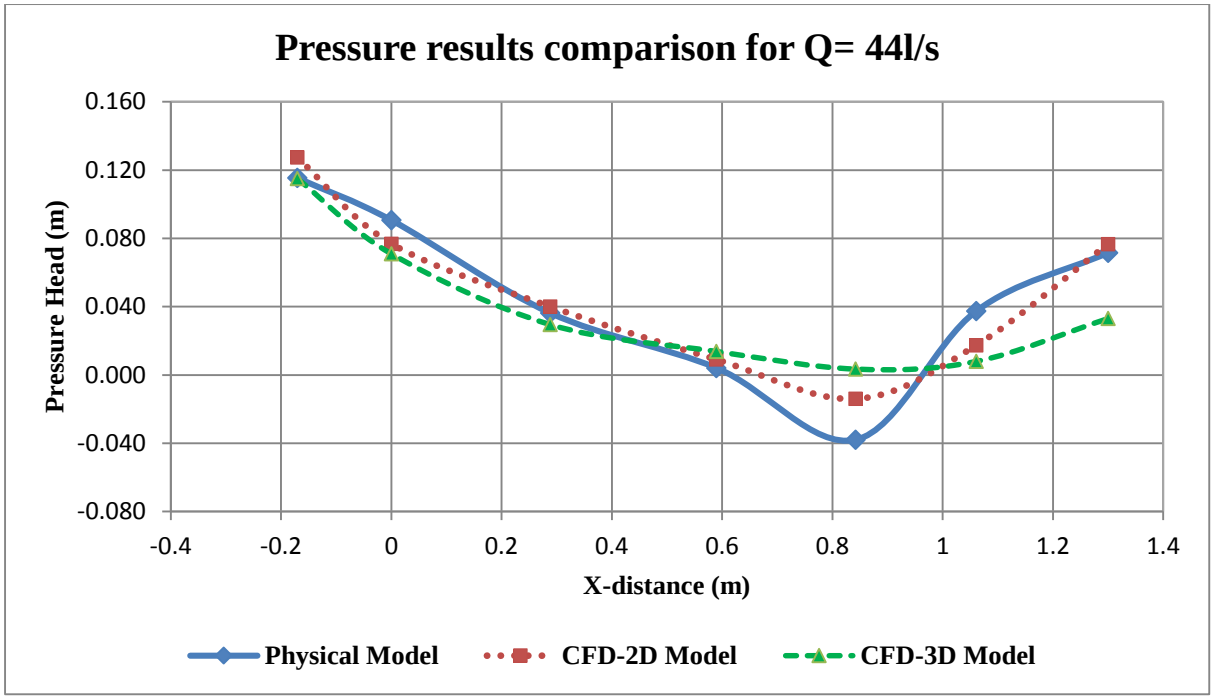

Figure D- 12: Comparison of stead CFD and average Physical model pressures for Q= 44 l/s (Case-2)

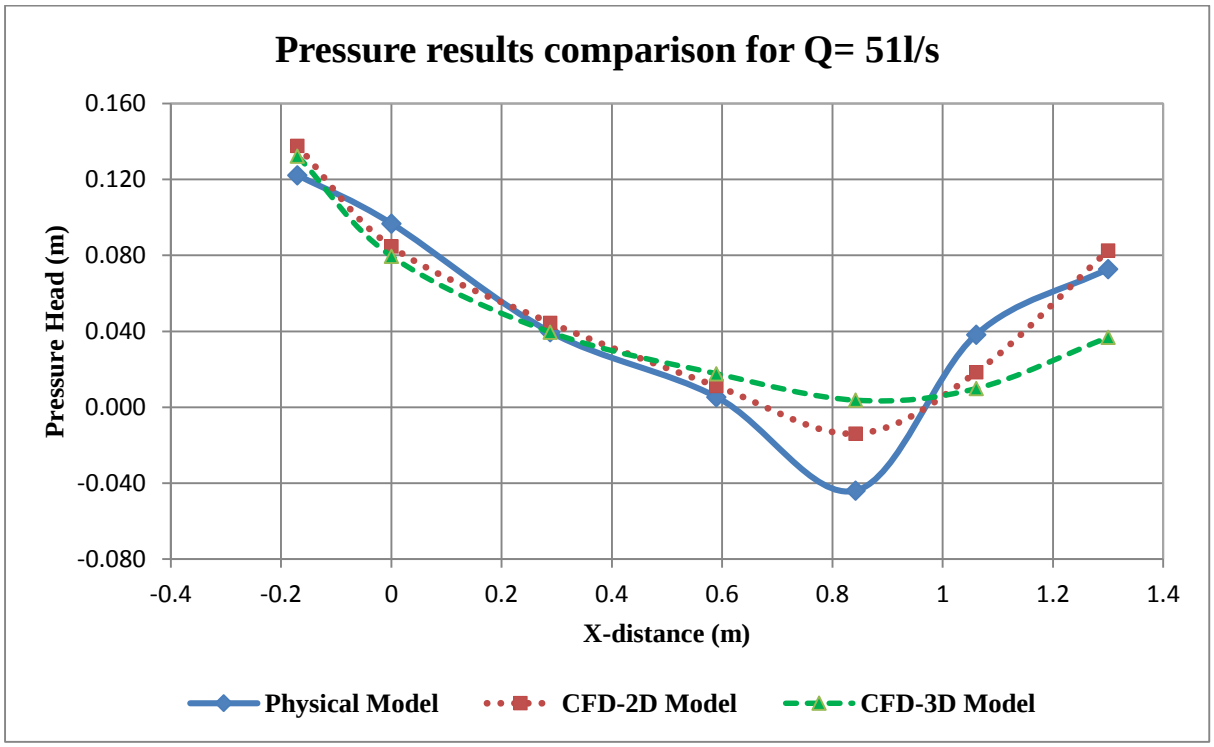

Figure D- 13: Comparison of stead CFD and average Physical model pressures for Q= 51 l/s (Case-2)

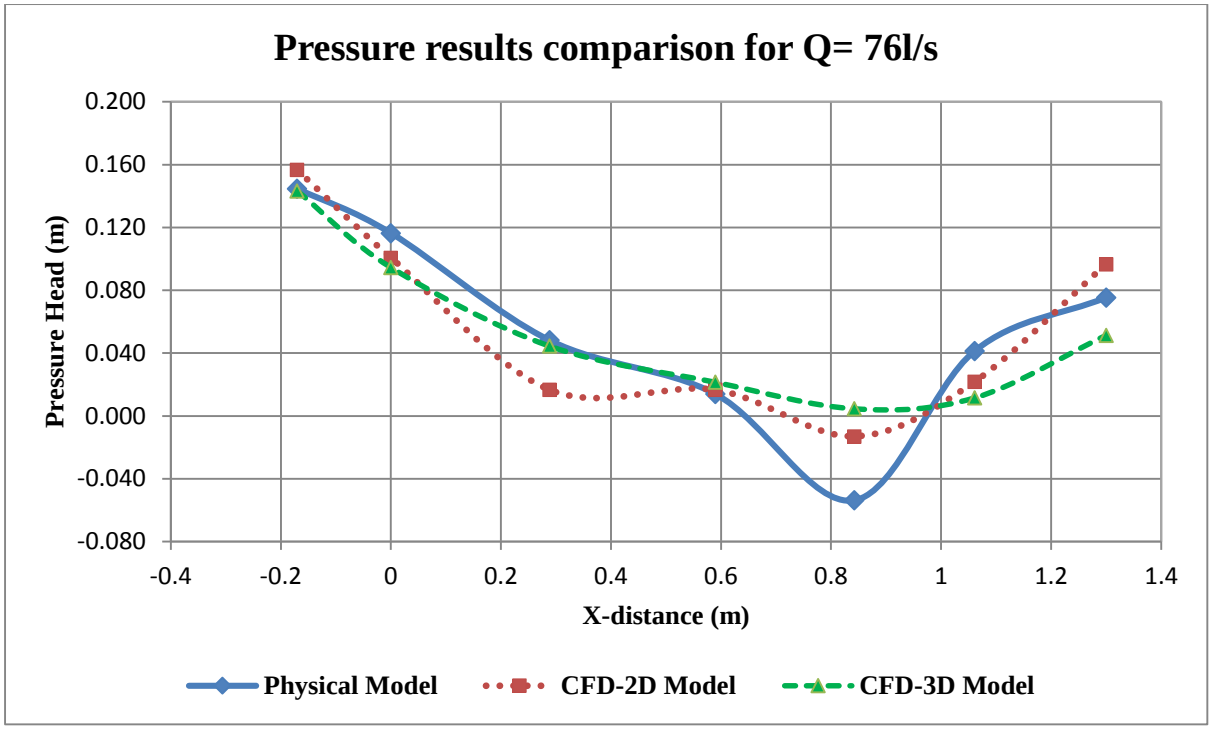

Figure D- 14: Comparison of stead CFD and average Physical model pressures for Q= 76 l/s (Case-2)

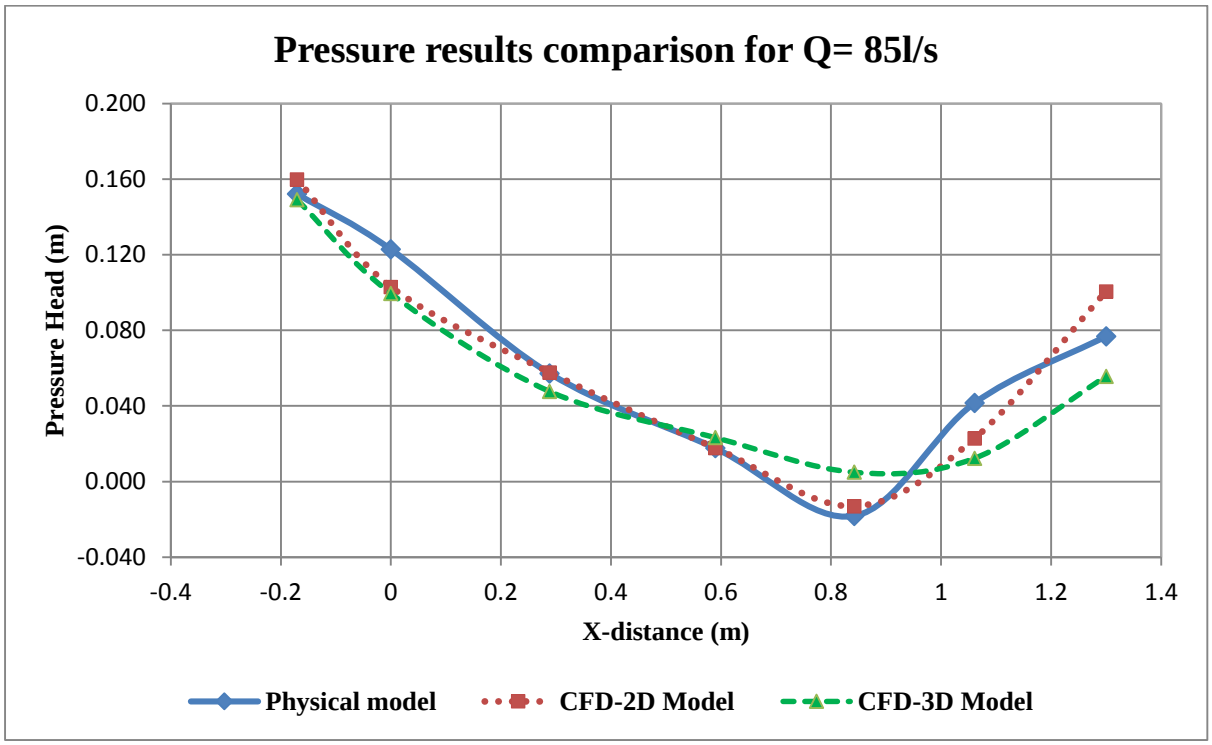

Figure D- 15: Comparison of stead CFD and average Physical model pressures for Q= 85 l/s (Case-2)

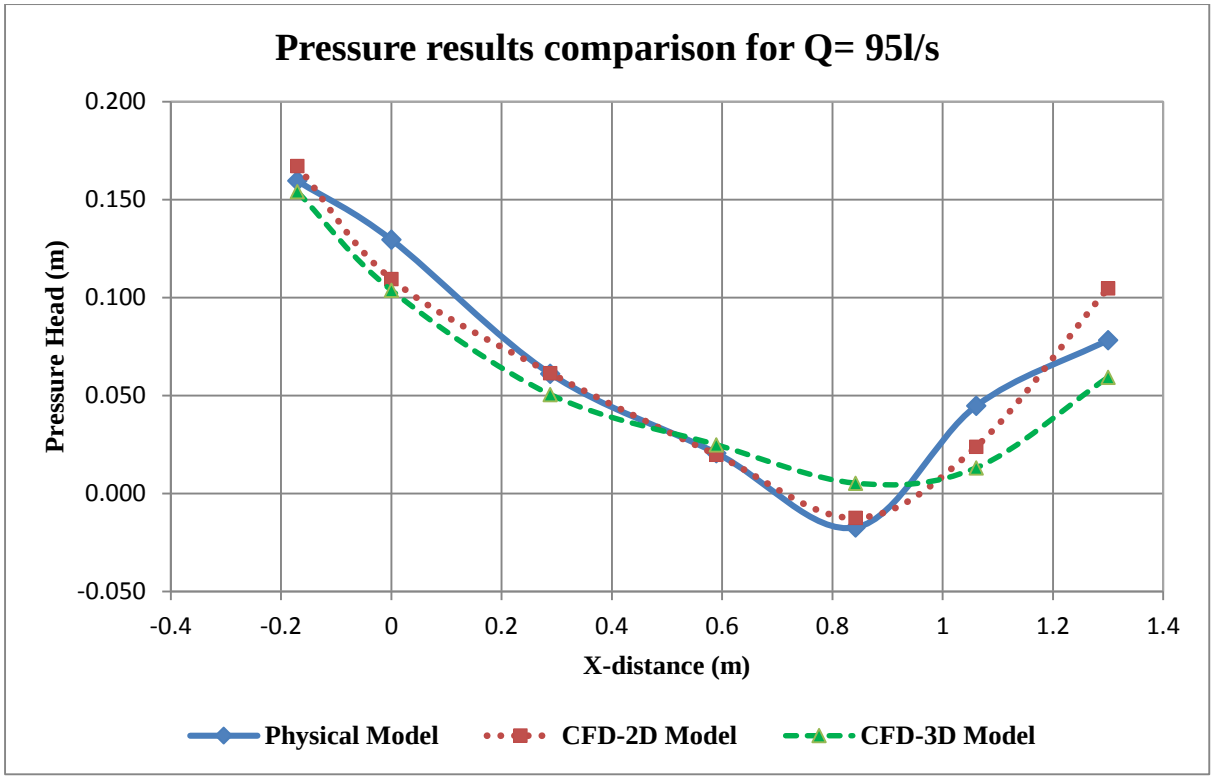

Figure D- 16: Comparison of stead CFD and average Physical model pressures for Q= 95 l/s (Case-2)

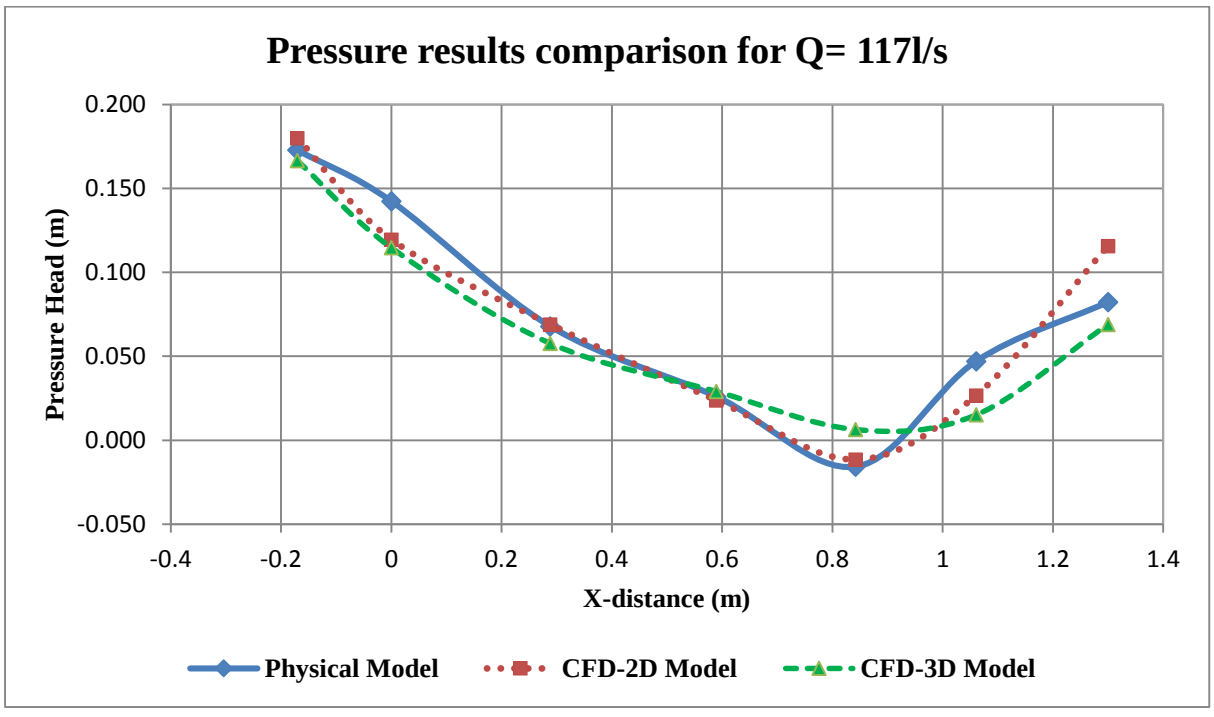

Figure D- 17: Comparison of stead average CFD and average Physical model pressures for Q= 117 l/s (Case-2)

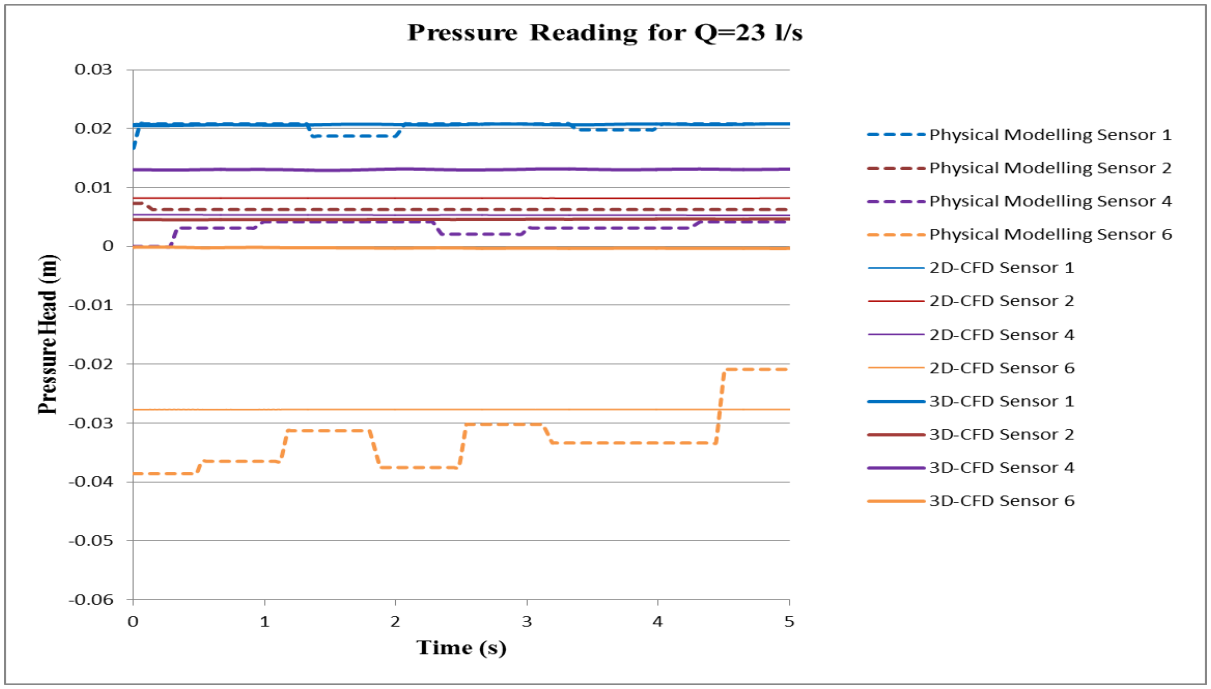

Figure D- 18: Physical modelling, 2D and 3D CFD fully hydrodynamic state pressure readings for 23 l/s for sensor 1, 2, 4 and 6 (Case-1)

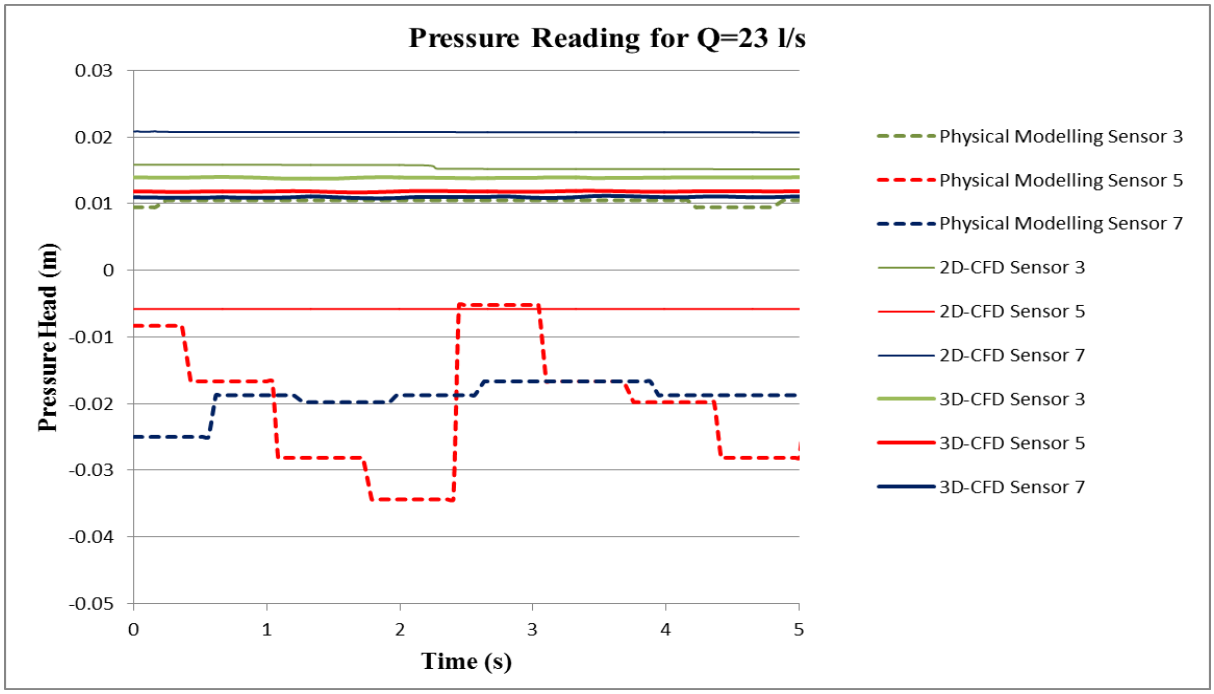

Figure D- 19: Physical modelling, 2D and 3D CFD fully hydrodynamic state pressure readings for 23 l/s for sensor 3, 5 and 7 (Case-1)

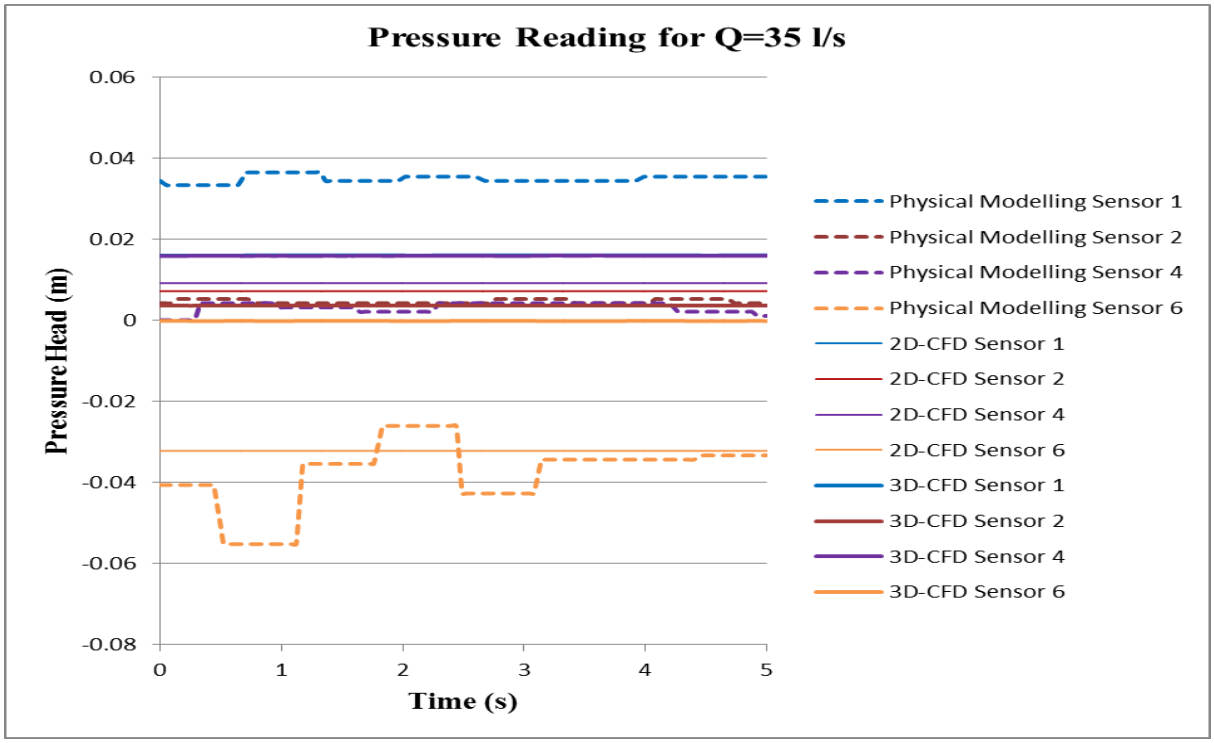

Figure D- 20: Physical modelling, 2D and 3D CFD fully hydrodynamic state pressure readings for 35 l/s for sensor 1, 2, 4 and 6 (Case-1)

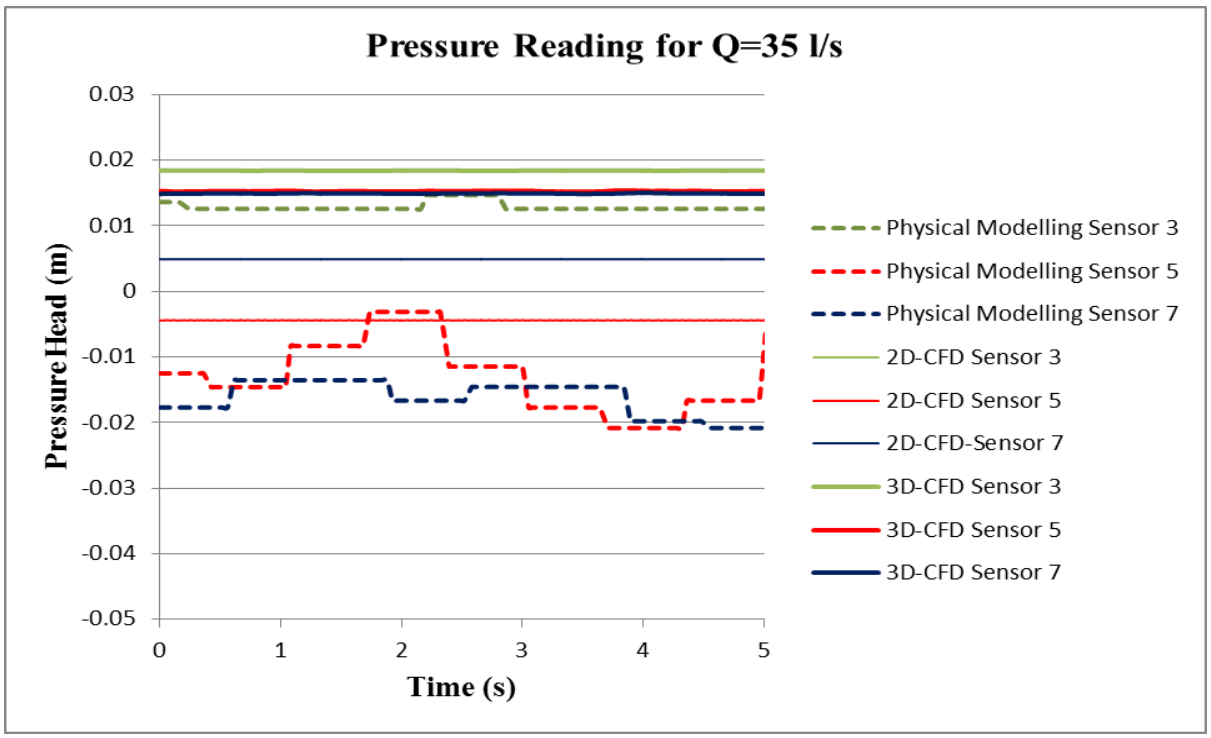

Figure D- 21: Physical modelling, 2D and 3D CFD fully hydrodynamic state pressure readings for 35 l/s for sensor 3, 5 and 7 (Case-1)

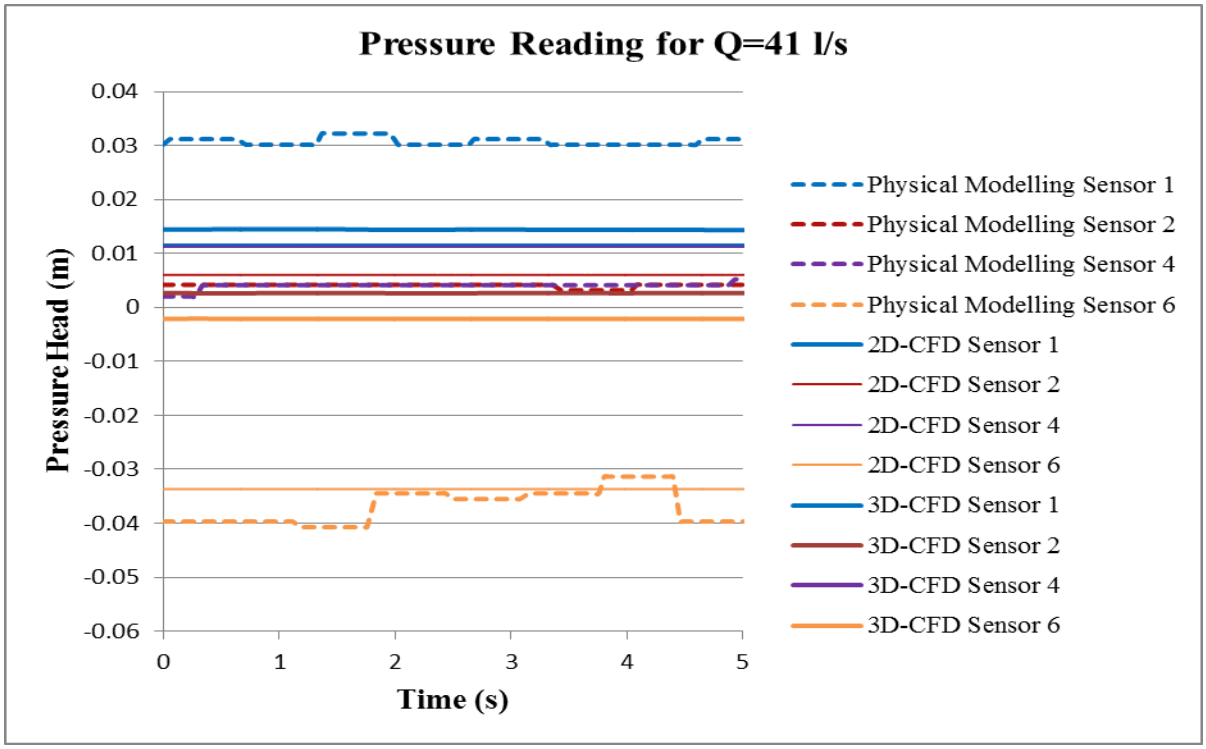

Figure D- 22: Physical modelling, 2D and 3D CFD fully hydrodynamic state pressure readings for 41 l/s for sensor 1, 2, 4 and 6 (Case-1)

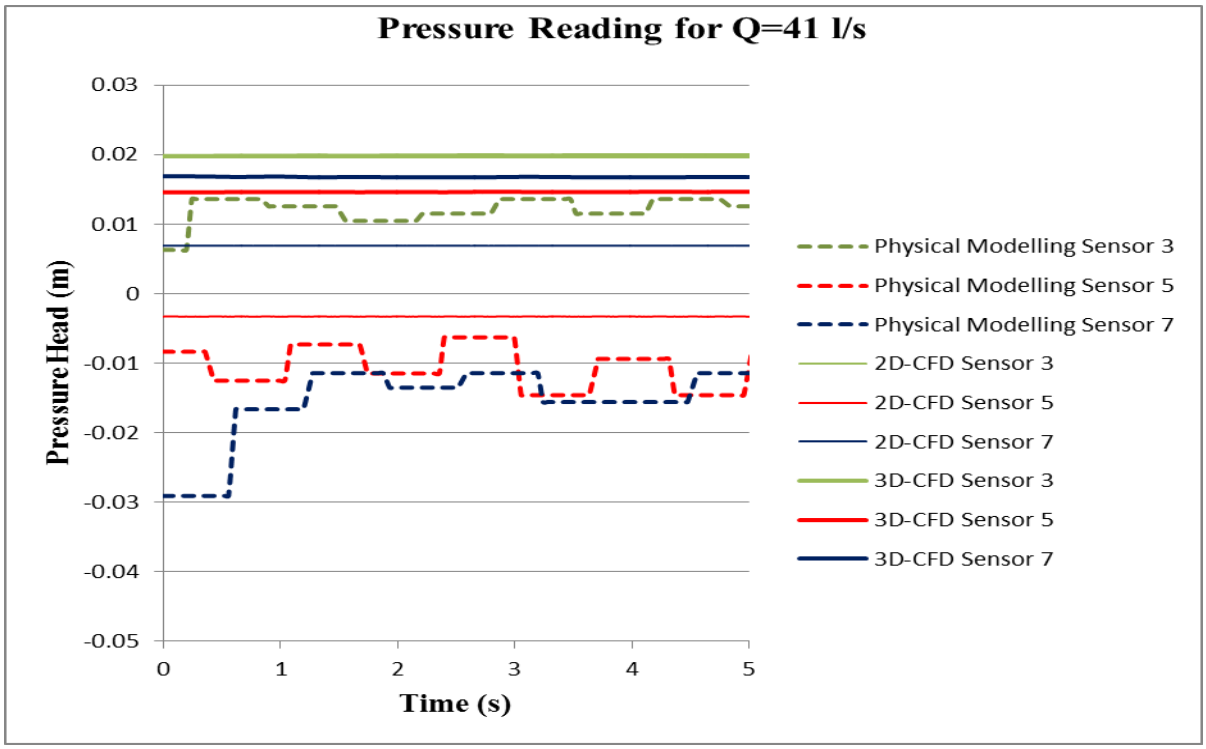

Figure D- 23: Physical modelling, 2D and 3D CFD fully hydrodynamic state pressure readings for 41 l/s for sensor 3, 5 and 7 (Case-1)

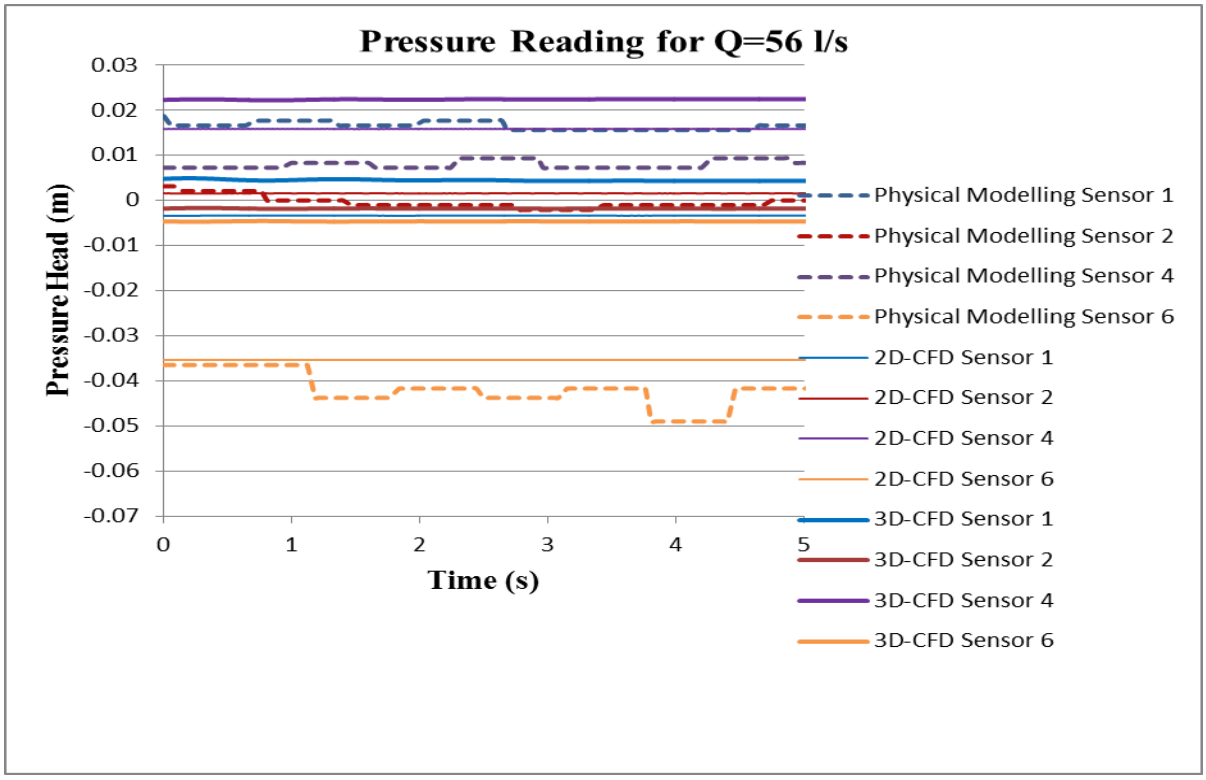

Figure D- 24: Physical modelling, 2D and 3D CFD fully hydrodynamic state pressure readings for 56 l/s for sensor 1, 2, 4 and 6 (Case-1)

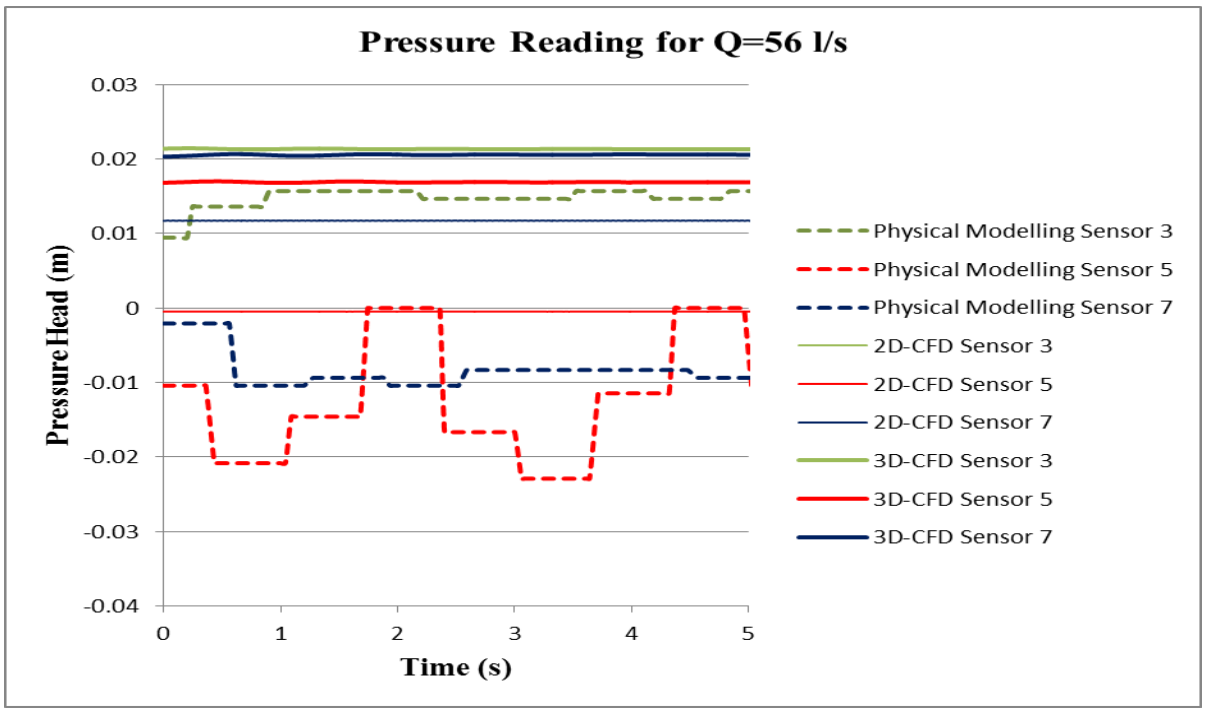

Figure D- 25: Physical modelling, 2D and 3D CFD fully hydrodynamic state pressure readings for 56 l/s for sensor 3, 5 and7 (Case-1)

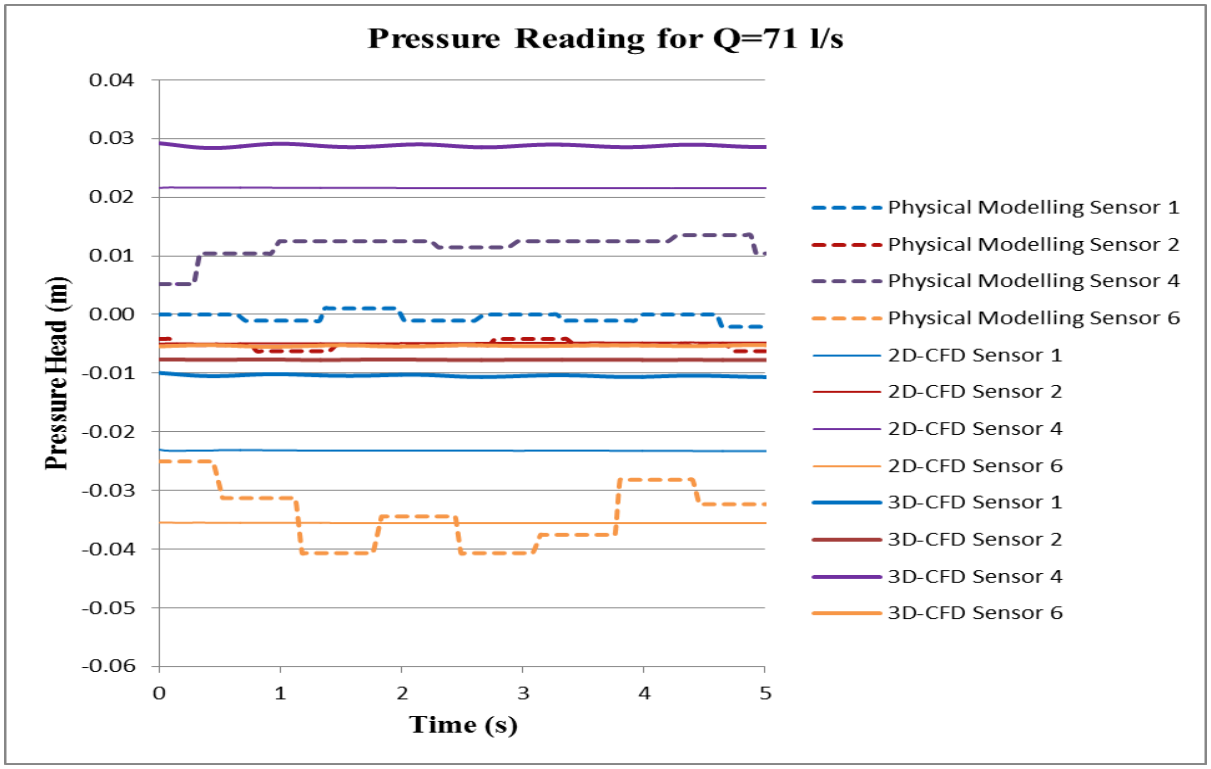

Figure D- 26: Physical modelling, 2D and 3D CFD fully hydrodynamic state pressure readings for 71 l/s for sensor 1, 2, 4 and 6 (Case-1)

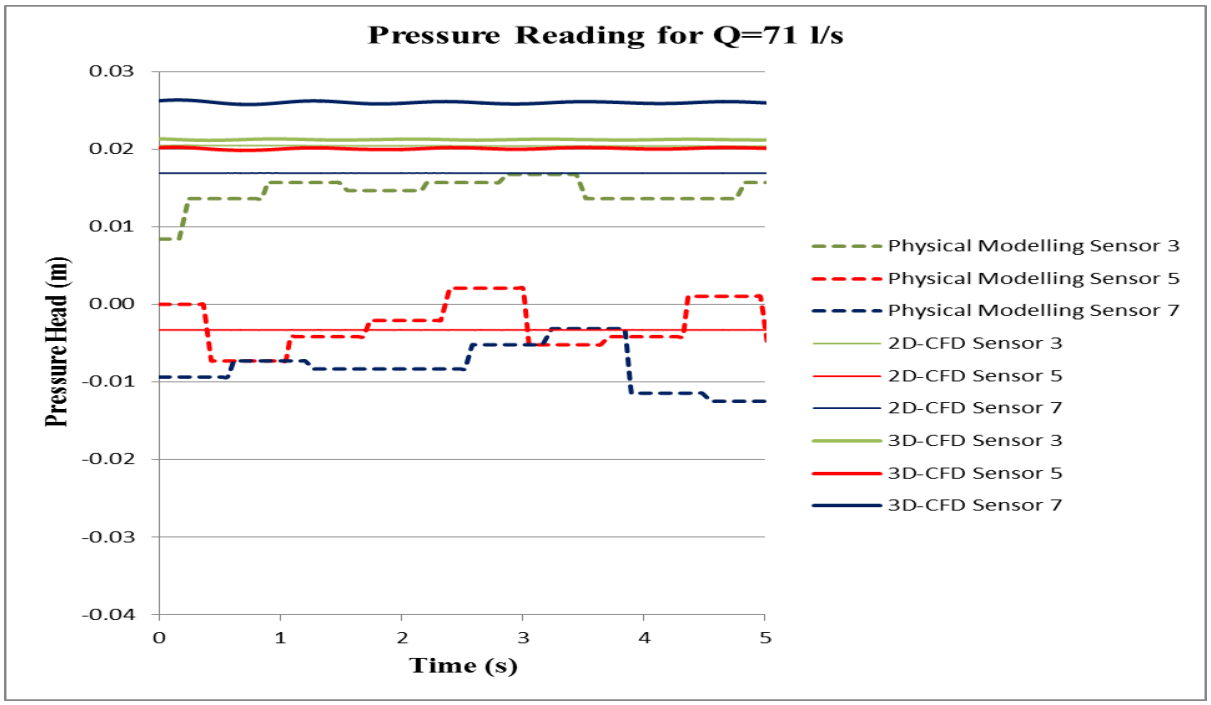

Figure D- 27: Physical modelling, 2D and 3D CFD fully hydrodynamic state pressure readings for 71 l/s for sensor 3, 5 and7 (Case-1)

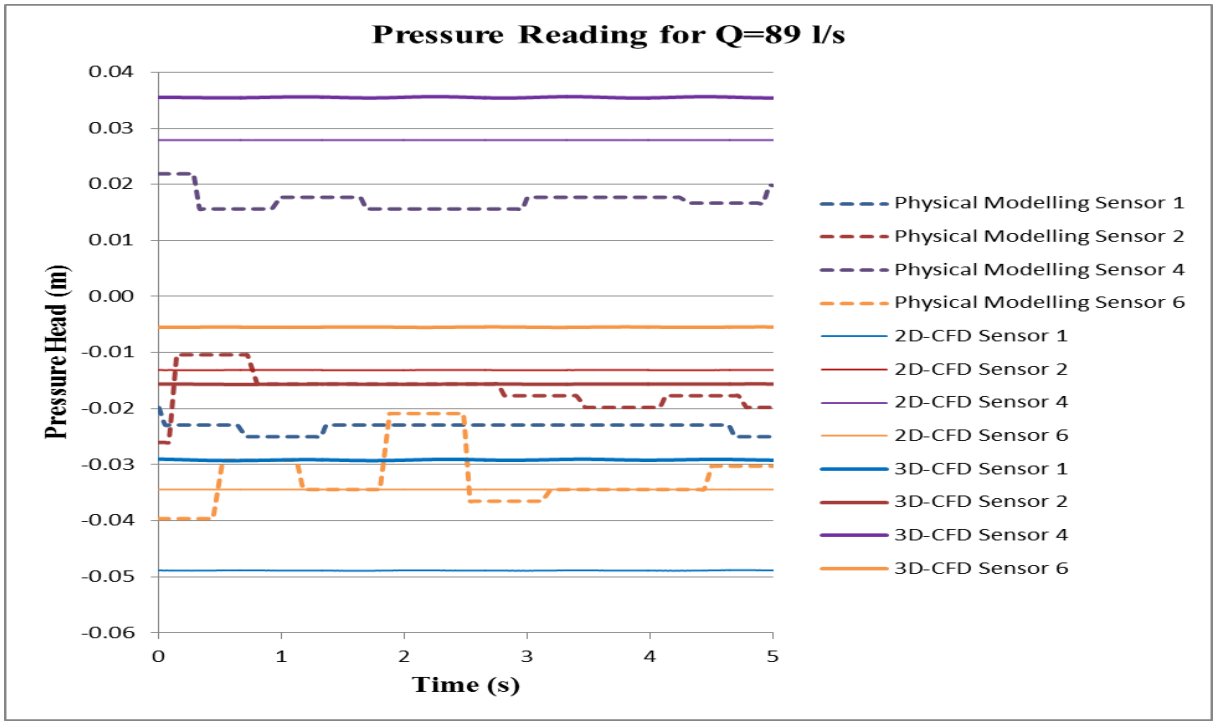

Figure D- 28: Physical modelling, 2D and 3D CFD fully hydrodynamic state pressure readings for 89 l/s for sensor 1, 2, 4 and 6 (Case-1)

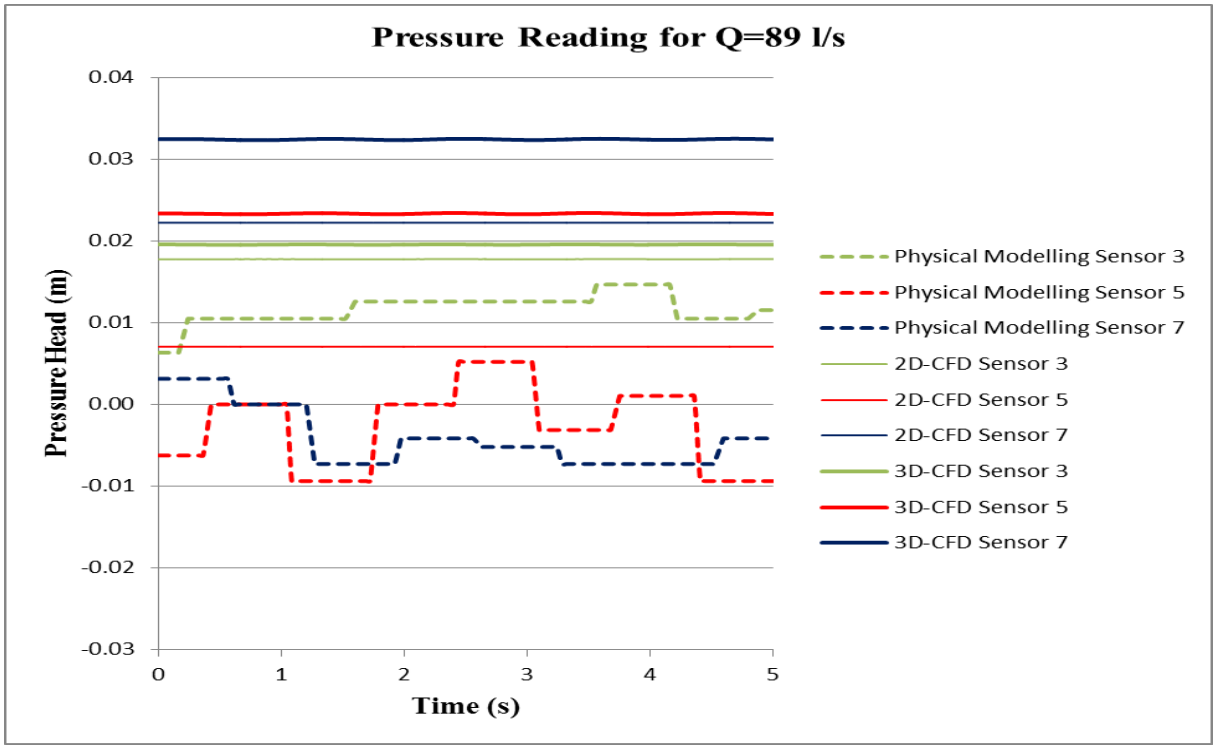

Figure D- 29: Physical modelling, 2D and 3D CFD fully hydrodynamic state pressure readings for 89 l/s for sensor 3, 5 and7 (Case-1)

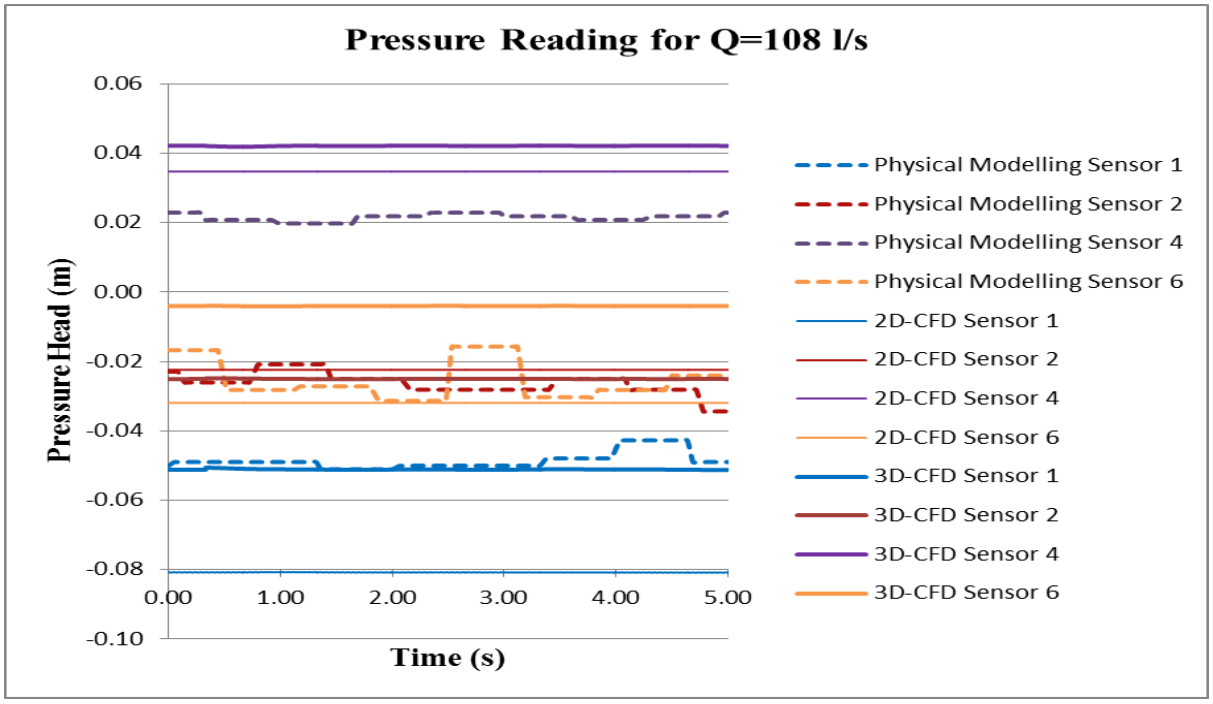

Figure D- 30: Physical modelling, 2D and 3D CFD fully hydrodynamic state pressure readings for 108 l/s for sensor 1, 2, 4 and 6 (Case-1)

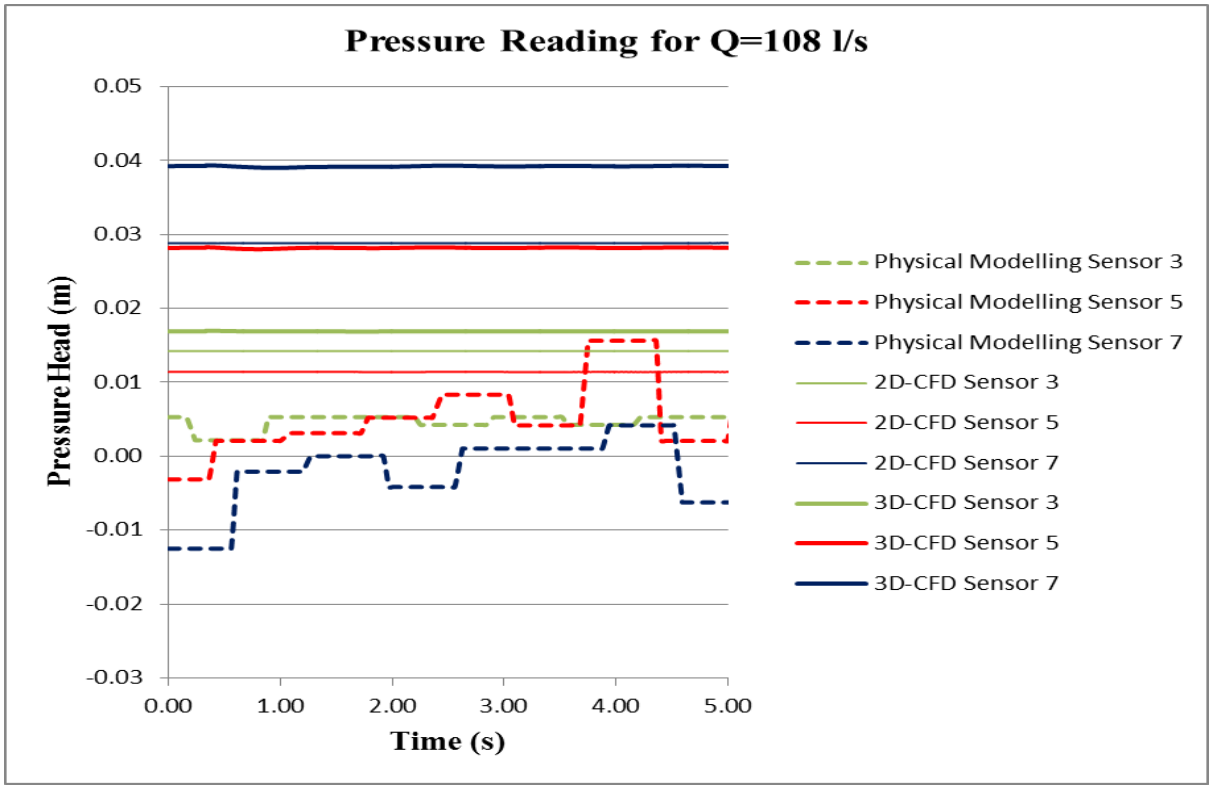

Figure D- 31: Physical modelling, 2D and 3D CFD fully hydrodynamic state pressure readings for 108 l/s for sensor 3, 5 and7 (Case-1)

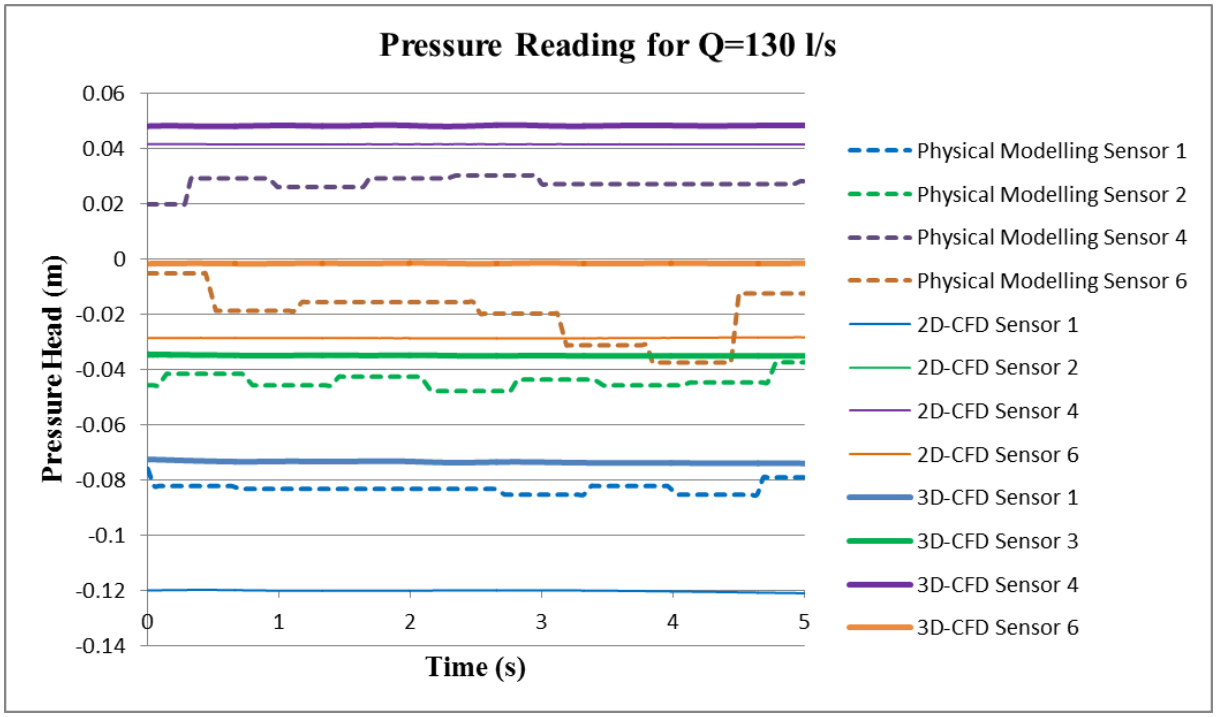

Figure D- 32: Physical modelling, 2D and 3D CFD fully hydrodynamic state pressure readings for 130 l/s for sensor 1, 2, 4 and 6

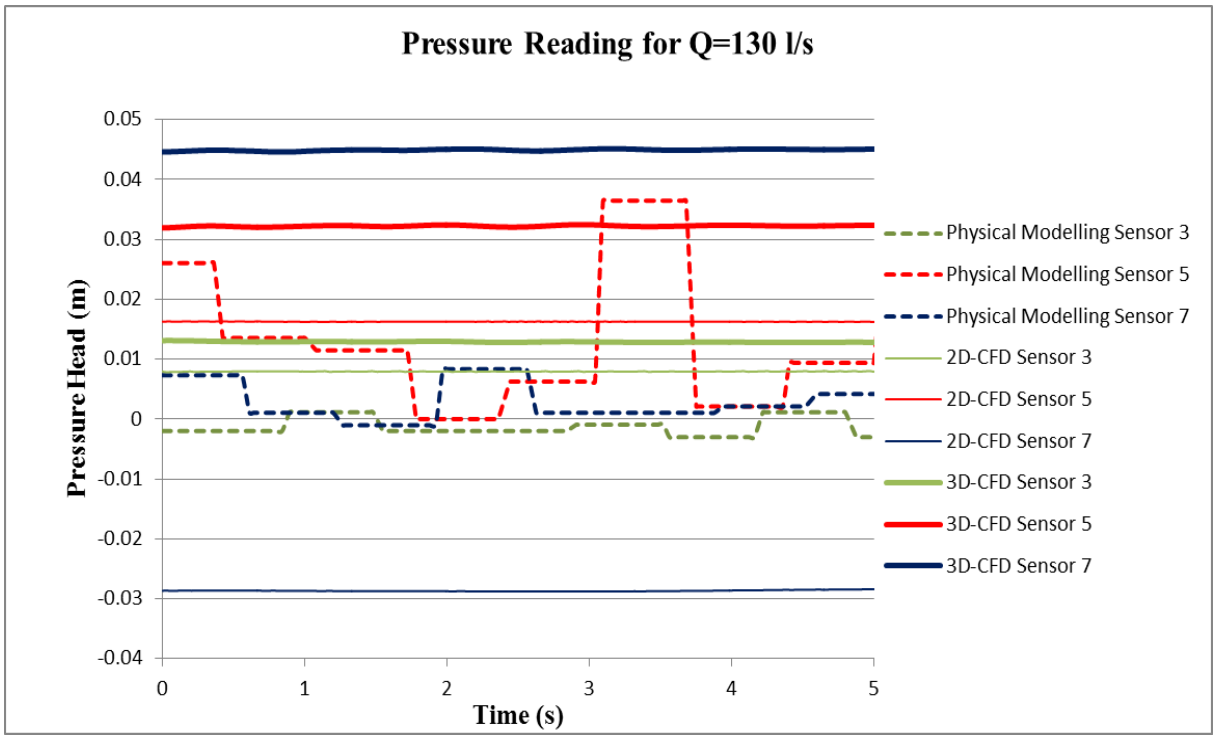

Figure D- 33: Physical modelling, 2D and 3D CFD fully hydrodynamic state pressure readings for 130 l/s for sensor 3, 5 and7 (Case-1)

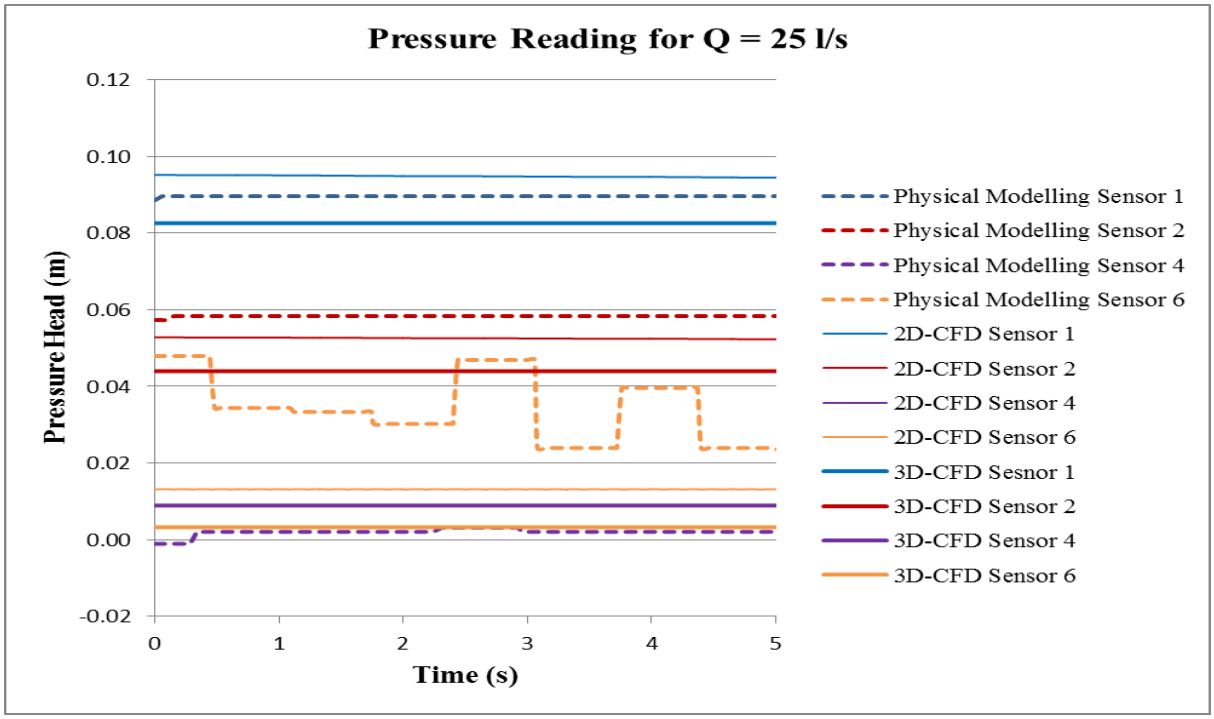

Figure D- 34: Physical modelling, 2D and 3D CFD fully hydrodynamic state pressure readings for 25 l/s for sensor 1, 2, 4 and 6 (Case-2)

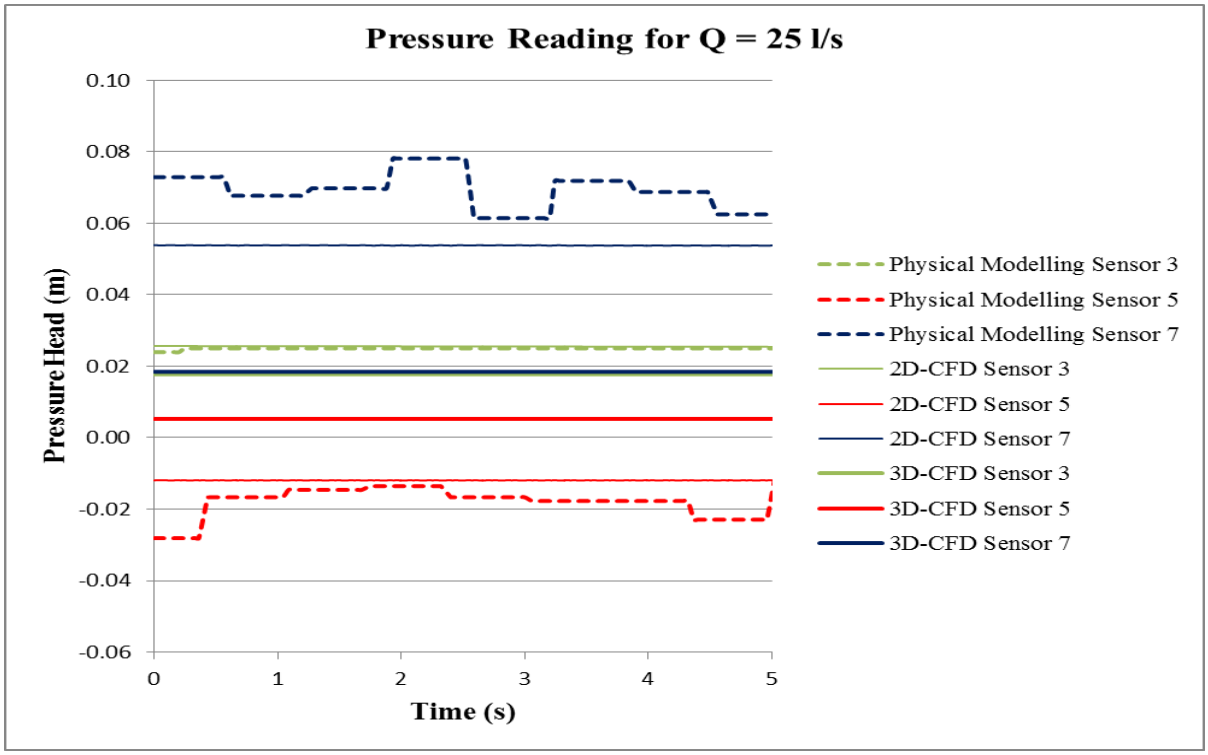

Figure D- 35: Physical modelling, 2D and 3D CFD fully hydrodynamic state pressure readings for 25 l/s for sensor 3, 5 and7 (Case-2)

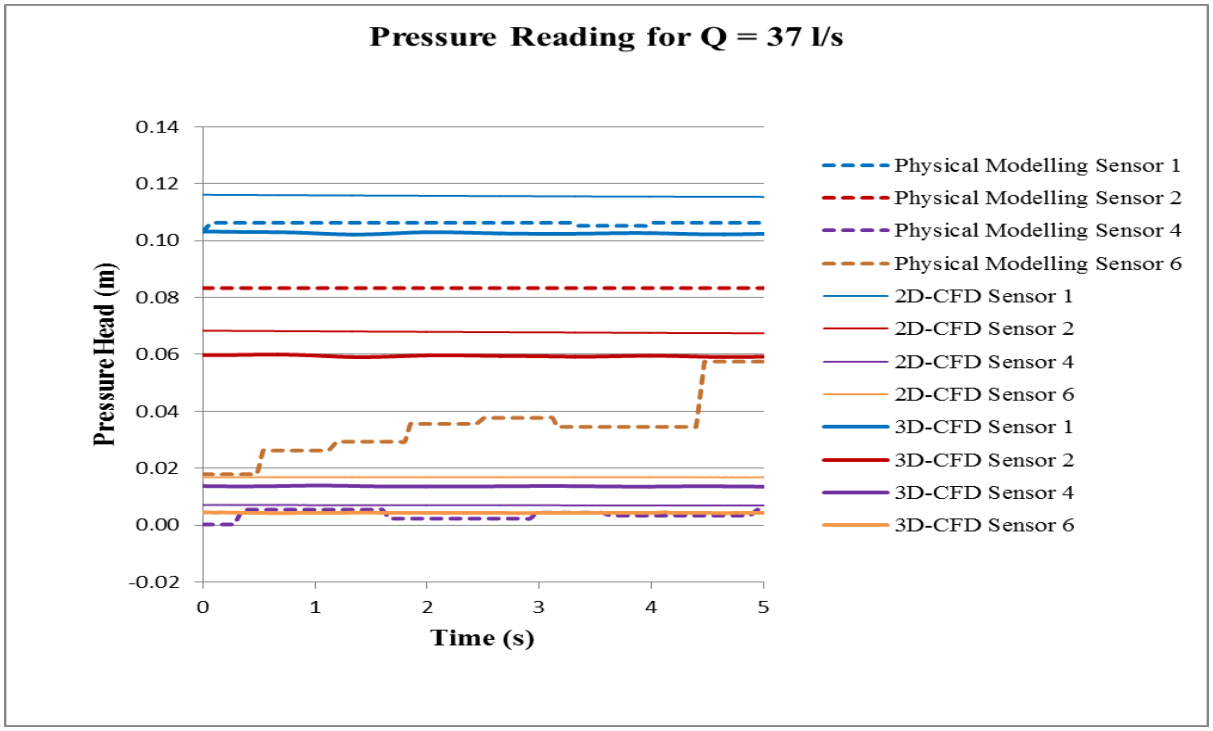

Figure D- 36: Physical modelling, 2D and 3D CFD fully hydrodynamic state pressure readings for 37 l/s for sensor 1, 2, 4 and 6 (Case-2)

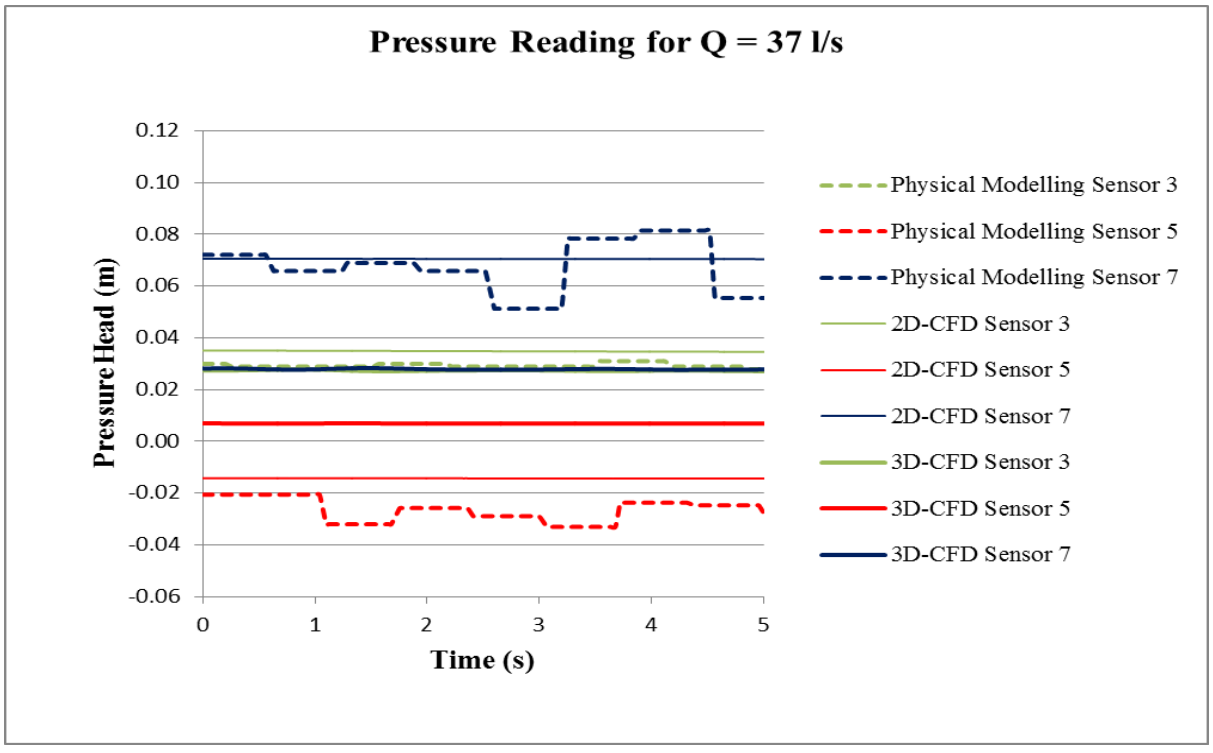

Figure D- 37: Physical modelling, 2D and 3D CFD fully hydrodynamic state pressure readings for 37 l/s for sensor 3, 5 and7 (Case-2)

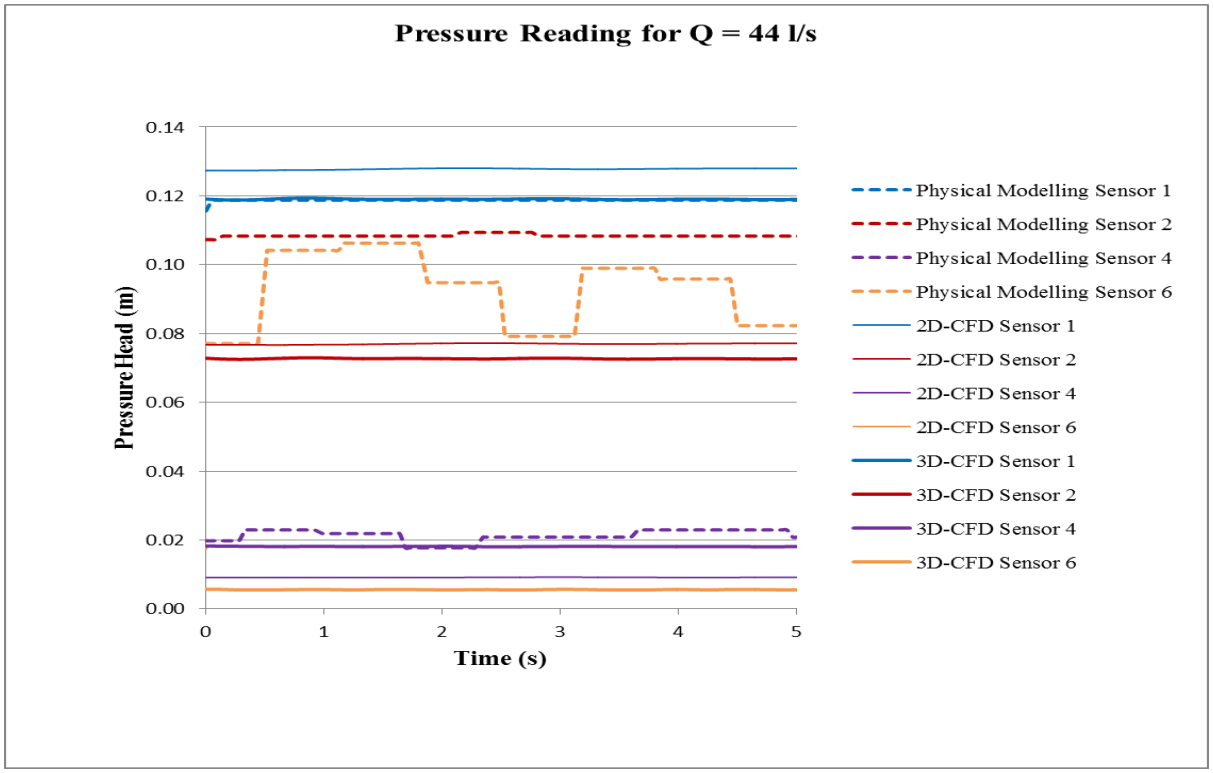

Figure D- 38: Physical modelling, 2D and 3D CFD fully hydrodynamic state pressure readings for 44 l/s for sensor 1, 2, 4 and 6 (Case-2)

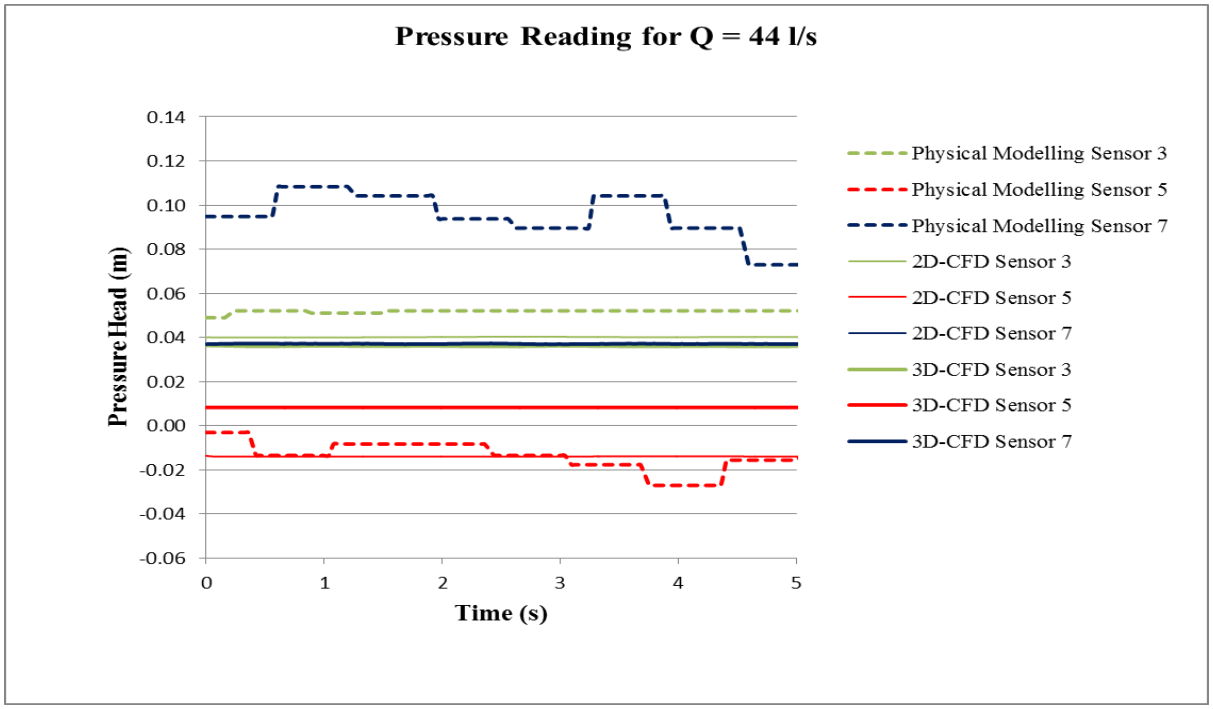

Figure D- 39: Physical modelling, 2D and 3D CFD fully hydrodynamic state pressure readings for 44 l/s for sensor 3, 5 and7 (Case-2)

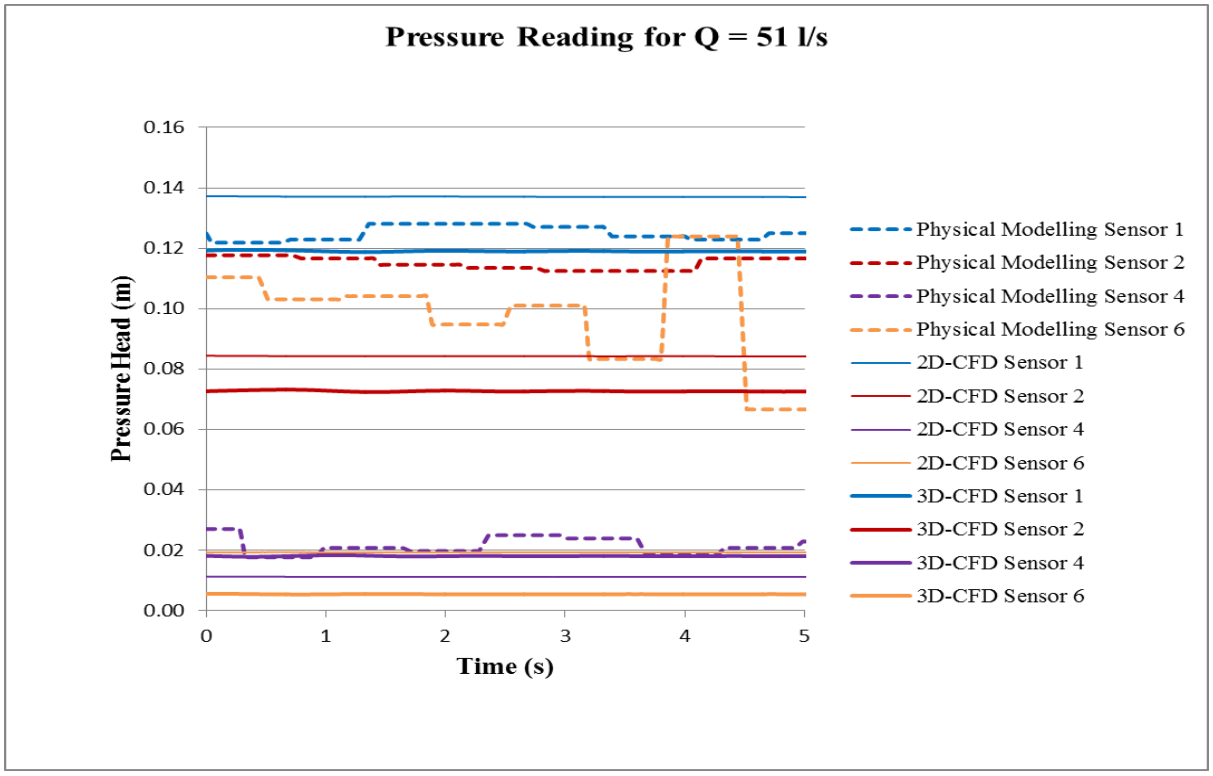

Figure D- 40: Physical modelling, 2D and 3D CFD fully hydrodynamic state pressure readings for 51 l/s for sensor 1, 2, 4 and 6 (Case-2)

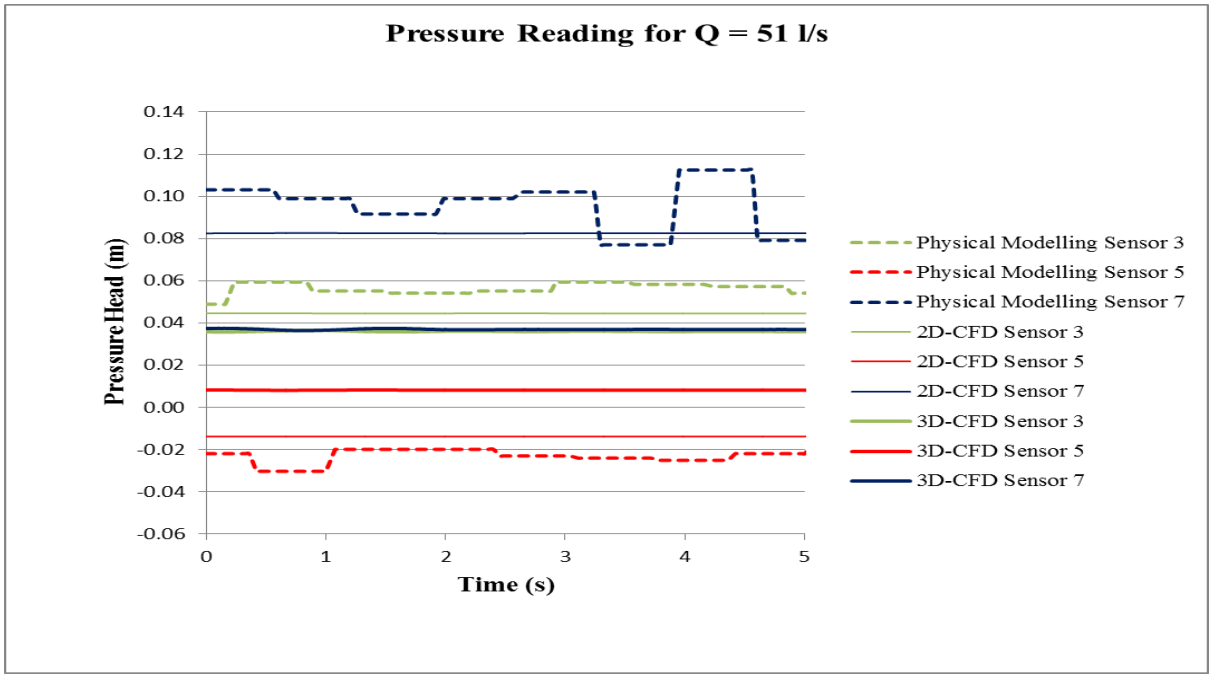

Figure D- 41: Physical modelling, 2D and 3D CFD fully hydrodynamic state pressure readings for 51 l/s for sensor 3, 5 and7 (Case-2)

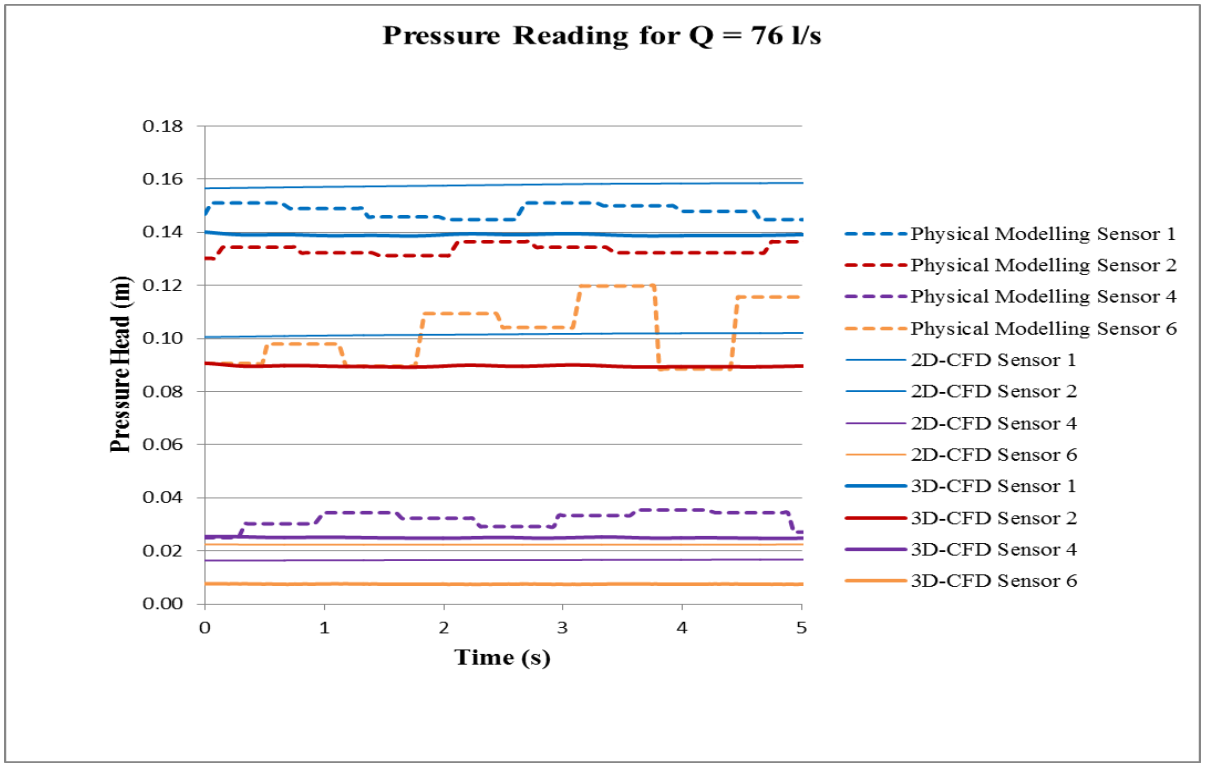

Figure D- 42: Physical modelling, 2D and 3D CFD fully hydrodynamic state pressure readings for 76 l/s for sensor 1, 2, 4 and 6 (Case-2)

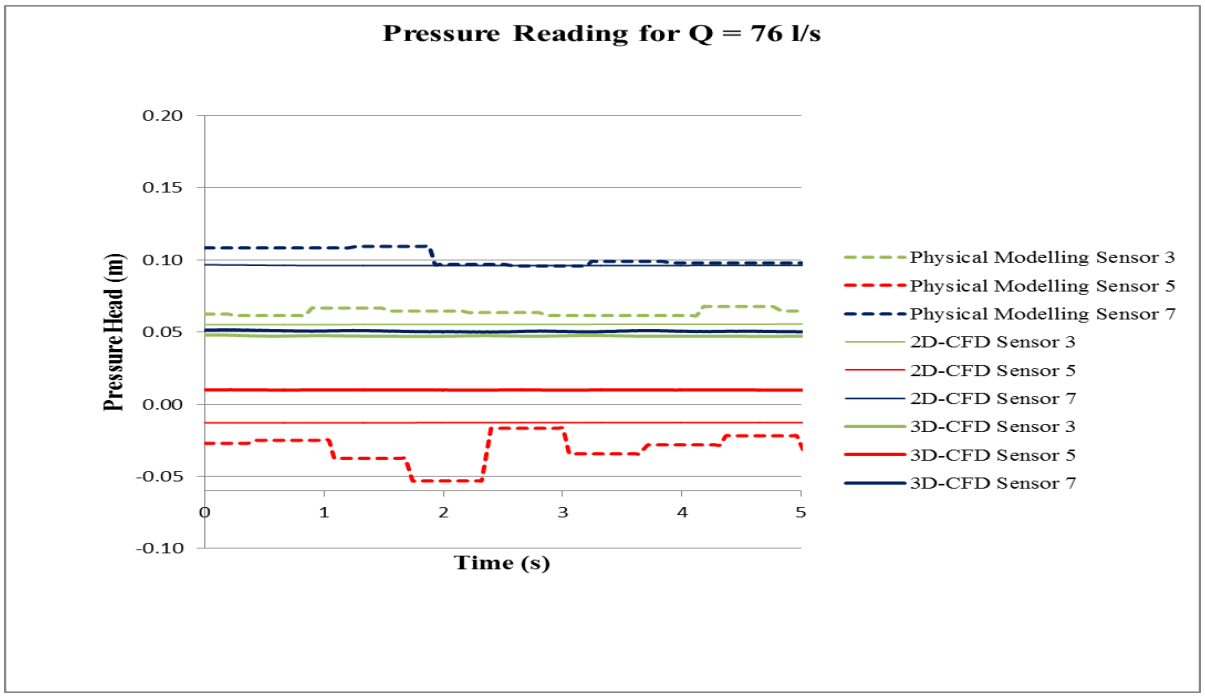

Figure D- 43: Physical modelling, 2D and 3D CFD fully hydrodynamic state pressure readings for 76 l/s for sensor 3, 5 and7 (Case-2)

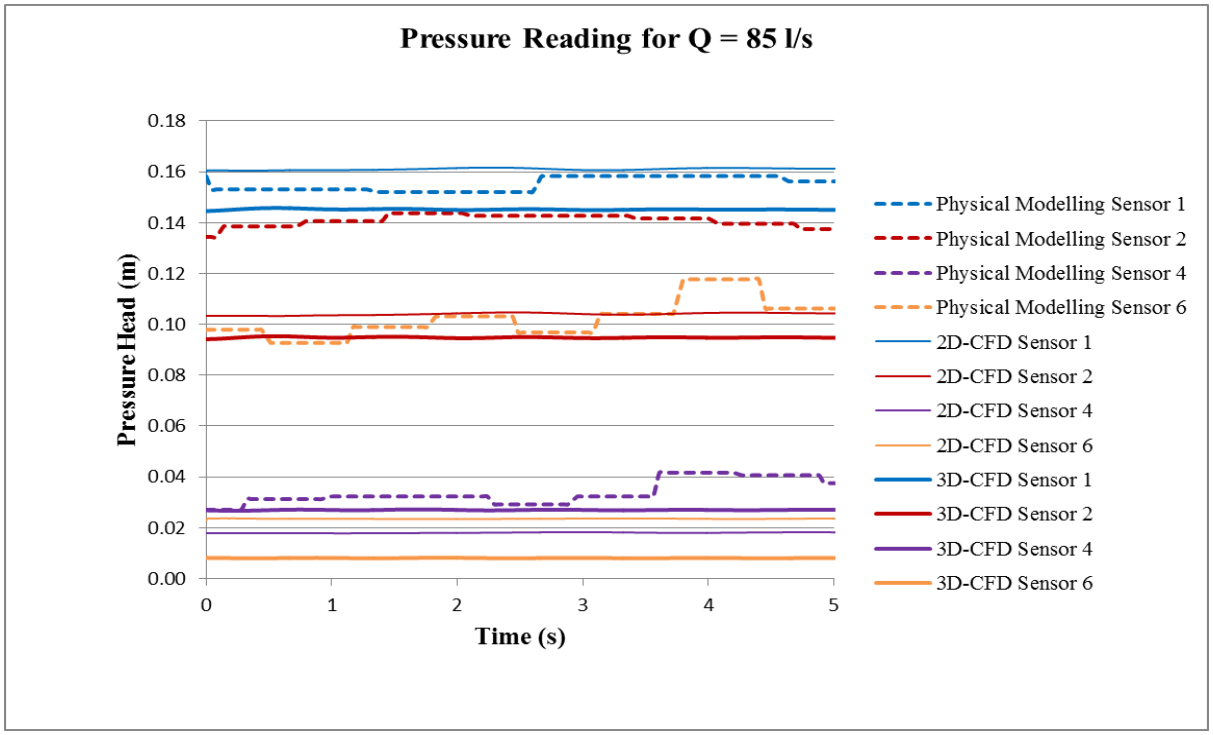

Figure D- 44: Physical modelling, 2D and 3D CFD fully hydrodynamic state pressure readings for 85 l/s for sensor 1, 2, 4 and 6 (Case-2)

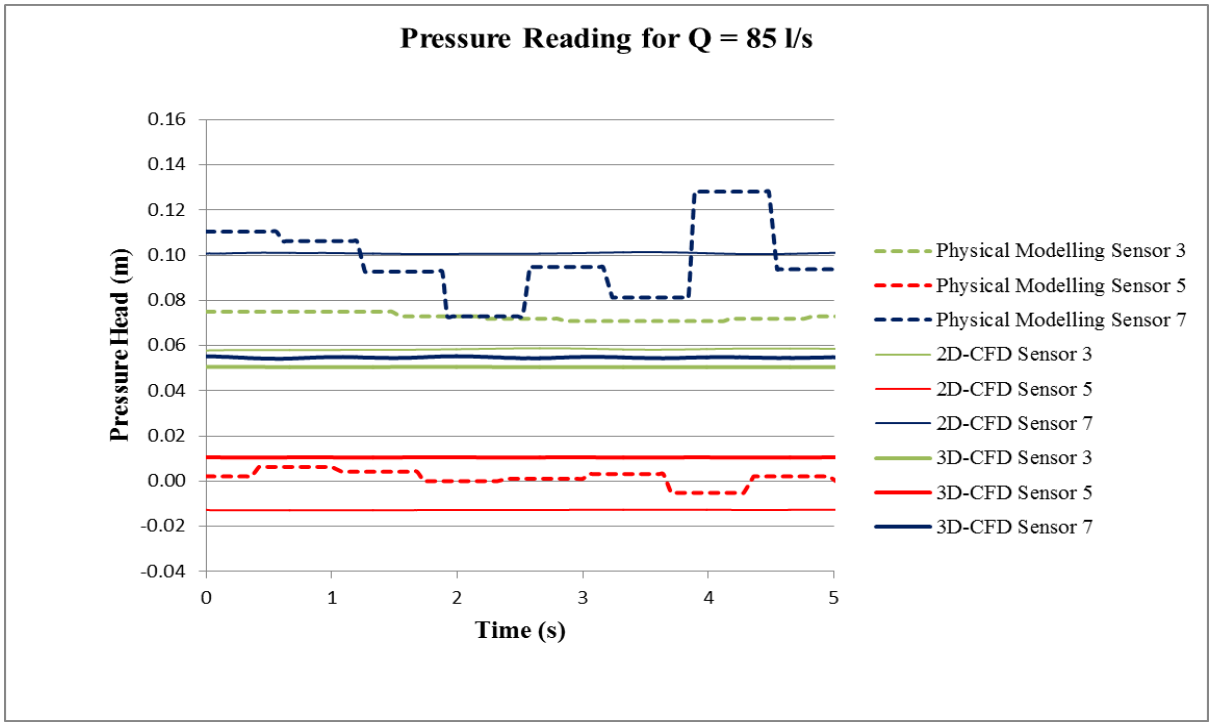

Figure D- 45: Physical modelling, 2D and 3D CFD fully hydrodynamic state pressure readings for 85 l/s for sensor 3, 5 and7 (Case-2)

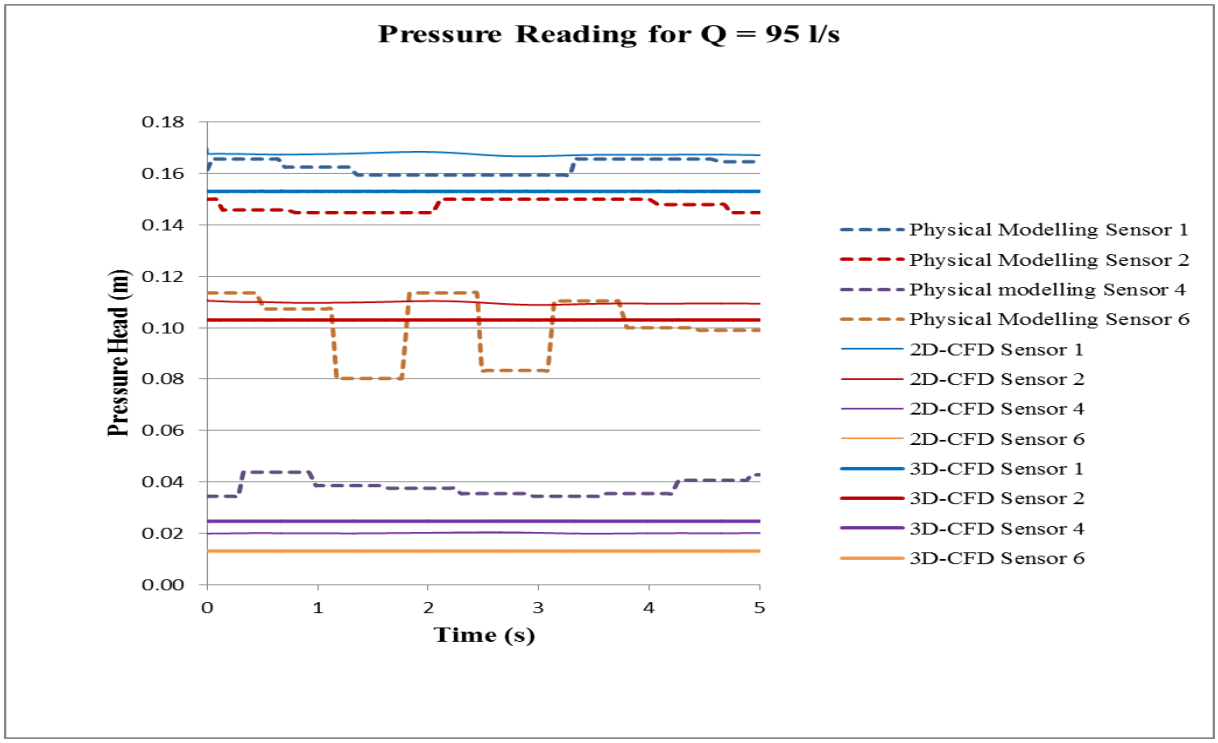

Figure D- 46: Physical modelling, 2D and 3D CFD fully hydrodynamic state pressure readings for 95 l/s for sensor 1, 2, 4 and 6 (Case-2)

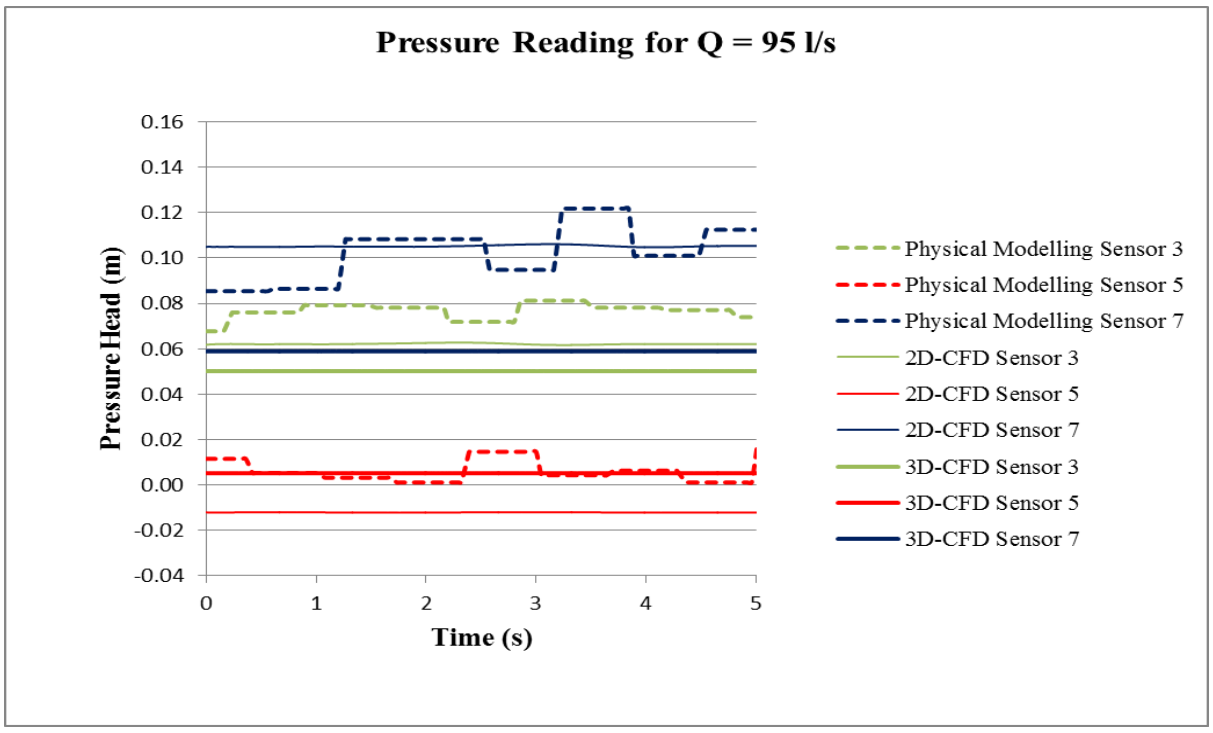

Figure D- 47: Physical modelling, 2D and 3D CFD fully hydrodynamic state pressure readings for 95 l/s for sensor 3, 5 and7 (Case-2)

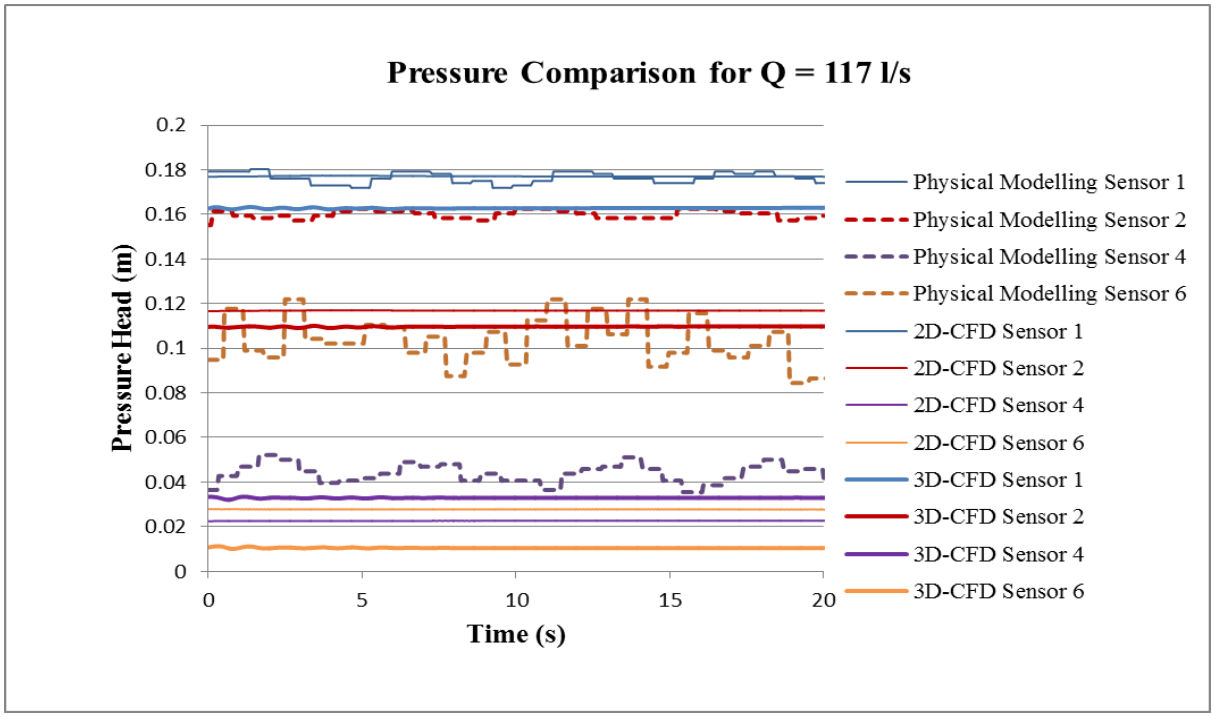

Figure D- 48: Physical modelling, 2D and 3D CFD fully hydrodynamic state pressure readings for 117 l/s for sensor 1, 2, 4 and 6 (Case-2)

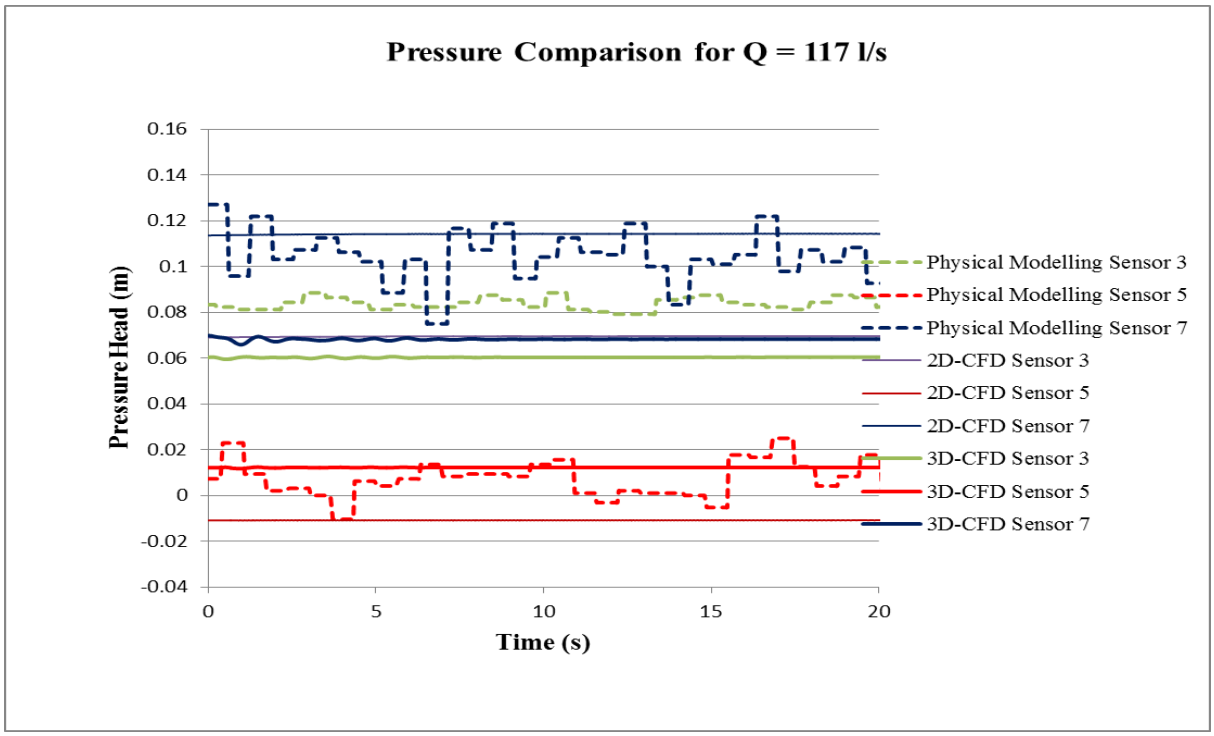

Figure D- 49: Physical modelling, 2D and 3D CFD fully hydrodynamic state pressure readings for 95 l/s for sensor 3, 5 and7 (Case-2)

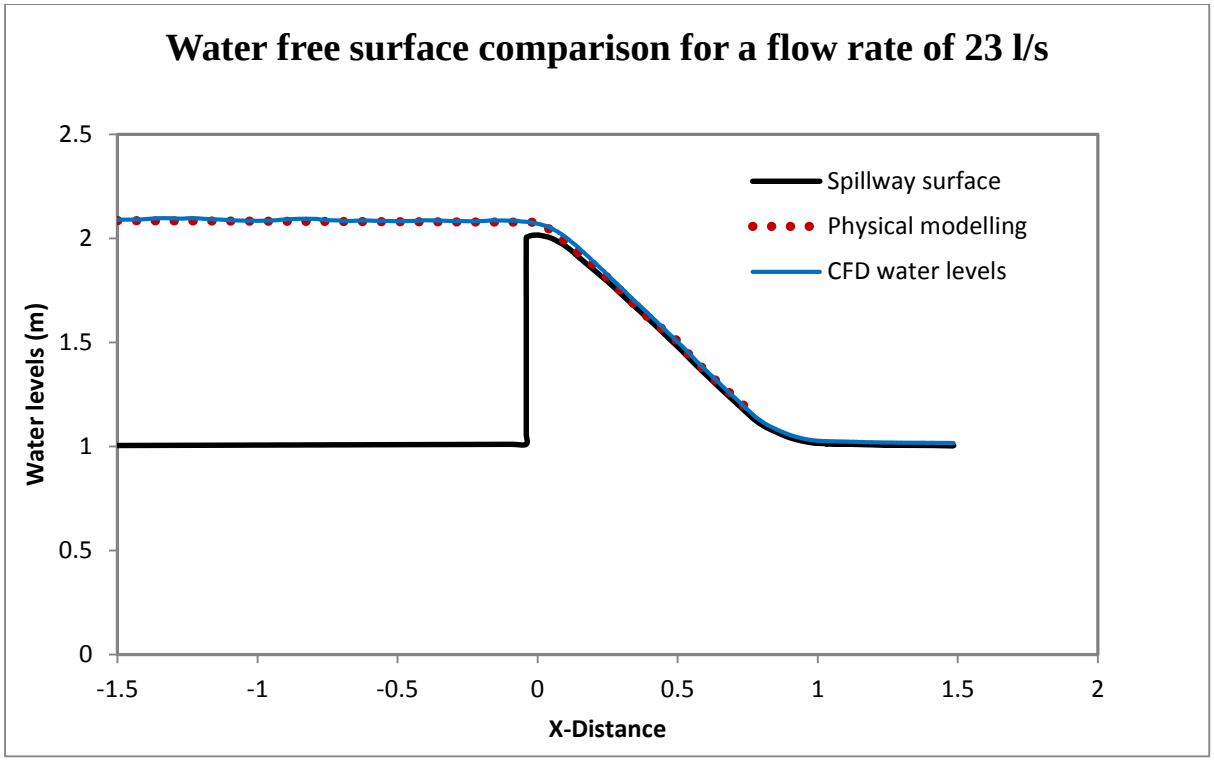

Figure D- 50: The comparison of CFD and experimental free surfaces for 23 l/s (Case-1)

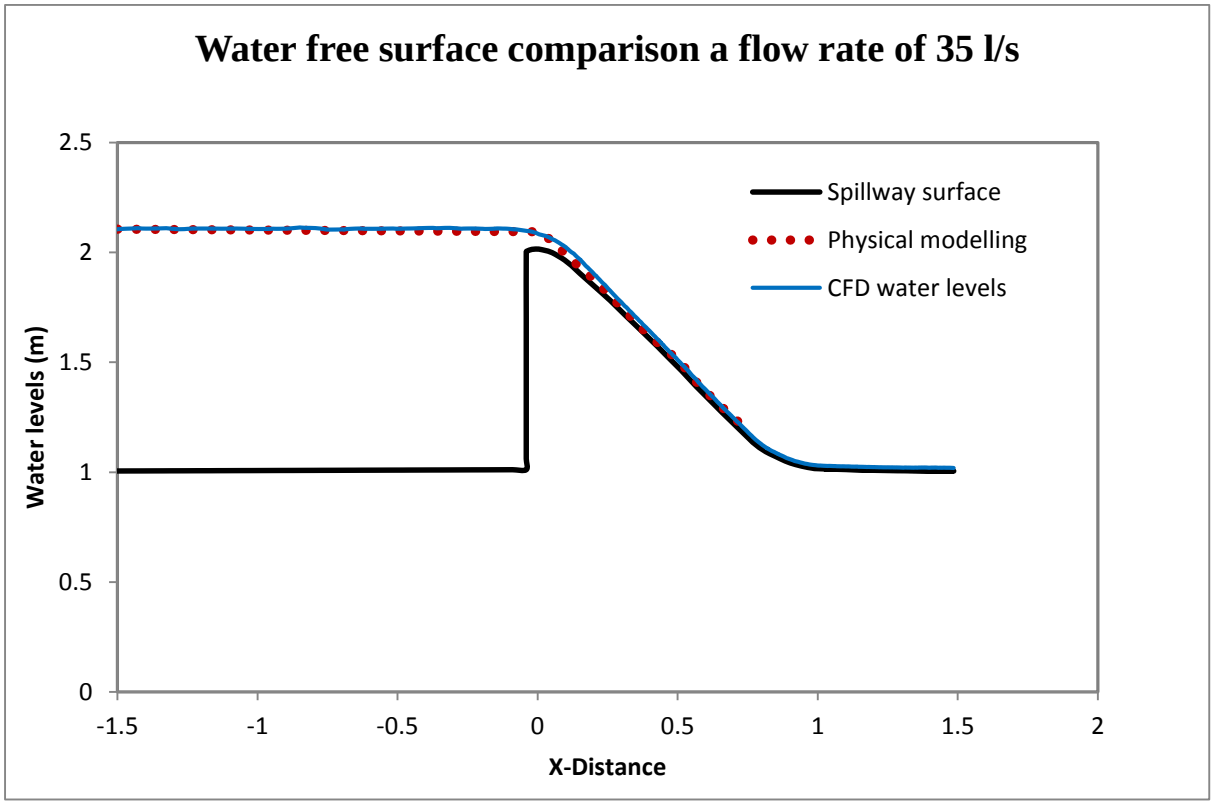

Figure D- 51: The comparison of CFD and experimental free surfaces for 35 l/s (Case-1)

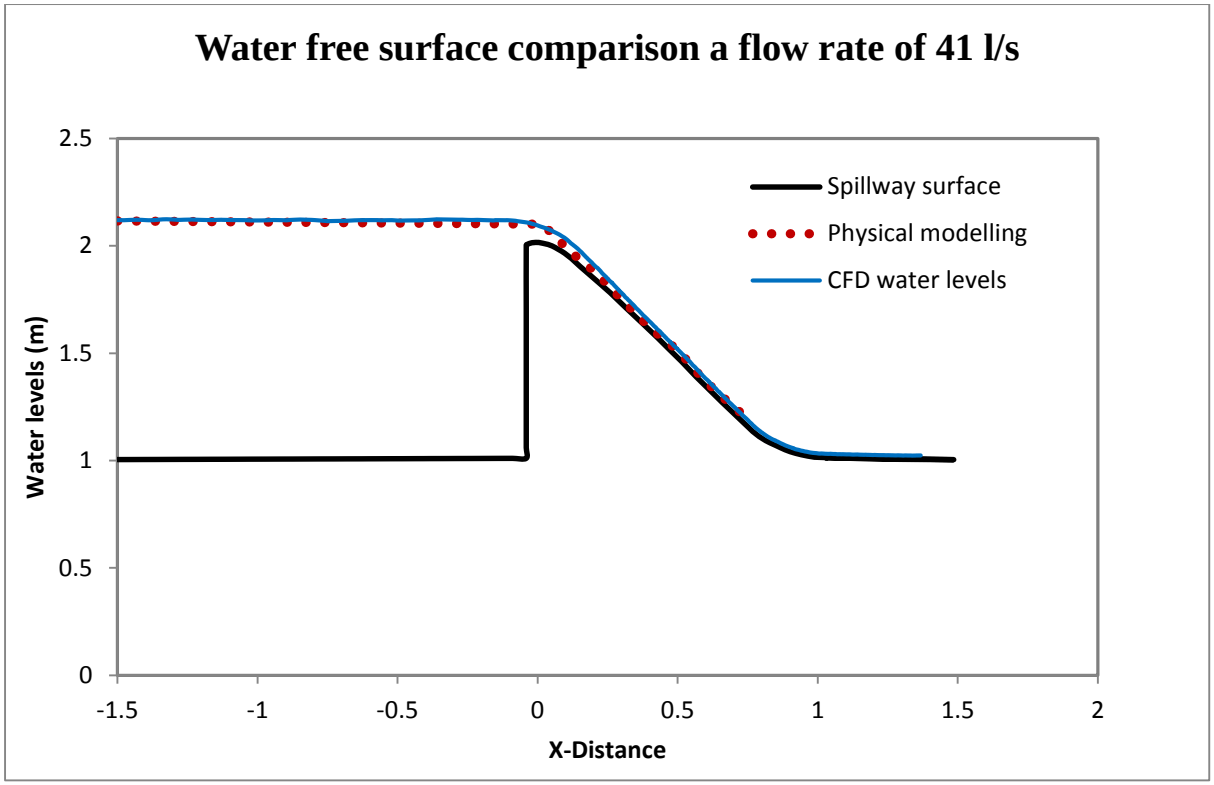

Figure D- 52: The comparison of CFD and experimental free surfaces for 41 l/s (Case-1)

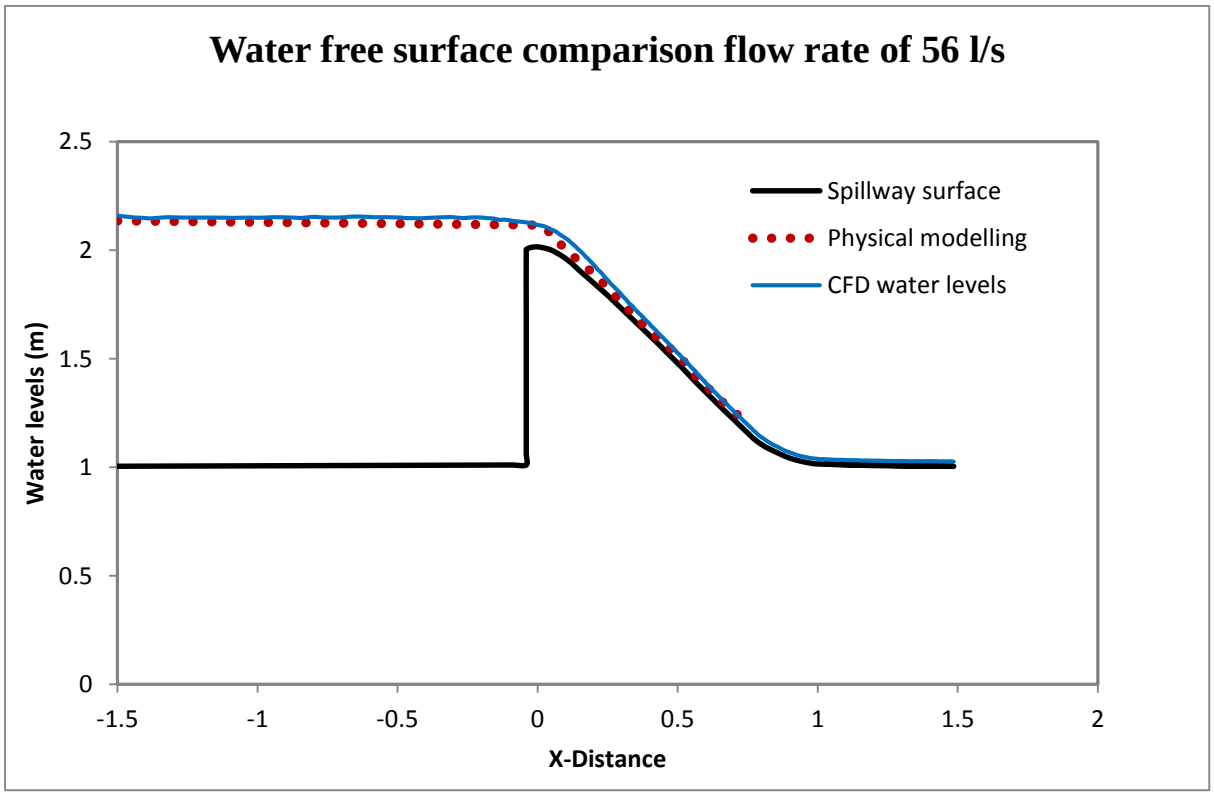

Figure D- 53: The comparison of CFD and experimental free surfaces for 56 l/s (Case-1)

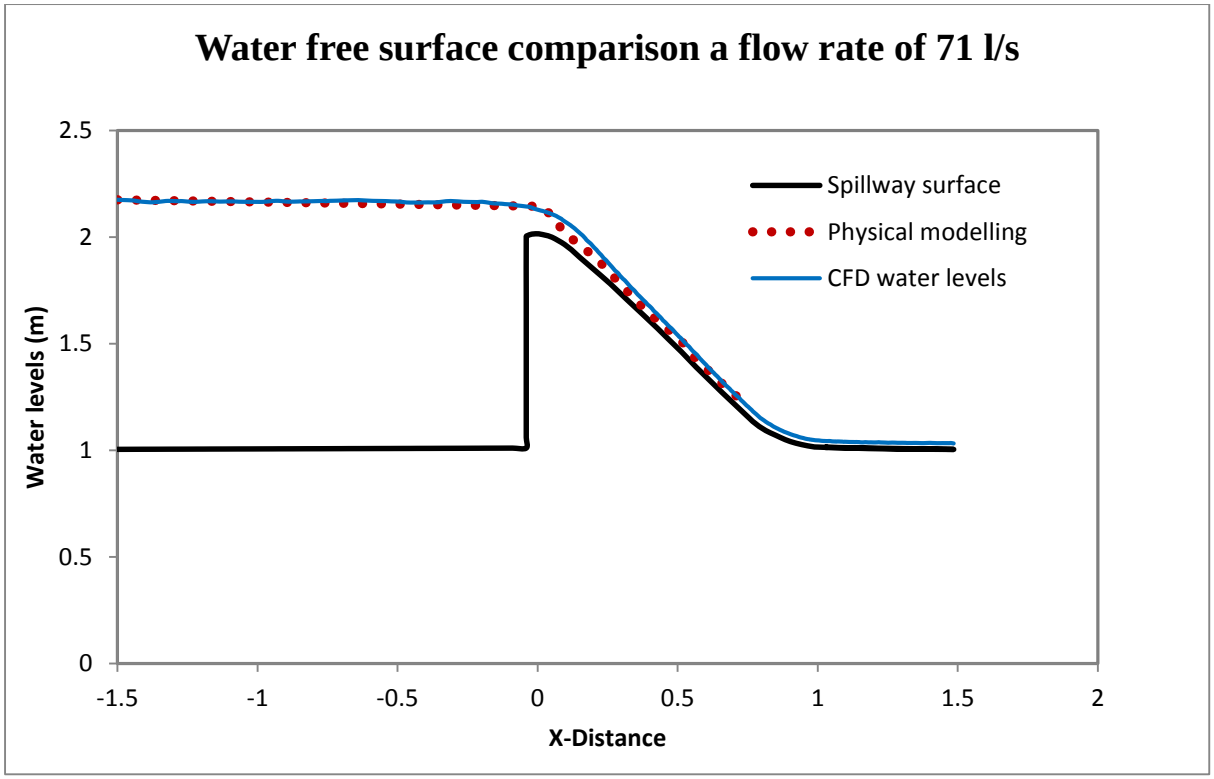

Figure D- 54: The comparison of CFD and experimental free surfaces for 71 l/s (Case-1)

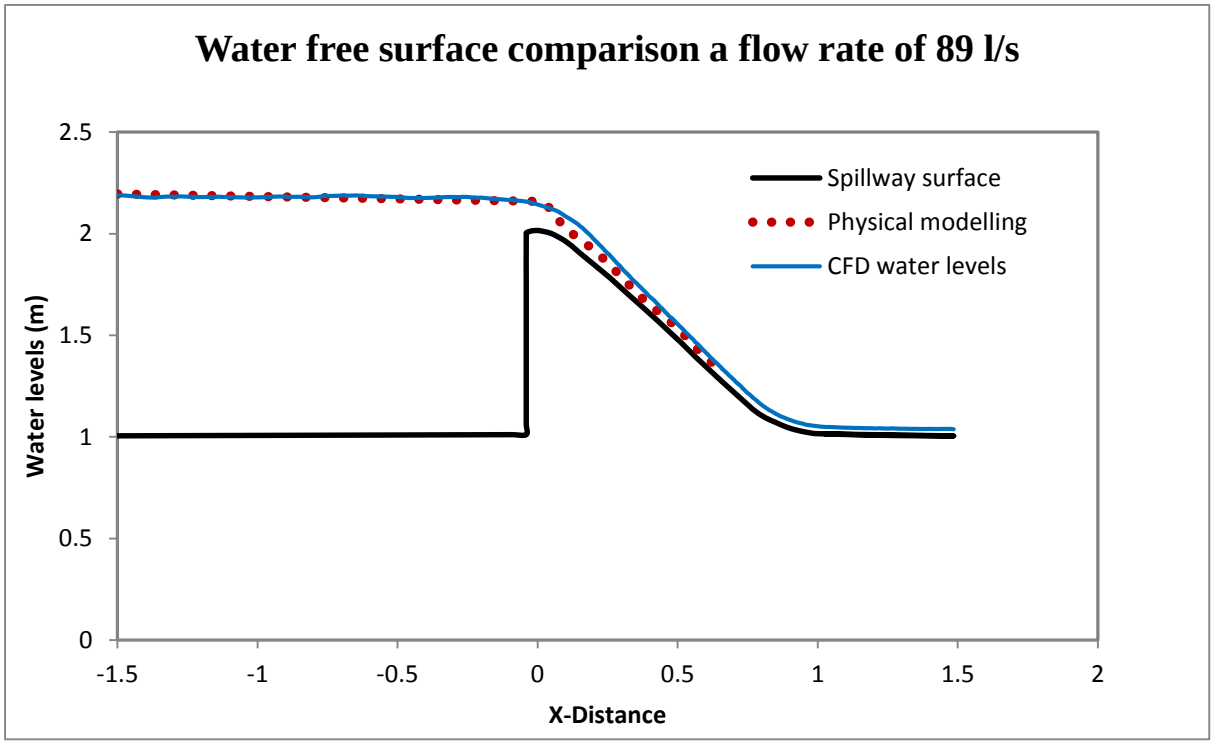

Figure D- 55: The comparison of CFD and experimental free surfaces for 89 l/s (Case-1)

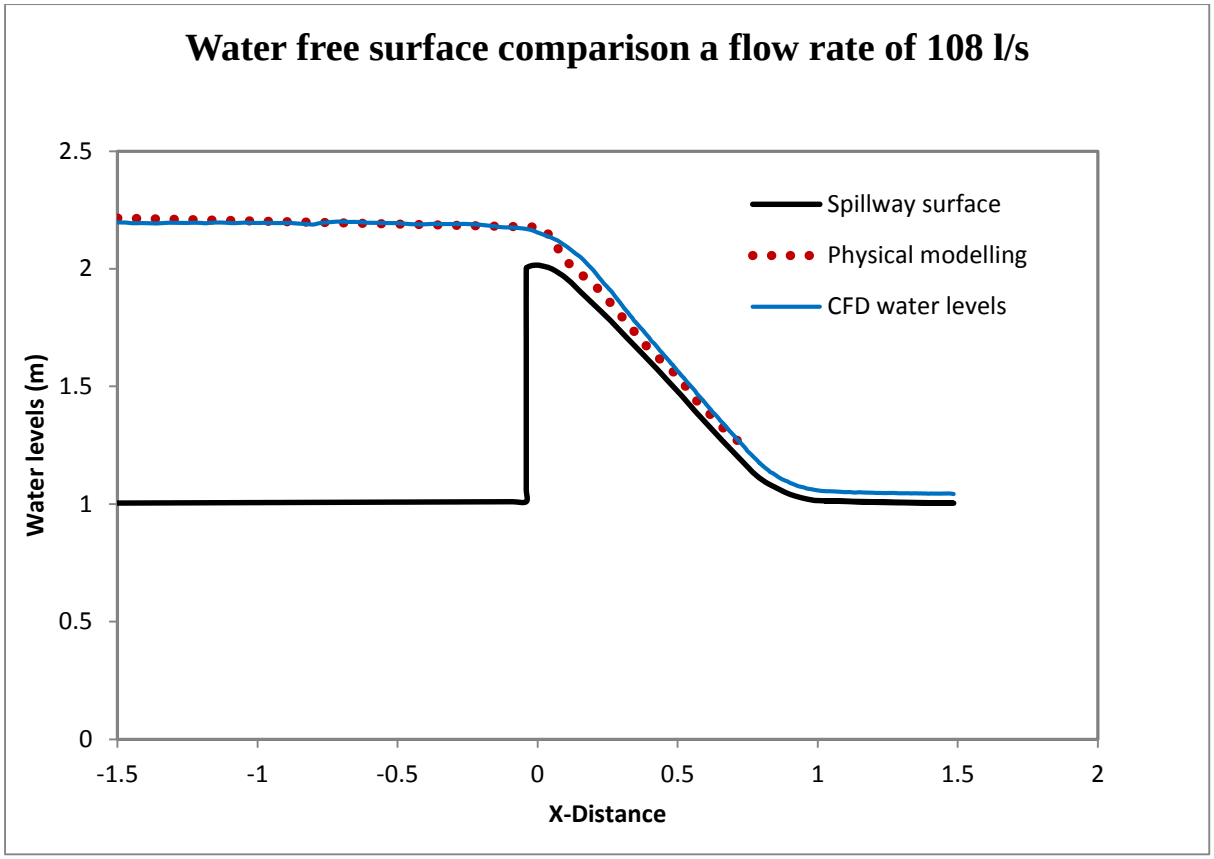

Figure D- 56: The comparison of CFD and experimental free surfaces for 108 l/s (Case-1)

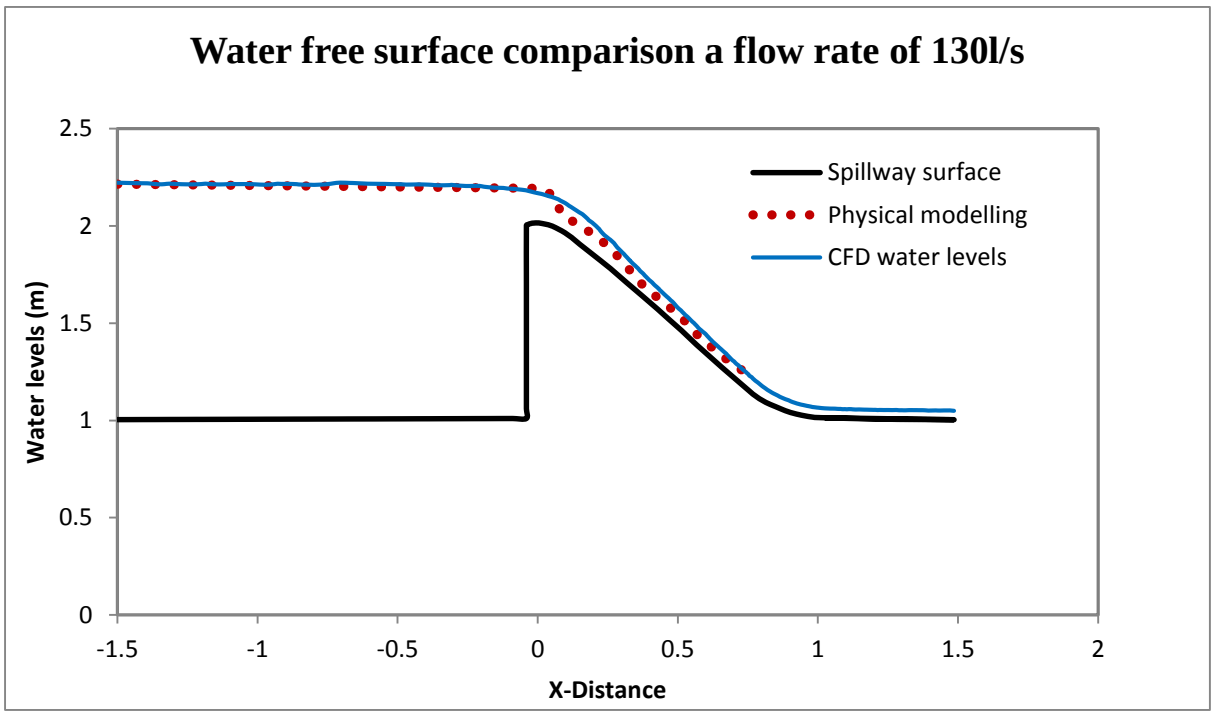

Figure D- 57: The comparison of CFD and experimental free surfaces for 130 l/s (Case-1)

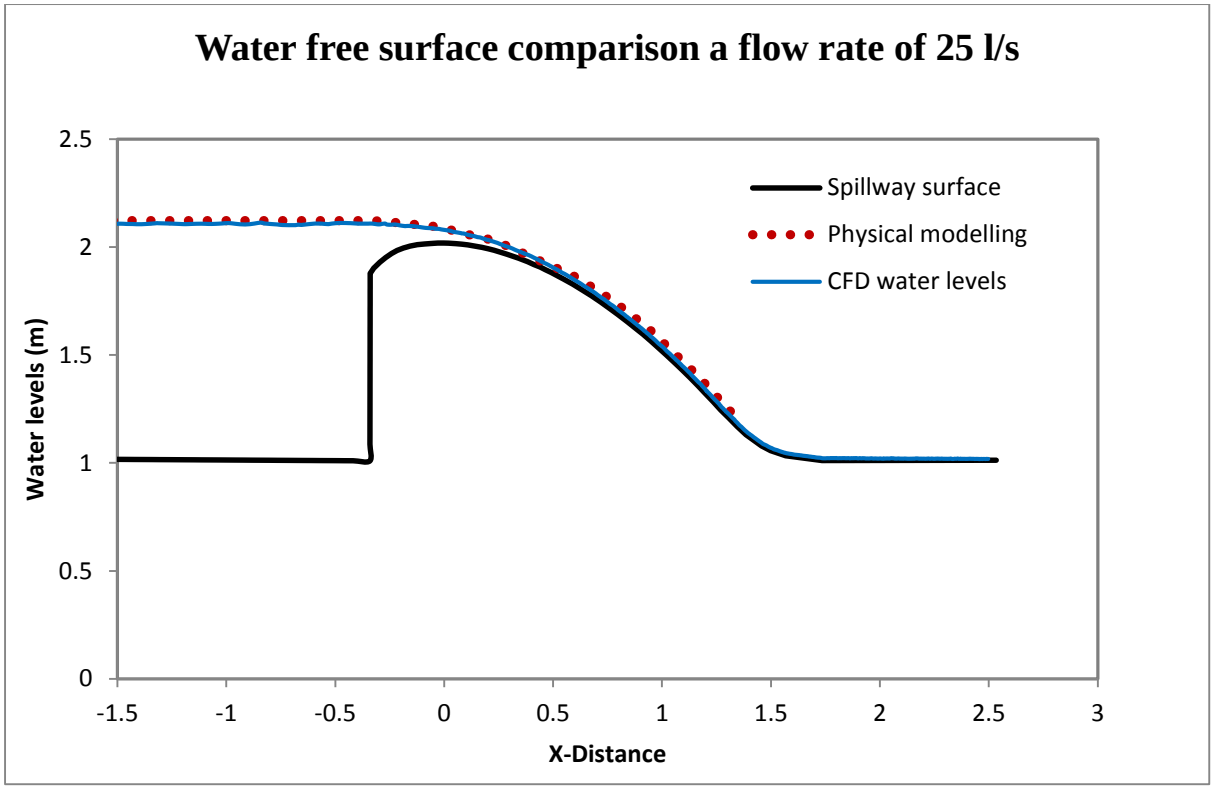

Figure D- 58: The comparison of CFD and experimental free surfaces for 25 l/s (Case-2)

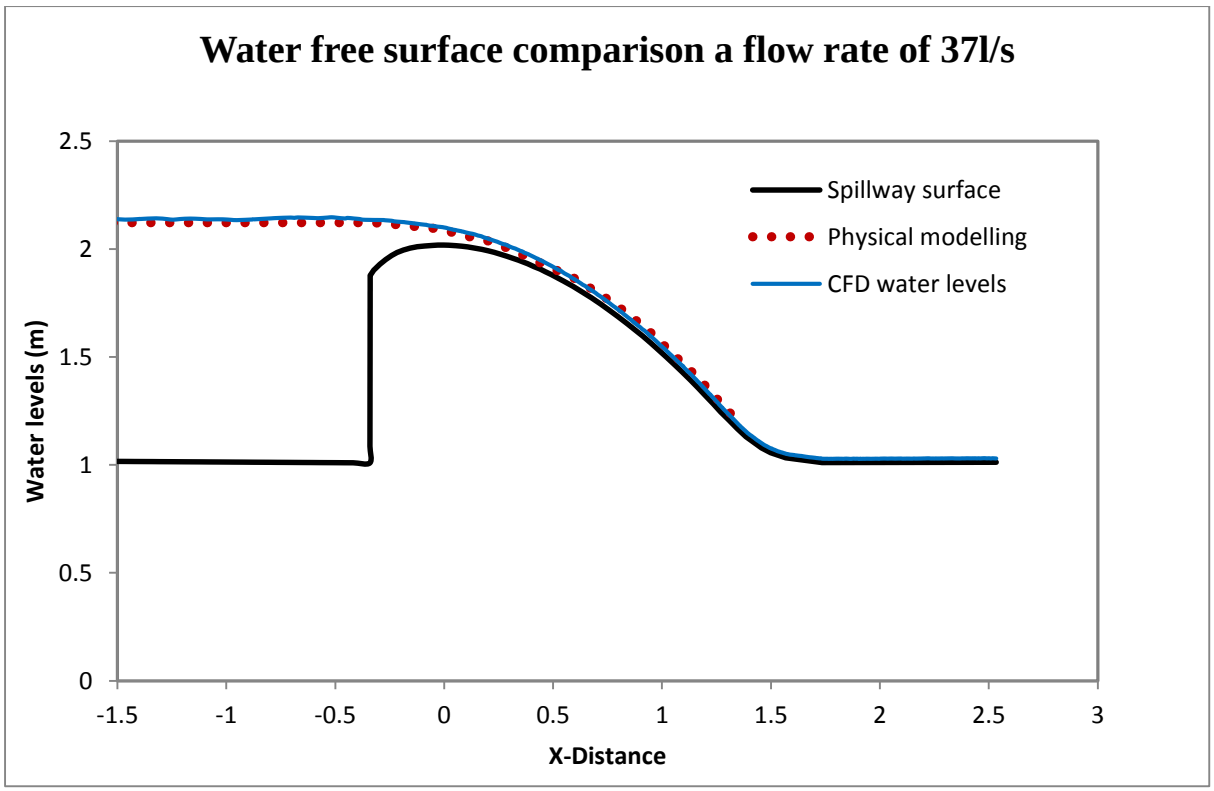

Figure D- 59: The comparison of CFD and experimental free surfaces for 37 l/s (Case-2)

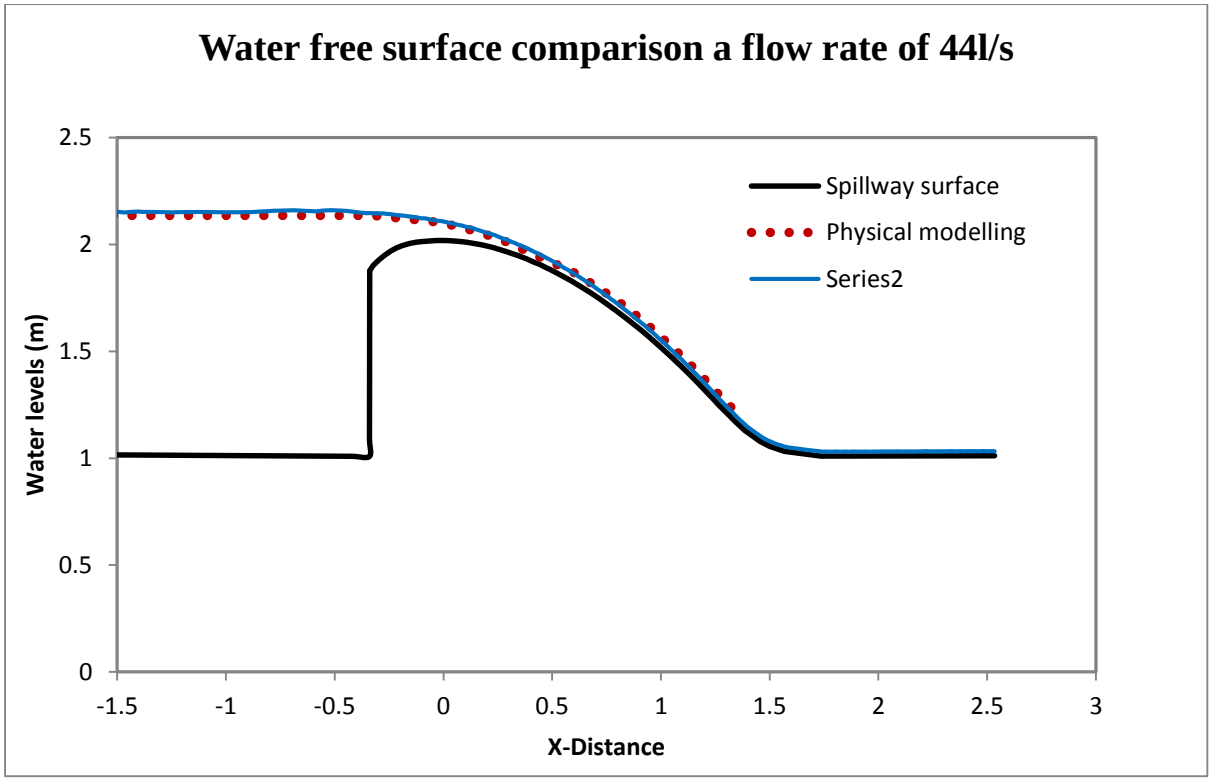

Figure D- 60: The comparison of CFD and experimental free surfaces for 44 l/s (Case-2)

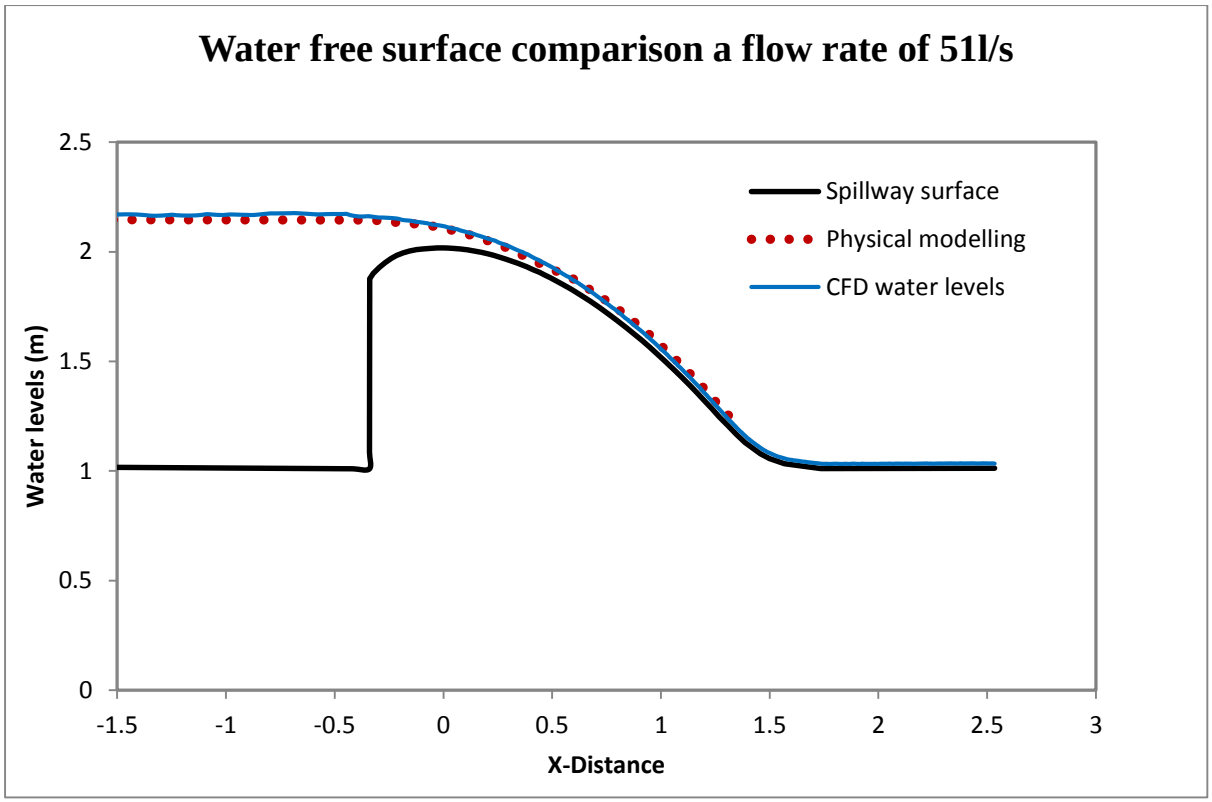

Figure D- 61: The comparison of CFD and experimental free surfaces for 51 l/s (Case-2)

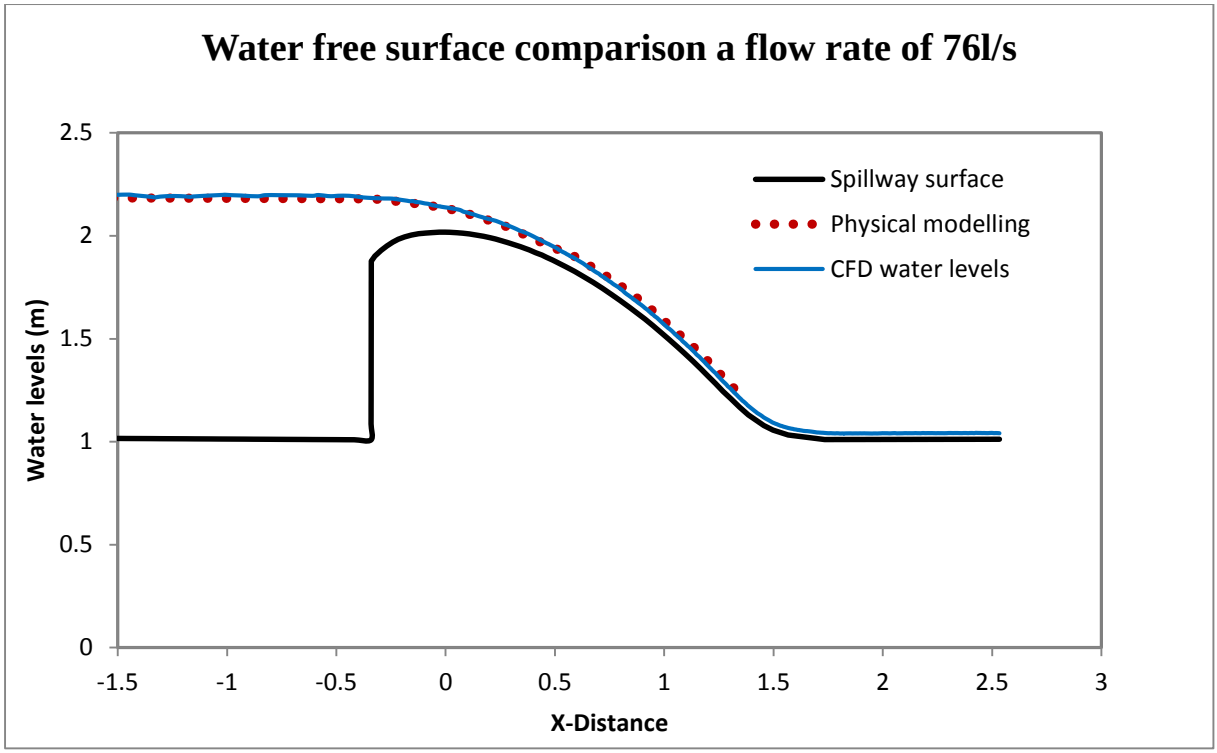

Figure D- 62: The comparison of CFD and experimental free surfaces for 76 l/s (Case-2)

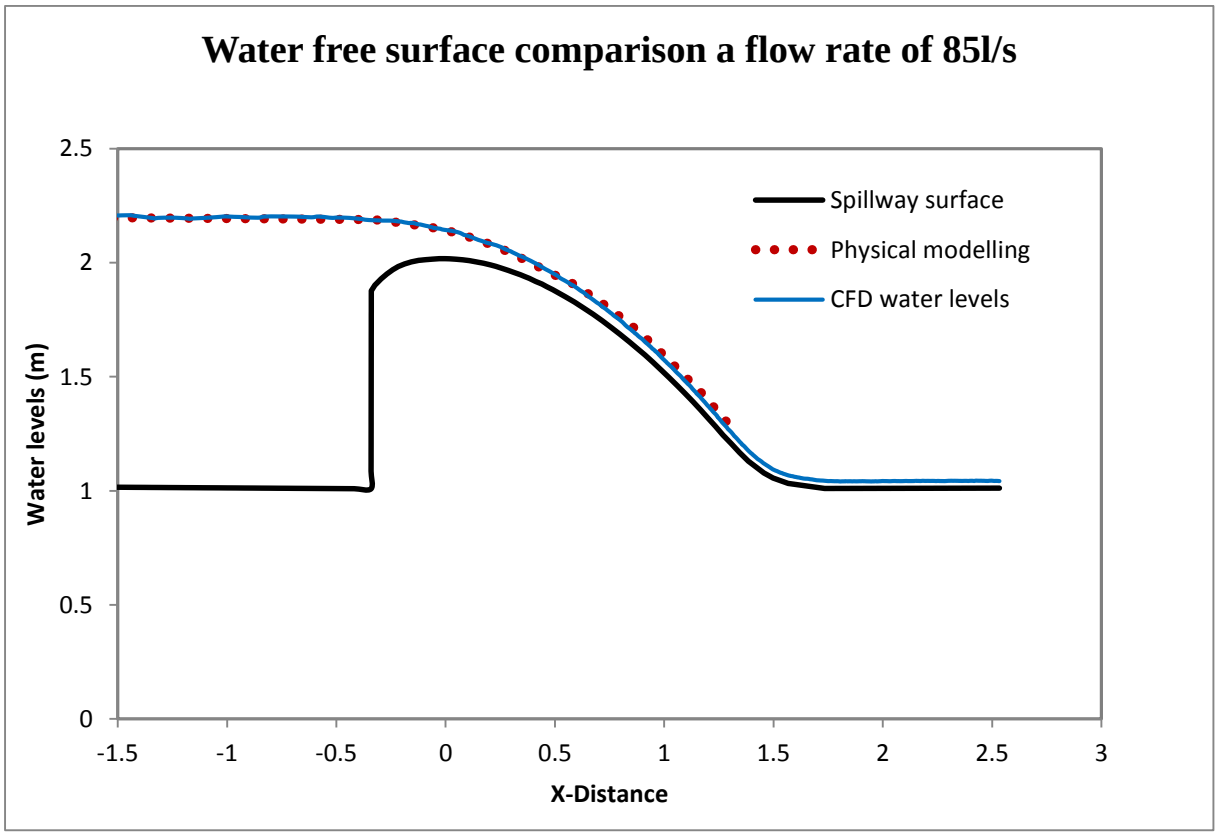

Figure D- 63: The comparison of CFD and experimental free surfaces for 85 l/s (Case-2)

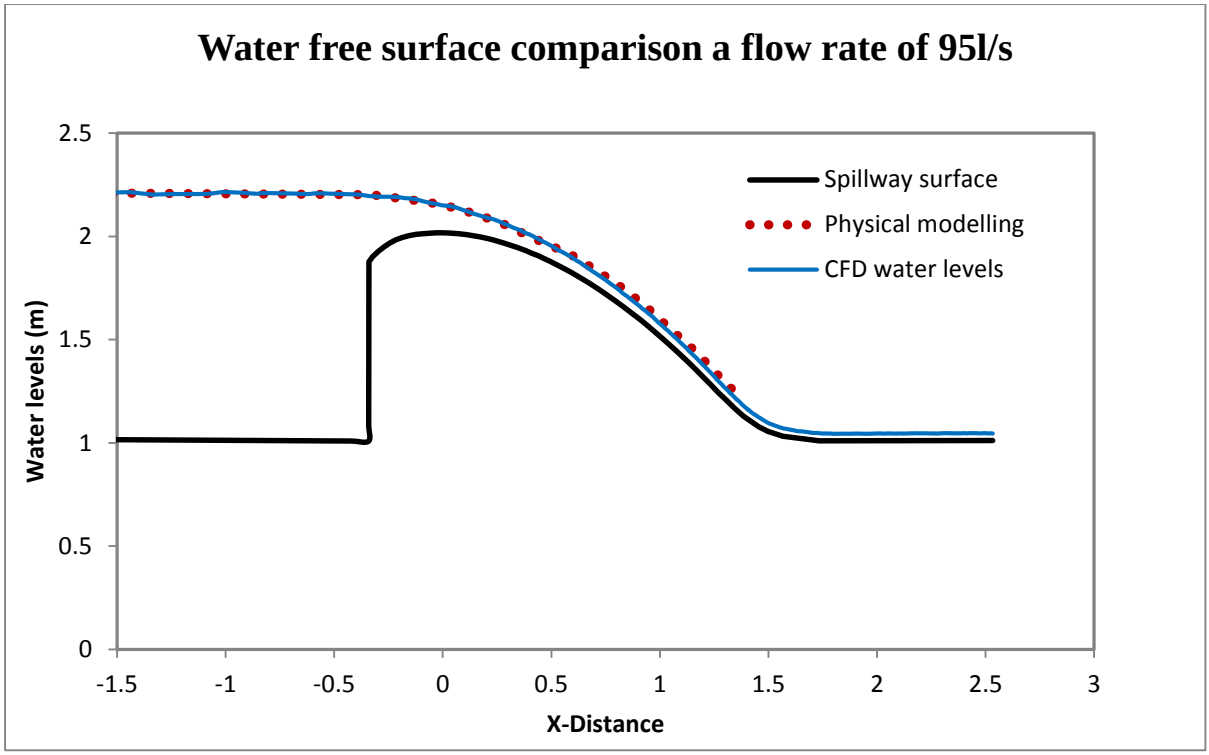

Figure D- 64: The comparison of CFD and experimental free surfaces for 95 l/s (Case-2)

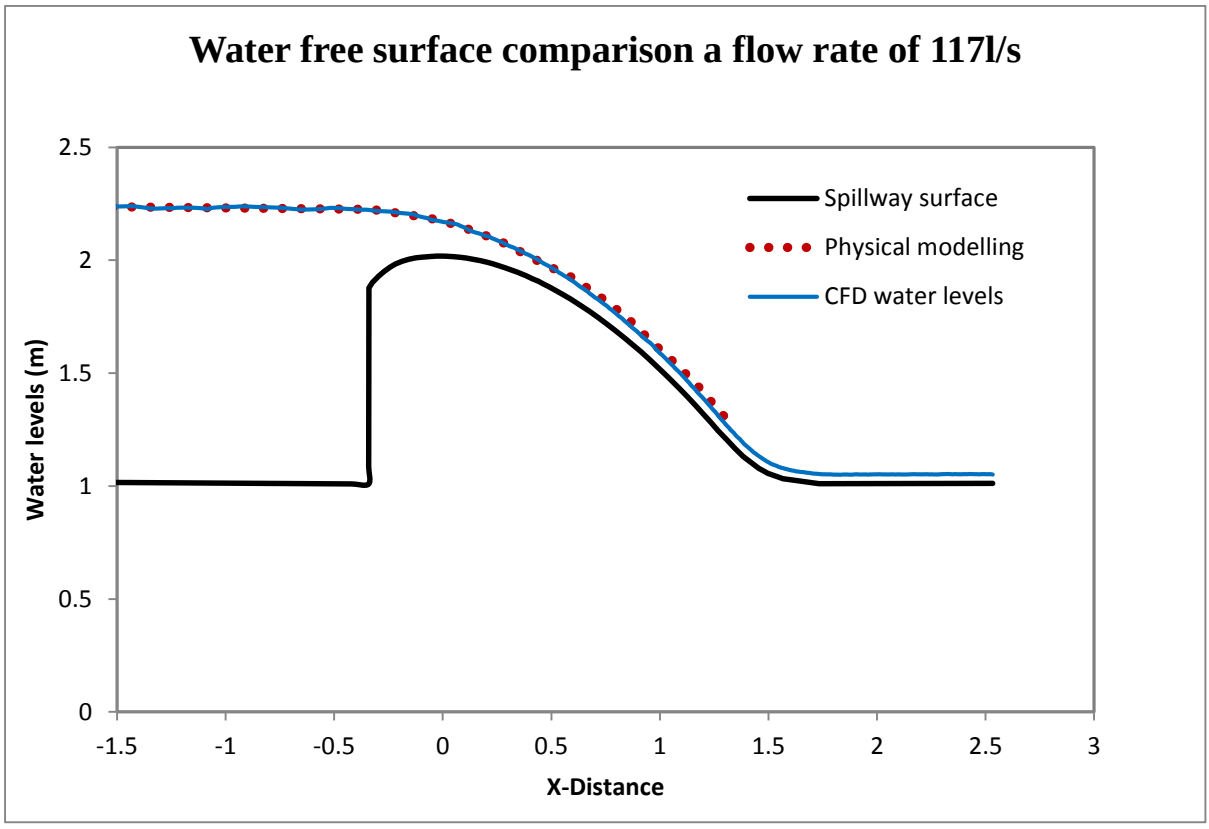

Figure D- 65: The comparison of CFD and experimental free surfaces for 117 l/s (Case-2)